Determining the Mechanisms Governing Transient Liquid Phase Bonding of Nickel-based Superalloys using Boron Containing Filler Metals

by

Eric D. Moreau

Submitted in partial fulfilment of the requirements
for the degree of Doctor of Philosophy

at

Dalhousie University
Halifax, Nova Scotia
April 2020

Dedication Page

I dedicate this work to my loving wife Danielle and our beautiful son Elio. None of this would have been possible without your endless support, patience, and uplifting spirit.

I love you both so very much

Table of Contents

LIST OF TABLES

TABLE OF FIGURES

ABSTRACT

During TLPB, an initial boron uptake (IBU) phenomena was quantified using DSC and microstructural analysis of a IN625 base metal (BM)/BNi-2 filler metal (FM) joint. A conceptual model was developed to quantify both the extent of isothermal solidification (IS) and IBU, in terms of the redistribution of boron from the liquid phase into the base metal, as precipitated borides.

An explanation for the formation of precipitated borides as a diffusionally affected zone (DAZ), was developed using diffusion path theory applied to a simple ternary Ni/Ni-Si-B (BNi-3) braze joint. The combined use of Thermocalc modelling and microstructural analysis confirmed that the DAZ formed in accordance with equilibria requirements in a multi-component system.

Ni200/BNi-3 and IN600 (Ni-Fe-Cr)/BNi-3 couples were examined to isolate the effects BM Cr-content has on the IBU, DAZ and IS rate. A substantial reduction in the rate of IS resulted as a result of the Cr in the BM. This was due to the formation of a low volume fraction of CrB versus, high volume-fraction, Ni_3B in the DAZ of Ni200, as predicted by calculated phase equilibria.

A broader examination on the TLPB behaviour of IN718/BNi-2, IN718/BNi-3 Ni200/BNi-2 and IN600/BNi-2 allowed a systematic, comprehensive assessment of BM and FM composition on TLPB behaviour. From this work, the IBU appears to be independent of BM/FM composition, leading to an IS zone (2WISZ) in the range of 23 to 43 μm. A base metal dissolution (BMD) process, which lead to braze gap widening, was governed by the compositional similarity between BM and FM. A greater BM to FM compositional difference equated to a greater degree of BMD. Gaps with no BMD (i.e. IN625/BNi-2) remained at 80 μm, while BMD lead to gaps as large as 167 μm (i.e. Ni200/BNi-2). Isothermal solidification was controlled by the rate at which boron is redistributed as metal borides within the BM - the DAZ. This was dependent on BM boride former content (Ni in the case of Ni200 and Cr, Nb, Mo for IN625, IN600, and IN718). The rate of IS was shown to increase linearly with the boride former concentration.

LIST OF ABBREVIATIONS USED

ASZ	Athermally Solidified Zone
BM	Base Metal
BMD	Base Metal Dissolution
DAZ	Diffusionally Affected Zone
DSC	Differential Scanning Calorimetry
EBSD	Electron Back Scatter Diffraction
EDS	Energy Dispersive Spectroscopy
FM	Filler Metal
ICP-OES	Inductively Coupled Plasma – Optical Emission Spectroscopy
IS	Isothermal Solidification
ISZ	Isothermally Solidified Zone
SEM	Scanning Electron Microscopy
TLPB	Transient Liquid Phase Bonding

ACKNOWLEDGMENTS

I would first like to thank all of my committee members; Dr. Paul Bishop, Dr. Dominic Groulx and Dr. Andre Phillion for their time and assistance throughout the course of the program.

I must also express my immense gratitude to my supervisor Dr. Stephen Corbin for his guidance, friendship and support. His approach to learning and discovery was refreshing and stimulating and has consequently further enhanced my passion and enthusiasm for the field. Furthermore, I would like to extend my appreciation and admiration for my all of co-workers in the HTTAL team that have come and gone throughout the journey; Addison Rayner, Colin Tadgell, Joel Chapman, Clare MacIsaac, Shannon Clemens, Cathy Whitman, Dan Cluff, Julian O'Flynn, and Clark Murray. Whether it be pondering over new findings, scratching our heads over a conundrum or taking a breather at a local watering hole, their input, humour, and compassion has made the experience ever more enjoyable.

The entirety of the research would have not been possible if not for the financial support provided by the NSERC/Pratt and Whitney Canada research chair; the opportunity of which I am incredibly grateful for. I would also like to acknowledge the invaluable assistance provided by Dan Chevalier (Mineral Engineering Center, ICP-OES) as well as the Patricia Scallion (Institute for Research in Materials (IRM, SEM/XRD Technician).

Lastly, I must thank my wonderful wife Danielle for her patience, understanding and kindness throughout the years, my mother for her love, encouragement and boundless support throughout my life, my father for instilling me with an innate sense of determination, curiosity and passion in all my endeavors, Jeff Franklyn for always supporting my enthusiasm and never ending questions towards the sciences, and the remainder of my family, friends and acquaintances which have undoubtedly made me who I am today.

CHAPTER 1 Introduction

The hot section of modern gas turbine engines which consists of the combustion and compressor stages (low- and high-pressure) demands the use of the most heat-resistant alloys currently available, as temperatures in excess of 1300°C are commonly encountered [1, 2]. The materials must therefore possess an adequate combination of oxidation resistance and strength to withstand the adverse effects of high-temperature fatigue and creep. Historically, Ni-based superalloys have dominated such applications due to their ability to maintain structural integrity under such conditions for their intended service life. Such alloys are heavily engineered; from their complex, highly tailored chemistry to manufacturing involving advanced multi-stage heat treatments, forming processes, etc. Consequently, superalloys are generally exceedingly difficult to machine and form into the wide assortment of components which comprise the hot section. Although direct casting of superalloys into complex shapes is capable of producing polycrystalline, directionally and single crystal components, their cost is generally prohibitively high. Furthermore, casting defects such as chemical segregation and porosity can greatly diminish their mechanical properties.

More recently powder metallurgy has shown great promise as a means of alleviating such issues, however, superalloy powders are also typically very difficult to compress and generally necessitate hot isostatic pressing (HIP) to achieve the mechanical properties of their wrought counterparts. Modern powder metallurgy techniques may one day remedy such issues however the technology is still currently in its developmental stage. As extensive machining is both costly, time consuming and wasteful. alternative methods of creating complex shapes is sought.

Although not a direct manufacturing method, one potential remedy involves an “additive” approach to generating complex components by combining simpler components using conventional joining methods, thereby minimizing secondary machining, reducing material costs (waste), etc. Many joining techniques currently exist, each with their own advantages and disadvantages, as shown in Figure 1-1.

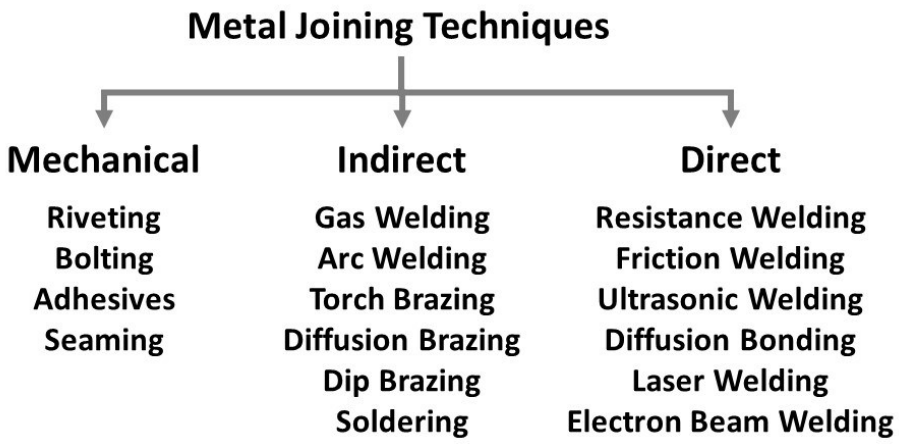

Figure 1-1 - Methods of joining metals [3].

Mechanical joining techniques are generally the least expensive of the joining methods, providing strong bonding without altering the microstructure of the base metal as they do not involve heating/melting and therefore are suited for joining dissimilar metals. Mechanical fasteners are however limited to simple, flat shapes, and typically reserved for low temperature applications. Comparatively, the wide variety of welding and brazing techniques which exist, categorized as either direct or indirect, can be implemented for a wide assortment of geometries and service conditions.

Indirect joining involves the use of an additional filler metal, while direct joining is accomplished through metallurgical bonding of the substrates alone. For instance, Gas and arc welding involve the melting of a consumable electrode (arc) or filler (gas) material along the joint region of the base metal which is also locally liquified. Comparatively, melting of the base metal is negligible in brazing and soldering processes as the filler materials are designed to melt and spread at temperatures far below the melting temperature of the base metal. Comparatively, torch, diffusion and dip brazing differ only by the method by which heating of the couple is achieved, i.e. gas torch, electrical resistance (diffusion brazing), dip (molten salt flux), etc. Lastly, soldering typically implies relatively low temperature, $< 450°C$ brazing in accordance with American Welding society (AWS) and principally used in the electronics industry [4].

Direct joining techniques are typically reserved for high-throughput production of welds and seams, such as the production of pipe from sheet metal, which are generally manufactured using resistance or friction welding. An example of components created using linear friction

welding is illustrated below in Figure 1-2. The lack of a substantial quantity of liquid phase requires the application of considerable pressure to encourage solid-state bonding achieved through a combination of plastic deformation and chemical diffusion.

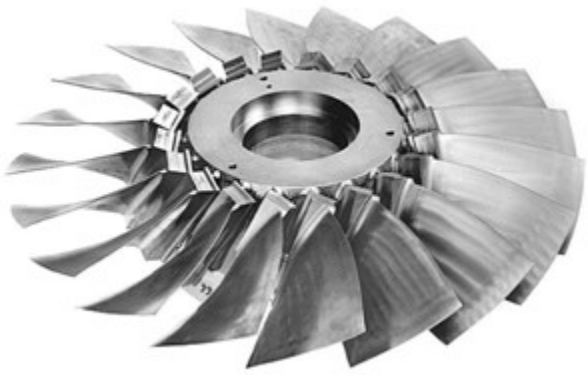

Figure 1-2 - A blisk (compressor blades and disk) created using linear friction welding [5].

Proper joining requires careful considerations of the materials under consideration and their application. For instance, elevated temperature exposure resulting from welding processes can have adverse effects through the formation of a heat affected zone (HAZ). Ideally, bonding of two components would result in negligible distortion, warpage and/or misalignment. For instance, most welding achieves bonding by melting of a filler metal and the substrate material, leaving a fusion line. Welding is therefore best suited for bonding thin components, although misalignment can be corrected through adequate jigging, the fusion line must be mechanically removed, and the bond is limited to the accessible surfaces. Lastly, since melting of the base metal occurs, the microstructure is permanently altered, thus representing a mechanical/microstructural discontinuity wherein fracture would likely preferentially emanate. It is therefore clear that welding techniques are unsuitable for joining of heat-resistant alloys given the demanding requirements of the compressor section of jet turbine engines.

One form of welding known as *diffusion welding*, circumvents issues related to excessive temperature and fusion of the base metal. This is achieved by subjecting the components to elevated temperature (solid-state) for an extended period of time under high pressure static loading supplied by jigs, fixtures and supports. Welding of the substrates occurs through a combination of plastic deformation and chemical diffusion; the primary disadvantages are however, the extensive processing times required to achieve a void-free joint, distortion/warpage of the component(s) as

a consequence of the large loads, and most importantly issues related to joints of variable width and sensitivity to surface cleanliness.

A relatively recent method was developed which combines the advantages of liquid phase bonding (welding) with the dimensional stability of diffusion welding, known as *Diffusion Brazing* [6-8]. Also known as *Transient Liquid Phase Bonding* (TLPB), diffusion brazing involves controlled heating of a metallurgically compatible, low-melting point filler metal sandwiched between the components, generally with a small static load to maintain alignment. The filler metals are designed such that minimal melting of the parent metal occurs at the process temperature. Upon forming a sufficient quantity of liquid phase, capillary actions promote subsequent spreading and wetting of the liquid phase within the joint region with the progressive diffusion of the chemical constituents into the base metal. as the filler metal is typically a very thin interlayer or powder/paste, progressive mass transport of the species into the base metal results in progressive *Isothermal Solidification* (IS) of the liquid phase until completely consumed, leaving a solid joint ideally indistinguishable from the parent metal. Below are some the major benefits of diffusion bonding, particularly regarding Ni-based superalloys [3,4,8,9]:

1. High reproducibility
2. Excellent control of final joint width
3. Exceptional joint area filling
4. Tight control of melt flow/spillage
5. Less sensitive to surface contamination, self-fluxing filler metals
6. Greater control of processes parameters (temperature, heating rates, atmosphere, etc.)
7. Low melting point filler metals < 1100°C, minimizes the deleterious effects of high temperature exposure on the components while reducing operation costs.

Since its original inception in the 1970s, the technique has found application is vast array of materials ranging from advanced titanium alloys and intermetallics, to the hermetical sealing of borosilicate-glass with superalloys [10]. Consequently, continuous research and development has generated a wide assortment of filler metals (FM) designed to provide a superior combination of wetting, spreading, melting temperatures and alloying characteristics to optimize compatibility between substrate and filler metal as shown in Table 1-1. Aside from OEM and joining of superalloy components, the most common application of TLPB is for wide-gap repairing of cracks which may have formed during service of turbine blades, and/or other components of the compression stage, as shown in Figure 1-3 [2,4,7,11-12]. Despite the effectiveness of the

technique, further focus and development is required to overcome the relatively lengthy processing times and adverse effects of intermetallics, grain growth, etc.

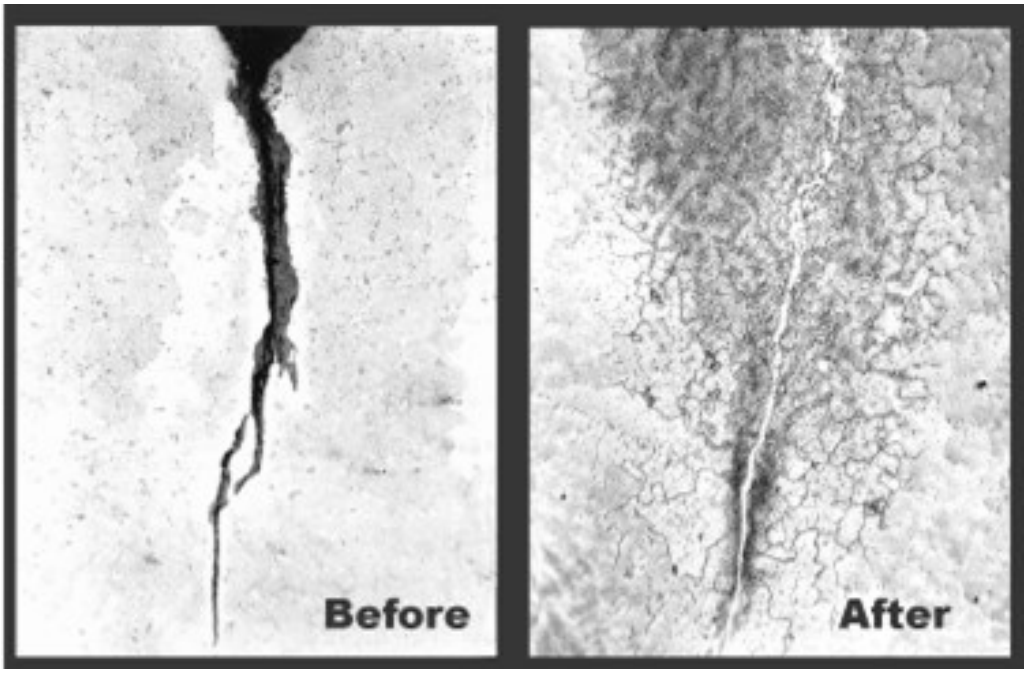

Figure 1-3 - Compressor blade repaired using TLPB [13].

Table 1-1 - Aerospace applications for various brazing alloys during diffusion brazing of superalloys [14-16].

Brazing Alloy	Elements	Base Material(s)	Engine Section
AMS4058	Ni-Pd-Cr-B-Si	Hastelloy, Inconel	LP turbine stage
AMS4786	Au-Ni-Pd	Hastelloy, Inconel	Blade Repair
AMS4787	Au-Ni	Inconel 600 and 625	Fuel Sys., Comp.
AMS4778	Ni-Si-B	Hastelloy, Inconel, Waspalloy	APU
AWS4777	Ni-Cr-Si-Fe-B	Hastelloy, Inconel, Waspalloy	Compressor

Wetting and spreading is a complex interfacial phenomenon highly sensitive to a variety of factors, including but not limited to; surface contaminants (organics, passivation/oxidation), temperature/viscosity, pressure, atmosphere, and more importantly the characteristics of the FM. As most vacuum brazing is performed in the absence of any fluxing agents, best practice generally involves extensive cleaning/degreasing treatments, acid treatments, polishing/sand blasting, plating, and in the most demanding cases; aggressive fluoride-ion cleaning [13]. Vacuum brazing minimizes issues associated with porosity resulting from vaporization of organics and/or trapping

of gasses between the BM, it is however inherently a batch process which greatly limits production rates.

The following introductory sections have been provided as a basis for the current work, which emphasis the fundamentals of transient liquid phase bonding (TLPB) and the chemistry of braze alloys. Additional information will be allocated to differential scanning calorimetry (DSC) and other processing/characterization equipment implemented in the present research.

1.1 Transient Liquid Phase Bonding (TLPB) in Aerospace Applications

Nickel superalloys were one of the first materials to exploit Transient Liquid Phase bonding (TLPB) as a joining process through the use of a binary Ni-4B eutectic FM [6,7]. Since then, a plethora of FMs have been designed to ensure compatibility with the vast number of superalloy compositions currently in service and to address key issues such as sufficient wetting and spreading. Conventional welding creates a heat affected zone, which will typically act as point of failure to the detriment of the alloy. Comparatively, TLPB can yield joints indistinguishable from the parent (base) metal in a far more controlled and repeatable process. Other major benefits include relatively low joining temperatures, the ability to operate at or slightly above the joining temperature, reduced fixturing requirements, high tolerance for fluxes and surface contaminants, etc. Thus, it is for the reason described above that TLPB has been the primary route by which aerospace components are joined, as they typically possess considerably stricter tolerances, and strength requirements, particularly at elevated temperatures. Vacuum brazing or TLPB of superalloys is currently, however, limited to the less demanding components which make up the gas turbine engine, in part due to the strict requirements, but also due to the inferior mechanical performance of TLPB joints as a consequence of porosity, secondary phases, poor wetting [12].

The FM alloys adopted are typically in the form of atomized brazing alloy powders with or without organic binding agents, thin (rolled) foils, and ultra-thin amorphous melt spun foils. Other methods involve electroplating, cladding, or chemical vapor deposition (CVD) of the substrates with the desired brazing alloy. Amorphous foils are preferred in many production environments as they; can easily be stamped into preforms, display a narrow melting range and do not contain binders. They are however far less common to the fine atomized powder which are highly suited for repairs, wide-gap brazing, and situations requiring application of the braze outside

the actual joint wherein capillary forces inevitably draw the liquid within the joint [17,18]. Any binders present are quickly pyrolyzed at intermediate temperatures. Electroless Ni-P and Boronized (CVD) coatings are effective means of creating the FM directly to the substrate. Such techniques are designated eutectic bonding or *reactive bonding* such as that used in heat exchangers [19, 20].

Typically, once the TLPB couple i.e. BM/FM/BM is prepared it is common to secure the couple using clamps and/or fixtures to promote bonding, maintain alignment and reduce porosity. The resulting braze assembly in then suitable for the actual brazing operation. Vacuum furnace brazing is generally the method of choice for high-throughput production of aerospace components as compared to much less elaborate techniques such as flame brazing, the principal advantages being [15]:

1. Minimal jigging requirements (i.e. fixtures).
2. Removal of gaseous by-products (binders and/or contaminants)
3. Reproducible and consistent processing.
4. Flux-less brazing – no need for post-braze cleaning.
5. Enhanced Process Control (temperature, atmosphere, etc.)

The current variety of Ni-based, boron-bearing FMs are a consequence of progressive tailoring and development to address issues related to optimizing wetting, spreading, the repair and joining of wide-gaps, corrosion resistance, mechanical performance and most importantly, metallurgical compatibility between the numerous Ni-based alloys currently in service and continuously in development. For instance, BNi-1A (Ni-14Cr-3.2B-4.5Si-4.5Fe) alloys have been used to bond gas diffuser components in the hot section using Ni-based superalloys owing to its excellent fracture toughness. The BNi-1A alloy however lacks the free-flowing characteristics of alloys such as BNi-2 and BNi-3 and issue which in certain situations can be overcome using preplaced preforms or paste on the faying surface as opposed to in the fillet region, reducing the need for fluidity [21]. BNi1A was actually a refinement of the original carbon rich (0.75 wt% C) BNi-1 created to improve compatibility with carbon steels and stainless steels which contain significant concentration of carbon in comparison to Ni-based superalloys.

The fact that Ni-Cr-Si (BNi-5), Ni-P (BNi-6), and Ni-Cr-P (BNi-7) alloys cost less than 0.003$/sq. inch (at 0.001” gap width) as compared to 6.45$ for Ni-80%Au (BAu-2) highlights the

major economical incentive which has continuously encouraged adopting precious metal-free FMs [21]. Both B- and P- bearing FMs display excellent wetting/spreading, gap filling characteristics (self-fluxing), however Boron-containing alloys have become increasingly popular as they yield significantly stronger joints (less brittle), despite the fact that those containing B are far more prone to deleterious intermetallic precipitation in the parent metal. The interstitial diffusivity of Boron also greatly accelerates the rate of IS versus that of phosphorus containing alloys which do not display appreciable levels of precipitation [22]. Opting for Phosphorous rather than Boron is generally required for the nuclear industry as it has a strong influence on the fission rate (large neutron absorption cross section) [21].

In summary, proper FM selection (compatibility) is a highly case-by-case decision due to the great number of variables involved in brazing, thus most often, adopting for a robust trial and error approach is the most effective route for optimizing joint performance. This is however laborious, time consuming and costly thereby representing a great inefficiency which could be minimized through improved understanding of the numerous parameters governing the process. The following material has been provided as a reference to the fundamental aspects of TLPB in which they relate to Ni-based superalloys with boron-bearing FMs.

1.2 Nickel and Ni-based Alloys

Pure Nickel is a remarkable metal which possesses an array of desirable properties which include excellent corrosion resistance, ductility, high strength and ferromagnetisms. Its applications in its elemental state ranging from decorative plating, catalyst, alloying additions, etc. Over 50% of Nickel produced is used in the creation of stainless steel via the intermediate product ferronickel [1]. However, like most base metals (BM) its performance and attributes are optimized when alloyed with other elements such as Cr, Co, Fe, Nb, Al, W, and Ti, to name a few. Most alloys involve highly tailored chemistries typically intentionally designed with over 6 elements, hence the designation, S*uperalloys* [2,23]. This also applies to the far less commonplace Cobalt- and Iron-based alloys. Strengthening in superalloys is achieved through the principal metallurgical strengthening mechanisms - the most significant being solid-solution and precipitation strengthening. Many elements display appreciable solid-solubility with Nickel, however the most common solid-solution strengthening elements include; Fe, Cr, Co, Al, Ti, Mo, W, and Ta - some of which may contribute through other strengthening mechanisms, depending on their

concentration (i.e. Al, Ti, Nb, Cr, Nb, etc.) [23]. Precipitation strengthening in Ni-base superalloys is unique as it relies on the formation of a large volume-fraction (< 70 %) of coherent γ'-Ni_3(Al, Ti) and/or γ"-Ni_3Nb precipitates which greatly enhances mechanical performance, particularly at high temperatures. Lastly, precipitate/dispersion strengthening refers to the contribution of discrete secondary phases such as Carbides, Borides, Nitride, and other incoherent phases, which enhance high-temperature creep resistance via pinning of the grain boundaries. The stability of various carbides is illustrated schematically in Figure 1-4, revealing the elements constituting the "carbide formers i.e. Ta, Nb, etc.

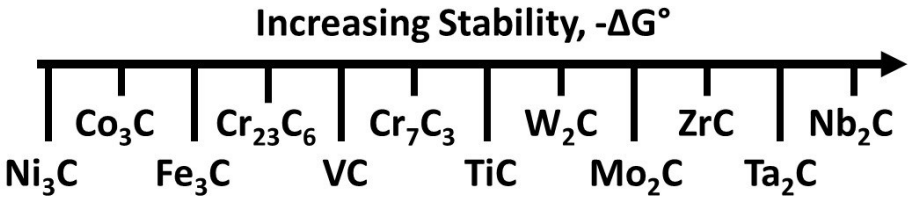

Figure 1-4 - Stability of common carbides at 1400°C [24].

The mechanical performance of Ni-based superalloys INCONEL625 (solid solution strengthened) and INCONEL718 (γ'-Ni_3Al and γ"-Ni_3Nb precipitation hardened) are provide below in Figure 1-5, to further illustrate the influence between the differing strengthening mechanisms as a function of temperature. Alloys designed for precipitation hardening display exceptional strength with a minor decrease in ductility, generally attributed to increased alloying with Al, Ti and/or Nb + Ta. Although, their mechanical properties exceed those of IN625, it is at the cost of corrosion resistance (a considerable amount of Fe used to minimize cost) and creep life which depreciates at a rate far greater than that of IN625. Nonetheless, both alloys are used extensively in a variety of demanding applications ranging from aerospace, pharmaceutical, nuclear, and cryogenic applications [23].

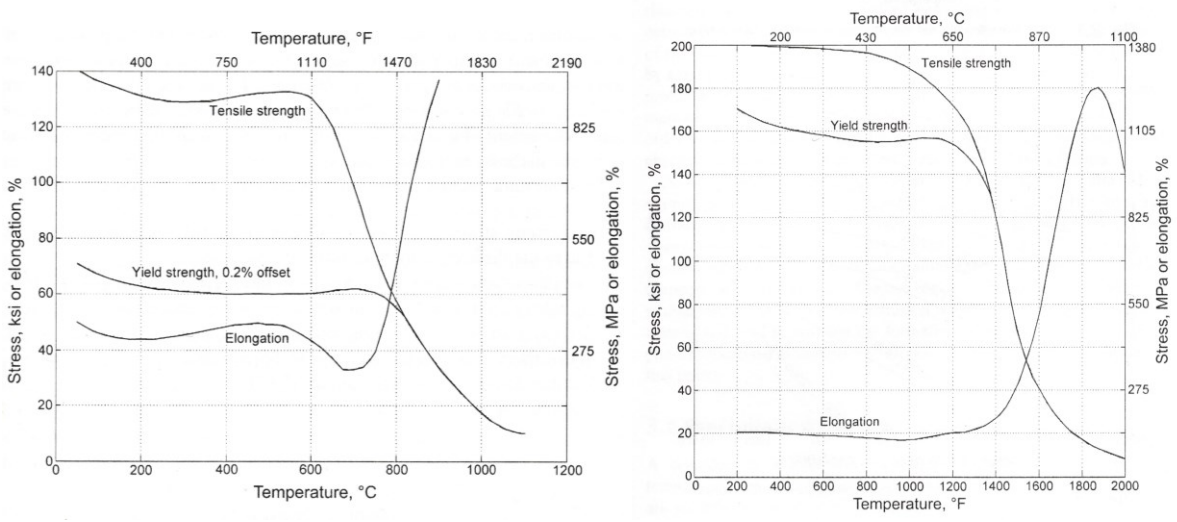

Figure 1-5 – High-temperature mechanical properties of IN625 (Left) and IN718 (Right) [1].

As with other metals, Ni-superalloys can be created using a variety of processes including casting, forging and powder metallurgy, depending on their application and geometry. Traditionally, turbine blades and other complex geometries have been produced using lost-wax investment casting, yielding components with equiaxed, directional, or single crystal microstructures, while other components can be forged or created using near-net shape processing or powder alloys. More recently, the latter has received increasing attention due to the advantages of near-net shape processing (cost, dispersion strengthening, process control, etc.) yielding a variety of next generation Ni-based superalloys alloys manufactured using highly processed powder alloys typically formed using hot isostatic pressing (HIP) [23]. It is therefore apparent that the most important parameter governing the manufacture and processing of superalloys is creating a microstructure which can maintain adequate mechanical properties at elevated temperatures and under highly oxidizing conditions. The latter can be circumvented using thermal barrier coatings and proper alloy selection, the former however requires carefully designed manufacturing, heat treatment, and overall design to minimize the deleterious effects associated with recrystallization, grain growth, precipitate coarsening, etc. [25-27].

1.3 Boron-containing Nickel-based Brazing alloys

Many of the commercially available brazing alloys consist of nickel-based eutectic or near-eutectic type compositions as they greatly decrease the temperature required to achieve a stable (though transient) liquid phase, thereby reducing processing costs, increasing service temperatures and

minimizing the deleterious effects elevated temperatures pose on the mechanisms governing the high-temperature mechanical properties of Ni-based superalloys (precipitation strengthening, dispersion strengthening, etc.). The design of brazing alloys requires the calculated addition of solutes which provide the most significant reduction in melting point, T_M in the lowest concentrations possible as to limit the formation of intermetallics which tend to be brittle and therefore degrade mechanical performance. In Nickel-based alloys these additions, also known as melting point depressants (MPDs) generally include three elements: Boron, Phosphorous and Silicon.

Binary Nickel-based Brazing Alloys

The addition as little as 3.6 wt% Boron (17 at% B) e.g. the Ni-rich eutectic composition of the Ni-B system, reduces the melting point of pure Ni (~ 1455°C) to 1093°C [28-30]. Similarly, binary Ni-Si and Ni-P eutectic concentrations of 19 wt% Si and 11 wt% P yield eutectic melting temperatures of 1143°C and 870°C, respectively [28]. In practice however, such binary brazing alloys are uncommon as further reductions in solute concentrations and/or melting point can be achieved using alloys consisting of three component (ternary) or more. Ultimately, interlayer (or braze) selection is a difficult compromise between the time required to achieve complete IS, the minimum melting point, the formation of intermetallic phases, and most importantly the quality of wetting and spreading. Other binary alloys which do not involve the typical B, P and Si MPDs are Ni-Au (AMS4787), Au-Pd (Paloro) and Ni-Pd (Palni) alloys which typically yield joints with superior ductility, corrosion resistance, and reduced grain boundary penetration associated with boron-containing FMs [11]. Furthermore, due to their extensive solid solubility do not suffer from the formation of embrittling secondary intermetallic phases. Precious metal containing FMs are however prohibitively expensive and limited by their respective maximum service temperatures; > 925°C (50 at% Au) and > 1225°C (50 at% Pd) [21].

Boron is a light interstitial metalloid element with properties akin to that of Carbon and Silicon. Although the majority of the demand for boron is in the manufacture of borosilicate glass, ceramics, and cleaning products, in its elemental state it is reserved for niche applications which include, superconductors, magnets, wear coating, boron-steels, and brazing alloys. Binary Nickel-Boron brazing alloys have limited commercial application due to their relatively high liquidus temperature which can be significantly decreased through minor additions of Si, Fe, Cr, etc. The

complete and Ni-rich regions of the Ni-B binary phase diagram are shown below in Figure 1-6, illustrating three key features; (1) the effectiveness of B as a MDP in Ni, (2) the negligible solubility of B in γ-(Ni) and Ni in (B), and lastly the presence of four adjacent eutectics and their corresponding stoichiometric intermetallic phases, Ni_xB. As most commercial Ni-B filler metals contain less than 4 wt% B, the most important eutectic melting reaction with regards to TLPB is that of, L → (Ni) + Ni_3B, which occurs at 3.6 wt% B and 1093°C [4,15]. The maximum solubility of B in (Ni) is approx. 0.15 wt% (0.3 at%) at the (Ni)/Ni_3B eutectic temperature, thus doping of superalloys with B generally leads to the formation of hard intergranular borides; a technique intentionally applied in Ni-superalloys to significantly improve high temperature creep resistance associated with grain boundaries [2]. However, due to the increased tendency for micro porosity during casting B levels are typically maintained below 0.01% for cast alloys [31].

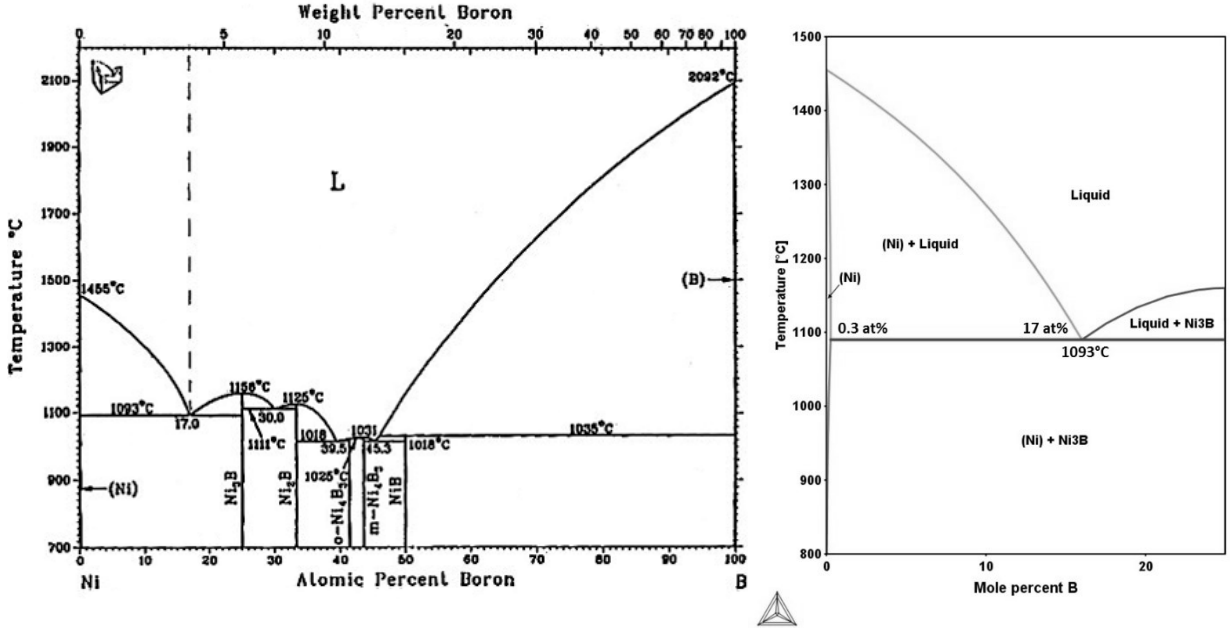

Figure 1-6 - Experimental and calculated (Thermocalc®) Ni-B binary phase diagrams [28].

Boron displays extremely rapid diffusivity in Ni as a consequence of its small size, permitting interstitial diffusion of B in vacant octahedral sites rather than relying on vacancies through considerably more sluggish substitutional diffusion. This enhanced diffusivity is likely responsible for the accelerated kinetics observed during TLPB using B-containing FMs, e.g., the initial rapid equilibration and BM dissolution stages [28-30].

Multicomponent Nickel-Boron-X Brazing Alloys

Nicked-based alloys such as those based on the Ni-B systems have limited applicability in brazing due to their elevated solidus and liquidus temperatures; a constraint which can be easily remedied through the addition of an additional element such as Si, Cr, Fe, Co, etc. as illustrated in Table 1-2 - a summary of the most commonly used commercially available Boron-containing FMs.

Table 1-2 - Most common commercially available Boron-containing Ni-based filler metals [14].

AWS	Composition (wt%)					Solidus/Liquid
BNi-#	B	Si	Cr	Fe	Other	Temperature Range
1	3.1	4.5	14	4.5	-	977-1077°C
2	3.2	4.5	7	3.0	-	971-999°C
3	3.2	4.5	-	-	-	982-1038°C
4	1.8	3.5	-	-	-	982-1066°C
5	-	10	19	-	-	1079-1135°C
6	-	-	-	-	11 P	-
7	-	-	14	-	10 P	-
8	-	7	-	-	23 Mn, 4.5 Cu	982-1010°C
9	3.6	-	15	1.5	-	979-1054°C
10	2.5	3.5	12	3.5	16 W,0.5 C	971-1160°C
11	2.7	3.8	11	3.3	12 W,0.4 C	971-1093°C
12	-	-	25	-	10 P	882-949°C

Clearly, with the exception of alloys which rely on Phosphorus as MPDs and the recently new advances in boron-free brazing alloys focused on Manganese and Copper (BNi-8), those containing appreciable levels of Boron and Silicon represent most of the commercially available alloys. This is in part due to their low melting requirements but also due to their excellent wetting/spreading characteristics, ease of use and ability to form amorphous foils, tapes, powders, etc. favouring the production and manufacturing environment.

In most cases, the presence of Si in superalloys is generally a result of Nickel refining were Si is used as a deoxidizer, thus Si levels (similar to Mn) are generally kept to a minimum, as even small concentrations have shown to be deleterious to the mechanical properties, particularly

ductility and fracture toughness with no significant benefits [32]. With the exception of Boron (and Phosphorous), Silicon additions provide the most significant MPD, particularly when combined with Boron in proportions corresponding to the low-melting point Ni-rich Ni-Si-B ternary eutectic. Furthermore, Silicon, unlike Boron possesses an appreciable solid solubility in (Ni) which increases with increasing temperature thereby reducing the tendency to form hard intermetallic Nickel Silicides, Ni_xSi within braze joints at low concentrations (< 5%) depending on the cooling rates.

Most of the popular brazing alloys generally include either Boron and/or Silicon, in addition to other alloying additions as an additional means of a providing strengthening, corrosion resistance, and a minor decrease in the solidus temperature. Commercial BNi-3 (AMS4778) is a ternary Ni-4.5Si-3.2B (at%) braze alloy similar to the far more prominent BNi-2 (AMS4777) which also includes Fe and Cr. The ternary liquidus projections corresponding to the Ni-Si-B and Ni-Cr-B systems are illustrated below in Figure 1-7 along with the approx. compositions of AWS BNi-3 and BNi-9 alloys for reference. In either case, solidification would either initiate with the solidification of γ-(Ni) (or Ni_3B), followed by the γ-(Ni)/Ni_3B binary eutectic, and finishing at the invariant ternary eutectics of γ-(Ni)/Ni_3B/Ni_6Si_2B or γ-(Ni)/Ni_3B/CrB for the Ni-Si-B and Ni-Cr-B systems, respectively. It is uncertain why the nominal composition of either BNi-3 and BNi-2 deviate from the exact invariant reactions, whether its is a technical aspect or inaccuracies of the nominal compositions and/or equilibrium data. Regardless, isothermal solidification involves the progressive consumption of the liquid phase (ternary composition).

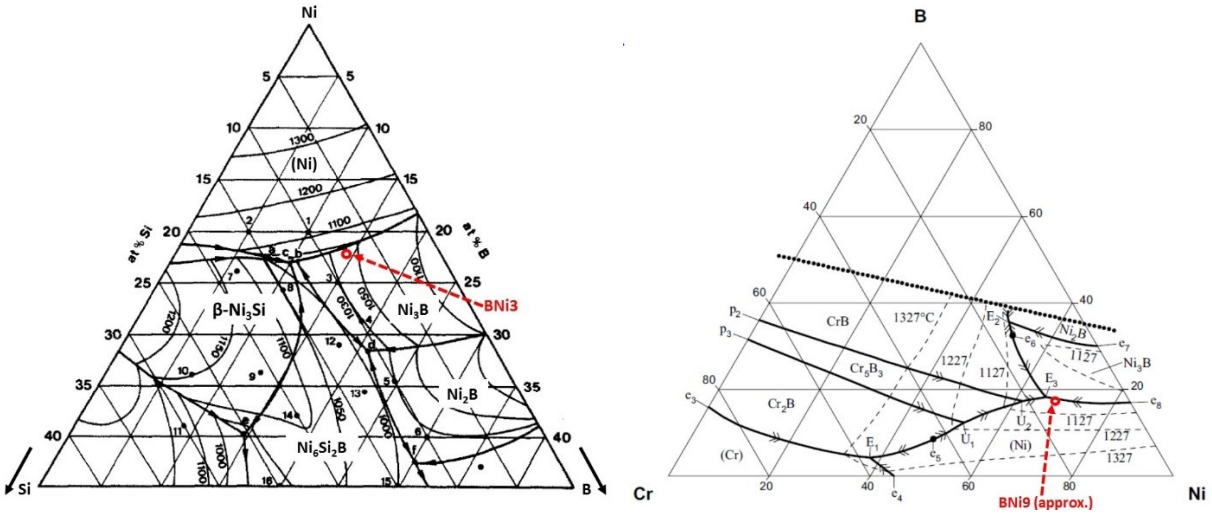

Figure 1-7 - Ternary liquidus projections for the Ni-B-Si (left) and Ni-B-Cr (right) systems. Nominal concentration of BNi-3 and BNi-9, ternary filler metals provided for reference. [32,34-35]

Significant melting point suppression is clearly achieved through the addition of Si to the Ni-B system, the solidus displaying an additional reduction from 1093°C (Ni-Ni_3B eutectic) to approx. 993°C (Ni-Ni_3B-Ni_3Si eutectic). It is for this reason that the relative concentrations of Si:B are generally maintained as they provide the most significant MPD. Additional alloying accomplished using Fe, Cr, W yields further reductions in the solidus temperature, albeit to a lesser extent.

Manufacture of Boron-Brazing Alloys

The eutectic nature of boron-containing FMs makes them highly suited for high-throughout production of ductile amorphous foils using *melt spinning*; a technique which involving the rapid solidification of a melt on a rapidly rotating, water cooled Copper cylinder, yielding thin (30-100 μm) amorphous foils. Such materials possess several advantages with regards to TLPB such as enhanced compositional uniformity/homogeneity which as a consequence yields a narrow melting range (short diffusion pathways) and the ability easily create pre-forms for large scale manufacturing. Furthermore, unlike powders, foils are free of organic binders and solvents and less sensitive to issue related to flow and spreading as the preforms are placed directly in the joint, as opposed to powder fillers which are generally introduced along the fillet region of a joint. Alternatively, rapidly solidified (gas atomized) powder filler metals are also commonly employed combined with a binder (and solvent) enabling application as a paste in the fillet regions of a braze

joint. During melting, the liquid formed is “wicked” into the space between substrates as a result of capillary forces, thereby forming a completely filled joint. Powder filler metals are advantageous in that they allow for modification through blending with others. They however pose a contamination concern as a result of residual organics, leading to oxidation, porosity, etc.

Although, not as widespread is the use of various depositions techniques providing a thin coating of a base metal with a metal or metals which will serve as a filler metal. Such techniques are advantageous but are limited by the geometry and application. Several methods include:

- Electrolytic Deposition
- Electroless Coating (Ni-Boron and Ni-Phosphorous)
- Vapour Deposition
- Magnetron Sputtering

The aforementioned techniques generally produce thin, high-purity coatings in intimate contact with the base metal. There primary disadvantages relate to limited compositional variability and high cost relative to braze powders and foils.

1.4 The Transient Liquid Phase Bonding (TLPB) Process

Classical TLPB theory as originally proposed by Duvall et al. [6, 7], and subsequently further refined by Tuah-Poku et al. [9], and Nakagawa et al. [36], is generally believed to proceed according to the following stages:

1. **Melting of Filler Metal (FM)**
2. **Dissolution of the Base Metal (BM)**
3. **Isothermal Solidification**
4. **Homogenization**

The sequential stages can be understood by examining the solidification sequence of a finite quantity of binary eutectic alloy as mass transport of solute (B) to a semi-infinite source of component A (BM) transpires, as shown in the hypothetical binary phase diagram, Figure 1-8 and corresponding diffusion couples Figure 1-9.

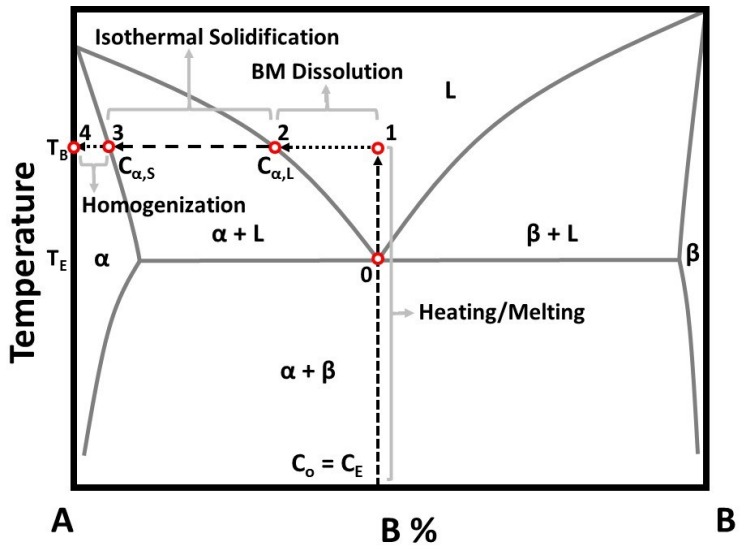

Figure 1-8 - Hypothetical binary phase diagram.

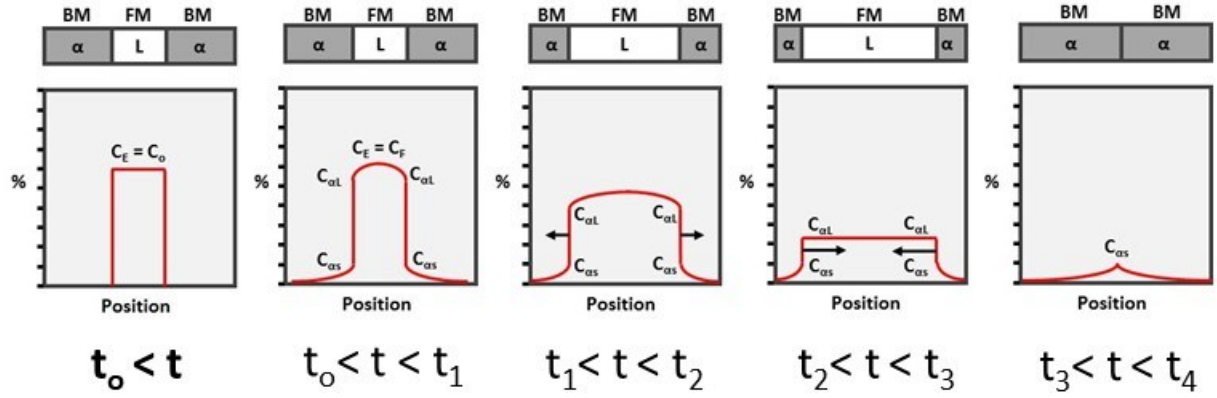

Figure 1-9 – Solidification process during TLPB of eutectic interlayer in accordance with Figure 1-8.

Depending on the heating rate, peak temperature and nature of the FM/BM interface (clad, plated, etc.), some solid-state diffusion can occur prior to the onset of melting, however in most cases no actual metallurgical bond or diffusion exists between the FM and BM prior to FM melting as depicted in Figure 1-9 (**$t_o < t$**). Once a couple is heated above the solidus of the FM, melting begins concomitantly with the progressive wetting/spreading as the quantity of liquid increases. As the liquidus concentration decreases from **C_E** to **$C_{\alpha L}$** during heating from the eutectic temperature, **T_E** (liquidus) to the brazing temperature, **T_B**, (**0→1**), thermodynamic equilibrium necessitates dissolution of BM (**A**) to attain the equilibrium concentrations (**C_L**) between the liquid (**C_o**) and solid (**A**) phases - increasing the quantity of liquid phase with an associated partial dissolution of the solid (**A**). This stage is also known as the *equilibration* or *widening* stage, as the

thickness of the liquid phase increase as a result of BM dissolution at the solid/liquid interface with the simultaneous countercurrent diffusion of the solute (**B**) into the BM as a means of re-establishing localized chemical equilibrium (Figure 1-9, $\mathbf{t_1 \rightarrow t_2}$). During this stage, the liquid attains its corresponding liquidus temperature, while the solid phase achieves a composition corresponding to that of the equilibrium solidus for that system (**1→2**) (Figure 1-8). Once the interfacial concentrations of the solid and liquid attain the equilibrium concentrations corresponding to the brazing temperature, T_B, dissolution ceases and isothermal solidification (IS) (**2→3**) governs the remainder of the solidification process. This stage is considerably more time consuming, as it involves solid-state diffusion of solute B throughout the BM, typically requiring several hours to days, depending on the system, gap thickness, temperature, etc. Once complete, a joint essentially indistinguishable from the BM is formed with only minor compositional variance i.e. $\mathbf{C_{\alpha S} \rightarrow 0}$. If desired, IS can be followed by a lengthy post braze homogenization treatment (**3→4**) which further eliminates residual concentration gradients. However, if for any reason IS is terminated prematurely (liquid remains), the remaining liquid phase solidifies athermally, usually resulting in a eutectic. This solidified structure is very different than the BM or isothermally solidified microstructure which can result in poor joint properties. It for this very reason that achieving complete IS of utmost concern, especially for superalloys brazed with boron containing filler metals where the centreline eutectic contains brittle borides. Owing to their simplicity, many authors have explored the phenomenon of TLPB using idealized binary systems, as depicted in Figure 1-8, while attempting to model the processes [36], this has unfortunately limited the application of TLPB theory to actual Ni-superalloy systems as will be discussed throughout the current work.

1.4.1 *Stage 1: Heating and Melting*

Adopting the Nickel-Boron system with the conventional TLPB process described in Figure 1-9, eutectic melting would involve the rapid liquidation of the FM upon exceeding the eutectic temperature of the Ni-Ni_3B eutectic (≈1093°C), while near-eutectic compositions would involve a 2-stage melting; melting of the Ni_3B followed by the Ni (hypo-eutectic) or vice versa (hyper-eutectic). Eutectic alloys would generally be preferred over near-eutectic FMs for it rapidly generates sufficient quantities of liquid which encourages proper wetting and spreading rather than progressive wetting and spreading which must compete with the diffusional effects of subsequent

stages which initiate immediately upon proper wetting. For instance, upon exceeding its eutectic temperature, a hypo-eutectic filler metal would progressively melt as the temperature increases to the actual brazing temperature, which given a sufficiently sluggish heating rate may compromise wetting and spreading, possibly inhibiting diffusional solidification (IS). The heating rate may also have a pronounced impact on the quality of the final joint, as shown below in Figure 1-10. To summarize, if the diffusivity of the solute elements is quite high, diffusional solidification may occur concomitantly with heating, meanwhile if heating is sufficiently slow as is the situation in large industrial vacuum furnaces and further encouraged if a hypo-eutectic alloy is used. Ultimately, the goal is to obtain a joint with complete wetting and spreading thereby maximizing performance and the rate of IS, which may otherwise be compromised if the progressive formation of liquid is continuously consumed through diffusional solidification, preventing spreading and wetting. Therefore, heating must be sufficiently rapid to ensure the proper formation of a complete joint.

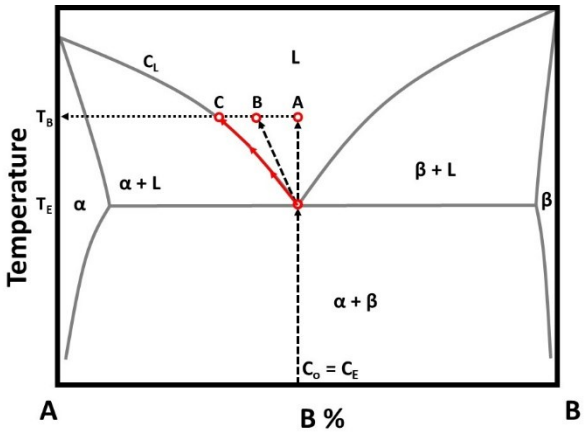

Figure 1-10 - Hypothetical binary phase diagram demonstrating the influence of heating rate on eutectic alloys.

1.4.2 *Stage 2: Base Metal Dissolution*

The degree of base metal dissolution can be easily interpreted from equilibrium data by the difference between the liquidus, $\mathbf{C_L}$ and the composition of the liquid phase, $\mathbf{C_o}$ (original FM), as shown in Figure 1-10. Base metal dissolution can be minimized by reducing the degree to which the FM is overheated above its liquidus composition and temperature e.g. $\mathbf{\Delta C = C_E - C_L}$ and $\mathbf{\Delta T = T_B \rightarrow T_E}$. Thus, BM dissolution could in theory be minimized for a eutectic FM by brazing just above $\mathbf{T_E}$ or through the use of a Hypoeutectic FM with a liquidus temperature close to $\mathbf{T_B}$ (i.e.

composition of C_L). However, in practice some degree of overheating is necessary due to heating rate and near-eutectic limitations as described previously. Consequently, optimal brazing is achieved when the temperature is such that sufficient liquid is generated to facilitate complete spreading/wetting, thereby minimizing the effects of overheating i.e. excessive BM dissolution, displacement of the components, and the deleterious effects of elevated temperature exposure.

The typical decrease in the solidus composition (solubility) which occurs with increasing heating above the eutectic temperature results in the reduced solubility of the solute(s) in the BM. This is highly undesirable for several reasons; (1) the time required to attain IS are typically lengthy thus larger quantities of liquid would likely aggravate the situation despite the kinetics gains of increasing temperatures, (2) The reduced solubility of the solute(s) in the BM inhibits the progressive elimination of liquid phase through transport of solute into the BM, (3) the elevated temperature exposure, adversely affecting the microstructure of the BM aggravating issues such a grain boundary penetration, and (4) excessive and undesirable depletion of the BM of its chemical constituents.

Although the transient nature of the BM dissolution greatly complicates analytical and numerical investigations, it has been examined by numerous authors all of which adopted Fick's 2nd law. Nakao et al. [37]

$$C_L = C_{\beta L}\left[1 - exp\left(-\frac{KAt}{V}\right)\right] \quad \textbf{Eq. 1-1}$$

Where, K is a dissolution rate constant, A is the surface area of solid, and V is the Volume of the liquid interlayer. Differentiating Eq. 1-1, yields Eq. 1-2 shown below, where W, W_o and W_{max} denote the instantaneous, initial and maximum width of the FM, respectively, and P the dissolution parameter.

$$P = Kt = \frac{W_o}{2}\left[ln\frac{W_{max}(W+\rho W_o/2)}{\rho W_o/2(W_{max}-W)}\right] \quad \textbf{Eq. 1-2}$$

Experimental results obtained using Ni-Cr-B FMs demonstrated a linear relationship between P and time, however as the model assumed semi-infinite solids, BM dissolution would appear to proceed without constraint. In an attempt to resolve such issues Nakagawa et al. attempted to model BM dissolution during TLPB of binary Ni/Ni-P and ternary Ni/Ni-P-Cr

couples, by solving Fick's second law using a finite difference approach, thereby assuming dissolution occurs in a stepwise manner [36]. In addition to the relationship observed between heating rate and BM dissolution described above, the work suggested that BM dissolution may also be sensitive to the width of the initial FM, such that thick filler metals (approx. 200 μm) lead to severe BM dissolution due to the greater chemical heterogeneity of the liquid phase. The work also inferred that the rate at which the solid/interface advanced was proportional to the square root of the solute's diffusivity in the liquid, rather than that in the solid.

Liu et al. [38] applied the general error function in an attempt to model BM dissolution concomitantly with liquid formation during heating. Although the method predicted the solute distribution with reasonable adequacy, it assumes no solute diffusion into the base metal and is only applicable to infinite to semi-infinite substrates; both of which make it unsuitable for actual systems.

Dissolution of the BM into the liquid phase is a direct consequence of mass conservation and results in appreciable expansion of the liquid phase perpendicular to the faying surface, leading to an apparent *widening* of liquid phase. Although some believe it follows BM dissolution as an additional stage, this would only be the case where it is assumed that the liquid width remains unchanged during BM dissolution, as described by Tuah-Poku et al. [9]. Therefore, in the context of the current work, BM dissolution and concomitant widening phenomena will be categorized as a single stage identified as base metal dissolution (BMD).

1.4.3 *Stage 3: Isothermal Solidification*

Once the composition of the FM or liquid phase shifts towards that of the liquidus through the process of BMD (Figure 1-9, $\mathbf{t_1 \rightarrow t_2}$), isothermal solidification (IS) proceeds in the manner represented schematically in Figure 1-9 ($\mathbf{t_2 \rightarrow t_3}$) i.e. the progressive reduction of the quantity of liquid, as dictated by the lever rule. Theoretically, this assumes that neither the composition of the solid nor the liquid change, which is generally acceptable for simpler binary systems, but far more complex with multi component systems. Adopting the common assumption of a liquid of homogenous composition, infers that the process of IS is governed by solid-state diffusion of the solute throughout the BM from liquid/solid interface. This occurs primarily through mass transport via volume diffusion and grain boundary diffusion, the later typically displaying enhanced

diffusivity [39]. It is therefore well accepted that diffusion-based analytical calculations and predictions provide the basis for understanding, predicting and modeling IS during TLPB.

In comparison to the other stages of TLPB, the fundamentals of isothermal solidification are generally more established as assuming a constant temperature greatly simplifies calculations and examination. Analysis typically involves adopting Fick's 2nd law of diffusion and assumptions such as one-dimensional solute diffusion, constant liquid concentrations, etc. Nonetheless, numerous authors have successfully modelled the rate of solidification for numerous systems with reasonable accuracy [8, 9,20, 29, 36-38]. Fick's first law of diffusion postulates that concentrated matter will spontaneously (and irreversibly) be transported to regions of lower concentration as a means of reducing the overall free energy by increasing entropy. Thus, a diffusive flux will proceed in the direction of decreasing concentration (high to low) and is consequently proportional to the spatial derivative(s) of concentration. For one-dimensional diffusion at steady-state, the flux can therefore be expressed as the following:

$$\boldsymbol{J = -D\left(\frac{dC}{dx}\right)} \qquad \textbf{and} \qquad \boldsymbol{D = D_o e^{\frac{-E_A}{RT}}} \qquad \textbf{Eq. 1-3}$$

Where J is the diffusional flux [$M{\cdot}L^{-2}{\cdot}T^{-1}$], D is the diffusivity or *diffusion coefficient* [$L^{2}{\cdot}T^{-1}$], C the concentration [$M{\cdot}L^{-3}$] and x the position [L]. Diffusivity is highly temperature dependent as demonstrated by the Arrhenius relationship, where; D_o is a pre-exponential factor [$L^{2}{\cdot}T^{-1}$], E_A the activation energy [$M{\cdot}L^{2}{\cdot}T^{-2}{\cdot}N^{-1}$], R the gas constant [$M{\cdot}L^{2}{\cdot}T^{-2}{\cdot}N^{-1}{\cdot}\Theta^{-1}$], and Temperature [$\Theta$]. A far more versatile relation that does not assume time-independent, steady-state behavior is expressed in Fick's 2nd law of diffusion, as shown in the following partial differential equation:

$$\boldsymbol{\left(\frac{dC}{dt}\right) = D\left(\frac{d^2C}{dx^2}\right)} \qquad \textbf{Eq. 1-4}$$

Eq. 1-4 indicates that concentration gradients, dC/dx change with position and time and assumes that diffusivity is independent of time and position. As a PDE, practical application generally necessitates simplification to a single dimension (x, y, or z). Furthermore, if a semi-infinite BM is assumed, diffusion can be modelled with reasonable accuracy using the gauss error function, given suitable boundary conditions [39]:

$$\boldsymbol{erf(x) = \frac{2}{\sqrt{\pi}} \int_{x}^{\infty} e^{-t^2} dt}$$

$$\boldsymbol{C(x = 0) = C_s}$$

$$\boldsymbol{C(x = \infty) = C_o}$$

$$\boldsymbol{C(x,t) = C_s + (C_o - C_s) erf\left(\frac{x}{2\sqrt{Dt}}\right)} \qquad \textbf{Eq. 1-5}$$

The gauss error function is a special function of sigmodal shape which is commonly applied to equations describing diffusion. It allows relatively simple numerical prediction of concentration as a function of both time (t) and position (x), with accurate values readily available. As the error function is constant the penetration depth of a specified concentration must be proportional to the square root of the time of diffusion i.e. x α $\sqrt{DT}$, for instance, erfc(0.5) ≈ 0.5, corresponds to a mean concentration (C_s and C_o) when ($x/2\sqrt{DT}$) ≈ 0.5 or x ≈ $\sqrt{Dt}$, where $\sqrt{Dt}$ is the thickness of the solute layer formed. Applying the necessary boundary conditions with the error function further emphasizes the square root dependence interface displacement displays with time, as described below in Eq. 1-6:

$$\boldsymbol{t_s = \frac{W_{max}^2}{16K^2D}} \qquad \textbf{Eq. 1-6}$$

Where, t_s is the time required to achieve complete isothermal solidification, W_{max} the maximum width (after dissolution), K a constant and D the diffusivity. A few authors have applied numerical methods in attempts to obtain solutions to the PDE (Eq. 1-4), which was met with varying degrees of success [40]. This is likely due to the efficacy of analytical solutions in modeling one-dimensional solute diffusion with time. However, 2-dimensional diffusion such as that involved with grain boundaries etc. have been explored [41]. Very few authors have yet to developed established understanding governing diffusion phenomenon in multi-component systems which make up most of the boron-based FMs [42, 43].

The fundamental understanding of diffusion and IS during TLPB typically assumes an ideal binary phase diagram wherein the solvent possesses a significant solubility for the solute or MPDs such that the solute is redistributed throughout what is assumed to be an essentially infinite supply of the BM - the solubility limit is never exceeded. For instance, the Ag-Cu system adopted

in the work conducted by Tuah-Poku et al. which has arguably established the fundamental theory of TLPB, obeys such theory very well i.e. significant solid solubility of Ag in Cu and vice versa, in addition to the lack of any intermetallic phases [9]. With regards to Ni superalloys, the Ni-Au and Ni-Pd system for which a variety of FM alloys currently exist displays an even greater mutual solubility and lack of intermetallic phases which also conform to existing theory. However, the development and widespread commercialization of Boron and Phosphorous bearing filler metals due to their lower cost, brazing temperature requirements and excellent wetting/spreading characteristics do not typically display such characteristics and are rarely binary. Unlike any other MPDs, Boron exists as an interstitial within Ni and consequently possesses considerably more rapid diffusivity than substitutional diffusers like Au, Pd, Si, P, etc. [44-48], as shown in Table 1-3. The divergence from fundamental theory during TLPB of Ni and Ni-alloys has been reported by numerous authors, which manifests through the formation and coarsening of brittle intermetallic borides at the faying surface with progressive isothermal solidification rather than being distributed and eventually solubilized long-range throughout the BM [42-43, 49-52], further inferring a solid-state diffusion mechanism. Although the rate of IS may display similar behavior to that of Ni-Au, the resulting microstructure contains brittle borides which greatly compromise mechanical performance as well as corrosion resistance owing to depletion of alloying additions, most notably Cr, Mo and Nb.

Table 1-3 - Diffusivity, D of Boron and Silicon in Nickel at 1100°C.

Species	Diffusivity, D $\{m^2/s\}$ in Nickel at 1100°C		
B	$6.22(10)^{-11}$ [53]	$5.10(10)^{-11}$ [54]	$1.56(10)^{-10}$ [29]
Si	$3.09(10)^{-14}$ [53]	$1.09(10)^{-14}$ [55]	

The diffusivities for other elements typically encountered in Nickel-based superalloys including; Cr, Fe, Co, Mo, Nb, W, Ta and Ni self-diffusion display diffusivities within the range of 10^{-15} to 10^{-14} m/s at 1100°C as summarized in the detailed review published by Hargather et al. [56-58]. It is therefore clear that B as will diffuse interstitially ahead of the other solutes in addition to the other FM solutes. If the composition of the liquid phase remains constant during IS, the solid state diffusion of B into the BM to form borides must be countered by an opposing solidification front wherein the isothermally solidified zone (ISZ), grows in thickness and the liquid later decreases in thickness.

During isothermal solidification, i.e. following Stage 2: BMD and preceding Stage 4: Homogenization the microstructure of any couple can be characterized into four regions:

1. **Athermally Solidified Zone (ASZ)**
2. **Isothermally Solidified Zone (ISZ)**
3. **Diffusion Affected Zone (DAZ)**
4. **Base Metal (BM)**

The ASZ is typically characterized by a highly lamellar eutectic-type morphology which forms upon solidification of any liquid phase that remains upon cooling. Its brittle nature and position in the center of joint make its presence a great detriment to mechanical performance, thus emphasizing the need to achieve complete IS. The *Isothermally Solidified Region* (ISZ) constitutes the Liquid solid interface which grows at the expense of the liquid phase (ASZ), it is of a singular solid-solution phase similar to that of the BM, however typically with significant chemical gradients. Its growth involves diffusion induced solidification resulting from diffusion of the solutes from the liquid phase through the ISZ and into the BM. In most cases the ISZ displays excellent ductility and strength akin to or approaching that of the BM. The DAZ constitutes the region adjacent to the original faying surface i.e. BM/FM, distinguishable from the parent metal by a localized excess in solute resulting from mass transport from the FM to the BM in the process of IS. This may also manifest in a region characterized by the presence of secondary, intermetallic compounds. In either situation, the DAZ is inevitable as it occurs simultaneously as with the opposing growth of the ISZ.

In practice, the TLPB behavior of a particular system is assessed through the width of the centerline eutectic which forms upon athermal solidification of residual liquid, thereby providing a measure of the degree to which TLPB has progressed. Most often the width of the centerline eutectic decreases linearly with the square root of time ($min^{1/2}$) which complies with the analytical solution expressed in Eq. 4-6. The relationship clearly demonstrates the influence liquid width has on the length of IS. It is for this reason that wide gap joining, or repairs require considerably longer times. Comparatively, thin gaps may solidify too quickly preventing complete wetting and spreading which can greatly comprise mechanical strength.

To summarize, if IS is terminated prematurely i.e. liquid remains when the brazing cycle is terminated, eutectic-type solidification occurs upon cooling (athermal solidification);

BM→DAZ→ISZ→ASZ. Comparatively if IS proceeds to completion, athermal solidification is prevented; BM→DAZ→ISZ. If then subjected to a homogenization treatment, the secondary phases and chemical gradients would then be eliminated (i.e. the DAZ layer would be removed), yielding a joint indistinguishable from the original substrate, i.e. BM, defined as the initial conditions chemically unaltered by the brazing process. It is therefore apparent that considerable chemical heterogeneity may exist across the braze joint, which in practice may very well be acceptable given the specified application. However, if deemed unacceptable, such compositional discontinuities can generally be alleviated through the application of a lengthy homogenization treatment, involving heating of the braze assembly at or near the brazing temperature for an extended period of time to improve the distribution of the MPDs in a more homogenous manner. Although, it is both costly and time consuming, the resulting brazed components exhibit mechanical and corrosion properties akin to that of the parent metal/alloy

1.4.4 *Stage 4: Homogenization*

Chemical Homogenization is the process of complete or near-complete elimination of microstructural discontinuities (gradients, intermetallics, etc.) remaining after IS with the goal of improving mechanical performance, corrosion/oxidation resistance, or to increase the *remelt* temperature (solidus). Achieving a homogenous distribution of the original BM constituents i.e. those added as strengtheners (Cr, Fe, Mo, etc.) and/or to enhance environmental resistance (Cr, Al) is always desired. Increasing the remelt temperature of the joint is also typically sought as it limits the maximum service application of a given joint. In systems possessing significant solid solubility with Ni (Ni/Au, Ni/Pd) the remelt temperature is a maximum in the BM and minimum in the solidified joint. Comparatively, when secondary phases are formed within the DAZ, the remelt temperature is dependent on the eutectic temperature of the intermetallics and solid-solution Ni. Thus, although intermetallic represents a brittle, and typically undesirable microstructural discontinuity of a joint, in many instances they may display a remelt temperature similar to the BM or even higher.

Chemical homogenization treatments are used extensively in many fields of materials processing, for instance post weld annealing treatments and solutionizing treatments used prior to quenching. Thus, the ability to approximately predict values such as the time required to achieve complete homogenization are of great interest.

As described in Figure 1-9 ($t_3 < t < t_4$), IS terminates upon diffusional solidification of the last remaining liquid phase leaving behind a singular solid-solution phase possessing some degree of chemical heterogeneity depending on the solute composition of the pure BM and its solidus, C_S. Subsequent heating promotes further chemical homogeneity through continued solid-state diffusion. Most often homogenization is performed above the brazing temperature owing to the enhanced diffusivity with increasing temperature, however lower temperatures may be necessary in certain sensitive alloys [15]. Although complete IS may be adequate for many commercial and industrial settings, the more physically demanding applications subject to harsh conditions generally necessitate some form of post-braze homogenization treatment. Table 1-4 compares the brazing conditions (i.e. Stage 3 - IS) and homogenization conditions for a number of Ni-based superalloy/FM combinations.

Table 1-4 - Brazing and homogenization parameters adopted by various authors in eliminating borides [59-62].

Base Metal	Filler Metal	Brazing		Homogenization		Notes
		T (°C)	time (hrs)	T (°C)	time (hrs)	
IN718	**BNi-2**	1050	1	1150	12	-
GTD111	**BNi-3**	1130	1.67	1150	4	DAZ Remained
IN738	**BNi-2**	1150	0.67	1100	5	-
IN738	**BNi-3**	1160	4	1000	168	DAZ Remained
Alloy 247	**BNi-9**	1240	16	-	-	No Homogenization
M247	**BNi-9**	1120	4	1180	4	-
IN938	**BNi-3**	1160	4	1000	168	DAZ Remained

1.4.5 *Additional Practical Considerations to TLPB*

Given that TLPB and thus IS is governed by solid-state diffusion of solute throughout the BM, understanding the mechanisms by which diffusion occurs i.e. whether diffusion is primarily through volume, surface or grain boundary diffusion it is clearly of great importance. This is particularly important for Ni-based superalloys as some of their most demanding applications necessitate the use single and/or oriented/columnar crystal components which may eliminate high-energy diffusion paths i.e. GB diffusion, thus relying primarily on volume or bulk diffusion.

In general, at any temperature the magnitude of the diffusivity diffusion along GBs (D_{GB}) and free-surfaces (D_S) relative to that within the defect-free lattice (D_B) are such that:

$$D_{GB} > D_S >> D_B$$

Defects such as GBs, dislocations, etc. provide a heterogenous, high-energy sites which reduce the activation energy required for interstitial or substitutional diffusion mechanisms. Although surface diffusion plays a significant role in most metallurgical phenomena, the total GB area is generally far greater than that of the surface thereby making GB diffusion one of the most effective diffusion paths available. The various diffusion mechanisms, all of which operate concomitantly are shown schematically in Figure 1-11. Enhanced diffusivity paths and their contribution to the overall diffusivity vary depending on the mean grain size, purity, temperature, etc. For instance, as diffusion along GBs progresses throughout the solid solute build-up within GBs promotes bulk diffusion from GB to bulk. This clearly transpires in superalloys with the preferential precipitation of secondary phases (i.e. carbides, intermetallics, nitrides, borides…) within the GBs.

The use of oriented or single-crystal alloys consequently (but also intentionally) reduces the role of GB diffusion on solute transport and other metallurgical phenomena thereby minimizing the effects of diffusion-based deformation mechanism i.e. Nabarro-Herring creep, coble-creep, grain boundary sliding, etc., [1, 3]. Although surface-diffusion may play a lesser role in monolithic substrates, its contribution to mass transport in emerging particulate-based materials (powder metallurgy) is significant, surpassing that (at least initially) of GB diffusion [63].

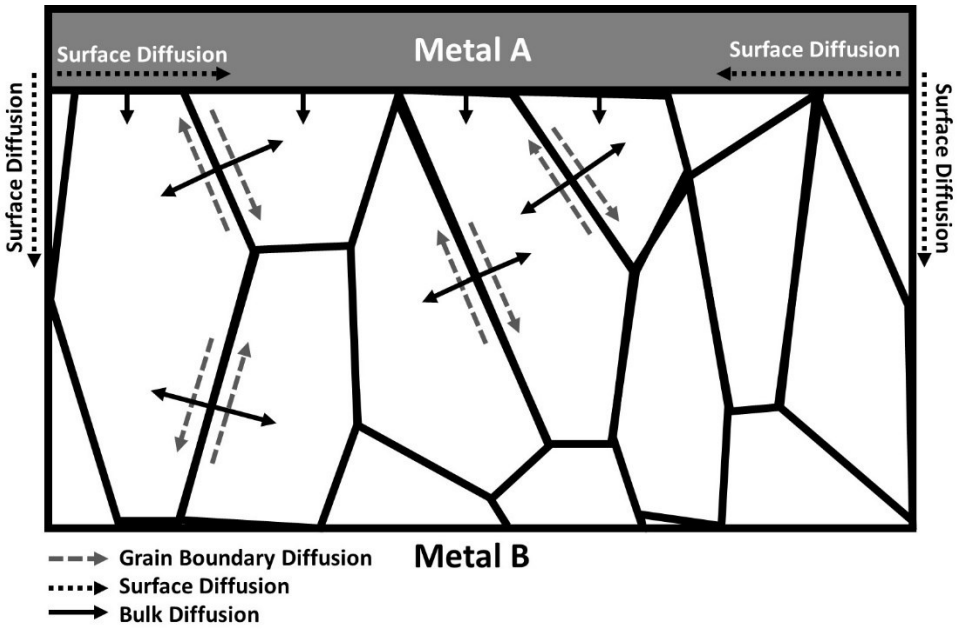

Figure 1-11 - Schematic representation of various possible diffusions paths.

With regards to TLPB of monolithic Ni-based superalloys, GB and bulk diffusion represent the dominant mass transport mechanisms. The existence of a liquid phase in intimate contact with the faying surface of the BM however also plays an important role, partly due to the generally enhanced diffusion displayed by liquids but also due to its ability to penetrate GBs preferentially - possibly altering the apparent surface area for further diffusion. Consequently, single and/or columnar crystal BMs display a reduced rate of IS due to the lack of accelerated GB diffusion versus their polycrystalline counterparts, as confirmed by the efforts of various authors [64, 65-66]. Furthermore, the irreversible (and spontaneous) grain growth expected at the typical brazing temperatures of Ni-based superalloys ($T > 0.5T_M$) would be expected to progressively decrease the apparent diffusivity of the couple [2, 65]. However, such phenomena have been shown to be less significant when boride precipitation is present as they have been shown to effectively "pin" GBs [67-68].

1.5 Differential Scanning Calorimetry (DSC)

Calorimetry is a well-established thermoanalytical research method which involves examining the heat evolved (exothermic) or absorbed (endothermic) during chemical reactions and phase changes. More recently, differential scanning calorimetry (DSC) has become one of the most prevalent thermochemical analytical techniques due to its ease of use, accuracy and ability to

characterize a variety of specimens within a range of temperatures. The instrumentation is either categorized as power compensated and/or heat-flux DSC, the latter involves adjusting the heat (power) required to maintain a constant temperature between a reference and the specimen, while the former measures the variation of the temperature difference (hence differential) between a reference and specimen. The result is the ability to measure fundamental thermodynamic properties such as heat capacity, onset temperatures of phase changes, enthalpy of reaction, glass transition temperatures, etc. Thus, DSC clearly provides a powerful tool for measuring the evolution of a variety of metallurgical systems at various temperatures with great precision. The results from either type of instruments are quantitative and virtually identical despite several subtle differences; a power compensation instrument for instance, can generally heat or cool faster, and provide better resolution for sharp events, but the signal is inherently less stable as it is comprised of the very small difference between two very large numbers. As a result, the baseline is less flat and stable, and the short-term noise is higher. By comparison, a heat flux instrument cannot achieve the rapid scan rates of a power compensation design - generally less than 200°C/min. However, the baseline is usually straighter and more repeatable thereby providing higher sensitivity for subtle events which, more recently has greatly contributed to its preference and as an industry standard. Precision DSC analysis requires a thorough understanding of the numerous parameters involved with both the equipment and the experimental setup, as a complex interplay exist which can have a profound effect on the resulting measurements, as listed below:

- Heating/cooling (scanning) Rate
- Specimen properties (thermal conductivity, heat capacity, mass, density)
- Specimen position – thermal contact resistance (proximity to thermocouple)
- Atmosphere

The DSC in the present work is of the heat-flux-type which functions by the principle illustrated schematically in Figure 1-12, and summarized as follows:

1. Two identical crucibles are situated in identical radial positions within a furnace such that the temperature of each is assumed to be identical.
2. The temperature of each crucible is continuously measured via S-type thermocouples positioned underneath the carrier, as shown schematically in Figure 1-12A.
3. The temperature difference, $\Delta T = T_S - T_R$, creates a corresponding measurable potential or voltage difference which is continuously recorded by the controller.

4. Any endothermic and/or exothermic event that transpires within the sample will result in a corresponding increase (exothermic, $0 > \Delta T$) or decrease (endothermic, $0 < \Delta T$) in the measured temperature, T_S thereby, producing a measurable change in ΔT (Figure 1-12B).

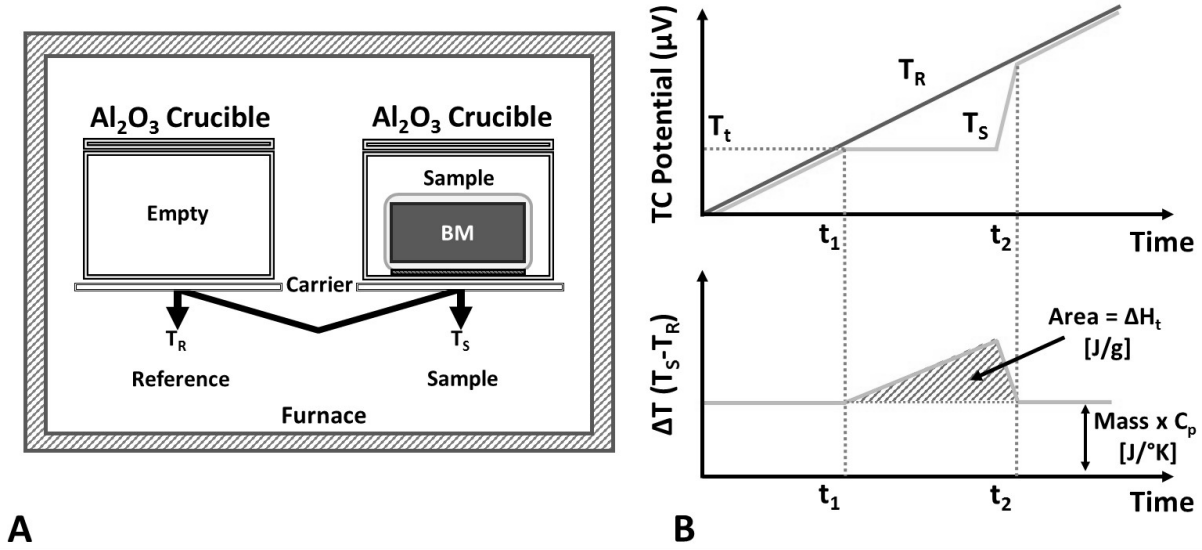

Figure 1-12 - Typical Heat-Flux-type DSC arrangement used in current work (A) and method by which precision measurements are obtained from temperature traces (B).

ΔT can be related to the heat flow, dQ/dt as described by Newton's Law, for each of the crucible as provided below [69]:

Sample: $$\frac{dQ_S}{dt} = \frac{1}{R}\Delta T_S = \frac{1}{R}(T_H - T_{S'})$$

Reference: $$\frac{dQ_R}{dt} = \frac{1}{R}\Delta T_R = \frac{1}{R}(T_H - T_{R'})$$

Where, T_H is the temperature of the heat source, R the thermal resistance, while $T_{S'}$ and $T_{R'}$ denote the measured temperature of sample and reference, respectively. Assuming both the sample, reference and carrier are heated at the same rate, in the absence of any thermal events in the sample (or crucible) the heat flow for both sample and reference can be related to as follows:

Sample: $$\frac{dQ_S}{dt} = C_{S'}\frac{dT}{dt} + C_S\frac{dT}{dt}$$

Reference: $$\frac{dQ_R}{dt} = C_{R'}\frac{dT}{dt} + C_R\frac{dT}{dt}$$

Where, C_S, C_R, and $C_{S'}$, $C_{R'}$ are the heat capacity of the sample, reference, carrier (sample side) and carrier (reference side) respectively. Thus, combining all the previous equations and noting that in practice, $C_{S'} = C_{R'}$. The change in temperature, ΔT can be simplified to:

$$\Delta \boldsymbol{T} = \boldsymbol{T_{S'} - T_{R'} = R\frac{dT}{dt}(C_R - C_S)}$$

Thus, $\Delta T \rightarrow 0$ (zero signal) as the heat capacity of the two sides are identical e.g. two empty crucibles. However, in practice, the sample will generally display a greater heat capacity, C_S than that of the empty reference crucible thus, $\Delta T < 0$, as shown in Figure 1-12B. In response to a thermal event, such as that illustrated schematically in Figure 1-12B, the associated enthalpy, ΔH is related to the measured area, A by experimentally determined constant, K.

$$\Delta \boldsymbol{H = A \times K}$$

Determination of R and K necessitates a two-stage calibration process involving the controlled heating of a variety of high purity standards of known melting point and enthalpy e.g. heat of fusion. Thereby accounting for the thermal resistance, R (sensitivity calibration) and constant, K (temperature calibration).

1.5.1 *Application of DSC Analysis to TLPB of Ni-based Superalloys*

DSC can provide a wealth of information related to precipitation events, melting/solidification, phase changes, heat capacities, etc. thereby greatly facilitating the optimization of Ni-superalloys manufacturing techniques, as well as heat treatment, joining, and more. One of the most common applications for DSC in advanced structural components is heat treatment development. Specimens are generally solutionized at some specified temperature for an extended period then cooled at a controlled rate, during which the heat evolved during precipitation and solidification (exothermic) or dissolution and melting (endothermic) events are monitored, as shown below in Figure 1-13. This enables rapid optimization of heat-treatment parameters governing the mechanical performance of Ni-based superalloys as well as steels, aluminum alloys, titanium, etc.

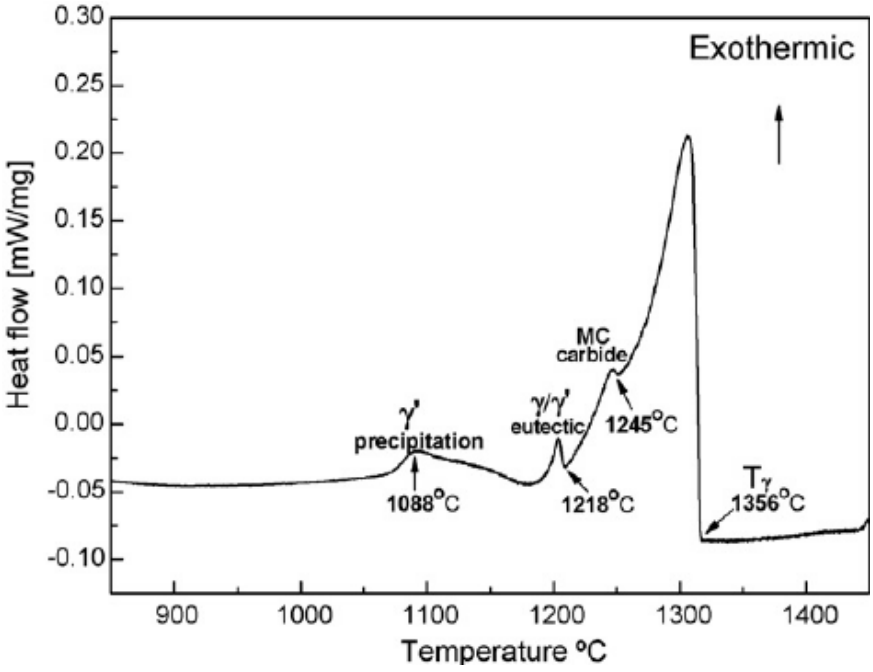

Figure 1-13 - DSC cooling trace for an experimental Ni-base superalloy [70].

1.5.2 *Quantitative DSC Analysis*

Since TLPB involves the progressive IS of a liquid phase as a consequence of atomic diffusion between liquid interlayer and substrate, DSC is aptly designed to examine such phenomena. The technique is capable of generating valuable quantitative information such as the rate of depletion of the liquid phase based on the change in enthalpy of fusion, ΔH_f. It can also determine the temperature(s) corresponding to the melting/solidification and/or dissolution/precipitation of a particular phase and identifying the remelt temperature of joints thereby offering a very efficient and attractive means of optimizing thermal processes given a particular base metal/interlayer system. Additionally, such methods can be used to predict valuable practical information pertaining to the expected time required to achieve complete solidification of a joint, the maximum permissible gap width, and the influence of surface characteristics on the efficiency of said processes. To date, very few researchers have applied DSC analysis to TLPB processes and even less have adopted the use of cyclic temperature profiles wherein the temperature is repeatedly varied enabling repeated measurement of the exothermic and corresponding endothermic reactions i.e. diffusional solidification/Melting, etc. [70-93]. The technique originally developed by Turiff et al. involved a study of the TLPB brazing of Clad Al sheets [72]. Further refinements to the method were made by Murray et al. which enabled easy correlation between the enthalpy

measurements obtained through cyclic DSC to the relative quantity of liquid phase remaining and associated width (or joint gap width) [78]. Figure 1-14 illustrate one example of cyclic DSC applied to Ni/Au-Ge couples as a potential low-temperature (soldering) FM for Ni [79]. This technique greatly reduces the number of specimens required and provides "In-situ" measurements which can be used to evaluate the kinetics of various transformations. This technique is ideal for measuring the progression of IS which transpires during TLPB as well as solid-state diffusion bonding, providing an efficient means of identifying the time required to form stable joints.

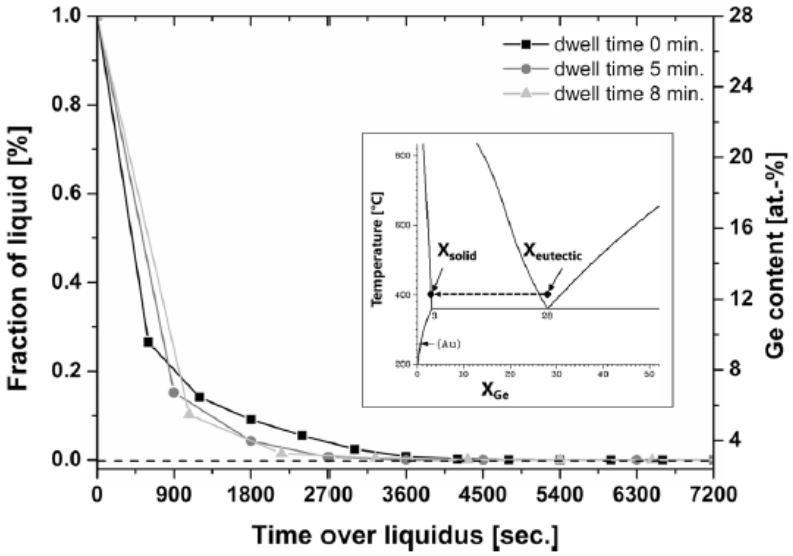

Figure 1-14 - Application of cyclic DSC during low-temperature TLPB of Ni/Au-Ge couples. Temperature cycled between 280 and 400°C with and without hold/dwell times at 400°C [79].

1.6 Thesis Structure, Scope and Objectives

Several key aspects related to the TLPB behaviour of Ni based superalloys are investigated in the principal technical chapters 4 to 5. Each chapter contains its own literature review pertaining to the specific chapter topic, as well as results and discussion section.

In conventional TLPB as described in Figure 1-10, the solute atoms B have complete solubility in the base metal at the brazing temperature. It is generally assumed that this solubility is essential to a successful TLPB process wherein solute atoms readily diffuse into the BM, resulting in isothermal solidification. The solubility of boron in Ni and its alloys is on the order of 0.15 wt% B at the Ni-rich eutectic temperature [33]. Instinctively, this would infer that attaining complete isothermal of Ni systems is impossible Ni system when boron is present in the liquid

phase. However, in practice IS does occur primarily through the formation of a diffusionally affected zone (DAZ), whereby metal-borides precipitate in the BM matrix adjacent to the solid liquid interface as illustrated below in Figure 1-15. The isothermal solidification zone (ISZ) is generally a Ni-rich single-phase solid solution layer essentially free of boron/borides. If the braze joint is cooled before complete IS, the liquid solidifies, forming an athermal solidification zone (ASZ) possessing an overall boron content similar to the original filler metal composition.

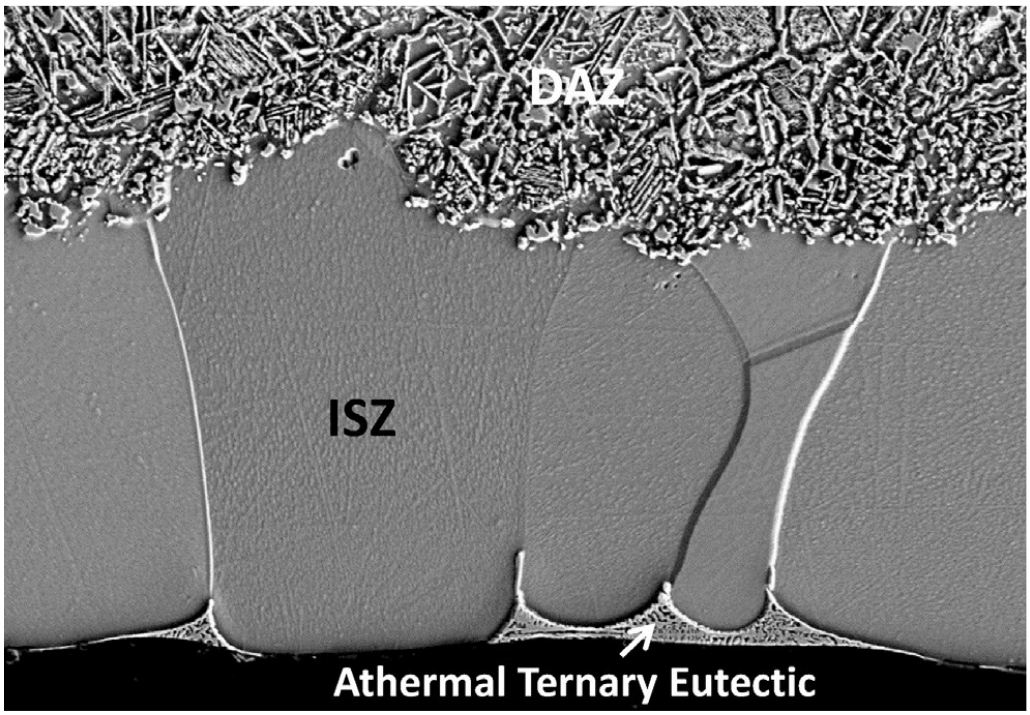

Figure 1-15 - Boride precipitation creating a diffusionally affected zone (DAZ) during TLPB of a IN625 Ni-based superalloy with boron-containing AMS BNi-2 (Ni-Cr-Fe-Si-B) Filler metal [78].

One consequence of the DAZ/ISZ formation is a marked initial boron uptake (IBU) by the base metal during filler metal melting. Consequently, considerable diffusional solidification transpires during heating, resulting in a reduced starting liquid width. The poorly understood IBU phenomena is explored in detail in Chapter 4 using IN625/BNi-2 braze couples.

Despite the prevalence of the DAZ/ISZ structure in Ni-based superalloy TLPB research, a basic explanation of its formation is lacking in the literature. Chapter 5 provides an explanation for the DAZ/ISZ formation based of diffusion path theory, phase equilibria using Thermocalc thermodynamic modeling predictions and experimental examination of a simple ternary system consisting of a pure Ni/Ni-Si-B base metal/filler braze couple.

The important role that base metal and filler metal composition have on the IBU phenomena, dissolution and isothermal solidification kinetics is investigated in Chapters 6, 7 and 8. Specifically, in Chapter 6 the role base metal Cr-content has on the nature of TLPB with Boron-FMs is isolated through an investigation of pure Ni/Ni-Si-B and Ni-Fe-Cr/Ni-Si-B braze couples. In Chapter 7 the influence of base metal/filler metal compatibility has on dissolution and general TLPB behaviour was confirmed using IN718/BNi-2 and IN718/BNi-3 braze couples. Such work permitted the evaluation of age hardenable base metal alloys and the role their composition plays on TLPB. In Chapter 8, the role filler metal Cr-content has on TLPB of Ni-based alloys with boron-containing FMs was determine through a comparison of Ni200/BNi-2 and IN600/BNi-2 alongside the Ni200/BNi-3 and IN600/BNi-3 braze couples examined in Chapter 6. Lastly, Chapter 9 investigates the trends in the TLPB response exhibited by the 7 braze couples studied, in order to draw overall conclusions from the entire body of work.

CHAPTER 2 Materials

A total of 4 substrates (BMs) were adopted in the current work; commercial grade Ni (Ni200), Inconel 625 (IN625), 718 (IN718) and 600 (IN600); the compositions of which are displayed below in Table 2-1. All Ni alloys were procured in the form of sheets which were subsequently electrical discharge milled (EDM) into 3.175 mm diameter pucks of varying thickness; ≈ 1.67 mm for Ni200, IN718, and IN625 and ≈ 2.38 mm for IN600. The FMs used included BNi-3 (AMS4778, MBF30) Ni-3.2B-4.5Si (wt%) and BNi-2 (AMS4777, MBF20) Ni-7.0Cr-4.5Si-3.2B-3.0Fe (wt%) procured from Vitta Corporation® and Aimtek®, respectively. Both FMs were used exclusively in the form of ≈ 48 μm thick amorphous foils. Studies involving the dilution of BNi-3 interlayers were conducted using either fine (< 125μm), high-purity (99.996%) Nickel powder (Puratronic®, Thermo Fisher Scientific) or filings of wrought materials (IN600). A suspension created by combining Yttria, Y_2O_3 derived from an aerosol spray and acetone (solvent) was used as a diffusion barrier coating on all surfaces except the faying surface, thereby preventing any inadvertent wetting/spreading of FM away from the joint region.

Table 2-1 - ICP-OES measurements (wt%) performed on all materials adopted in the studies.

Material	Ni	Fe	Co	Cr	Al	Ti	Mo	Nb	Cu	Mn	Si	B
Ni200	**99.29**	0.04	0.03	-	0.09	-	-	-	0.05	0.14	0.16	-
IN600	**73.04**	**9.4**	0.05	**16.1**	0.14	0.23	0.10	0.15	0.30	0.34	0.15	-
IN625	**60.69**	**4.01**	0.19	**20.75**	0.61	0.03	**8.9**	**3.65**	0.11	0.28	0.28	-
IN718	**52.15**	**18.74**	0.41	**18.11**	0.74	**1.09**	**3.22**	**5.07**	0.06	0.25	0.09	-
BNi-3	**93.65**	0.07	0.02	-	0.02	-	-	0.01	-	0.03	**3.43**	**2.86**
BNi-2	**78.13**	**3.15**	-	**7.01**	-	-	-	-	-	0.03	**3.80**	**2.94**

CHAPTER 3 Experimental Methods

3.1 Differential Scanning Calorimetry (DSC)

All solidification/melting studies were performed in a Netzsch Pegasus 404 differential scanning calorimeter (DSC) under continuous flowing high purity (99.9999%) argon gas at a rate of 20 cc/min, following a dual evacuation/pressurization procedure (P = 10^{-5} mbar). Further improvements in the furnace atmosphere were achieved using a Titanium "getter" ring. The DSC itself was calibrated beforehand using the onset and enthalpy values obtained from the melting of a series of high-purity reference metals, in accordance with the manufacturer specifications. Alumina crucibles and lids where used in all instances as it prevented any inadvertent wetting and chemical interaction with the BMs and FMs. Complete assembly of the brazing couples involved the following procedure: light hand grinding/polishing of the BM(s) using 500 and 2000 grit SiC paper to obtain a smooth faying surface, ultrasonic cleaning of the FM and BM in acetone, coating of all surfaces, with the exception of the faying surface(s) using a suspension of Y_2O_3 and acetone and final assembly of couple as illustrated in Figure 3-1. A total of four different arrangements were used through the course of the research: standard full-joint (BM/FM/BM), half-joint (BM/FM), 100% liquid determination (BM//FM) and BM dilution simulations (BM + FM). The BM/FM half-joint arrangement has the dual purpose of improving the DSC signal as described by Turrif et al. [72] and providing a light pressure between BM and FM thereby enhancing spreading and wetting as encountered in the more practical full-joint. Thus, the vast majority of the specimens created were of the half-joint type, the full-joint configurations were used partly to validate the ability of half-joints to properly quantify TLPB kinetics. They were also used to confirm the influence of full joint gap width on the isothermal solidification times and IBU formation. The 100% liquid arrangement, otherwise denoted as BM//FM (e.g. Ni200//BNi-3) were identical to the half-joints however with the faying surface coated in yttria to prevent diffusional solidification, the purpose of which will be provided shortly. Lastly, the BM dilution arrangement was designed as a means of obtaining representative DSC measurements corresponding to the dilution of the FM with a finite quantity of BM.

Each arrangement depicted in Figure 3-1 was place in the sample side of the DSC measuring head as depicted in Figure 1-12A. With the exception of interrupted tests e.g. heat and

quench, a cyclic thermal profile similar to that shown in Figure 3-1 was implemented in most cases. This involved heating and subsequent cooling at 20°K/min between 870°C and a chosen braze temperature, T_B, following a 5 min hold; the purpose of which was to allow repeated enthalpy measurements during solidification (ΔH_S) and/or heating (ΔH_M) as discussed in greater detail by other authors [72-78]. This technique enables one to examine the rate of isothermal solidification (IS) with time (above solidus) using a single specimen, thus minimizing experimental variation while greatly reducing experimental preparation.

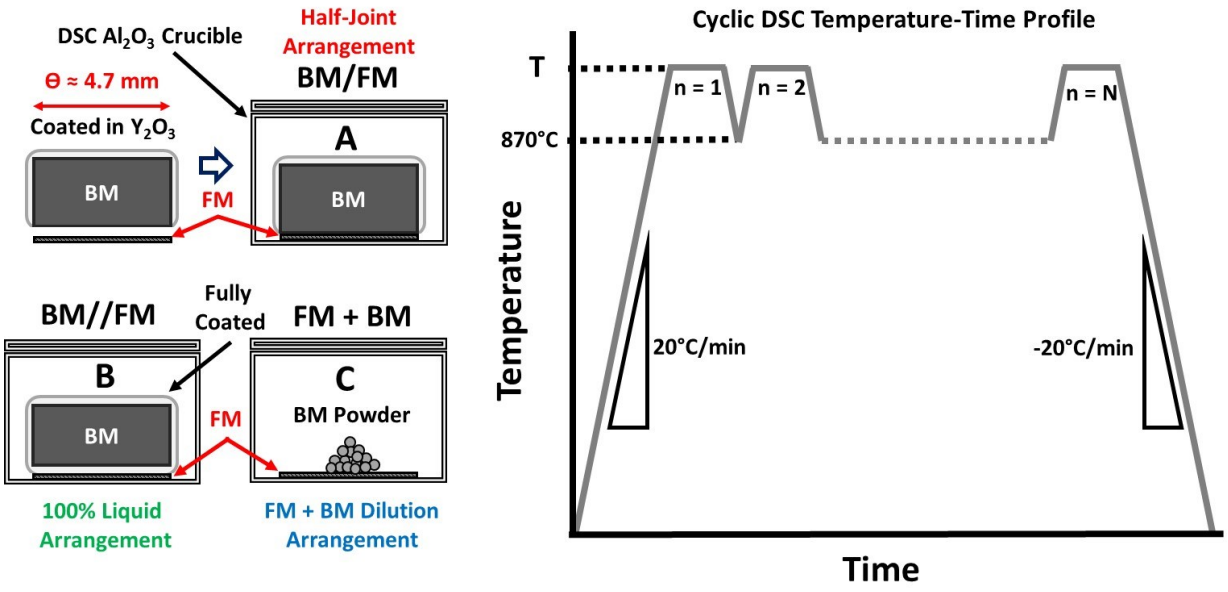

Figure 3-1 - Schematic of various experimental arrangements (left) and cyclic thermal profile (right) used during cyclic DSC Studies.

Enthalpy measurements (ΔH_t) were expressed as a fraction of the total enthalpy of melting of the FM (ΔH_o). A liquid fraction ($L_f = \Delta H_t/(\Delta H_o)$ below unity, indicates that not all the FM material placed at the joint, melted or solidified, such as the case wherein diffusional or isothermal solidification has occurred.

An experimental measurement of ΔH_o is influenced by the presence of the BM arrangement within the DSC sample crucible. To determine the value of ΔH_o for the half- and full-joint arrangements of Figure 3-1, an additional cyclic test was performed on the TLPB couples. In this case, the faying surface was coated in a thin layer of Y_2O_3 (BM//FM) to prevent diffusional bonding thereby generating several repeatable enthalpy measurements corresponding to the

TOTAL enthalpy of solidification (or melting), ΔH_o. Through the course of the work it was discovered that some degree of signal attenuation or *thermal dampening* resulted as a consequence of contact/interactions between with the FM and coated BM, as opposed to the FM alone. Generally, the enthalpy of melting/solidification of the FM was reduced by a factor of 10 to 20% depending in the specific base metal used and joint arrangement. Thus, each enthalpy measurement determined in the cyclic experiments, ΔH_t, could be expressed as a fraction of the total (100%) liquid present, using this Y_2O_3 (BM//FM) determined ΔH_o. This method is discussed in greater detail later (3.5.3 Thermal Dampening).

The potential experimental error inherent with the DSC apparatus is primarily governed by the accuracy and precision of the thermocouples. Therefore, for the current apparatus operating with S-type thermocouples, an accuracy of ±0.6°C to ±1.5°C is expected. Furthermore, the device was calibrated using various high purity standards; In, Sn, Zn, Al, Ag, Au and Ni, designed such that the experimentally calculated peak areas are related to known enthalpy values for a range of temperatures. In the current work, the Ag, Au, and Ni enthalpy measurements covered the most pertinent temperature range e.g. 961.8°C, 1064.2°C, and 1455°C for Ag, Au, and Ni, respectively, which displayed % errors of 1.3 and 2.9, 3.8 respectively. The reproducibility of the enthalpy values measured for Au, Ag, and Ni can be quantified by the standard deviation between experiments which were determined to be 2.72, 0.122, 1.7 for Ag, Au, and Ni, respectively. It should be noted that such values may shift with extended periods of time, fortunately however, most values provided in the current work were normalised using data acquired at that particular time thereby minimizing the influence of the percent error as absolute enthalpy values were not of great importance. Furthermore, given the importance of data analysis, all temperature and enthalpy measurements were performed in iterative manner as described in Section 3.5 – Preliminary Assessment of Enthalpy Measurements to minimize experimental bias. Owing to the linearity of much of the TLPB data, linear regression analysis curve fitting was performed such that the data displayed a coefficient of determination, R^2 of > 0.95 (in most cases, $R^2 > 0.98$).

3.2 Microscopy

All DSC specimens were hot mounted in a conductive thermosetting resin (Struers Polyfast) containing graphite to improve SEM examination. Grinding and polishing of the mount involved

longitudinally grinding (500 grit SiC), followed by sequential polishing using 9 μm and 3 μm colloidal diamond suspensions. The final polishing stage involved a colloidal silica suspension (Struers, OP-S, 0.04 μm). All imaging was then performed in the etched condition (Kalling's waterless) using either optical or scanning electron microscopy (Hitachi S4700 CFE). SEM imaging was performed using a working distance of 12-13 mm and mixed lower and upper SE detector configuration. The latter was adopted as it provided enhanced atomic contrast imaging as a result of the greater backscatter diffraction signal (SE3, lower detector) [80-81]. The operating conditions varied between 5kV/20μA and 15kV/15μA depending on the focus of chemical analysis, as discussed below.

3.3 Energy-Dispersive X-ray Spectroscopy (EDS)

The detection of lighter elements such as Boron using EDS and/or EPMA is notoriously difficult as a consequence of Boron's electronic structure typically limiting analysis to qualitative examination. Nonetheless, it is possible to optimize the equipment thereby tailoring it for boride analysis. The SEM described above was equipped with an Oxford X-max (80 mm^2) energy-dispersive spectrophotometer (EDS) for chemical analysis, which operates "windowless" e.g. without a Beryllium window traditionally designed to prevent condensation/contamination of the Si detector. Consequently, the detector is theoretically capable of measuring the characteristic K-lines associated with many of the light elements, 4 (Be) > Z < 11 (Na) (e.g. Boron), which, would otherwise be impossible (11 > Z (Na)). Another strategy for enhancing the detection of B involves optimizing the column conditions. For instance, the application of low accelerating voltages can effectively reduce the background noise thereby greatly enhancing resolution, yielding repeatable, near-quantitative measurements (< 5 kV). This however limits the detection to lower energy orbitals e.g. the lower intensity L-lines as opposed to the characteristic K-lines, possibly compromising the accuracy of other species of interest, e.g. K_α(Ni), L_α(Ni) and K_α(Si)= 7.46, 0.85, 1.74 eV, respectively [82]. Other issues relate to the difficulty in preventing carbon contamination and related masking of the B peak i.e. K_α(C) = 0.277 eV and K_α(B) = 0.183 eV. Ultimately, optimizing the analysis of boron-containing phases (borides) required adopting low-voltage (5 kV) high-current (20 μA) conditions for reasonable accuracy and repeatability, for phases such as Ni_3B. Under such conditions, the accuracy of the wt% reported for B improved considerably, however as stated above at the expense of other elements. For instance, the analysis of the complex borides

generated in superalloys i.e. M_xB_y (M = Cr, Mo, Nb, etc.) once again proved difficult due to the difficulties in detecting their characteristic K-lines given the low accelerating voltages, therefore necessitating the measurement of the less distinct, lower voltage L-lines. Therefore, in the context of the current work semi-quantitative results are sufficient and the operational conditions will be provided in each case.

3.4 Thermocalc® Thermodynamic Modeling Software

Thermo-Calc® thermodynamic modeling (Database: TCNI9/2019.01.25.12.06.45) was used to generate ternary and isopleth diagrams. All isopleths used at fixed ratio of the various constituents (composition), in most cases adopting for the Boron content (at%) on the x-axis. Since the quantity of FM is finite relative to the BM (Semi-infinite) such diagrams are therefore very informative means of predicting both the processes of IS and BMD, by demonstrating the progressive reduction of all solute (dilution) with time.

3.5 Preliminary Assessment of Enthalpy Measurements

The importance of enthalpy measurements to the current body of work warrants a detailed overview of the process by which enthalpy measurements were made, and the factors taken into account to optimize accuracy, while correcting for the various issues encountered through the course of the research. As described in section 1.5 Differential Scanning Calorimetry, an enthalpy measurement is simply the integral (area above or below) of the DSC trace within the region corresponding to a particular thermal event. The integration can be easily and quickly computed with the assistance of the dedicated software. However, depending on the nature of the data, distinguishing the limits of integration may prove difficult or, in certain cases, nearly impossible. The following section(s) will briefly cover the baseline fitting methods available and further elaborate on the various issues encountered in the current work and means used to correct for them.

3.5.1 *Baseline Fitting*

Figure 3-2 illustrates a typical melting endotherm (solid line) obtained during melting of a BNi-3 FM alongside its derivative (dashed line). In the simplest and ideal cases baseline fitting can be easily executed by identifying the limits of a thermal event wherein the differential of the original signal approaches zero.

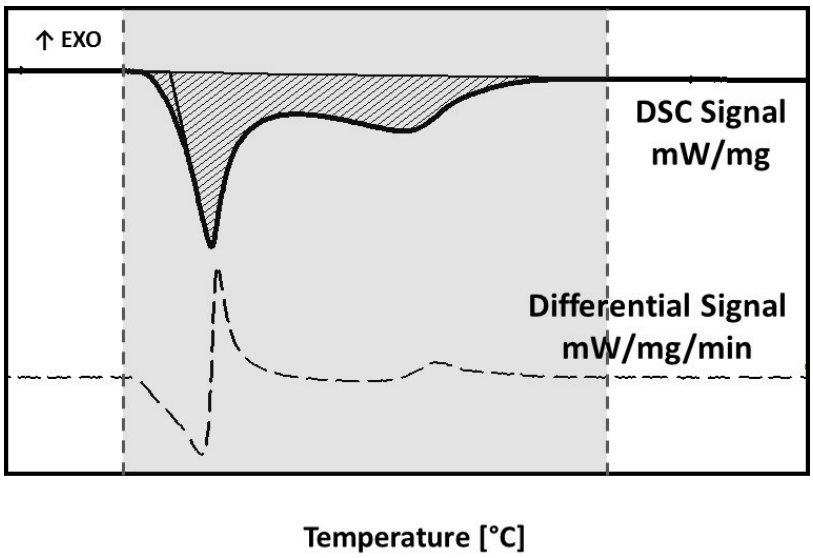

Figure 3-2 - Determination of the limits of integration of a thermal event.

The software used to analyze the DSC results provides a total of 8 methods for obtaining a baseline fit, however throughout the work only four were used: linear, bezier, tangential left-started and horizontal left-started, as shown schematically below in Figure 3-3. The exact method used depended on the nature of the DSC traces. For instance, linear fitting was appropriate in most circumstances since the melting and solidification peaks exhibited the characteristics illustrated in Figure 3-2 and Figure 3-3A. However, it was only feasible if the signal clearly returned to the baseline value (Figure 3-3A) preferably with minimal baseline shift e.g. $\Delta Cp \approx 0$. If a clear baseline shift was observed, a linear or (most often) bezier fit was adopted (Figure 3-3B and C). Since most of the systems exhibited a clear return to baseline, linear and Bezier constituted the principle method of fitting the baseline of enthalpy measurements. When Ni200 couples were examined however, it was necessary to apply the tangential and horizontal left-started fitting models. This was a consequence of the aggravated base metal dissolution, resulting in significant shifting of the thermal events to higher temperatures. Subsequent solidification peaks occurred in very close proximity to the cooling transient e.g. isothermal to cooling hysteresis (Figure 3-3D and E). Tangential fitting was implemented when the baseline value changed with temperature, and horizontal when a flat baseline was confirmed.

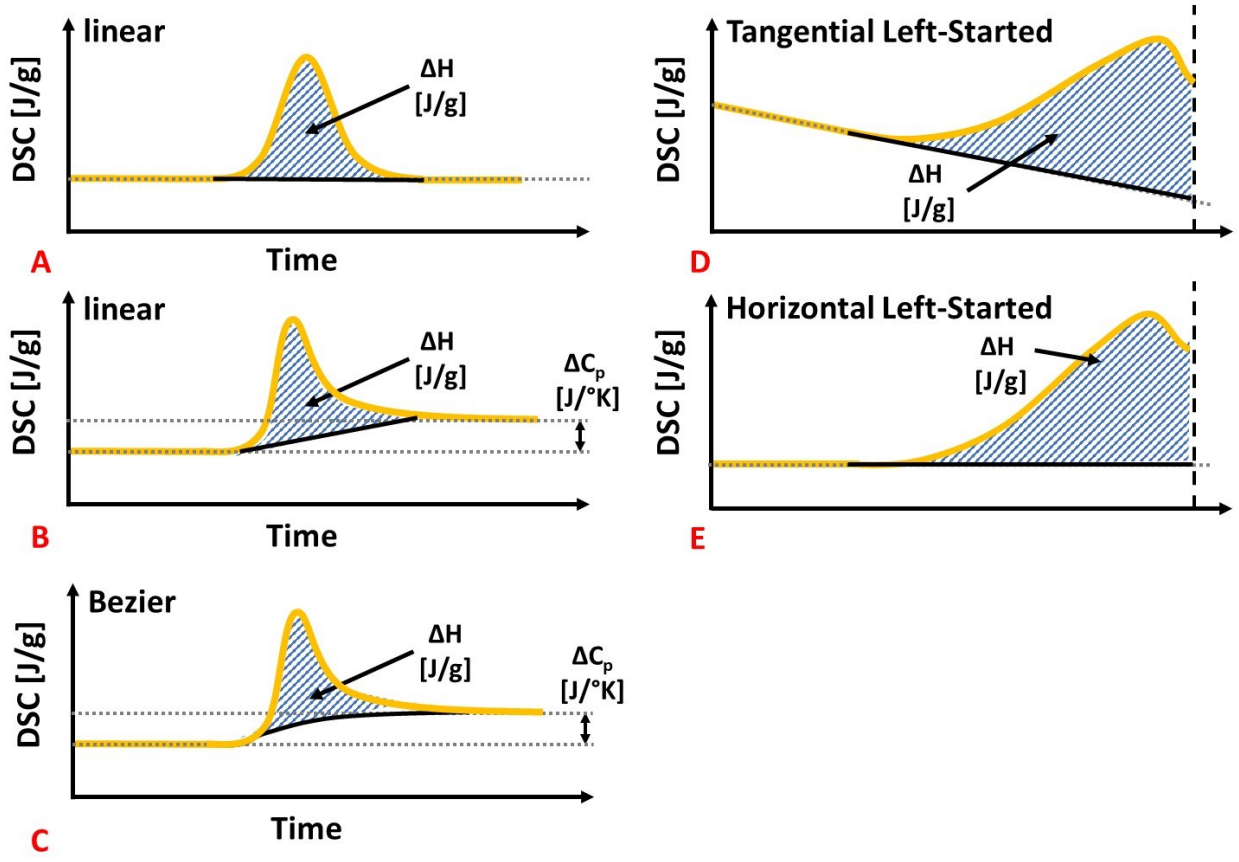

Figure 3-3 - Principal baseline corrections methods adopted in current work.

3.5.2 *Signal Stabilization*

Changes in the heating rate such as that which occurs during a transition from cooling segment to a heating segment or from an isothermal hold to a cooling cycle have a significant influence of the stability of the signal as the controller and heating source must quickly compensate for the drastic changes by adjusting the power input in order to stabilize the scanning rate as per the set value. This artifact is best illustrated through examination of actual cyclic data (Figure 3-4) with the following thermal profile: Heating at 20°C/min → 5 min isothermal hold at 1050°C (not shown) → cooling 20°C/min, repeat.

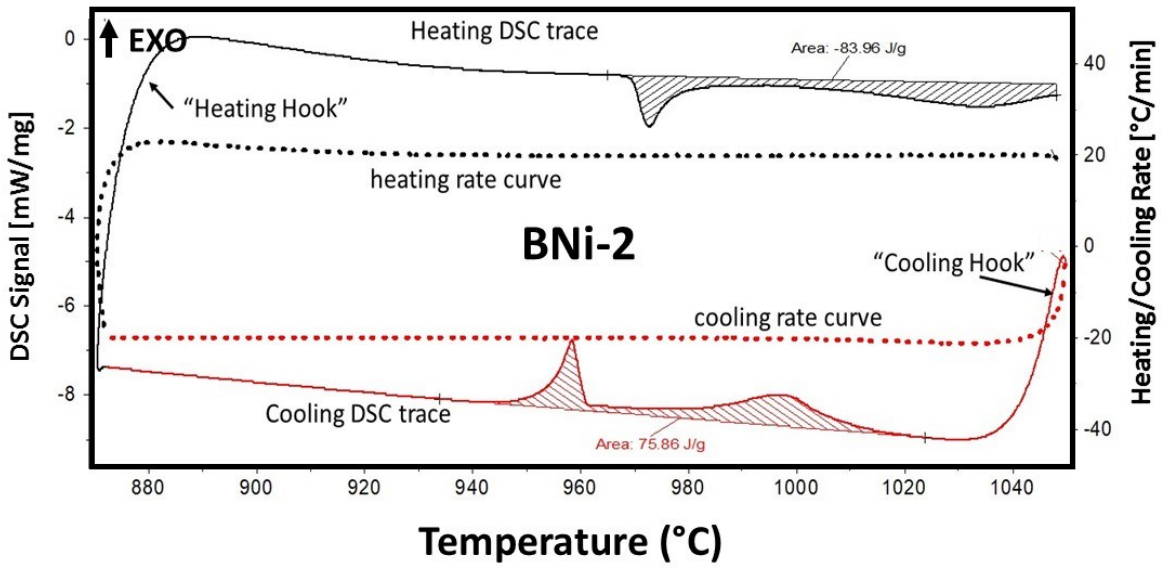

Figure 3-4 - Cyclic data illustrating heating and cooling "hooks" resulting from rapid changes in heating and cooling.

This data plots the heating rate along with the typical DSC heat flow (mW/mg) for which it is evident that stabilization of the signal requires over 10°C from an isothermal hold (not shown) which follows the heating segment. In this case, it is possible to resolve the exothermic solidification event (940 – 1020°C). Immediately upon cooling from 1050°C, the cooling rate increases to the programed rate of 20°C/min. This creates the characteristic "hook" in the DSC heat flow trace in the temperature range of 1050 to 1035°C. Below 1035°C, a stable, programmed cooling rate is established. Due to undercooling, the liquid phase does not begin solidification until 1020°C. The solidification peak does not overlap with the hook, resulting in a stable baseline before and after solidification is complete. This allows a linear baseline construction to be used to measure the solidification enthalpy.

For systems involving pure nickel (Ni200), it became evident early on that interactions between the FM and BM had caused the solidification temperature range of the liquid phase to shift to higher temperatures as illustrated in Figure 3-5. Undercooling of the liquid FM is less significant, such that the solidification peaks overlap with the cooling 'hook' artifact, making it difficult to distinguish the baseline for accurate enthalpy measurements. For instance, an attempt using the Bezier-type baseline fit was used to approximate the shape of the heat flow baseline for the Ni200/BNi-3 solidification peak with poor success as the values were drastically underestimated due to the baseline masking. Furthermore, attempts at measuring heating enthalpy

were also questionable as the peak shifting appeared to have resulted in incomplete/interrupted melting thus no return to a stable baseline being established after melting, making it difficult to choose an appropriate baseline construction. In such cases tangential and horizontal left-started would be possible but may underestimate values of the melting enthalpy, a portion of the event being lost during the hysteresis from heating to the isothermal hold. However, in most cases the solidification enthalpy measurements corresponded closely to the melting enthalpies, indicating that this underestimation is not significant.

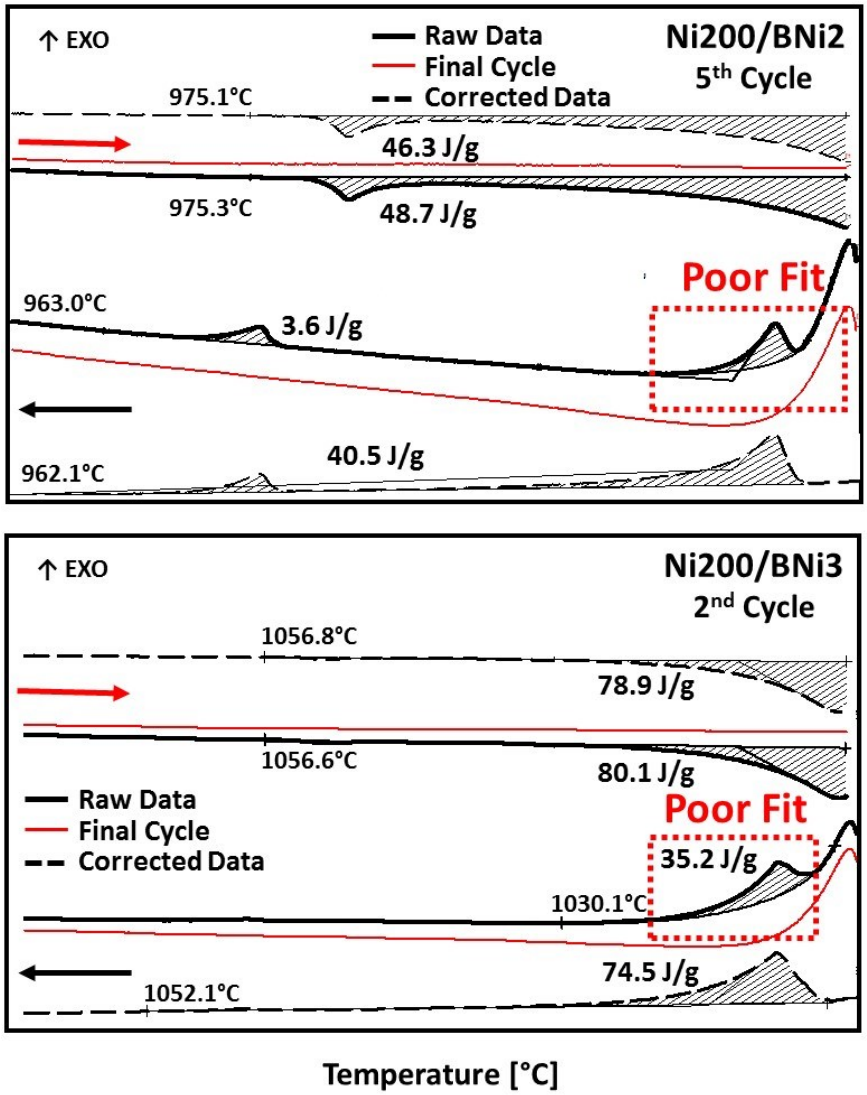

Figure 3-5 - Experimental data from cyclic DSC experiments illustrating masking of thermal event by cooling transients and self-subtraction method implemented to eliminate both baseline line shift and "hooks".

A common practice to achieve a flat or corrected baseline is to run a "correction file" which typically involves an empty sample crucible, or in the current case only the base metal without a braze foil in the sample crucible. An example of this is shown in Figure 3-6 where the curve labelled "baseline correction" is a run with a Ni200 base metal only in the sample crucible and the "raw data" curve is a typical experimental run with Ni200 and BNi-2 foil in the crucible. The "corrected data" is achieved by subtracting the Baseline correction file from the raw data file. In can be seen that this substantially flattens the baseline, particularly removing the large hook developed during initial heating from room temperature to 200°C. It also flattens the baseline over the melting and solidification event during heating and cooling respectively.

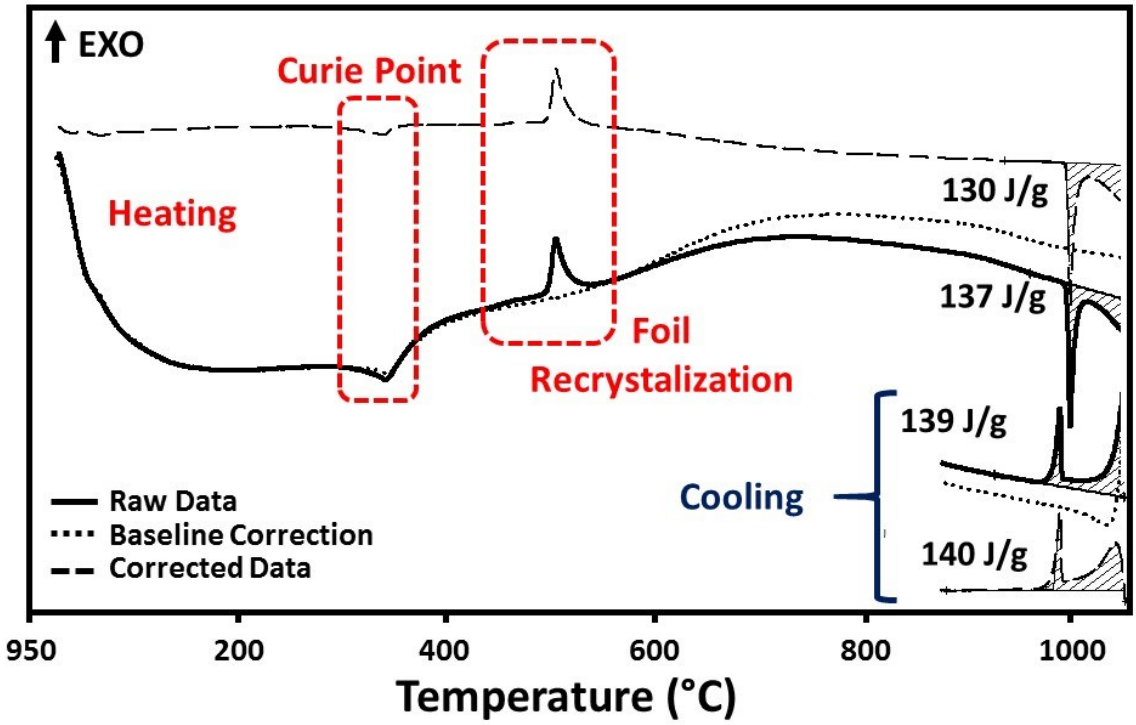

Figure 3-6 - Influence of using a baseline correction on the DSC results.

It was generally found that this method for baseline was subject to variation and dependent significantly on small mass difference between samples and even the position of the sample in the crucible and the crucible on the carrier plate. A good example of the problem in Figure 3-6 is the subtle endotherm corresponding to the curie point the Ni200 base metal (approx. 350°C). This peak should have been completely removed by the baseline correction. However, the thermal event was still present despite best efforts to minimize the discrepancies in mass and position of the base metal within the crucible.

An alternative method was therefore developed to assist in such situations which involved the use of the final cycle (e.g. complete IS) heat flow trace shown by the thin red curve in Figure 3-5. These traces show no discernible traces of any thermal events, thus confirming complete Isothermal Solidification. In this way, it represents an ideal “baseline correction” since it is the same sample but without the phase transformation of interest. As expected, the cooling trace still exhibits the cooling “hook” which is an artifact of the method and independent of the thermal events occurring in the sample. The shape of this hook was found to be consistent for all cooling cycles for a given sample. The method was preferred as it avoids issues related to the inability to replicate the exact conditions (mass, position, etc.) in a separate correction run and avoided the

laborious task of having to repeat each experiment, which would have resulted in doubling the workload.

The Netzsch software allows the subtraction of curve segments providing the thermal profile is identical. In this case the last cooling/heating cycle was used as a subtraction/correction for all heating/cooling segments that still exhibited solidification/melting peaks. The results of this subtraction for the 2nd cycle of the Ni200 data, are denoted by a dashed line in Figure 3-5. This correction method creates a flat baseline on the cooling curves such that a linear baseline construction can be used to determine solidification enthalpies. Note that the curve subtraction correction method does not significantly alter the shape of the melting or solidification peaks and measurements for the majority of samples that exhibited the DSC traces described Figure 3-5 and Figure 3-4. This is reasonable since the hook artifact and the transient cooling/heating rate regions do not overlap with the melting/solidification peaks in these samples. The same can be said for all melting peaks (i.e. those including Ni200 materials).

The subtraction results show that enthalpy measurements made from the cooling curves increase and are at a level similar to the enthalpies obtained from the heating curves. For consistency sake, the curve subtraction method was applied to all cooling curves from this study. The only exception was for the IN600/BNi-3 braze couple, where a final cooling curve without some solidification was not achieved even after 40 cycles. In this case the solidification peaks were below the cooling hook as described in Figure 3-4, thereby making a subtraction correction unnecessary. Enthalpy measurements in this case were made using a standard liner baseline construction.

3.5.3 *Thermal Dampening*

Figure 3-7 presents the heating and cooling data for; (A) the BNi-3 FM alone and (B) the Ni200//BNi-3 (configuration B, Figure 3-1) e.g. the BNi-3 beneath Y_2O_3 coated Ni200. The results confirm a degree of thermal dampening as a consequence of the Ni200 acting as a heat sink. This phenomenon was reported by Turrif et al., albeit much more severe wherein the FM was located on top of the substrate [19872]. The dampening effect is clearly evident by the relative magnitude of the melting and solidification enthalpies (Figure 3-7A) in addition to the low temperature recrystallization event (Figure 3-7B). In the present work a ratio of the two values is used to relate

measured enthalpy values to those obtained with either the FMs only or, in certain cases, modified version of the FMs used to account for compositional modification of the liquid phase as a response to TLPB.

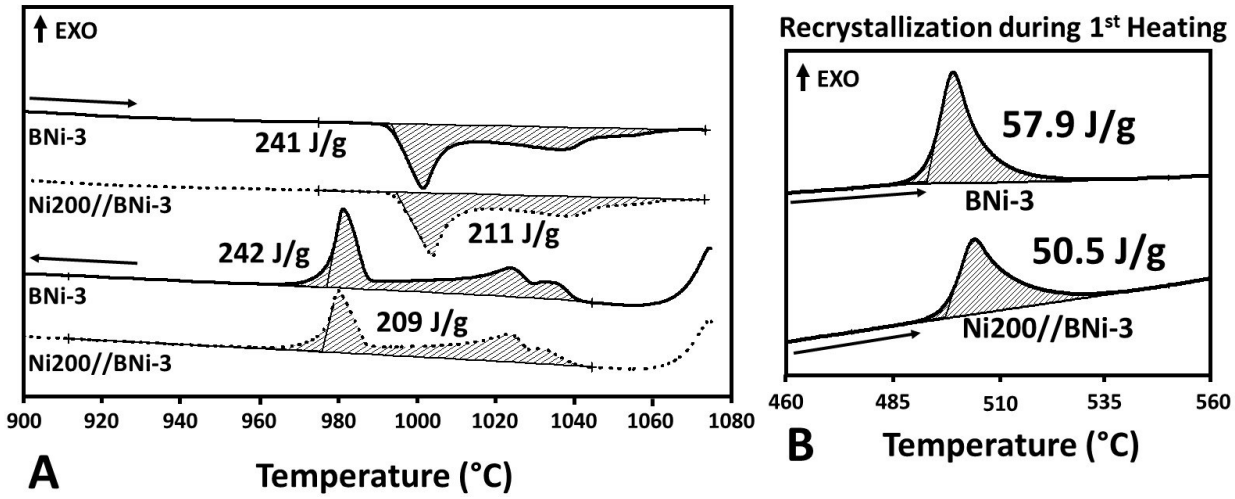

Figure 3-7 - DSC cooling and heating traces illustrating influence of substrates on the magnitude of the enthalpy measurements. (A) Melting and solidification events and (B) low-temperature recrystallization event.

CHAPTER 4 Initial Boron Uptake and Kinetics of Transient Liquid Phase Bonding in Ni-based Superalloys

E.D. Moreau, S. F. Corbin

Department of Mechanical Engineering, Dalhousie University,
1360 Barrington Street, P.O. Box 15,000, Halifax, Nova Scotia, B3H 4R2, Canada

Status: Pending Publication in Journal of Metallurgical and Materials Transactions A (2020)

Authors Contribution: All experimentation performed by E. D. Moreau with direct guidance by S. F. Corbin.

Abstract

The present work details a quantitative investigation into the braze gap width dependence on the initial boron uptake (IBU) phenomena – an event which manifests during the initial stages of brazing of boron-containing filler metals. This was accomplished using in-situ cyclic DSC of both full- and half- joint TLPB couples i.e. IN625/xBNi2/IN625 and IN625/xBNi2. All joints demonstrated a linear relationship between the isothermally solidified gap width with the square root of time which were in excellent agreement with conventional metallographic analysis methods. A conceptual model designed to quantify both the extent of isothermal solidification and IBU during TLPB in terms of the redistribution of boron as borides was implemented. The investigation demonstrated excellent agreement with microstructural and DSC results further supporting the crucial role boride formation has on the kinetics of TLPB. Notable was the similarity between the MBC values as time approached zero (y-intercept) of approx. 20 μm for all specimens, which indicate a stage of rapid initial solute uptake (ISU) prior to reaching the braze temperature, which is independent of gap width.

4.1 Introduction

Metallurgically, diffusion brazing, (also known as transient liquid phase bonding, TLPB) generally involves the following sequential stages; melting of the filler metal, spreading and wetting of the base metal surfaces, dissolution which leads to widening of the initial liquid region, and the progressive isothermal solidification (IS) of the liquid phase, occasionally followed by a post-homogenization treatment [6, 9, 36, 71, 83-85]. Aside from the post-homogenization stage, the isothermal solidification (IS) stage represents the lengthiest portion of furnace brazing, typically requiring anywhere from a few hours to a day to complete; a stark contrast to the melting and gap widening (or dissolution) stages which transpire within minutes [71-83]. Many authors have attempted to quantify the process of isothermal solidification through a variety of techniques, the simplest of which involve assessing the extent of IS by metallographically measuring the thickness of any residual athermally solidified liquid as a function of brazing time [71,83-89]. This route is however laborious, time-consuming and prone to experimental uncertainties, since multiple samples and extensive metallographic analysis are needed for each gap thickness and brazing time. A more efficient method, first developed by Partz and Lugscheider [90] and later employed by Arafin et al. [88] and Sakamoto et al. [91], consisted of placing a filler metal powder in a low-angle wedge, created from two plates of the desired base metal (BM), thereby creating a continuously varying braze gap dimension. Brazing of a series of samples at different times allows the determination of the maximum permissible clearance required to avoid the formation of athermally solidified structures per the given conditions (temperature, composition, time, etc.). The work ultimately provided a measure of the maximum brazing clearance (MBC), a key parameter in avoiding brittle centerline eutectic phases and achieving satisfactory TLPB. While the MBC analysis has great practical importance, it also allows interpretation of the more fundamental kinetics of TLPB, which will be utilized in the current study.

Since the isothermal solidification stage is the most significant step during TLPB, it has been extensively modelled [9, 36, 85, 88, 91]. A widely accepted prediction for the complete IS time, t_f in a generalized form is;

$$(t_f)^{1/2} = \frac{2w_{max}}{k} \qquad \textbf{Eq. 4-1}$$

where $2w_{max}$ is the starting gap width and k is a rate constant. The rate constant k is dependent on the diffusivity of the melting point depressant (MPD) element into the base metal and its

concentration in the liquid and solid adjacent to the interface. In conventional TLPB, the expectation is that dissolution of the base metal occurs during initial heating, such that gap widening occurs prior to the isothermal solidification stage. In Eq. 4-1, dissolution is represented by $2w_{max}$ which is generally expected to be greater than the original gap or braze insert dimensions $2w_o$. From equation (1) the starting gap width present (or assumed) has a key influence over the complete IS time.

In most studies of Ni-based superalloy brazing, a linear relationship between the quantity of liquid phase remaining and the square root of time exists, which would be expected from the form of equation (1) [84-89]. In the case of MBC curves, this translates to an increase in the isothermally solidified zone (ISZ) thickness with the square root of brazing time. Close examination of the MBC curves produced by Partz and Lugscheider [90], Arafin et al. [88] and Sakamoto et al. [91] revealed that the MBC curves, when extrapolated to zero braze time, predict a non-zero ISZ width. In other words, a significant degree of diffusional solidification has occurred prior to attaining the peak brazing temperature. In other work, where a braze foil insert is place between two base metal plates, it is generally assumed that the foil insert thickness is the thickness of the original liquid or centerline eutectic at zero braze time (i.e. dissolution is assumed to be negligible) [83-89]. Examination of plots of centerline eutectic width versus the square root of time from these studies, reveal that the predicted initial liquid present at zero braze time in less than the original insert thickness. This also indicates that some diffusional solidification occurs during initial heating to the braze temperature.

Ruiz-Vargas et al. [71] performed a detail examination of the melting stages of a BNi-2 foil against a pure Ni base metal. They established that boron diffusion into the base metal occurs as soon as the solidus temperature is reached. This resulted in Ni_3B precipitation and the formation of a diffusionally affected zone (DAZ). Despite some evidence of base metal dissolution during further heating, once at the peak braze temperature, a significantly developed DAZ layer and boride precipitation remained below the solid/liquid interface.

It can be concluded that, for the case of Ni-based TLPB, where boron is used as a MPD, an initial boron uptake (IBU), which reduces gap width, dominates over gap widening by dissolution. Therefore, in examining the kinetics of TLPB using the form of equation (1), it is important to understand the IBU process in detail, since it will determine the starting gap width at

the beginning of the isothermal hold time and the IS completion time. The purpose of the current study is to examine. quantify and explain the IBU as a function of braze gap width.

BNi-2 was chosen as the braze alloy due to its wide commercial use and the fact that it contains two of the most important melting point depressants (i.e. B and Si). IN625 was chosen as the base metal also due to its wide commercial use, relatively simple microstructure as a solid solution alloy, yet containing many of the important boride formers including Cr, Mo and Nb as outlined recently by Pouranvari et al. [92].

4.2 Results and Discussions

DSC Analysis of Liquid Fraction

One goal of the current work was to validate whether the DSC technique described above using half-joints was capable of accurately simulating isothermal solidification of an actual full-joint e.g. BM/FM/BM. IN625/2xBNi2/IN625 (full-joint) and IN625/1xBNi2 (half-joint) TLPB couples were examined for an extended period under identical conditions. Figure 4-1 compares the melting and solidification peaks for the full and half joints for various brazing cycles and times. The cycle number (i.e. 1C, 2C, etc.) and equivalent liquid duration time in minutes are indicated next to each cyclic curve.

The measurements clearly illustrate the progressive decrease in enthalpy, ΔH_t, resulting from IS as indicated by the shaded area under the melting and solidification peaks. Furthermore, ΔH_t for both full and half joint arrangements decrease at similar rates. Additionally, the liquidus and solidus temperatures are relatively unchanged as IS progresses. As confirmed by numerous authors [76,89-90], the dual melting and solidification peaks observed are associated with the ternary and binary melting/solidification events involving γ-(Ni), Ni_3B, and β-Ni_3Si. A small third peak, which occurs at the lowest temperature and only present during the initial heating (point A), is believed to pertain to a minor quantity of Chromium-rich borides formed during delayed recrystallization from the amorphous FM [71, 90].

The repeated enthalpy measurements, ΔH_t can be related to liquid fraction, L_f providing there is a means of assessing the progress of IS. This involves creating an additional specimen identical to that under investigation, however with the faying surface coated with Y_2O_3 as

described in the methodology. For comparison purposes, the enthalpy of fusion ΔH_o for the BNi-2 foil alone was measured as 220 J/g. The same foil melted in the presence of a fully coated (Y_2O_3) BM for the half and full joint arrangements, had enthalpy values of 218 J/g (ΔH_{oh}) and 132 j/g (ΔH_{of}), respectively. This reduced enthalpy in the presence of the BM is due to a thermal dampening effect as first described by Kuntz et al [76].

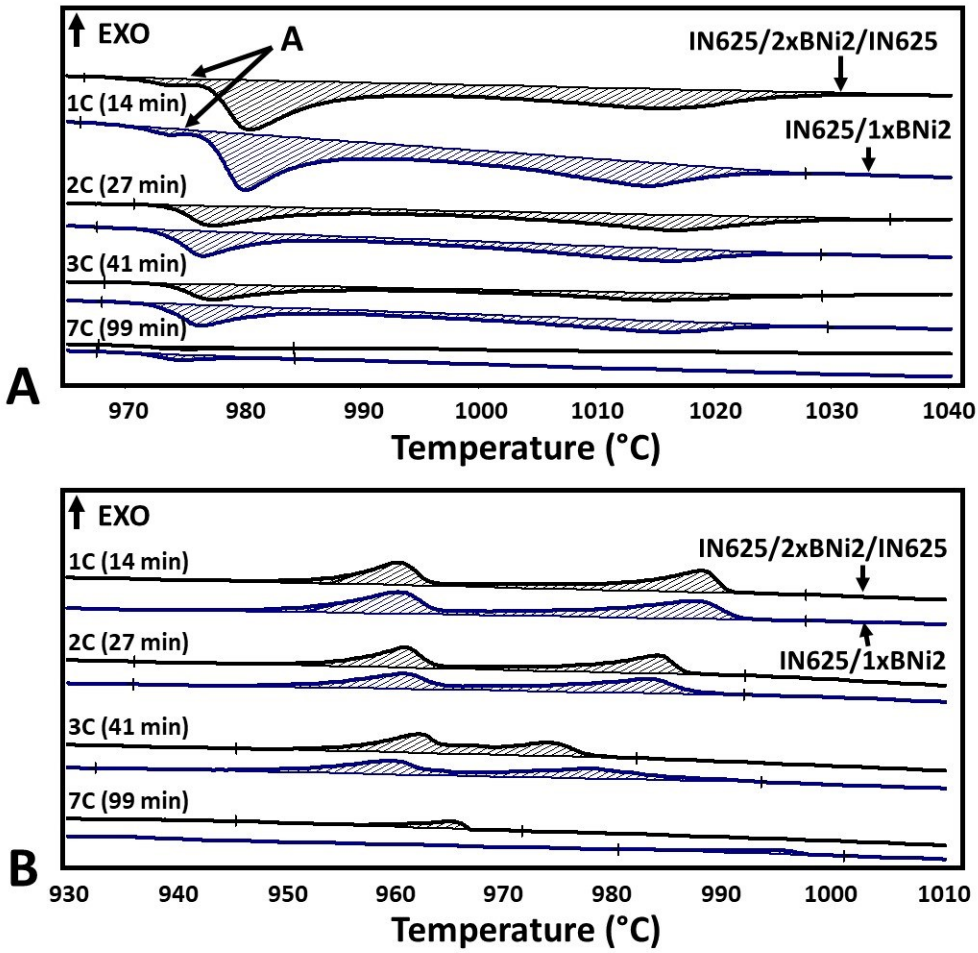

Figure 4-1 - Cyclic DSC melting (A) and solidification (B) measurements for IN625/2xBNi2/IN625 (full joint) and IN625/1xBNi-2 (half Joint) TLPB couples.

Using the above ΔH_{oh} and ΔH_{of} values, the liquid fraction L_f data versus time ($min^{1/2}$) was determined for; the half joint using a single BNi-2 foil and full-joints using 1x, 2x and 3x BNi-2 foils. The results are plotted in Figure 4-2, which demonstrate a linear relationship ($R^2 > 0.95$) between L_f and $t^{1/2}$ such that linear regression can be applied to obtain the following equation;

$$\frac{\Delta H_t}{\Delta H_{oh}} = L_f = -k_L\sqrt{t} + L_o \qquad \textbf{Eq. 4-2}$$

where ΔH_t and ΔH_{oh} (or ΔH_{of}) have their previously defined meanings in {J/g}, L_f is the corresponding liquid fraction remaining at time t, $-k_L$ the solidification rate {fraction/min$^{-1/2}$}, and L_o the initial liquid fraction present at t = 0. The time for complete IS, t_f, can be derived from Eq. 4-2 when $L_f = 0$, or:

$$t_f = \left(\frac{L_o}{k_L}\right)^2 \qquad \textbf{Eq. 4-3}$$

Figure 4-2 demonstrates that both L_o and t_f decrease as the number of BNi-2 foils decreases, which corresponds to a decreasing gap width, $2w_o$. The data for the 1x foil half joint and the 2x full joint

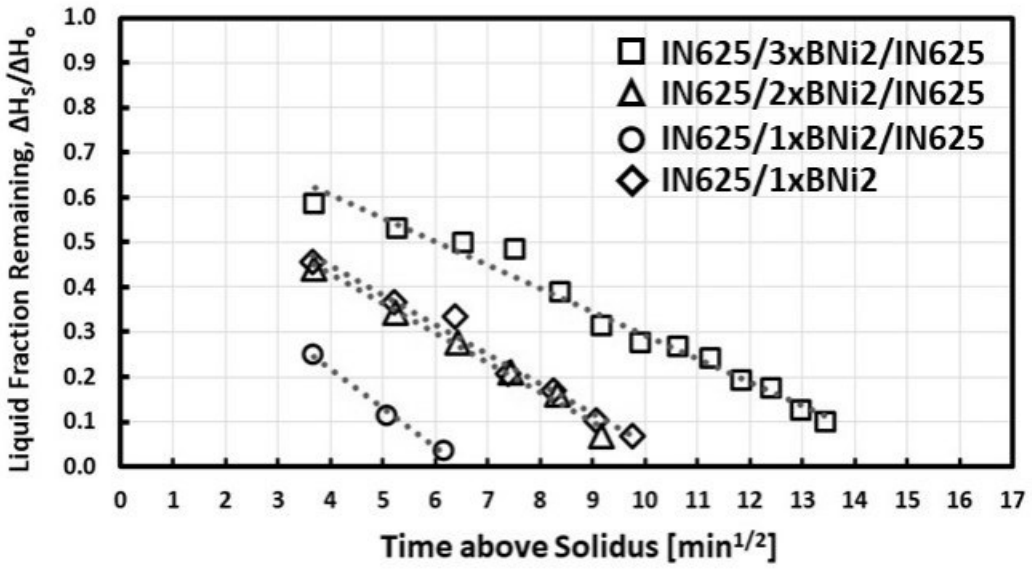

Figure 4-2 - Liquid fraction remaining ($L_f = \Delta H_t/\Delta H_o$) as a function of brazing time (min$^{1/2}$) for 2xIN625-1xBNi-2, -2xBNi-2, -3xBNi-2 full joints and 1xIN625-1xBNi-2 half joint. T_{MAX} = 1050°C.

are similar, resulting in a similar value for t_f. This confirms that DSC analysis of the half joint arrangement can correctly represent a full joint geometry with an equivalent gap width.

As pointed out by Murray and Corbin [78], the L_f measurements acquired from the DSC measurements can be converted to the width of liquid phase remaining in the gap, $2w_t$ {μm} providing that the original thickness of the braze gap, $2w_o$ is known;

$$2w_t = \frac{\Delta H_t}{\Delta H_o} 2w_o = L_f 2w_o \qquad \textbf{Eq. 4-4}$$

Combining Eq. 4-3 and Eq. 4-4:

$$2w_t = 2w_o\left(-k_L\sqrt{t} + L_o\right) = -k_w\sqrt{t} + 2w_i \qquad \textbf{Eq. 4-5}$$

Where, $k_w = 2w_o k_L$ {μm/min$^{1/2}$} and $2w_i = 2w_o L_o$ {μm}.

For each sample, a value of w_o was obtained from multiple measurements of FM thickness made on post braze polished cross sections of the DSC samples. Using these measurements, the liquid fraction data of Figure 4-2 was replotted as the liquid width remaining, $2w_t$ in Figure 4-3.

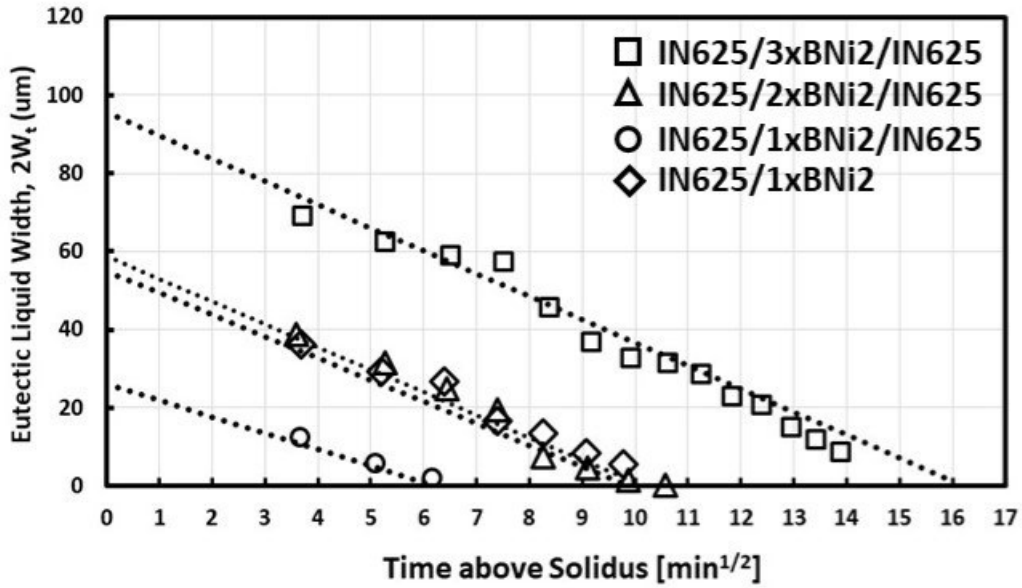

Figure 4-3 - Corresponding width of eutectic liquid remaining (2wt) as a function of brazing time (min$^{1/2}$) for 2xIN625-1xBNi-2, -2xBNi-2, -3xBNi-2 full joints and 1xIN625-1xBNi-2 half joint. T_{MAX} = 1050°C.

The plot shows that repeated enthalpy measurements made using the DSC can provide a measure of the degree of IS in terms of the thickness of the remaining liquid phase. This thickness can be

validated by measuring the width of athermally solidified eutectic, as described in the section below.

Microstructural Validation of DSC Isothermal Solidification Analysis

To validate the DSC results, an additional IN625/1xBNi2 half-joint was heated to the brazing temperature (1050°C) and immediately furnace quenched (approx. 50°C/min). Figure 4-4 illustrates the polished cross section of this sample which experienced a liquid duration brazing time of less than 8 minutes. Figure 4-4 also provides the microstructure of the half joint configuration corresponding to the DSC data from Figure 4-1 and Figure 4-2 for comparison. The cycled half-joint exhibited a liquid duration of 96 Minutes (1.6 hours). Figure 4-4 illustrates the three regions typical of a TLPB Ni-based superalloy joint: an isothermally solidified zone (ISZ), the diffusionally affected zone (DAZ), and the athermally solidified zone (ASZ). As a result of the brief, 8 minute braze time, the quenched specimen has a significant liquid fraction (ASZ) present. With longer brazing time, the sample of Figure 4-4B exhibits nearly complete IS, with only a small layer of ASZ at the top of the joint. This is consistent with the DSC data which indicates this sample had a liquid fraction, $L_t = 0.07$ (7%) at the end of the braze time (see the IN625/1xBNi-2 data set of Figure 4-2).

Rate of IS and the Maximum Brazing Clearance (MBC)

Determining the liquid width, either through DSC analysis, or from post brazing centerline eutectic metallography, has been the primary way to quantify the kinetics of IS during TLPB [83-89]. One limitation of this approach is that the liquid width (or centerline eutectic width) values depend on the initial gap width, as demonstrated by the full joint analysis of Figure 4-2 and Figure 4-3. The basic kinetics of IS should only be dependent on the compositions of the filler and BM and the brazing temperature. This can be further explained by Figure 4-5 below.

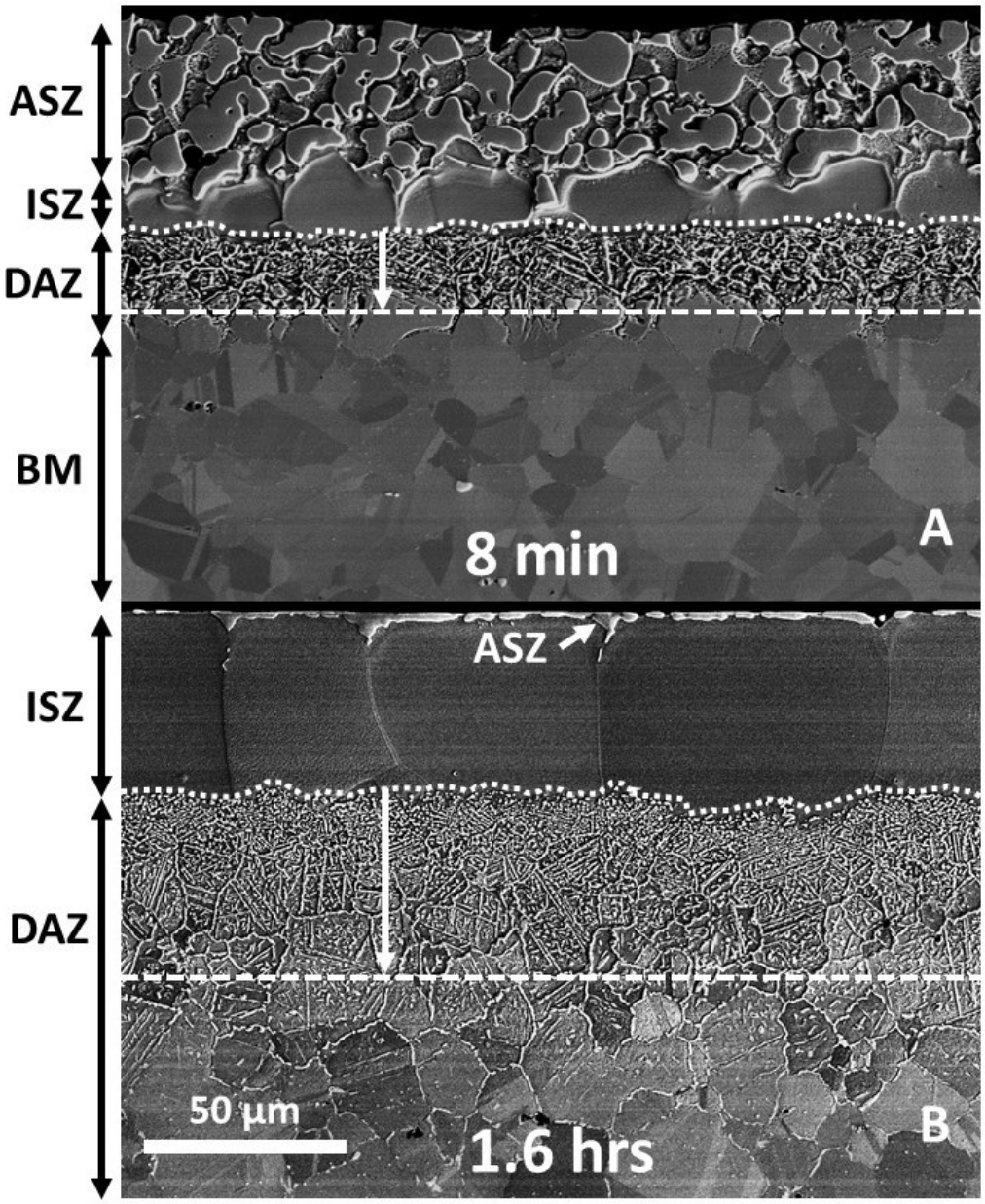

Figure 4-4 - Microstructure of the interrupted (A) and Cycled (B) 1xIN625/1xBNi2 half-joint specimens. The purpose of the white arrows will be discussed in section 4). T_{MAX} = 1050°C.

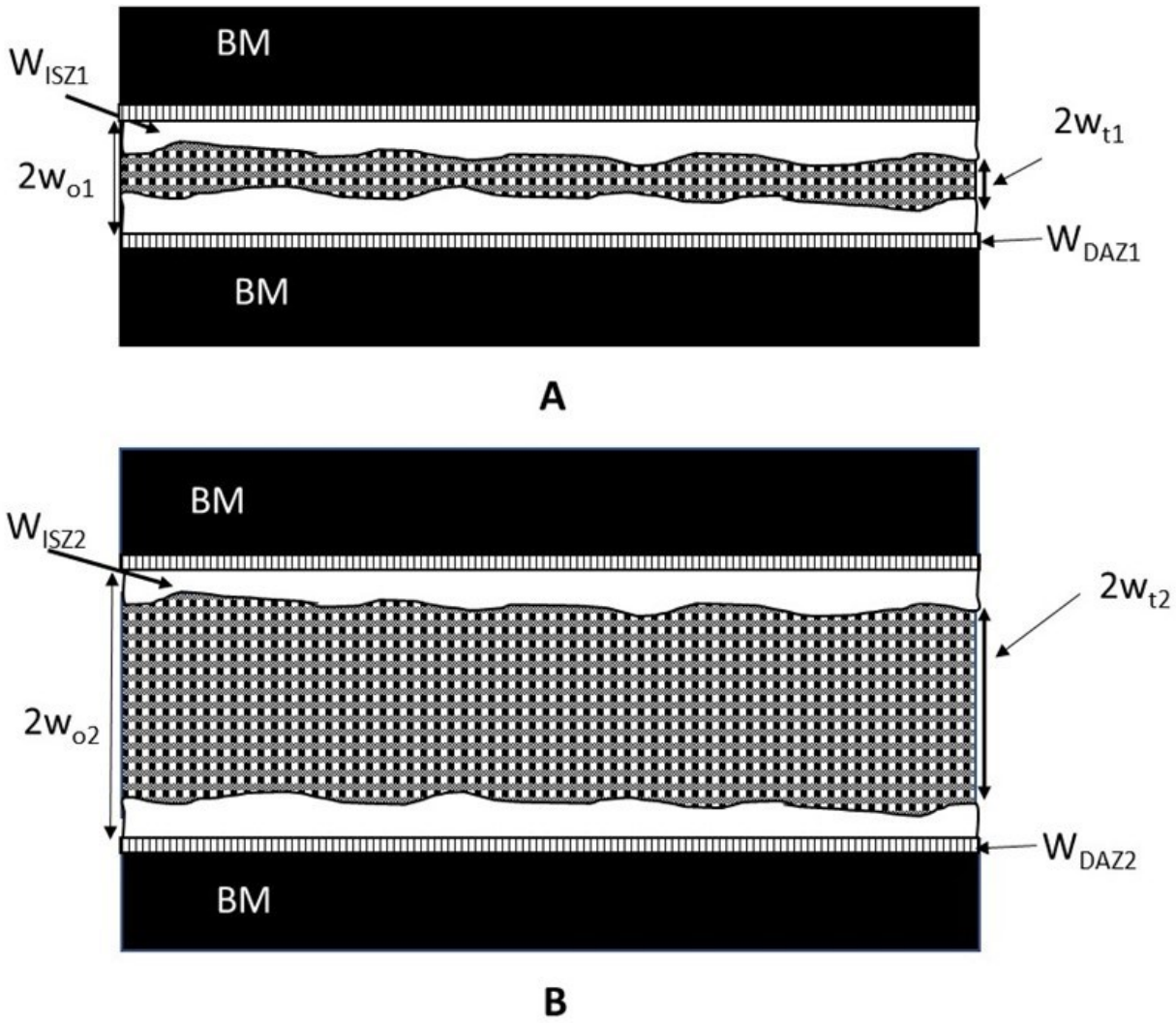

Figure 4-5 - Schematic illustrating the influence that initial gap width has on the liquid width of a joint during brazing. (A)-small gap width, (B)-large gap width.

The schematics A and B in Figure 4-5 depict two braze joints of different initial gap widths ($2w_{o1} < 2w_{o2}$). Both joints are assumed to have experienced the same braze temperature and time, such that a small amount of isothermal solidification has occurred. The liquid width, $2w_{t1}$ and $2w_{t2}$ are different since the initial gap widths are different. However, since the growth of the ISZ and DAZ regions are dependent only on the rate of diffusion and not the initial gap width, their thickness should be identical for both joints (i.e. $2w_{ISZ1} = 2w_{ISZ2}$ and $2w_{DAZ1} = 2w_{DAZ2}$). In other words, the following relations hold;

$$\boldsymbol{2w_{ISZ1} = 2w_{ISZ2} = (2w_{o1} - 2w_{t1}) = (2w_{o2} - 2w_{t2})} \qquad \textbf{Eq. 4-6}$$

Further, if both sides of Eq. 4-6 are divided by $2w_{o1}$ or $2w_{o2}$ we get;

$$\frac{2w_{ISZ1}}{2w_{o1}} = \frac{(2w_{o1}-2w_{t1})}{2w_{o1}} \quad \textbf{or} \quad \frac{2w_{ISZ2}}{2w_{o2}} = \frac{(2w_{o2}-2w_{t2})}{2w_{o2}} \qquad \textbf{Eq. 4-7}$$

Recognizing that $L_f = 2w_t/2w_o$ Eq. 4-6 can be rearranged to;

$$\boldsymbol{2w_{ISZ} = 2w_o(1 - L_f)} \qquad \textbf{Eq. 4-8}$$

As described by Eq. 4-2, the DSC measurements can determine L_f as a function of braze time. Using Eq. 4-8 the thickness of the ISZ layer as a function of braze time can be determined, providing the initial gap width $2w_o$ is measured from post brazing metallographic analysis.

Metallographic measurements of $2w_o$ for the 1xBNi-2, 2xBNi-2, 3xBNi-2 full joints and 1xBNi-2 half joint yielded mean values of 43, 89, 118, and 84 μm, respectively. Using these values and the L_f data of Figure 4-2, the ISZ thickness $2w_{ISZ}$ for all four samples is plotted versus the square root of time in Figure 4-6. A consequence of plotting the data in this way is that the growth rate of the ISZ layer is observed to similar for all samples and independent of gap width, as proposed above. The influence of gap width is only through the time of isothermal solidification, which increases as the gap with increases. This form of plot is also more useful in allowing the prediction of the isothermal solidification time, $t_x^{1/2}$ for any gap width, or MBC_x (or $2W_{ISZ,i}$) of interest, as noted in Figure 4-6.

The data also points out that, regardless of gap width, all joints exhibit a similar y-intercept value at zero brazing time. Linear regression analysis of the data contained in Figure 4-6, enables determination of this value, $2w_{ISZo}$;

$$\boldsymbol{2w_{ISZ} = k_w t^{1/2} + 2w_{ISZo}} \qquad \textbf{Eq. 4-9}$$

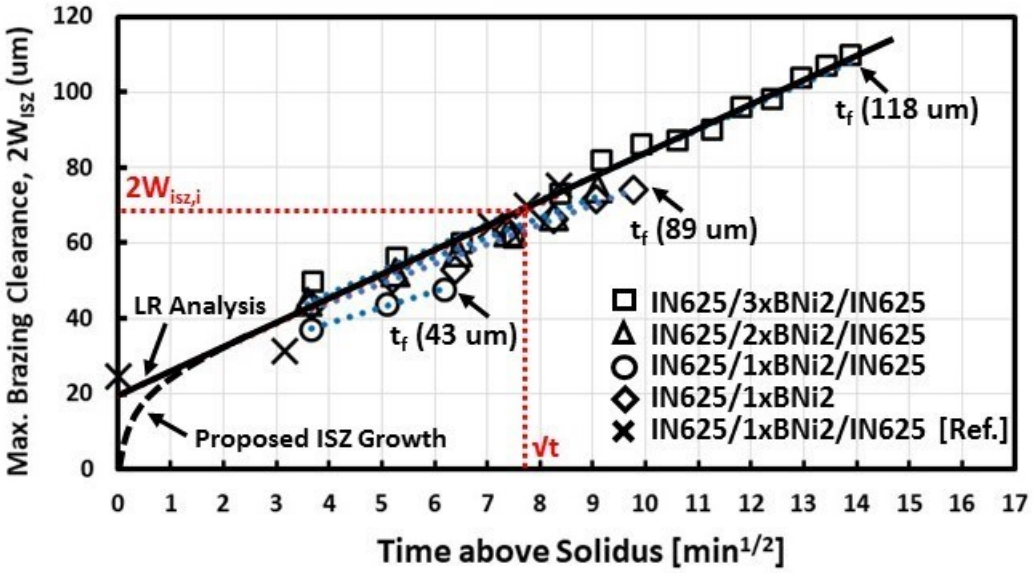

Figure 4-6 - Maximum Brazing Clearance ($2W_{ISZ}$) as a function of brazing time ($min^{1/2}$) for 2xIN625-1xBNi-2, -2xBNi-2, -3xBNi-2 full joints and 1xIN625-1xBNi-2 half joint. X data is taken from reference [88].

Where the rate constant k_w has the same value as before, but $2w_{ISZo}$ is the isothermally solidified width obtained by extrapolating $2w_{ISZ}$ to zero time (i.e. the Y-intercept). Table 4-1 lists the values from linear regression obtained from both Eq. 4-2 and Eq. 4-9. The value of $2w_{ISZo}$ is very close for all full and half joints studied. It also agrees very closely to data that can be derived from a wedge gap/metallography type analysis previously performed by Arafin et al. on IN625/BNi-2 brazed joints at 1050°C [88].

The value of $2w_{ISZo}$ (i.e. ~ 21 μm in the current case) is convenient mathematically but lacks physical meaning. As shown by Ruiz-Vargas et al. [71] and Murray and Corbin [78], no boron diffusion or ISZ formation occurs prior to reaching the solidus temperature of the filler metal (i.e. zero braze time). Furthermore, rapid growth of the ISZ has been observed during initial heating between the solidus and peak braze temperature [71-84]). Consequently, it is proposed that the rapid ISZ growth occurs while heating from the solidus to the braze temperature as a metallurgical interface is first formed between the BM and filler metal (see Figure 4-6). Once the braze temperature is reached the rate of ISZ growth follows the isothermal linear regression rate. Therefore, a more physically meaningful value for the initial ISZ width, is $2w_{ISZi}$ which can be determined from Eq. 4-9 using the time taken to heat from the solidus to the braze temperature, (i.e. t = 4.3 minutes, resulting in a $2w_{ISZi}$ ~ 33 μm).

Table 4-1 - Results of linear regression from isothermal solidification data.

Sample	k_L [$min^{-1/2}$]	L_o	$2w_{ISZo}$ [μm]	$-k_w$ [$\mu m/min^{1/2}$]	$2w_o$ [um]
1xIN625/1xBNi2	-0.07	0.69	22.99	5.25	84±4
2xIN625/1xBNi2	-0.09	0.56	21.62	4.27	43±4
2xIN625/2xBNi2	-0.07	0.71	20.58	6.10	89±18
2xIN625/3xBNi2	-0.05	0.81	21.46	6.23	118±5

Arafin et al. [88]: $-k_w = 6.35$, $2w_{ISZo} = 19.61$ um

The impact of the presence of an IBU in interpreting TLPB kinetics can be demonstrated through the use of Eq. 4-1. The value of k can be determined using the isothermal solidification time measured for the three different full joints of this study e.g. 6.25, 10.1, and 16 $(min)^{1/2}$ for the $2w_o$ gaps of 43 89, and 118 μm, respectively. Assuming the starting gap widths ($2w_o$), the average k value for these three samples was 7.80 $\mu m/min^{1/2}$. Alternatively, if the IBU formation is taken into account, the actual starting gap width is $2w_t = 2w_o - 2w_{isz}$. Using the values of $2w_{isz}$ listed in Table 4-1, yields corresponding $2w_t$ values of 27.4, 62.4 and 96.5 μm for the increasing gap widths and an average k of 5.53 $\mu m/min^{1/2}$ when taking into account the IBU. From the work of Murray and Corbin [78], $k = 4erf^{-1}(C_s/C_o)D^{1/2}$ where C_s and C_o are the boron composition in the solid adjacent to the solid-liquid interface and in the filler metal respectively and D is the diffusivity of boron in the base metal at 1050°C. Using 0.3 and 13.7 at% for C_s and C_o along with the k values determined above for neglecting, and considering an IBU, results in diffusivity values of 1.7×10^{-10} and 8.5×10^{-11} m^2/s respectively. Both these values for diffusivity are within the range reported by other researchers. However, it is expected that the value of 8.5×10^{-11} m^2/s is a more accurate description for kinetics in this system since it uses a starting gap width that accounts for the IBU.

The microstructure of the completely solidified full joints (e.g. 1xBNi-2, 2xBNi-2 and 3xBNi-2) used to acquire the IS data are displayed in Figure 4-7. All three specimens consist of an ISZ which increases in width as the number of BNi-2 foil layers increase. The ISZ consists of large grains of solid solution of γ-(Ni). These grains grew epitaxially from each solid liquid interface, meeting in the middle when all the liquid was removed. All samples also have a DAZ due to the diffusion of Boron from the liquid (BNi-2) into the BM (IN625) forming Chromium-rich Borides (with Mo, Nb in minor concentrations). The thickness of the DAZ increases with

increasing MBC. This is partly due to the longer brazing times required to cause complete IS with an increase in MBC. There is also an increased quantity of boron within the MBC that must be removed during TLP brazing.

Figure 4-8 presents the compositional profiles within the ISZ layer for all three joints, as determined by SEM-EDS spot analysis. All joints exhibit a concentration gradient for all the elements. The gradient is steeper near the original solid/liquid interface, denoted by the dashed vertical lines. The composition becomes more uniform in the region near the centerline of the ISZ, particularly for the wider MBC samples. The compositions for each element vary in the same range, regardless of difference in MBC width for the three samples. Cr ranges from approximately 7 to 18 at%, Si ranges from 9 to 4 at%, Fe ranges from 2 to 6 at% and Nb and Mo both range from 0.25 to 1.5 at%. Si increases whereas all other elements decrease toward the centerline of the joint.

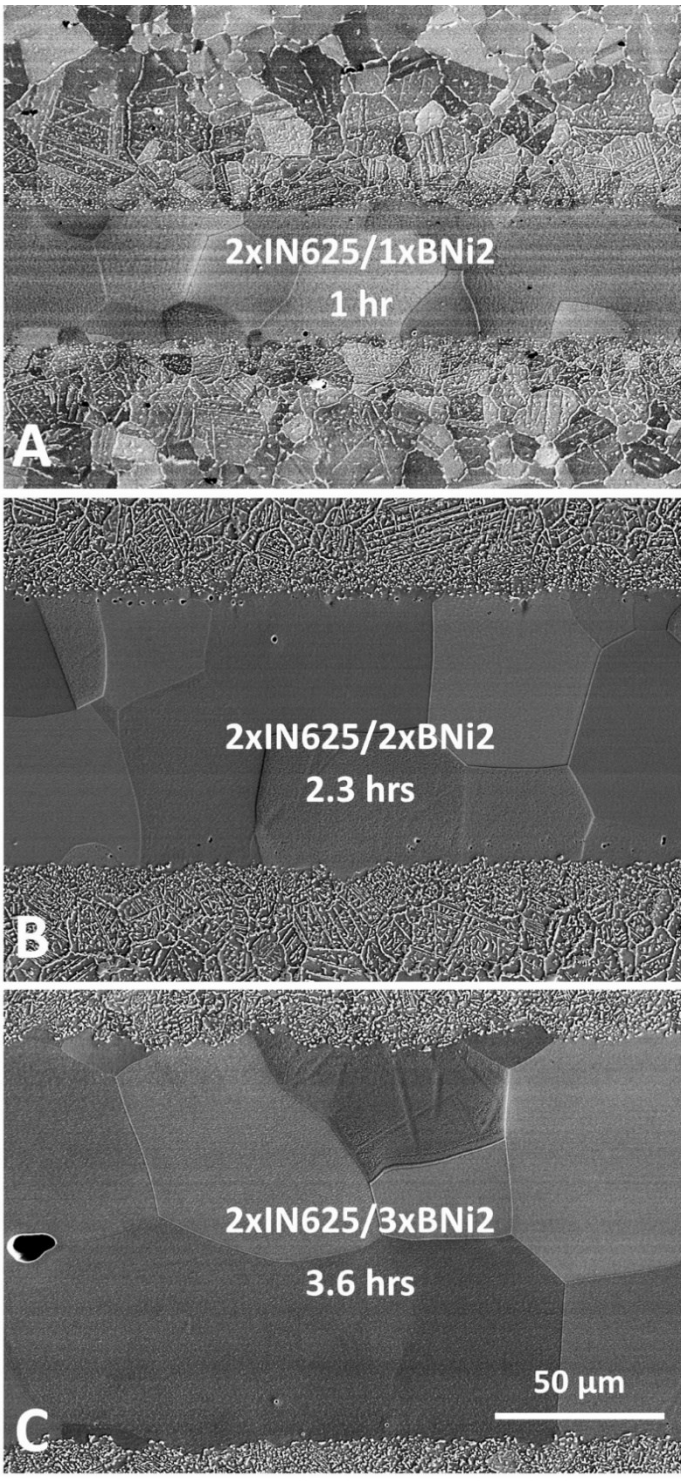

Figure 4-7 - SEM micrographs of all full-joint specimens, (A)-1 hr, (B)-2.3 hrs., (C)-3.6 hrs. T_{MAX} = 1050°C.

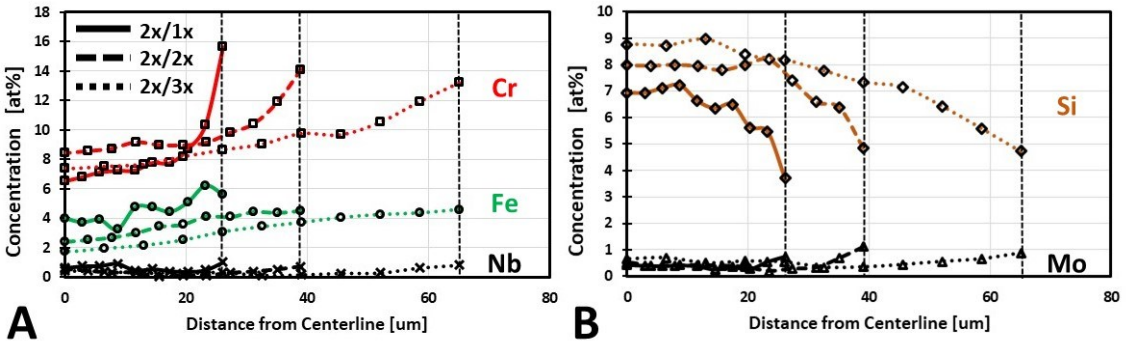

Figure 4-8 - Compositional profiles of ISZ region for full-joints 2x/1x, 2x/2x and 2x/3x couples shown in Figure 4-7. (A) Cr, Fe, Nb concentrations, (B) Si and Mo concentrations. Vertical dashed lines represent ISZ/DAZ interface.

If it is assumed that boron is the only element from the BNi-2 filler metal that diffuses into the BM, a normalized (or B free) initial BNi-2 composition can be calculated as 80.1 at% Ni -9.1% Si -7.7 at% Cr -3.1 at% Fe. It is interesting that the values of the Si, Cr and Fe elements near the centerline of the joint approximate these BNi-2 values. Furthermore, the region near the solid/liquid interface, where the compositional gradient is the greatest, also corresponds to the non-isothermal portion of the TLPB process over which the filler metal initially melts. It makes sense that the composition of the growing ISZ layer in this region would be variable, since full equilibrium and isothermal solidification conditions have not yet been reached. Conversely, once isothermal conditions are reached, the results of Figure 4-8 indicate that the composition of the growing ISZ layer become constant. With the assumption of minimal dissolution when the braze temperature is at the filler metal liquidus, it makes sense that this isothermally grown ISZ would have a composition close the B-free composition of the BNi-2 alloy.

Figure 4-9 plots compare the compositional profiles within the ISZ for a 2xIN625/1xBNi-2 full joint immediately after complete IS (i.e. 1 hour) and with some additional homogenization time (i.e. 1.6 hours). The Fe, Si and Nb content within the ISZ is relatively unchanged due to homogenization. Conversely, the Cr and Mo content increase, particularly near the BM interface, indicating back diffusion of these elements from the BM into the ISZ during solid-state homogenization.

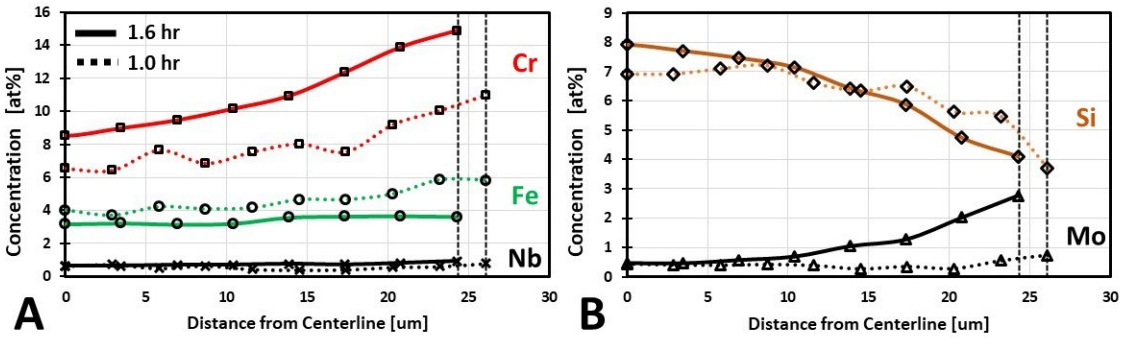

Figure 4-9 - Compositional profiles of 2x/1x couples subject to a total of 1.0 and 1.6 hours above solidus. (A) Cr, Fe, Nb concentrations, (B) Si and Mo concentrations. Vertical dashed lines represent ISZ/DAZ interface.

Figure 4-10 compares the compositional profiles for the 2xIN625/2xBNi-2 full joint and the equivalent 1xIN625/1xBNi-2 half joint. These results further confirm that the half joint simulation of the full joint condition is valid.

Further evaluation of the progress of IS as a function of both time and gap width was performed by comparing the severity of the DAZ as shown in Figure 4-11. As the gap width increases, the time needed for complete IS increases and this results in a thicker DAZ region. At the leading edge of the DAZ, the borides form along the grain boundaries. Over time the grains covered by the borides begin to form discrete boride particles followed by continuous needle shape borides. This progression of boride distribution from 1 to 3.6 hours indicate that boron diffuses first by grain boundary diffusion, followed by diffusion within the grains.

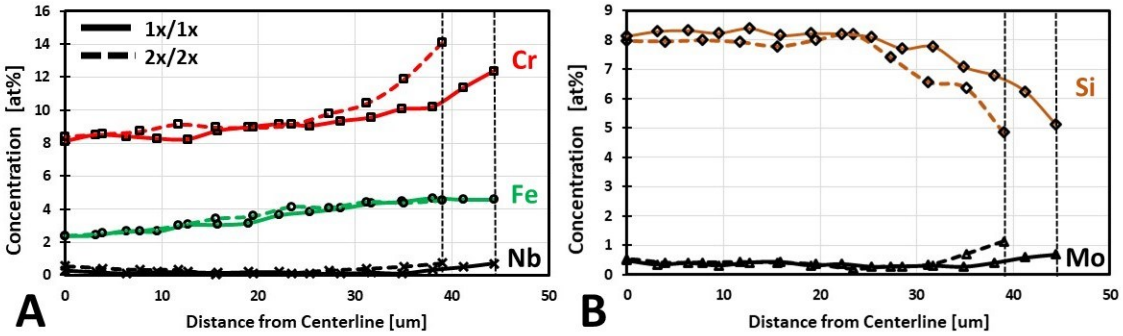

Figure 4-10 - Compositional profiles of 2x/2x (full-joint) and equivalent 1x/1x (half-joint) couples. (A) Cr, Fe, Nb concentrations, (B) Si and Mo concentrations. Vertical dashed lines represent ISZ/DAZ interface.

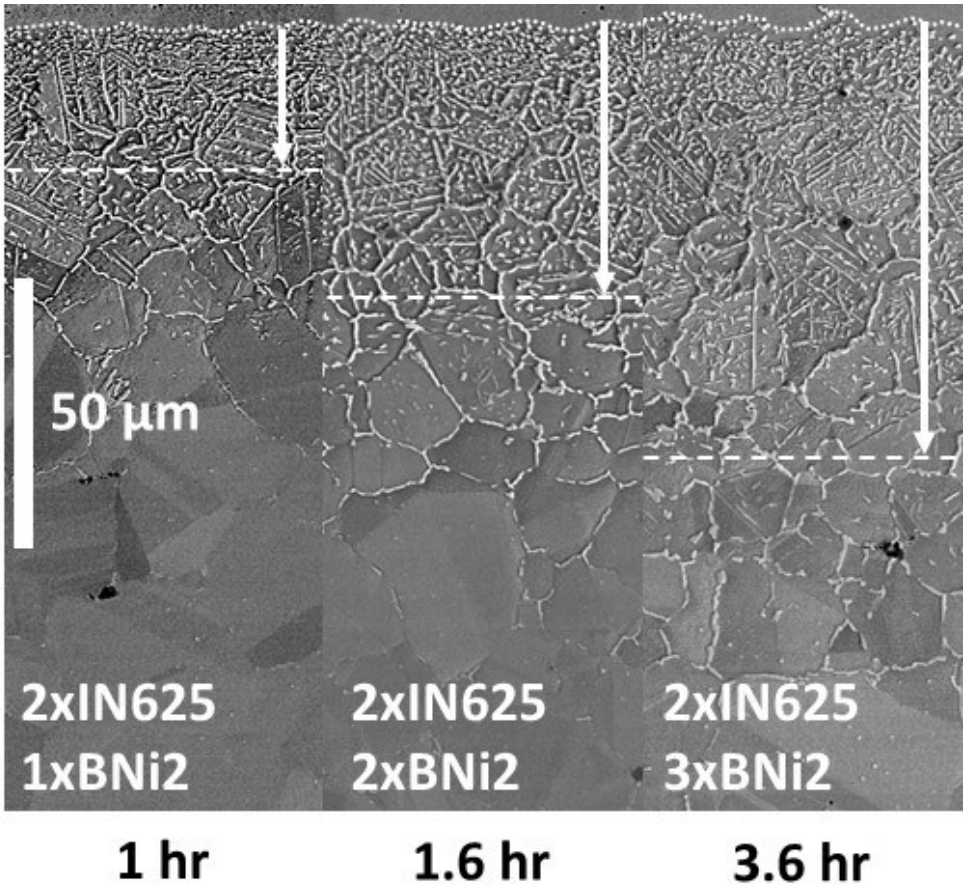

Figure 4-11 - DAZ of full-joints upon achieving complete isothermal solidification. The purpose of the white arrows will be discussed in section 4. T_{MAX} = 1050°C.

Conceptual Model for IBU and IS in Terms of Boride Formation

An explanation for the development of the IBU can be given with reference to the conceptual model of Figure 4-12. Prior to reaching the solidus temperature, the interface consists of the FM with a boron concentration, C_o and a base metal with a boron concentration of C_m. Once the solidus is exceeded some liquid forms, greatly accelerating mass transport. This allows the establishment of the required phase equilibria at the process temperature between the BM and FM. In the next thesis chapter, analysis of a simpler Ni-Si-B ternary braze system will shown that diffusion path theory determines the phase equilibria and structure at this interface. In Ni-B based systems this structure consists of an ISZ layer with a very low boron concentration C'_m and a DAZ containing a high boron concentration in the form of precipitated borides. With reference to Figure 4-13, the formation of this interface involves a transformation of a small volume element, $A_o\Delta w_{DAZ}$ from BM to DAZ. Similarly, it requires the transformation of a small volume element $A_o\Delta w_{FM}$ (or

$A_o \Delta w_{ISZ}$) from FM to ISZ. If it is assumed that the concentration of boron in the BM and ISZ is negligible (i.e. $C_m = C'_m = 0$), then the amount of boron that was contained in the small volume of FM must be redistributed to the DAZ layer. The quantity of Boron contained within the FM is known and can be expressed as;

$$m_{BFM} = V_{FM} C_o \qquad \text{Eq. 4-10}$$

where m_{BFM} is the mass of FM, C_o is the volume concentration of boron in the filler in g/cm^3 and V_{FM} is the volume of filler in the joint that has undergone isothermal solidification.

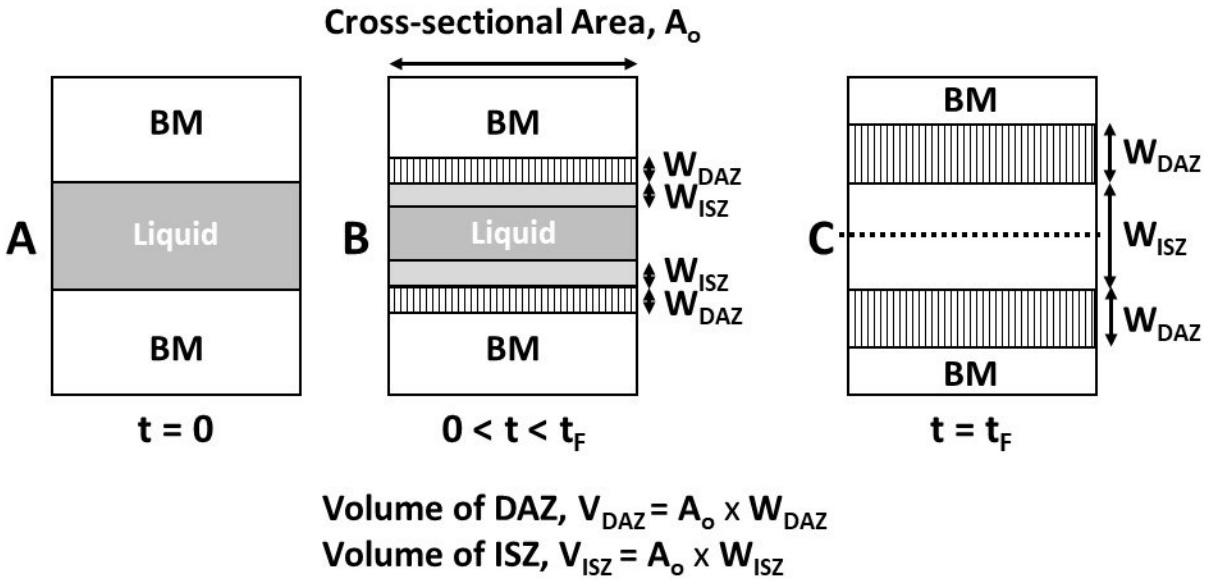

Figure 4-12 - Schematic representing redistribution of Boron from the liquid phase to borides in DAZ during TLPB, (A) time zero (t = 0), (B) intermediate time between zero and final ($0 < t < t_f$), (C) at complete isothermal solidification time ($t = t_f$).

The boron content within the DAZ is based on the volume fraction of borides and their concentration within the BM matrix. Solubility values for B in γ-Ni at 1050°C of 0.05 wt% B and 0.073 wt% were obtained using Thermocalc Thermodynamic modeling software for IN625 and Ni-7Cr-3Fe-4.5Si (i.e. the ISZ), respectively. Since these values are very low, the boron content in the IN625 matrix within the DAZ and ISZ were neglected, as mentioned above. The mass of boron in the DAZ, m_{BDAZ} can then be expressed as;

$$m_{BDAZ} = V_{DAZ} X_{DAZ} f_i \rho_i \quad \text{Eq. 4-11}$$

where X_{DAZ} is the volume fraction of borides present within the DAZ layer, V_{DAZ} is the volume of the DAZ layer, f_i the percentage (by weight) of the principal boride intermetallic based on its stoichiometry (at%) and ρ_i the specific gravity $\{g/cm^3\}$ of the precipitate (boride) phase, i. Under the assumption that the mass of boron removed from the FM as it undergoes IS is redistributed to the growing DAZ (i.e. $m_{BFM} = m_{BDAZ}$), Eq. 4-10 and Eq.4-11 combined becomes:

$$V_{DAZ} X_{DAZ} f_i \rho_i = V_{FM} C_o \quad \text{Eq. 4-12}$$

From Figure 1-12, $V_{DAZ} = A_o \Delta w_{DAZ}$ and $V_{FM} = V_{ISZ} = A_o \Delta w_{ISZ}$, thereby reducing Eq. 4-12 to:

$$\Delta w_{DAZ} X_{DAZ} f_i \rho_i = \Delta w_{ISZ} C_o \quad \text{Eq. 4-13}$$

The value of Δw_{ISZ} in Eq. 4-13 is the amount of FM that has undergone isothermal solidification, which can be determined as a function of braze time from the DSC analysis, using Eq. 4-9. A final rearrangement of Eq. 4-13 yields:

$$\Delta w_{DAZ} = \frac{\Delta w_{ISZ} C_o}{X_{DAZ} f_i \rho_i} \quad \text{Eq. 4-14}$$

The fraction of borides within the DAZ, X_{DAZ} was determined experimentally using image analysis applied to the polish cross sections of Figure 4-4A and Figure 4-11, as detailed in Appendix B. A magnification of 600x was used and the width of the image analyzed was 210 μm. In order to get enough depth resolution, the thickness of the individual elements analyzed for the short hold sample of Figure 4-4A was 2 μm , while an element thickness of 3.3 μm was used for the samples of Figure 4-11Figure 4-12. The data for these four samples is plotted as a function of depth within the DAZ layer in Figure 4-13. It was assumed that the distribution of borides within the DAZ was isotropic such that the volume fraction was equivalent to the measured area fraction. Due to the slightly uneven ISZ/DAZ interface, reliable area fractions within the first 2 μm of depth

were not possible. For positions of zero and 2 μm depth, it was assumed that the area fraction of borides was the same as that measured at a depth of 3.3 or 4 μm.

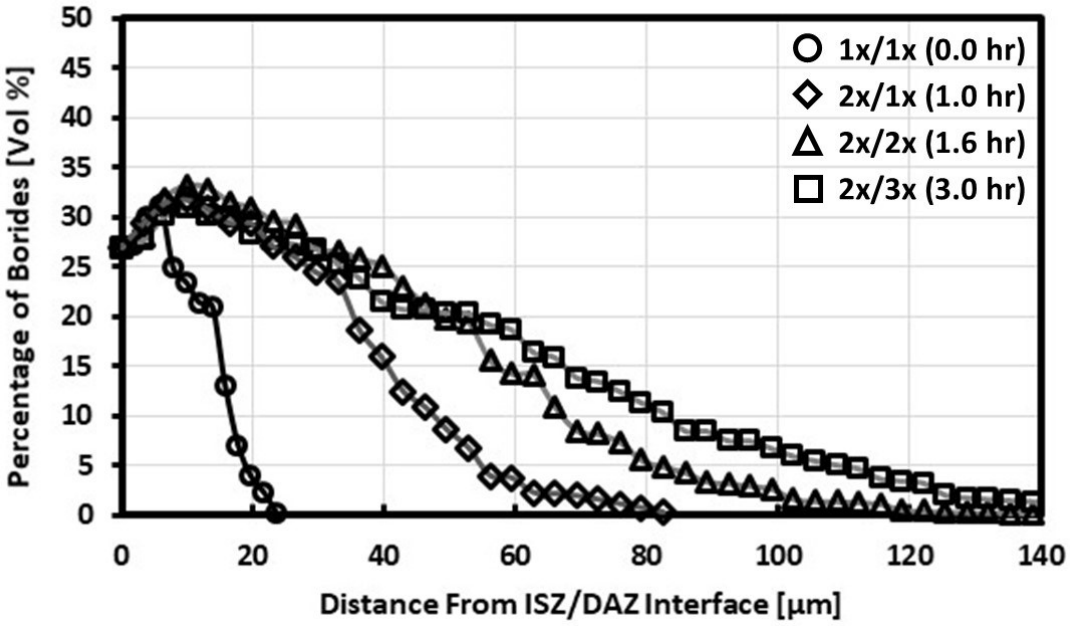

Figure 4-13 - Experimentally determined volume % of borides as a function of depth into the DAZ for half- and full- IN625/BNi-2 Joints. T_{MAX} = 1050°C.

Figure 4-13 suggests that the area fraction is highest near the ISZ/DAZ interface, varying in the range of 27 to 33 vol%. This maximum value is consistent for all braze joints regardless of the braze time or the gap width used. It highlights that there is a dense band of precipitates (DBP) that forms adjacent to the ISZ/DAZ interface. In this DBP, borides have formed along the grain boundary and within the grain interior. The microstructure transitions to borides covering the grain boundary with only isolated borides in the grain, corresponding to a drop in the boride volume below 20 vol%. Eventually, borides are only present at grain boundaries and their volume percent drops below 5%.

Figure 4-13 and Figure 4-4A suggest that the DAZ consists primarily of a DBP layer during the initial stages of brazing, which closely corresponds to the observed IBU formation. In the full joints cycled to complete IS, this region grows to a thickness of approximately 40-45 μm. The primary influence of gap size and longer braze times, is in the growth of the DAZ regions

containing boride volume fractions below 20 %. Using data from all four samples depicted in Figure 4-13, the average area percent of borides within the DBP region was determined to be 28%.

The values of f_i and ρ_i in Eq. 4-11 through Eq. 4-13 depend on the type of boride forming within the DAZ. A detailed characterization study performed by Zhang et al. [93] indicated that M_3B_2 and M_5B_3 were the dominant boride phases formed in a Ni-based superalloy MAR-M247, which contained W. These boride stoichiometries also appeared to be prevalent in other works where the base metals contained W, as summarized in a review published by Pouranvari et al. [92]. Recent work by Bai et al [94] used a novel XRD methodology which identified the predominant formation of MB type borides, while MB_2, M_5B_3 and M_3B_2 were also detected, in the W-free IN718 alloy. They also performed thermodynamic modelling using Thermocalc which confirmed the prevalence of MB borides in the DAZ of IN718. Since the alloy IN625 of this study is also W-free and has the same boride former elements as IN718 (i.e. Cr, Mo, Nb) it is expected that the predominant borides present in the DAZ should also be similar to IN718. EDS analysis was used to confirm this expectation.

The Oxford X-max (80 mm^2) EDS system used in the current study is equipped with a windowless EDS detector which allows the detection of boron. Using the low voltage condition of 5 kV outlined in [82] for quantitative boron measurements in superalloys, accurate boron concentrations in the DAZ borides were obtained. BSE imaging identified light contrast borides with an at% composition of 64 B, 16 Cr, 14.6 Mo, 2.3 Nb, 2.7Ni and 0.4 Fe and dark contrast borides with an at% composition of 59 B, 36 Cr, 2.7 Mo, 0.1 Nb, 2.0 Ni and 0.2 Fe. The light contrasting borides represented approximately 95% of the total borides. On the basis of these measurements it is concluded the boride types in the alloy are of the MB and MB_2 stoichiometry

With the type of boride selected, a value of $f_i = 0.211$ was used for the boron weight fraction in the borides. The densities reported for the most commonly encountered binary Cr-rich borides do not consider the presence of other common boride formers such as Mo, Nb, W, etc. which are commonly detected in boride precipitates [93-96]. Their influence is likely a minor increase in the overall density of a particular boride, given their greater molecular mass and mutual solubility e.g. M = Cr, Mo, W, etc. Considering the prominent MB stoichiometry expected in the current alloy within the DAZ, a value for ρ_i of 6.202 g/cm^3 was selected.

The thickness of the isothermally solidified layer formed during initial heating was determined from the DSC data to be $2w_{ISZi}$ ~ 33 μm. The volume concentration of boron in the BNi-2 filler, C_o = 0.247 g/cm^3. It is assumed that the DAZ at the IBU stage can be represented by the arithmetic mean of the X_{DAZ} data in Figure 4-13 (i.e. 0.178) and f_i and ρ_{in} are equal to the values stated above. Given such conditions, Eq. 4-14 predicts a DAZ thickness $2w_{DAZ}$ of 35.0 μm or w_{DAZ} (on a half joint basis) of 17.5 μm. The white arrow in Figure 4-4A, represents this prediction, which agrees well with the actual depth of the DAZ observed.

The mass balance equation (4-13) is also applicable to the complete IS cycles depicted in Figure 4-11. These full cycle samples are comprised of the DBP and the lower volume fraction boride precipitate region. In these cases, an average boride fraction was determined as 16.5, 15.3, and 14.0 for the 2x/1x, 2x/2x and 2x/3x joints respectively. The values of $2w_{ISZ}$ upon complete IS would be equal to the $2w_o$ values given in Table 4-1. Using the same values of C_o, f_i and ρ_i as above, Eq. 4-13 predicts the average half joint width of the DAZ, w_{DAZ} to be 22.8, 47.2 and 62.5 μm for the three increasing joint gaps. As indicated by the white arrows in Figure 4-11, these predictions are smaller than the full depth of the experimental DAZ width. This is due to the use of the average X_{DAZ} values used in Eq. 4-14. Therefore, the predictions represent the DAZ depth expected if the boride fractions were uniformly distributed at the average X_{DAZ} values of 16.5, 15.3, and 14.0.

4.3 Conclusions

The principal findings acquired in the present study have been summarized below:

1. Validated the use of IN625/BNi2 half-joint DSC configuration for quantitatively simulating TLPB behavior of IN625/2xBNi2/IN625 full-joint couples, which showed a strong agreement with prior literature reports using metallographic based analysis.
2. Successful extension of the analysis to determine the MBC curve for a given BM/FM and braze temperature from a single cyclic DSC experiment.
3. Solidification exhibited solid state-diffusion process governed by the diffusion of B from the liquid to the BM, forming Cr-rich (Mo, Nb) borides in the DAZ. Thus, the rate of IS was independent of the thickness of the gap, whereas the total solidification time depended

on the total quantity of Boron present. Consequently, the width of the DAZ is also proportional to the total Boron content and starting gap width.

4. Significant diffusional solidification occurs during initial heating/melting (IBU) such that approx. 20 μm of epitaxial growth of the ISZ develops prior to attaining the max. temperature (1050°C) as confirmed by both DSC and microstructural observations.
5. The conceptual model explored herein showed that the TLPB behavior of Ni-based superalloys using Boron-containing filler metals is not only dependent on the distribution of the borides, but also the type i.e. M_xB. The type of boride is largely determined by the base metal composition indicating that certain BM's may be more amenable to TLPB based on their boride forming characteristics.

CHAPTER 5 Application of Diffusion Path Analysis to Understand the Mechanisms of TLPB in the Ni-Si-B System

E.D. Moreau, S. F. Corbin

Department of Mechanical Engineering, Dalhousie University,
1360 Barrington Street, P.O. Box 15,000, Halifax, Nova Scotia, B3H 4R2, Canada

Status: Published in Journal of Metallurgical and Materials Transactions A (2019)

Authors Contribution: All experimentation performed by E. D. Moreau with direct guidance by S. F. Corbin.

Abstract

Diffusion path analysis was applied to the Ni-Si-B system to explain the deviation from classical transient phase bonding observed when using multicomponent systems containing Boron as a melting point depressant. This was achieved using a combination of differential scanning calorimetry, SEM-EDS microstructural and chemical analysis and Thermo-Calc modeling software of Ni/Ni-Si-B couples. Compositional analysis identified differing distributions of B and Si across the braze joint which were mapped onto isothermal sections of Thermo-calc generated phase diagrams. Below 1093°C, the inevitable formation of diffusionally affected zone (DAZ) and isothermally solidified zone (ISZ) is a direct consequence of the need for phase equilibria in the Ni-Si-B ternary system and is predicted by diffusion path analysis. Above 1100°C, diffusion path analysis also correctly predicts a persistent liquid phase observed to occur through the melting of the DAZ (i.e. a γ-Ni(Si)-Ni_3B eutectic reaction).

5.1 Introduction

The strict performance requirements of aerospace applications typically warrant the use of advanced joining techniques such as vacuum diffusion brazing, as it offers several advantages over other brazing and welding methods. Joining is accomplished through the melting of a low-melting point filler metal (FM) alloy and subsequent diffusionally induced solidification; hence the name *Transient Liquid Phase Bonding* (TLPB) [8,7]. Most often TLPB of superalloys is achieved using nickel-based brazing alloys containing either Boron, Phosphorous and/or Silicon in addition to other alloying additions. These alloys generally exhibit an excellent combination of wetting, spreading, low fusion temperatures, and relatively low joining times, similar to the prohibitively expensive Ni-Au (or Pd) alloys [15]. Despite their extensive service, considerable uncertainty remains with regards to the exact mechanism by which TLPB and isothermal solidification occurs in boron containing systems, since they deviate from classic TLPB theory [42-43,49,97]. In classic TLPB as described by Eager, Tuah-Poku, and others [6-9, 30, 36, 98] the filler metal is an ideal eutectic with melting point depressant (MPD) elements displaying appreciable solid solubility in the base metal (Figure 5-1A). During brazing the MPD solute atoms diffuse from the liquid to the solid solution (SS) matrix and subsequently redistribute and homogenize in the base metal (BM). The high soluble MPD allows for isothermal solidification and maintains a single-phase microstructure in the BM. The solute composition is assumed constant in the liquid phase, but has a decreasing concentration with increasing distance from the solid/liquid interface within the BM.

Conversely, the immiscibility of B in Ni (0.015 wt% max.) and its rapid interstitial diffusion in Ni [30,33,85] results in the heterogeneous distribution of embrittling borides in the vicinity of the joint (Figure 5-1B). The region of boride precipitates in the BM is known as the diffusionally affected zone (DAZ) and has been widely reported for Ni-base superalloys, in which segregation and progressive coarsening of metal borides adjacent to the original solid/liquid interface occurs – the exact type and composition governed by the materials involved [40, 66, 92, 100-102]. A (γ-Ni) solid solution single phase layer forms on the opposite side of the original solid/liquid interface and is known as the isothermally solidified zone (ISZ). During brazing, the DAZ and ISZ layers grow in thickness while the liquid layer deceases and eventually removed through diffusional solidification. The

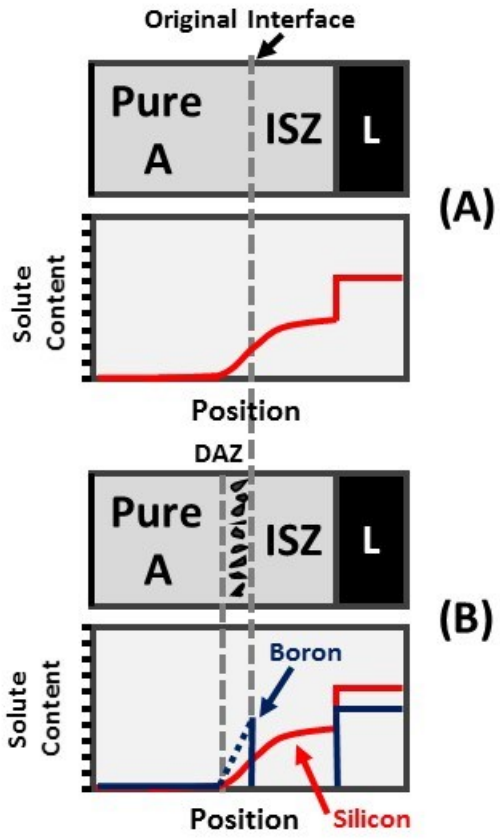

Figure 5-1 - Schematic illustrating the distribution of solute along a joint during; classic binary TLPB (A, Top) and TLPB involving multicomponent, Boron filler metals (FMs) (B, Bottom).

compositional profile of elements in the braze that are soluble in the (γ-Ni) have a similar distribution as for the classic case of Figure 1A. However, the B profile is markedly different, going to near zero in the ISZ layer, and discretely increasing to its concentration in the filler metal liquid. In the DAZ the boron is contained within the boride compounds (e.g. Ni_3B). The volume fraction of boride within the two phase DAZ layer decreases further into the BM. Therefore, the bulk composition of B is decreasing with distance away from the DAZ/ISZ layer, eventually reducing to zero further into the BM (bottom schematic of Figure 1B).

Considerable efforts have been made to adapt conventional TLPB theory and models to Ni-based superalloys with Boron-based FMs [42-43, 49, 66, 97, 101-102]. In most instances however, the adoption of Boron FMs results in either the in-situ formation of intermetallics precipitates or a significant reduction in the rate of isothermal solidification [42-43, 49, 97]. The former believed to be an artifact of the rapid diffusivity of B in Ni as compared to other solute elements; the latter related to the melting of intermetallic precipitates thereby increasing the

quantity of liquid. Nonetheless, the typical approach is to assume that the interface structure and compositional profile can be approximated by the arrangement depicted in Figure 1A, and considering B as the diffusing species that controls IS. Little effort has been spent to understand the more complex interface microstructure of Figure 1B that actually occurs in the joints. In this study it is proposed that this interface microstructure can be analyzed and understood on the basis of diffusion path theory as it applies to multicomponent systems [104-106]. The diffusion path approach requires a comparison between the experimentally determine interface structure and composition profile with the relevant multicomponent phase diagram. To facilitate this comparison, a ternary alloy system containing Ni was considered. The Ni-Si-B ternary composition was chosen since Si and B are the most common MPD additions in superalloy filler materials. The experimental TLPB behavior of a pure Ni BM/Ni-Si-B filler braze couple was determined using differential scanning calorimetry (DSC), metallography and Scanning Electron Microscopy and Energy Dispersive Spectrometry (SEM-EDS). The results were compared to various ternary phase diagram predictions developed using Thermo-Calc Software.

5.2 Results and Discussions

5.2.1 Thermal and Microstructural Characterization of BNi-3

Figure 5-2 illustrates the representative DSC results obtained after repeated cycling of a BNi-3 foil between 870 and 1100°C, wherein melting/solidification involves three thermal events; a sharp melting event between 994 and 1010°C, a second broader melting (994-1050°C) event believed to initiate concomitantly with the first event, and lastly a small melting event between 1050 and 1065°C (liquidus). The shape of the overall melting peak is characteristic of off-eutectic (hypo) melting behavior [69].

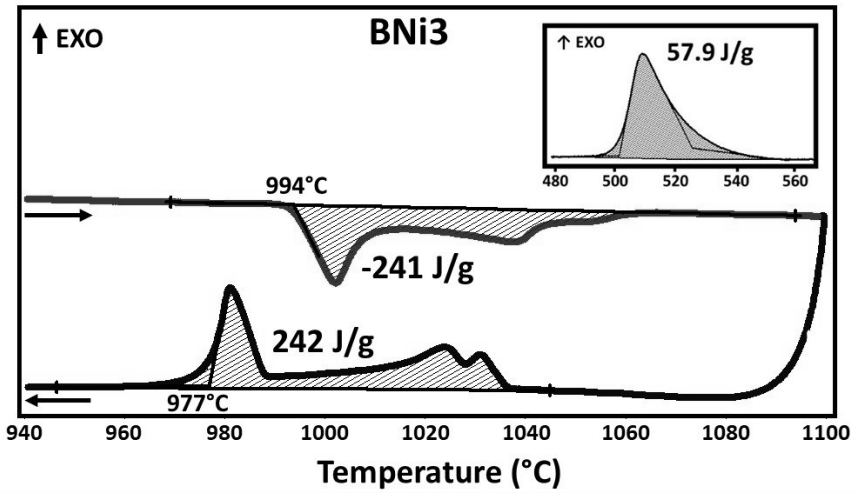

Figure 5-2 - DSC heating/cooling traces of BNi-3 specimens. Inset: Low temperature crystallization event of amorphous BNi-3 foils.

From Figure 5-2, the cooling trace also indicates three solidification peaks. The high temperature peaks onset below the liquidus of 1065°C due to the influence of undercooling. However, these peaks are broad and shallow, much like the 2nd and 3rd melting peak. A more intense peak with a sharp onset (much like the 1st melting peak), completes solidification. This comparison of the melting and solidification traces indicates that the same events occur during heating and then in reverse sequence during cooling. The individual peaks correspond to the individual melting/solidification events of primary and binary and ternary eutectics events as confirmed by thermodynamic modeling latter.

Figure 5-3 presents the microstructure of the BNi-3 sample after solidification from 1100°C. Numerous SEM-EDS spot scans were performed on the various microstructural constituents visible in the solidified BNi-3 using the targeted voltage and current conditions outlined in Chapter 3 (Experimental Methods). Two distinct phases, γ-Ni(Si) and Ni_3B and an additional Si-rich region (TE) likely corresponding to the last of the liquid phase to solidify are labelled in Figure 5-3. SEM-EDS analysis performed on the Ni_3B, γ-Ni(Si), and TE phases yielded concentrations of 26.9 ± 1.6 at% B, 9.5 ± 1.6 at% Si, 15.8 at% Si, respectively. The sub-stoichiometric Si content measured for what was believed to be the β phase (β-Ni_3Si) may be an artifact of the operating conditions i.e. the inability to measure low conc. of boron of Ni-Si-B phase. However in the context of the current work it is likely attributed to limitations of EDS to measure the very fine β-Ni_3Si precipitates alone, thereby yielding results intermediate between

that of β-Ni_3Si (25 at%) and γ-Ni(Si) (8 at% Si max.) [71,81,107]. As expected, the composition of the Ni_3B borides are nearly stoichiometric (25 at% B) and represent the only Boron-bearing phases, while the saturated γ-Ni(Si) is approx. that of the solubility limit at the given temperature [30, 33-34, 98, 87].

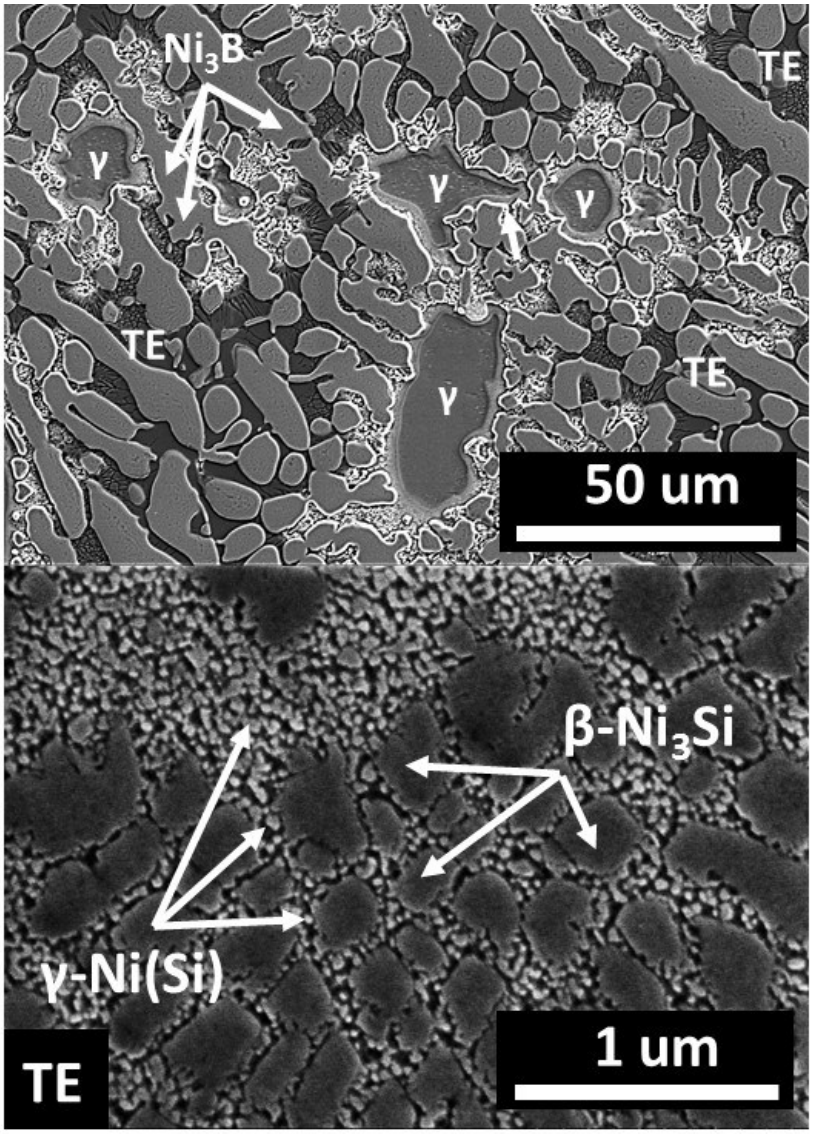

Figure 5-3 - SEM micrographs of BNi-3 foil heated to 1100°C then rapidly furnace cooled. Low magnification (Top) and high magnification revealing ternary eutectic (TE) comprised of large borides (top) and Si-rich TE consisting of supersaturated γ-Ni(Si) and β-Ni

To assist in understanding the sequence of solidification events observed on the DSC cooling trace and the resultant solidified structure of BNi-3, a Ni-rich isopleth with a constant Si:B ratio of 1:1.4 (wt%) was generated using Thermo-Calc software (Figure 5-4). The composition and

solidification sequence of BNi-3 is traced as a vertical line on the figure. The equilibrium sequence starts with solidification of; (1) primary γ-Ni(Si), (2) Ni_3B +γ-Ni(Si) binary eutectic (BE), and (3) Ni_3B+γ-Ni(Si)+β-Ni_3Si ternary eutectic (TE). Non-equilibrium freezing would produce the same sequence but modifying the relative quantities of phase(s). It should also be noted that the widespread precipitation of the γ'-Ni_3Si; the semi-coherent intermediate of β_x-Ni_3Si infers a significant degree of supersaturation of Ni with Si, preserved by the rapid solidification rate, as clearly evident in Figure 5-3.

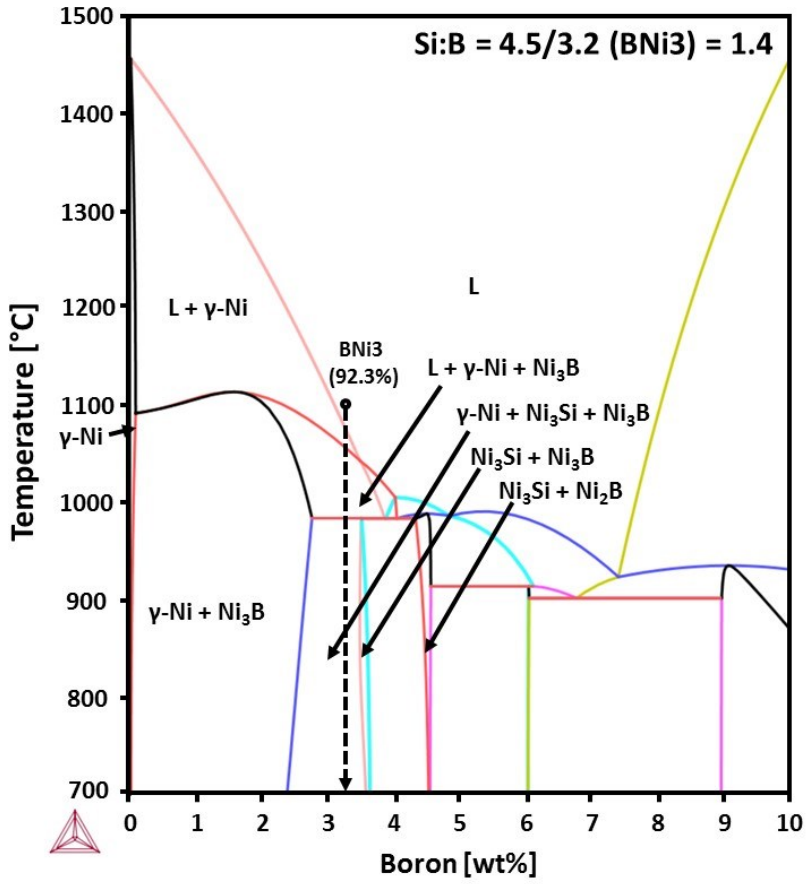

Figure 5-4 - Calculated Ni-B-Si isopleth with fixed Si:B ratio of 1.4 (Si = 4.5, B = 3.2, BNi-3) and nominal concentration of BNi-3 plotted at 1100°C.

5.2.2 Influence of Temperature on the TLPB Behavior of Ni/Ni-Si-B Couples

Following the thorough characterization of the BNi-3 FM, focus shifted towards assessing the TLPB response of Ni/Ni-Si-B (Ni/BNi-3) couples as a function of peak brazing temperature. Recommended brazing temperatures for BNi-3 range from 1010-1175°C [4], thus peak cyclic temperatures of 1020, 1050, 1075 and 1100°C were examined. Figure 5-5 illustrates the DSC heating (A) and cooling traces (B) associated with the first two heating/cooling cycles as well as that obtained after the final 19th cycle. It should be noted that the "hook" like shape of the DSC curve immediately upon cooling, is an experimental artifact caused by the transient nature of the cooling rate immediately upon cooling. Once the cooling rate becomes constant at the prescribed rate of 20 k/min, the baseline becomes stable. This hook persists throughout the additional cycling further confirming that it is a condition of the transient cooling rate and not an actual solidification event.

The 1020°C cyclic trace indicates that only the ternary eutectic portion of the BNi-3 foil melts and solidifies. This melting/solidification event persists throughout most of the cycles, but the peak decreases in magnitude, indicating a reduced amount of liquid and an isothermal solidification (IS) process. Despite only partial melting of the BNi-3 foil, wetting, bonding and joint formation with the Ni200 BM occurs at 1020°C (see Figure 5-6). Even with the short brazing time (Figure 5-6A), some diffusion of B into the Ni200 BM has occurred at 1020°C as evidenced by the Ni_3B precipitation in the solid BM forming the diffusionally affected zone (DAZ). The joint region of Figure 5-6A (which represents a brazing time of less than 3 mins) exhibits a matrix of re-solidified TE with dispersed, coarse Ni_3B particles throughout. Since complete melting of the binary eutectic (which involves Ni_3B) requires a temperature of approx. 1045°C (Figure 5-2), the coarse residual Nickel Borides remain as a solid fraction at 1020°C. It should be noted that the microstructure of the filler metal in Figure 5-6A is similar to that observed in the foil only, when furnace quenched from 1020°C.

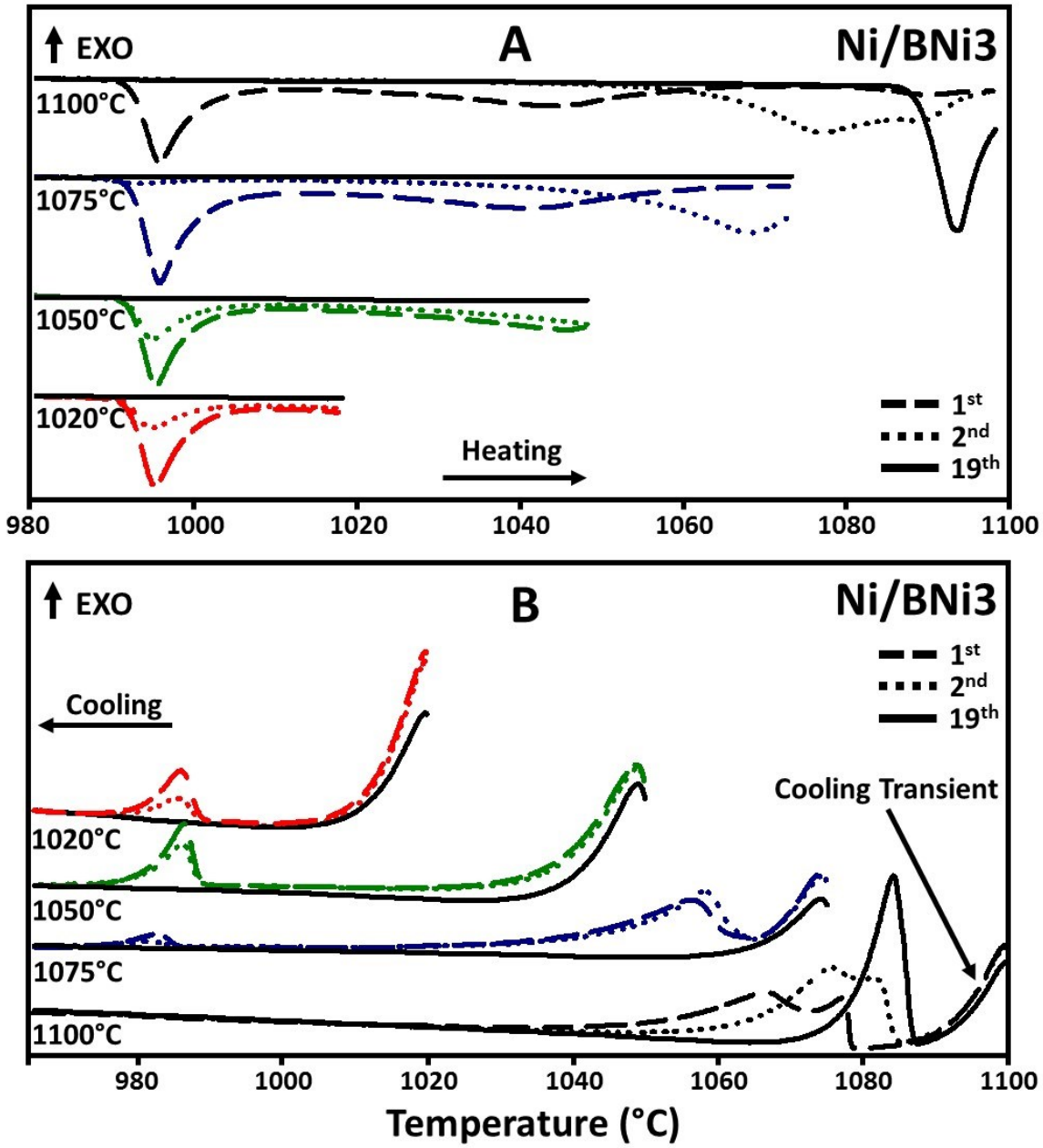

Figure 5-5 - DSC traces for the melting (Top) and cooling (Bottom) of Ni/BNi-3 couples subject to peak brazing temperatures of 1020, 1050, 1075 and 1100°C. 20x Cyclic DSC.

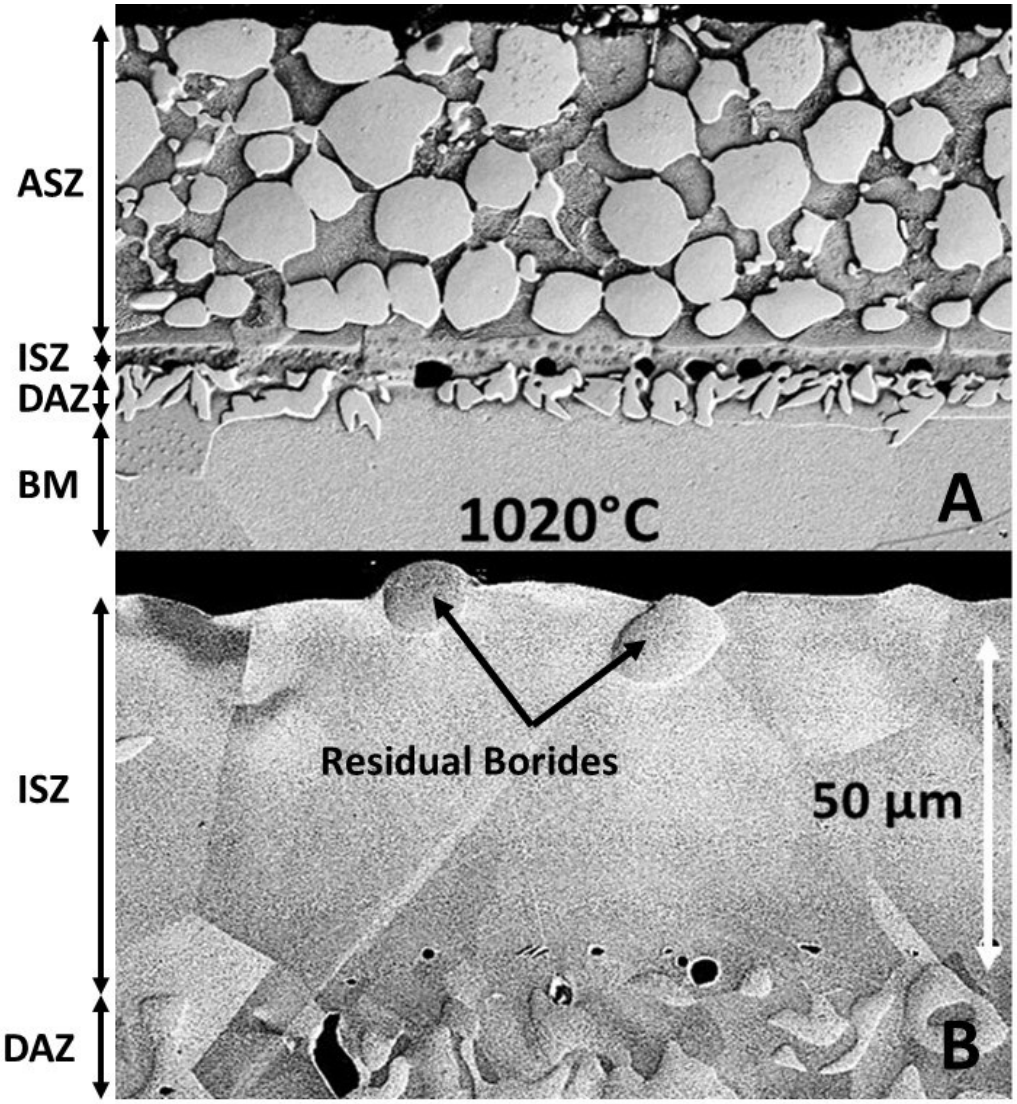

Figure 5-6 - SEM Micrographs of quenched (A) and 20x cycled (B) Ni/BNi-3 couples heated to 1020°C for a total liquid duration of approx. 5 mins and 163 min, respectively.

Despite only partial melting of the filler at 1020°C, the last heating/cooling cycle (cycle 19 in Figure 5-5) exhibits no melting or solidification event, indicating complete isothermal solidification of the TE liquid phase. Figure 5-6B confirms this observation microstructurally, where the filler region consists of a γ-Ni(Si) ISZ region with residual, unmelted Ni_3B dispersoids. The DAZ layer has grown in thickness through continued B diffusion and precipitation into the pure Ni BM.

For the sample brazed at 1050°C, the DSC trace also exhibits repeatable melting/solidification peaks in the vicinity of the TE with the addition of a broad BE melting peak up to 1050°C (Figure 5-5). The magnitude of the peaks decreased with brazing time, also indicating a reduced liquid fractions and IS process. The microstructure of Figure 5-7A indicates that near-complete melting of the BNi-3 occurred, when compared to the morphology observed in Figure 4 (i.e. well developed BE and TE structures are evident). Otherwise, the 1050°C sample exhibited similarities with the 1020°C sample in that complete IS occurred within 19 cycles, a DAZ was formed with the BM and some unmelted dispersed Ni_3B was present (Figure 5-7B).

The sample cycled at 1075°C (slightly above the liquidus of BNi-3) exhibited a distinctly different DSC trace following the first melting event (see Figure 5-5). The melting and solidification behaviour shift to a higher temperature range and there is no longer a distinct thermal event near the temperature associated with the TE. This is more evident when plotting all full melting/solidification cycles of this sample shown in Figure 5-8 wherein the peak associated with TE melting/solidification disappears after 2 cycles. This demonstrates that the high-temperature melting/solidification event persists but diminishes in magnitude until complete IS occurs by the 19^{th} cycle. With complete melting of the BNi-3 foil at 1075°C, the complete IS joint was free of residual Ni_3B dispersoids as indicated in Figure 5-9B.

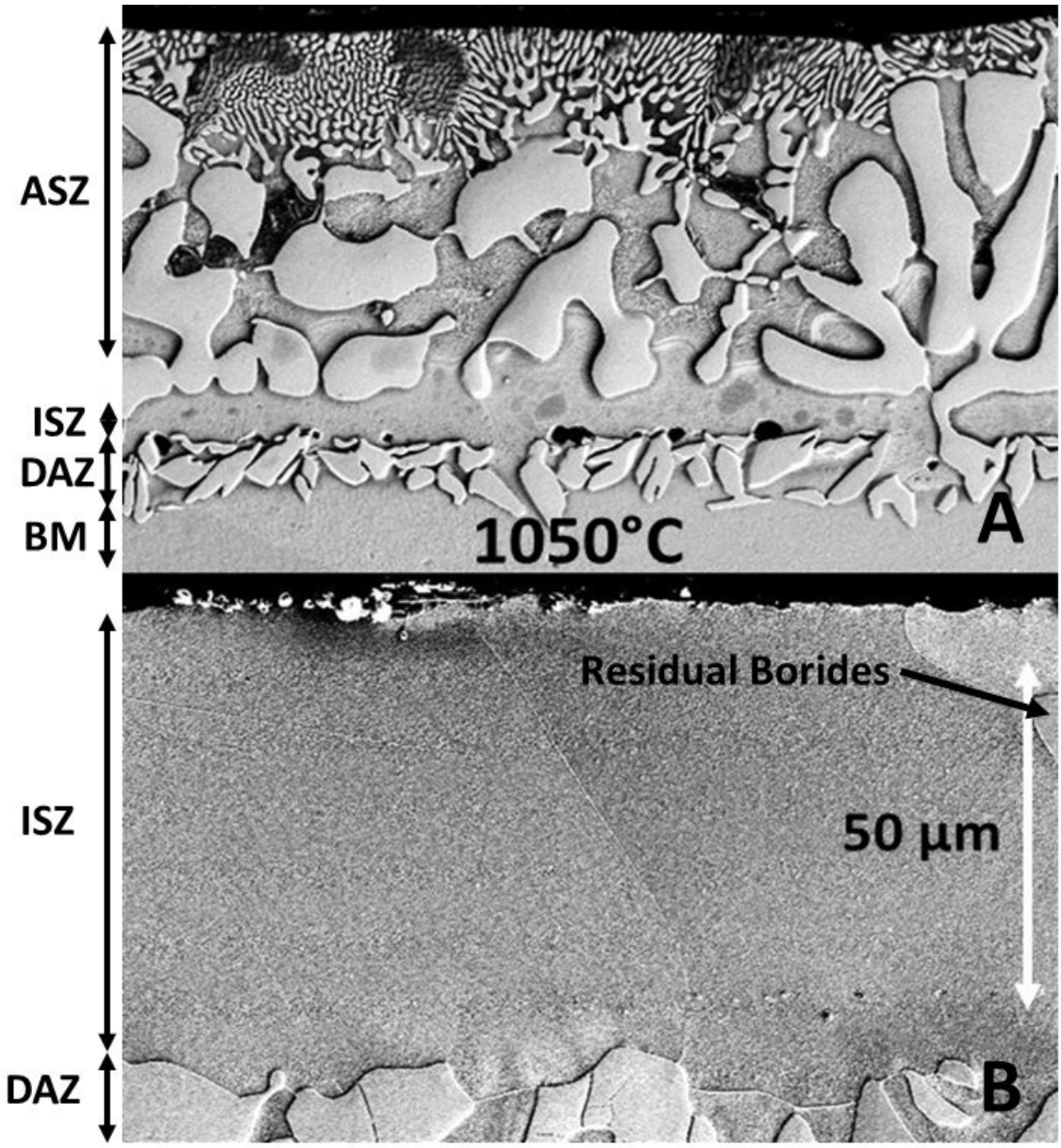

Figure 5-7 - SEM Micrographs of quenched (A) and 20x cycled (B) Ni/BNi-3 couples heated to 1050°C for a total liquid duration of approx. 6 mins and 144 min, respectively.

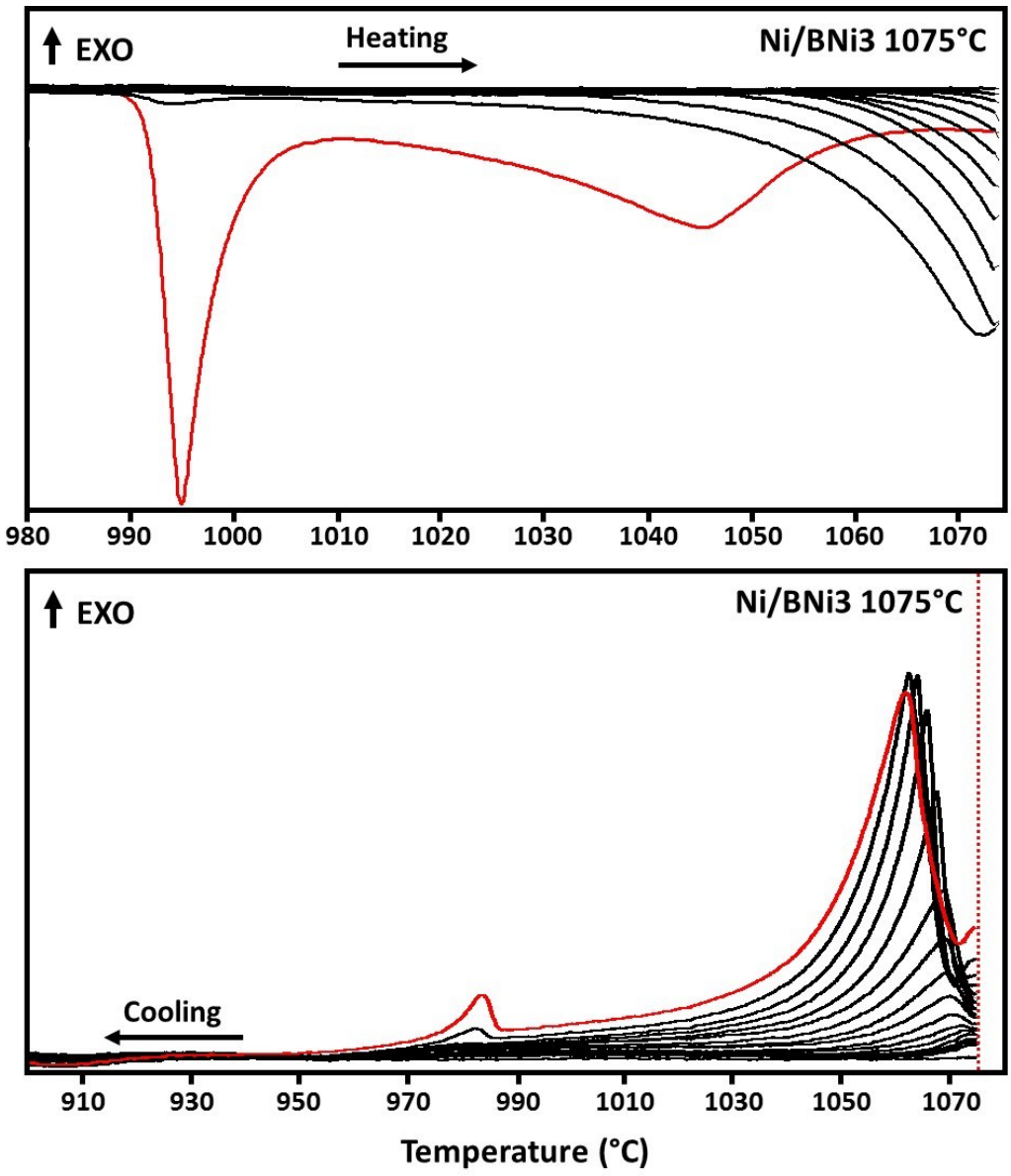

Figure 5-8 - Complete Heating (top) and Cooling (bottom) DSC traces for Ni/BNi-3 couple subject to approx. 6 hrs of cyclic heating at a peak temperature of 1075°C. Total liquid duration: approx. 131 min.

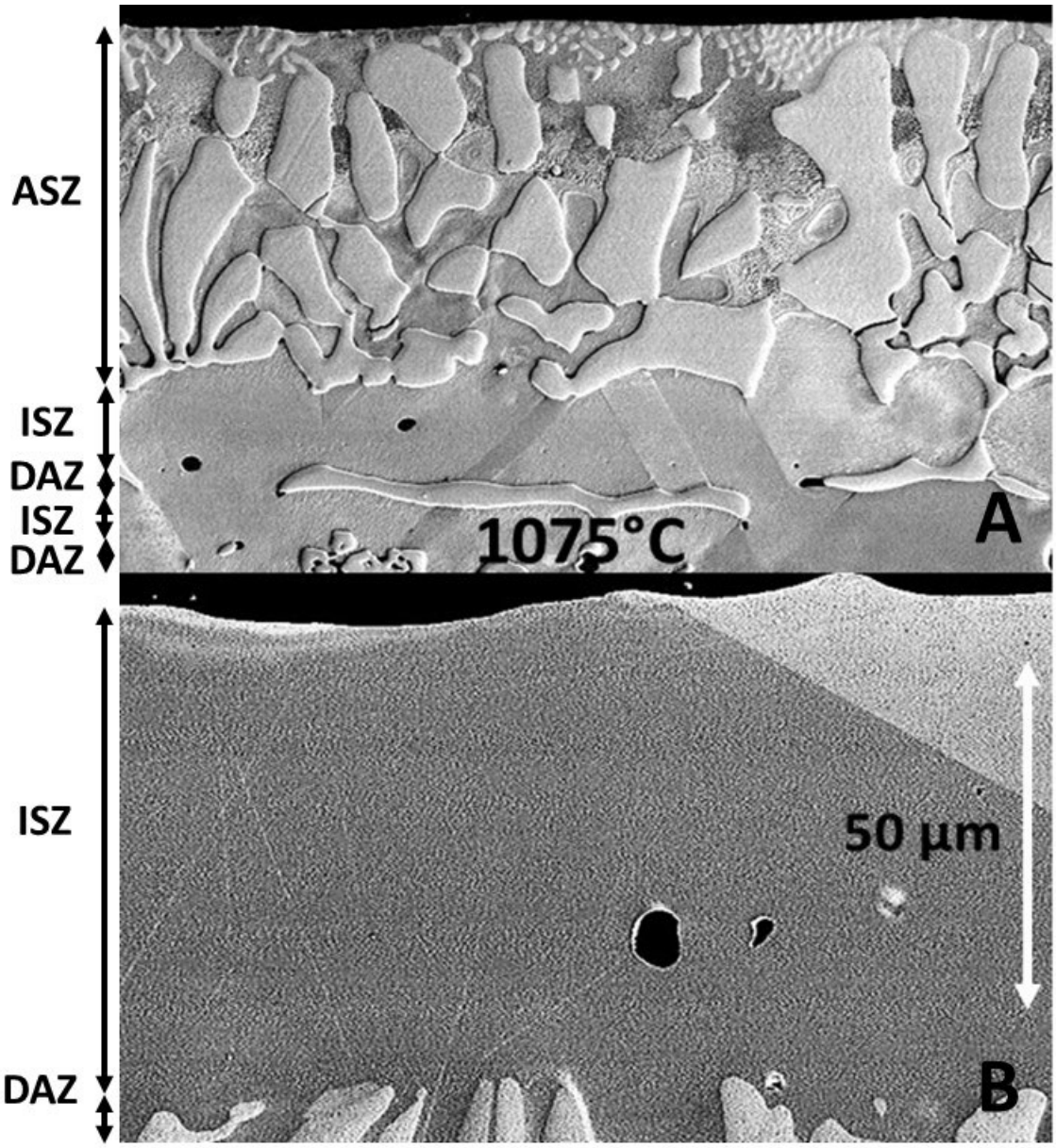

Figure 5-9 - SEM Micrographs of quenched (A) and 20x cycled (B) Ni/BNi-3 couples heated to 1075°C for a total liquid duration of approx. 7 mins and 131 min, respectively.

The 1100°C sample also exhibited different behaviour than the other samples. The DSC traces of Figure 5-5 indicate the development of a strong, melting/solidification event in the temperature range of 1090 to 1100°C. This event persists in a similar magnitude even after 19 cycles. The microstructure of this sample near the faying surface after 19 cycles is shown in Figure 5-10. The layered DAZ/ISZ structure present in the other samples is completely disrupted and absent in the 1100°C cycle. As will be discussed in more detail below, the DAZ layer of the joints

at 1020, 1050 and 1075°C have a composition and structure close to that associated with the Ni-Ni_3B binary eutectic which has a melting point of 1092°C [30, 33-34, 98, 87]. Therefore, it is likely that heating to 1100°C melted the DAZ layer as observed by Ruiz-Vargas et al. [107].

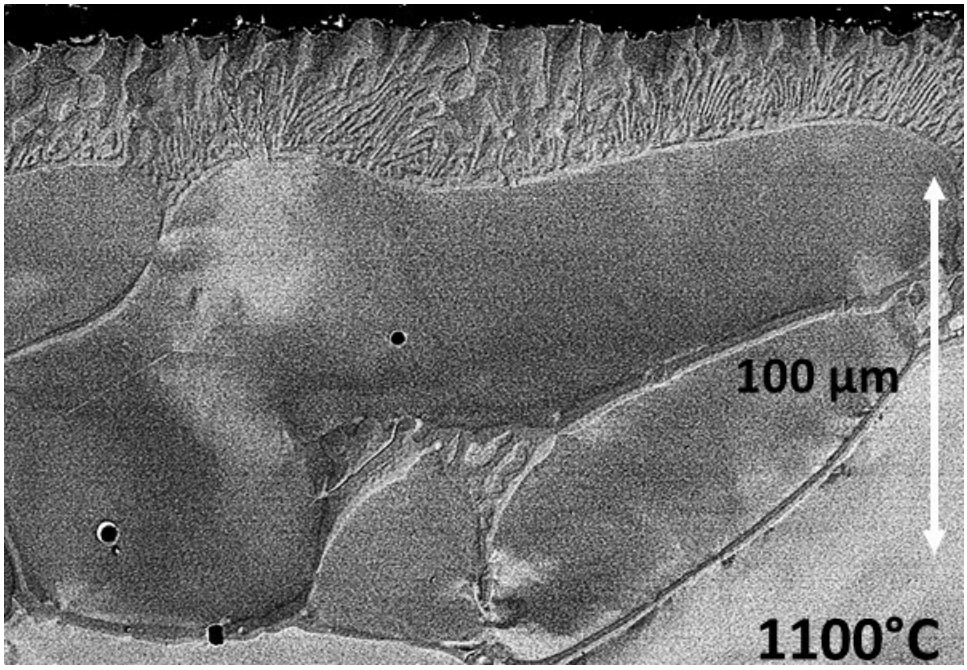

Figure 5-10 - SEM Micrographs of 20x cycled Ni/BNi-3 couple heated to 1075°C. Total liquid duration: approx. 149 min.

5.2.3 DSC Examination of Base Metal Dissolution Phenomena

The DSC trace for the sample brazed at 1075°C exhibited a distinct shift in its melting behaviour. It is assumed that this is a result of BM dissolution which enriches the Ni content of the liquid phase. To confirm this assumption, pure Ni powder was added to the BNi-3 foil in increasing amounts. These mixtures were then heated to 1350°C to completely melt and homogenize the mixtures. Samples were cycled up to 1350°C a total of three times to ensure homogenization and to determine the influence of Ni content on the melting behaviour. The melting traces for the last heating cycle for each mixture is illustrated in Figure 5-11. The results show the changing melting characteristics due to increasing Ni additions (i.e. simulating BM dissolution). Increasing the Ni wt% reduces the magnitude of the invariant TE melting peak, which onsets at 994 °C and continuously shifts the 2nd broader BE melting event to higher temperatures. An even broader peak extends to higher temperatures as the Ni content increases, reaching a temperature near 1300°C

when the Ni content reaches 96.3 %. The TE melting event disappears from the DSC trace at and above a Ni content of 94.7 wt%.

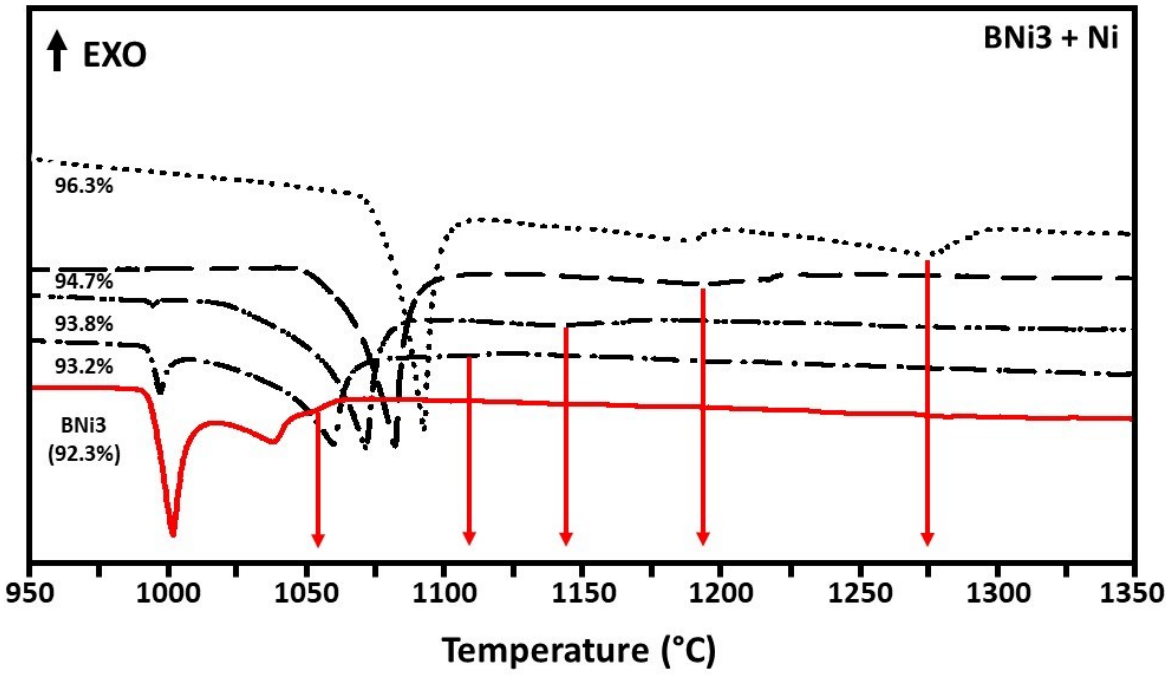

Figure 5-11 - Representative DSC heating traces of BNi-3 + Ni powder specimens heated to 1350°C. Inset: Cyclic DSC heating trace of Ni/BNi-3 couple for comparison.

The microstructures corresponding to the 93.2, 93.8, 94.7 wt % Ni samples from Figure 5-11 are displayed in Figure 5-12. Consistent with the DSC results, the 93.2 and 93.8 % Ni samples exhibit regions of TE and BE microstructure. Conversely the 94.7 % Ni sample indicated only the BE structure and a pronounced primary γ-Ni phase. Ni compositions of 96.3 and 99.8 % Ni had microstructures similar to the 94.7 % sample accept the primary γ-Ni phase increased in volume fraction. EDS analysis of the gamma-Ni grains yielded consistent Si concentrations of less than <0.5 at% both in primary γ-Ni and eutectic γ-Ni phases. Comparison of the melting curve of the 1075°C braze sample (Top plot of Figure 5-8) indicates that the absence of the TE and onset temperature of the BE melting event is very close to a liquid phase diluted to 94.7 wt% Ni

Figure 5-13 reintroduces the Ni-Si-B isopleth prediction from Thermocalc for the case of a fixed Si:B ratio of 4.5:3.2=1.4, shown previously, however also including the experimental compositions and corresponding peak temperatures acquired from the DSC dilution studies. The solidus temperatures for the TE and BE events were determined from the temperature at which the

endothermic peaks on the DSC traces of Figure 5-11 first deviated from the baseline. The BE and Primary liquidus temperatures were measured from the point of the maximum endothermic energy of the appropriate peaks (i.e. the "peak" temperature) to avoid an overestimation of the values that could be caused by thermal lag. The experimental values appeared to agree very well with the calculated predictions considering that the heating and cooling rate within the DSC was 20 K/min (i.e. non-equilibrium heating and cooling). More importantly, the comparison reinforces the melting/solidification sequence as a function of Ni composition observed and validates the Thermo-calc predictions.

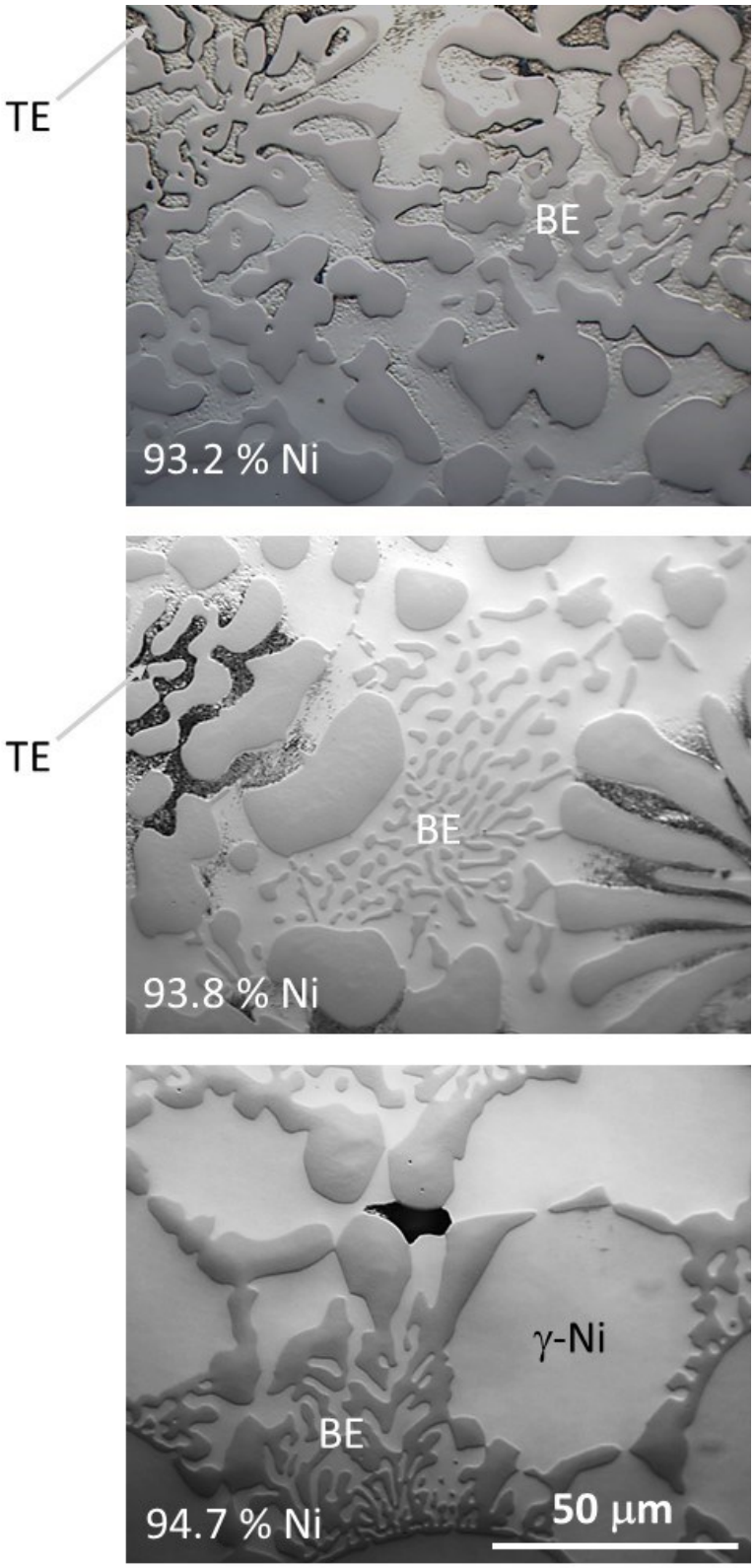

Figure 5-12 - Optical Micrographs of BNi-3 foil with increasing Ni powder additions. Samples obtained from DSC experiments shown in Figure 5-11.

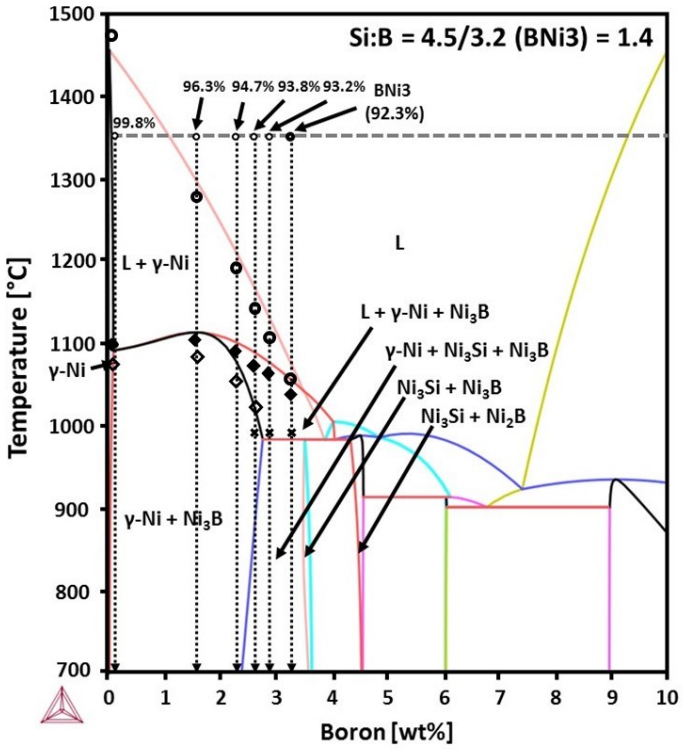

Figure 5-13 - Calculated Ni-B-Si Isopleth for a fixed Si:B ratio of 1.4 (Si = 1.4B, BNi-3). Markers denote experimentally measured peak temperatures of nominal dilution concentrations.

5.2.4 Solidification/diffusion Path Studies in the Ni/Ni-Si-B System

The isopleth analysis in the previous section is most applicable to alloys with a homogeneous composition or to help interpret the solidification behaviour of any remaining liquid in the braze joint upon cooling. Interpretation of diffusional or isothermal solidification of the braze joints, where the composition varies across the diffusion couple and phase equilibria at interfaces is imposed, requires isothermal sections of the ternary Ni-Si-B phase diagram along with diffusion path theory. Figure 5-14 presents a 1075°C isothermal section of the Ni-Si-B ternary phase diagram using the Thermo-Calc software. The isopleth used previously corresponds to a straight line intersecting the Ni apex and the nominal composition of the BNi-3 foil (dashed line 1 to 4 in Figure 5-13).

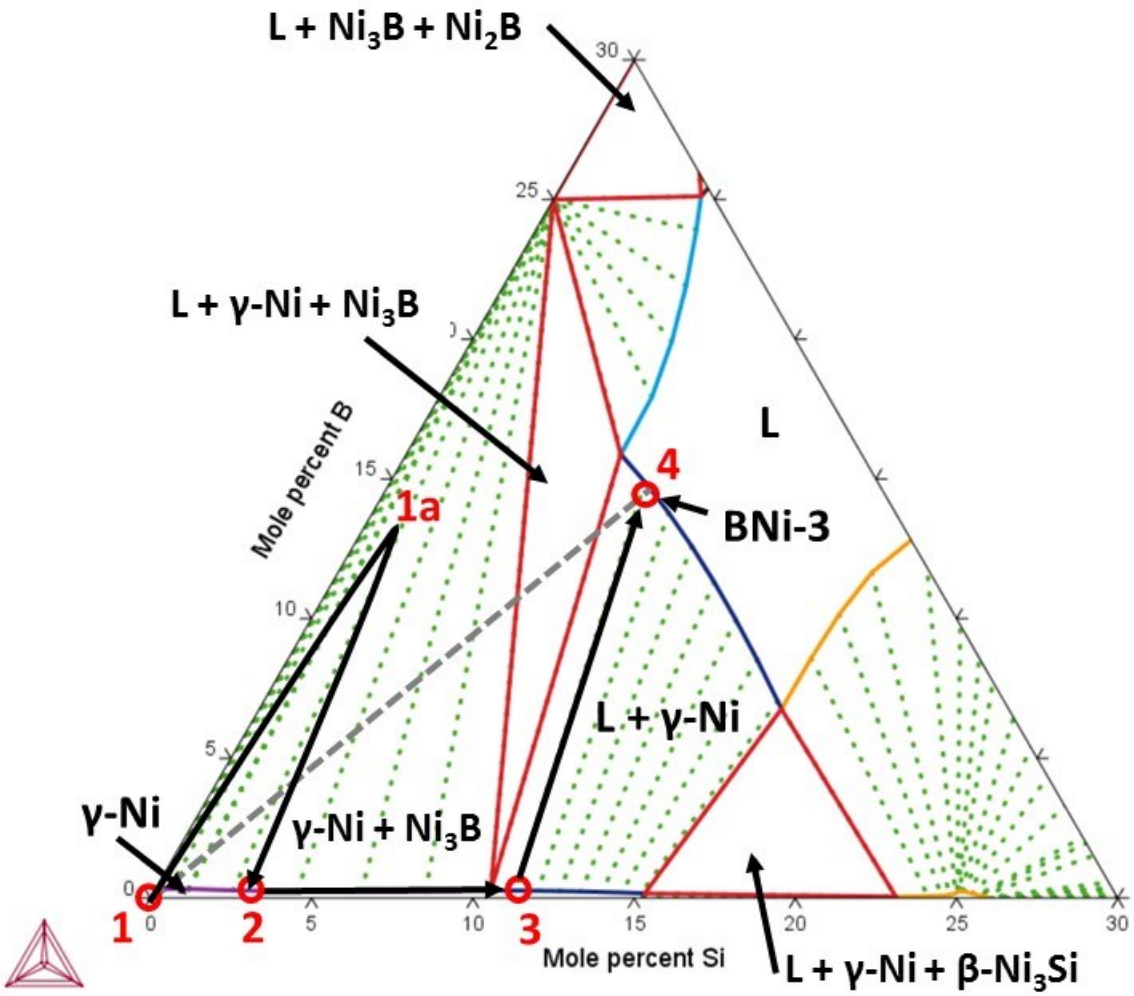

Figure 5-14 - Calculated 1075°C Ni-Si-B isothermal phase diagram with composition of BNi-3. Dashed and solid lines represent straight and initial boron uptake (IBU) paths, respectively.

and is very useful for monitoring the phenomena of BM dissolution. However, the heterogenous microstructure i.e. BM→DAZ→ISZ observed can be best understood using diffusion path theory. The microstructure of an additional sample cycled at 1075°C for only 6 cycles is shown in Figure 5-15 with the corresponding solute distribution as determined through EDS to assist in the analysis. The concentration of B and Si in the liquid are assumed to be nominal

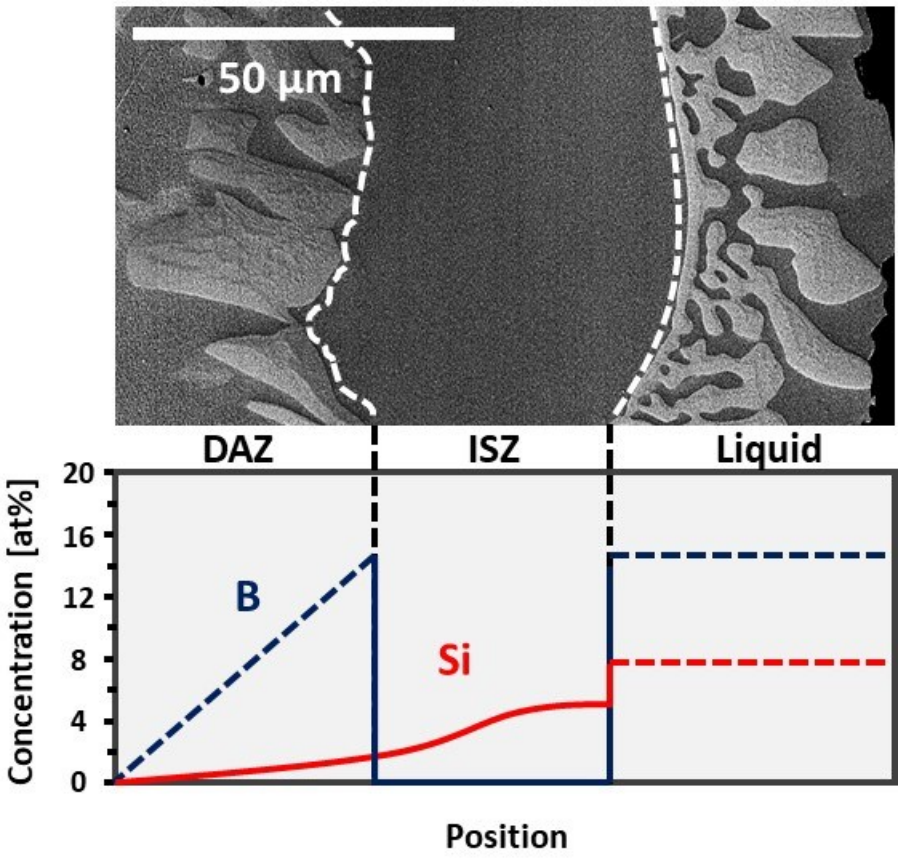

Figure 5-15 - Compositional profiles of B and Si during IS of a Ni/BNi-3 couple cycled at a peak temperature of 1075°C for a total liquid duration of approx. 60 min.

composition of the BNi-3 FM, while the boron concentration within the DAZ is predicted based on the bulk B content as inferred by the volume fraction of Ni_3B with position. The microstructure of the joint consisting of, i) a solute-free BM, γ-Ni(Si = 0) transitioning to ii) a region of isolated Ni_3B borides near the original faying surface γ-Ni with increasing Si concentrations iii) a boron free region of γ-Ni with an ever increasing Si composition and iv) terminating at a continuous interface of athermally solidified BE eutectic (γ-Ni(Si)/Ni_3B) corresponding to remaining liquid phase. A discrete change in the B and Si composition occurs which would be expected for the solid/liquid interface. The measured B and Si compositions from Figure 5-15 are mapped onto the isotherm of Figure 5-14 as a diffusion path, the solid line 1 - 1a - 2 - 3 – 4.

The main rules restricting the number of possible diffusion paths relates to; the morphology of the interfaces (columnar, lamellar, continuous) and the requirement that mass conservation be maintained as described in the conventions established by Clark [104]. Two of the most likely diffusion paths are the dashed line (1 – 4) and solid line (1 - 1a - 2 - 3 – 4) of Figure 5-14 given the microstructure and solute distribution displayed in Figure 5-15. The resultant microstructure for these two paths are represented schematically in Figure 5-16 centre and right.

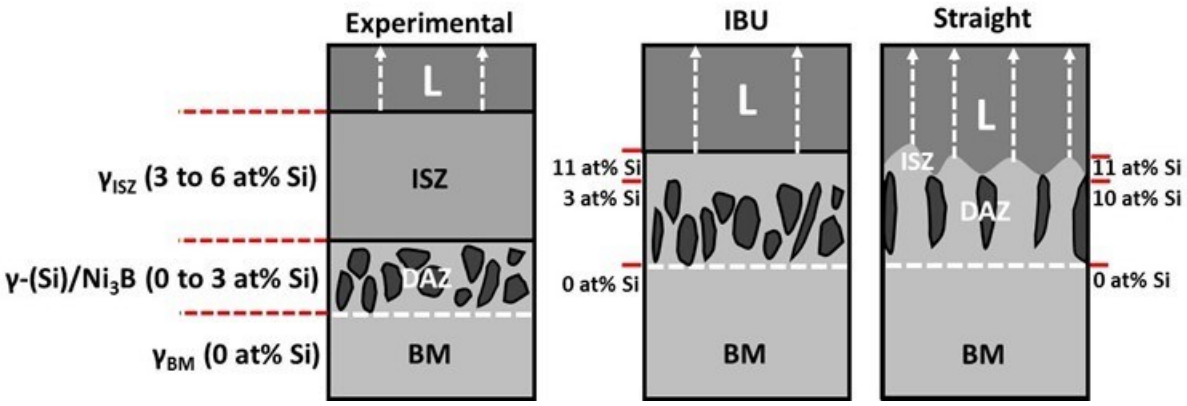

Figure 5-16 - Schematic illustrating experimentally observed diffusion couple (left) and two most likely diffusion paths (center and right).

The simplest path would involve a diffusion couple between the Ni apex and the nominal composition of the BNi-3 (diffusion path 1-4) thereby complying with mass conservation. However, this configuration poorly represents that observed experimentally in Figure 5-15, as it would result in the structure shown in Figure 5-16 (right). In this case the simultaneous, interpenetrating growth of γ-Ni and Ni_3B during isothermal solidification and considerably greater concentrations of Si within the DAZ would occur. These two phases would extend to the solid/liquid interface such that a three-phase equilibrium between of γ-Ni, Ni_3B and liquid could be established. No ISZ layer is predicted with this diffusion path.

The microstructure of the 1075°C joints clearly shows that the growing ISZ layer is the same phase as the pure Ni base metal. Furthermore, the interface with the liquid is that of this same single phase. Therefore, the Ni_3B within the DAZ represent isolated precipitates within the single phase γ-Ni(Si) solid solution. This DAZ structure is predicted by the diffusion path measured and

traced in Figure 5-14 i.e. 1→1a→2 since it corresponds to diffusion path convention No. 7 described by Clark [104] (see Appendix A for a more detailed description of Diffusion Path conventions). Namely, a diffusion path 'traversing a two-phase field in a curved path and returning to the same single-phase field (e.g. line d-e-f) represent isolated precipitates in a single-phase layer'. The growing ISZ layer is represented by the diffusion path 2→3 which is a compositional variation within a single-phase region. Diffusion path 3→4 with a dashed line crossing a two-phase region parallel to the tie lines, follow convention No. 4 described by Clark [104, Appendix A], with a corresponding interface separating the two-phases, in the current case, phase γ-Ni(Si) and convention. Consequently, the application of the Ni-Si-B diffusion path analysis fully explains the experimental diffusion couple and TLPB braze microstructure

The measured Si levels repeatedly show to be below those predicted by the calculated equilibrium data (approximately 11 at% at point 3 in Figure 5-14), this is believed to be a consequence of inaccuracies measuring Si using EDS and possibly the reduced solubility of Si at room temperature (the condition measured in the SEM).

The 1100°C Ni-Si-B isotherm shown Figure 5-17 was also created to assist in explaining the persistent liquid phase observed at this brazing temperature. EDS line scans gave a maximum Si concentration of 2 at% Si within the γ-Ni(Si) of the athermally solidified BE displayed in Figure 5-10. In most instances Si concentrations were below 1 at%, inferring a significant degree of base metal dissolution resulting from liquification of the DAZ. Figure 5-17 reveals new phase fields develop at 1100°C adjacent to the Ni-B axis and in the compositional range of 15 to mole% B, including a single-phase liquid field appearing near 0% Si, representing the melting of the binary eutectic Ni-Ni_3B. (T_m =1093°C). With a small increase in Si content, a three-phase region consisting of L + γ-Ni +$N_{i3}B$ develops. The triangular area of this field extends down toward the Ni-Si binary axis. Superimposing the 1→1a→2 diffusion path measured for the 1075°C couples indicates that the region near the DAZ-ISZ transition falls within the three-phase field. Therefore, this region of the diffusion couple would melt at 1100°C. Furthermore, the two-phase field adjacent to the Ni-B binary axis, which was γ-Ni + Ni_3B, has now become L +γ-Ni. These changes demonstrate that the DAZ-ISZ layer undergoes bulk melting creating a new liquid phase that is in equilibrium with a γ-Ni(Si) solid solution. The 1100°C isotherm indicates that the solubility of B in this phase is very low. The main sink of B in the solid phase at 1075°C and below was the

precipitated DAZ layer. With the melting of this layer and particularly Ni_3B, the low solubility of B in the remaining solid results in a persistent liquid phase. Such findings are further confirmed by the DSC results.

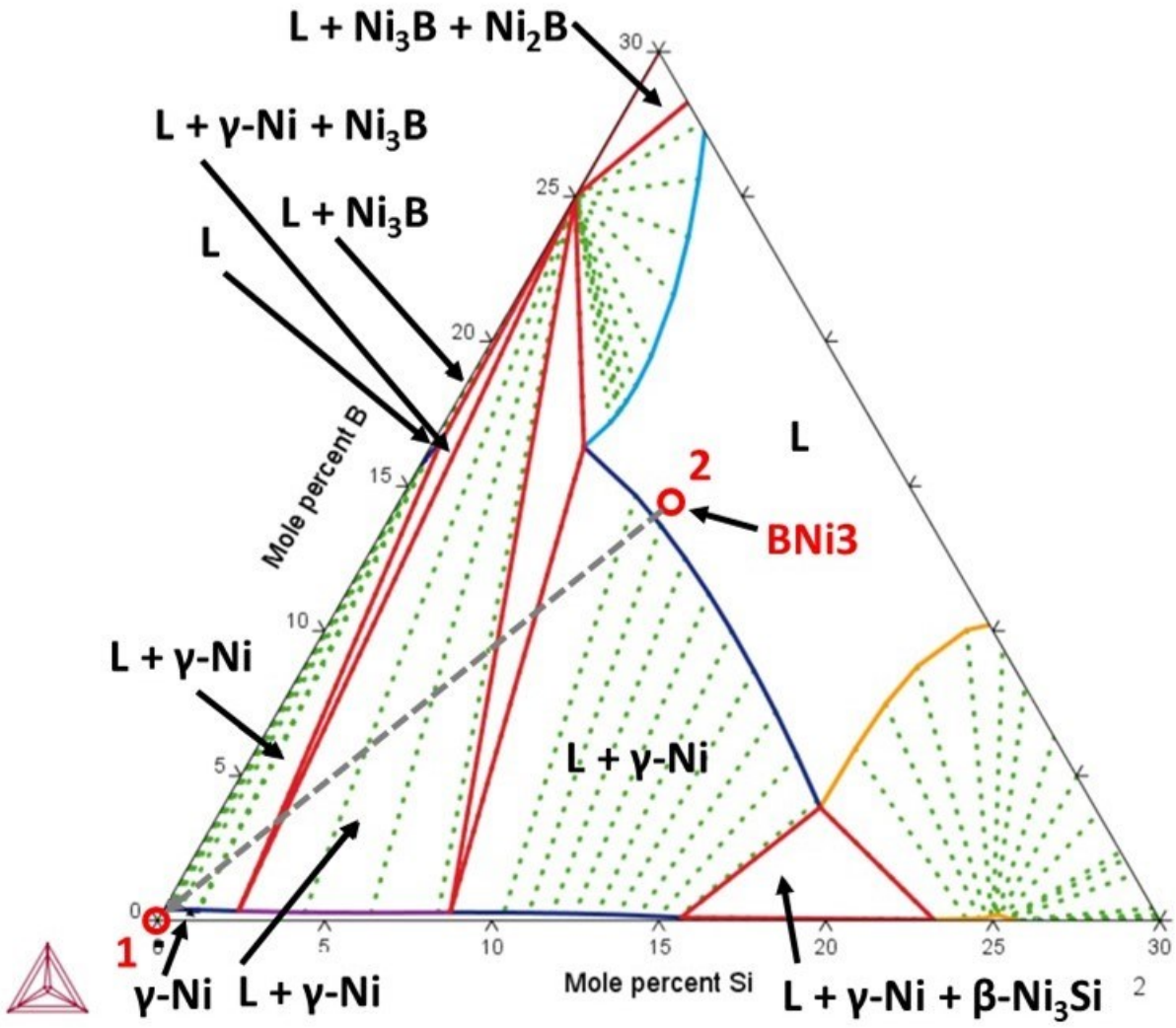

Figure 5-17 - Calculated 1100°C Ni-Si-B isothermal phase diagram with composition of BNi-3. Dashed line represents diffusion couple.

5.3 Conclusions

The application of diffusion path analysis in conjunction with SEM-EDS and thermodynamic modeling proved successful in explaining the underlying mechanisms responsible for the deviation from conventional TLPB theory in B containing diffusion couples. The primary findings are summarized below:

1. Below the binary γ-Ni/Ni_3B eutectic temperature of 1093°C, TLPB of Ni/Ni-Si-B couples resulted in a microstructure consisting of a network of Ni_3B intermetallics along the faying surface (DAZ) and related opposing growths of single-phase (ISZ)
2. Above 1093°C, melting of the DAZ occurred along with the formation of a persistent liquid phase as predicted by calculated ternary phase diagrams.
3. The deviation from conventional TLPB theory is attributed to the need to establish phase equilibria at the interface of a multi-component alloy system. In the case of the Ni-Si-B system this necessitates the formation of a B rich DAZ layer and Si rich ISZ layer at the former pure Ni/BNi-3 liquid interface. This interface structure is immediately developed as soon as the solidus temperature of the filler metal is exceeded.
4. During isothermal solidification, the width of the DAZ and ISZ layers increase while the liquid layer decreases. This allows isothermal solidification to proceed to completion.

CHAPTER 6 The Role of Base Metal Chromium in Determining the TLPB behaviour of Ni-Based Alloys using a Boron-Containing Braze

E.D. Moreau, S. F. Corbin

Department of Mechanical Engineering, Dalhousie University,
1360 Barrington Street, P.O. Box 15,000, Halifax, Nova Scotia, B3H 4R2, Canada

Status: Pending Publication in Journal of Metallurgical and Materials Transactions A (2020)

Authors Contribution: All experimentation performed by E. D. Moreau with direct guidance by S. F. Corbin.

Abstract

The TLPB behavior of Ni/Ni-Si-B and Ni-Cr-Fe/Ni-Si-B base metal/braze joints were examined to better understand the role Chromium has during joining of Ni-based alloys using a Boron-bearing braze metal. The isothermal solidification (IS) rate in these two braze joints at 1075°C was determined using DSC. Microstructural evolution within the diffusionally affected zone (DAZ) was examined both in terms of the type of boride forming and its volume fraction, using image analysis and phase equilibria predictions. Overall, the results show that when the base metal (BM) contains an appreciable concentration of Cr (and Fe) the IS rate decreases significantly. This was due to the formation of a low volume fraction of CrB within the DAZ, dictated by phase equilibria. Conversely, in the pure Ni base metal (BM) the thermodynamically favoured boride was Ni_3B, present at high volume fractions, resulting in rapid IS. A direct link between the boride microstructure of the DAZ and the rate of IS was established.

6.1 Introduction

Transient Liquid-Phase Bonding (TLPB) (or diffusion brazing) is an effective joining technique applied in the production and repair of advanced aerospace components subject to some of the most demanding applications within the hot-compression section of jet turbine engines. The strength and thermal stability of such carefully tailored alloys consequently make them difficult to form and join into more complex parts, thereby necessitating TLPB [8]. The process relies on diffusional solidification resulting from the progressive diffusion of a *melting point depressant* (MPD) such as Boron, from the liquid phase of a low-melting point filler metal (FM) into the substrate material [83]. Once formed, the liquid phase wets and fills the joint area and eventually solidifies isothermally, creating a strong metallurgical bond essentially indistinguishable from the base metal (BM).

As TLPB is governed by solid state diffusion from the MPD's into the BM, the manner by which the solutes distribute themselves must have a significant role in the rate of diffusional or isothermal solidification. For instance, in accordance with conventional TLPB, a MPD possessing an appreciable solid-solubility in the solid BM continuously diffuses out of the FM into BM, causing the liquid phase to solidify with the MPD redistribution [9,36]. Unfortunately, such FMs generally contain substantial quantities of precious metals, Au, Pd, etc. which greatly increase costs [21]. Alternatively, the adoption of the considerably more cost-effective Boron-containing FMs have become widespread. It is well known that B readily segregates as Cr-rich borides during the TLPB of Ni-based superalloys generating a *diffusionally affected zone* (DAZ), thereby weakening the joint [52, 71, 99, 100, 107-109]. However, many authors theorize the formation of such structure may enhance the rate of solidification as they promote solid-state diffusion of insoluble boron into the BM [59, 68, 92-93]. A direct quantitative link between boride formation within the DAZ and the rate of IS is currently lacking in the literature. In addition, while the role of BM composition on boride formation and isothermal solidification has qualitatively been examined [59, 62, 68, 92, 110], there has been no systematic study on this subject. The current work quantitatively examines the rate of IS using differential scanning calorimetry (DSC) techniques and DAZ boride formation using image analysis methods and Thermocalc predictions. These two approaches were combined to quantitatively establish the link between IS and DAZ development in a pure Ni base metal (Ni200) and the ternary Ni-Cr-Fe alloy, IN600.

6.2 Experimental Results

6.2.1 Thermal Analysis and TLPB Behavior

Figure 6-1 shows the heating and cooling traces obtained after cyclic heating of the Ni200/BNi-3 and IN600/BNi-3 couples to a peak temperature of 1075°C, with a 5 min hold for each of a total of 20 cycles. The first heating cycle is shown as a dashed line with subsequent cycles stacked vertically above this 1st cycle. The cooling cycles are stacked with the first cool on top and subsequent traces in sequence below. The overall reduction in the magnitude of the melting and solidification peaks is clearly shown to reduce as the cycles and braze time increase. This reduction is more significant for the Ni200 specimens indicating a much more rapid rate of isothermal solidification. Ni200 attained complete IS well within the 20 cycles, while IN600 samples still had liquid remaining, as evidenced by the presence of residual endothermic/exothermic peaks. Shifting of the first, low melting peak down to a lower temperature from its initial onset temperature occurred for the IN600/BNi-3 couple. This is likely due to dissolution of Fe and Cr from the BM into the liquid phase, thereby reducing the melting point of the invariant reaction. For the Ni200 couple, the melting point shifts to higher temperatures due to dissolution of Ni from the BM, as discussed in detail in the previous chapter. A comparison between the severity of dissolution for the IN600 and Ni200 and associated compositional measurements (EDS) is presented below.

The enthalpy of solidification obtained by integrating the area of the solidification peaks from the cyclic DSC signals are plotted for both the IN600 and Ni200 couples (Figure 6-2). Enthalpy measurements obtained from the melting peaks yielded similar results. Several separate runs are also plotted to assess reproducibility, for instance, in the case of the IN600/BNi-3 couple, 30 (765 min) and 40 cycle (1020 min) experiments were also performed, in addition to the standard 20 cycle experiments. Reproducibility in the three IN600/BNi-3 runs and two Ni200/BNi-3 is

excellent with a standard deviation of approximately ± 4 J/g (R^2 = 99.4%) and ± 11 J/g (R^2 = 95.2%), respectively.

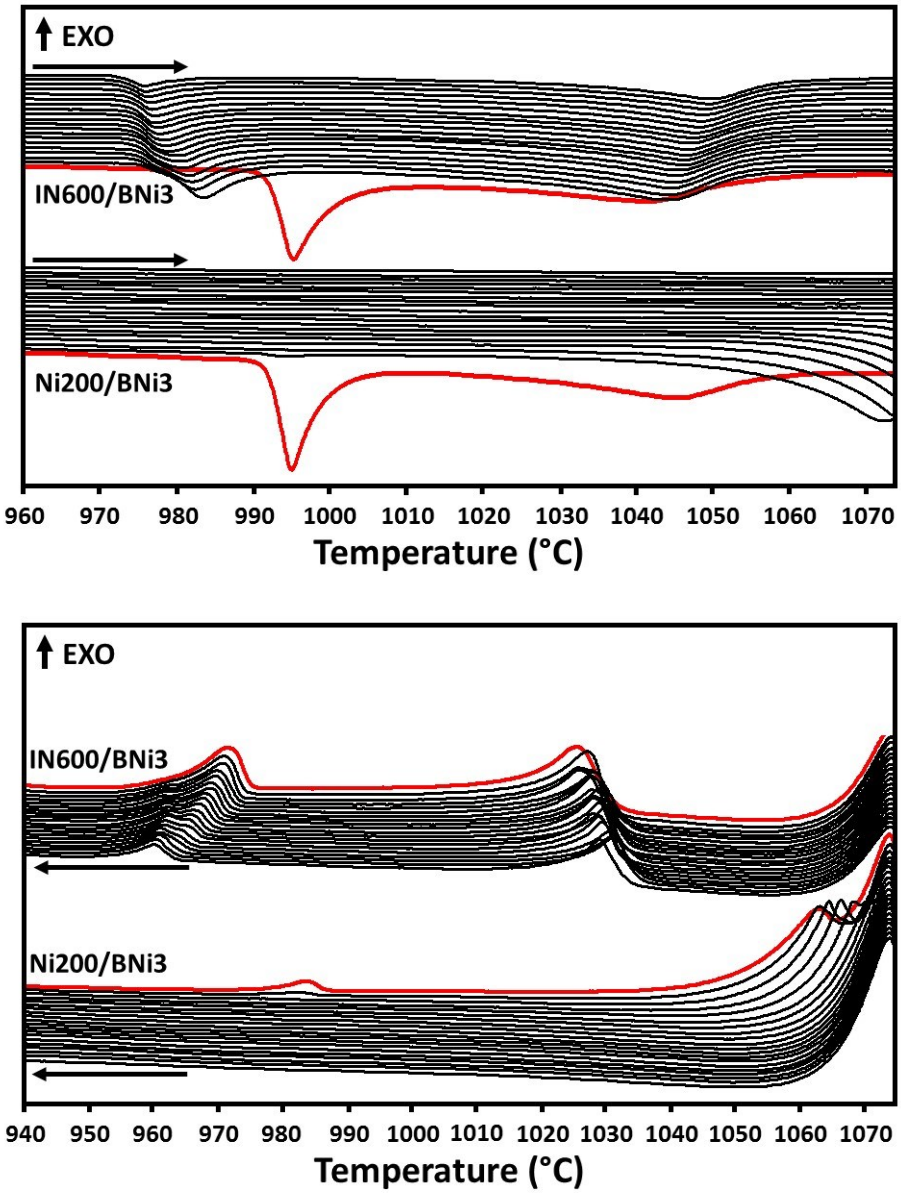

Figure 6-1 - Cyclic DSC heating (Top) and cooling (Bottom) results for Ni200/BNi-3 and IN600/BNi-3 half- braze joints. T_{MAX} = 1075°C.

Figure 6-2 provides a measure of isothermal solidification (IS) since the magnitude of the solidification enthalpy reflects the amount of liquid present in the joint. The plot indicates that no liquid remains in the Ni200 sample after 100 min of time above the solidus temperature (10 $min^{1/2}$) while measurable amounts of liquid still remain in the IN600 joint even after 650 min above the

solidus temperature (or 1020 min between 870 and 1075°C). In comparing the Ni200/ and IN600/BNi-3 20 cycle samples, the DSC traces clearly reveal two important differences. First, the times above solidus for each cycle are shorter for the Ni200/BNi-3 due to the higher solidus temperature of Ni200 (less time in the liquid state). Secondly, the rate of IS is much higher in the Ni200 joint such that it attains complete IS within 13 cycles. Therefore, this joint homogenizes in the solid state for the remaining 7 cycles. For brevity of discussion the number of cycles will be referred to in comparing the interrupted and cycled specimens.

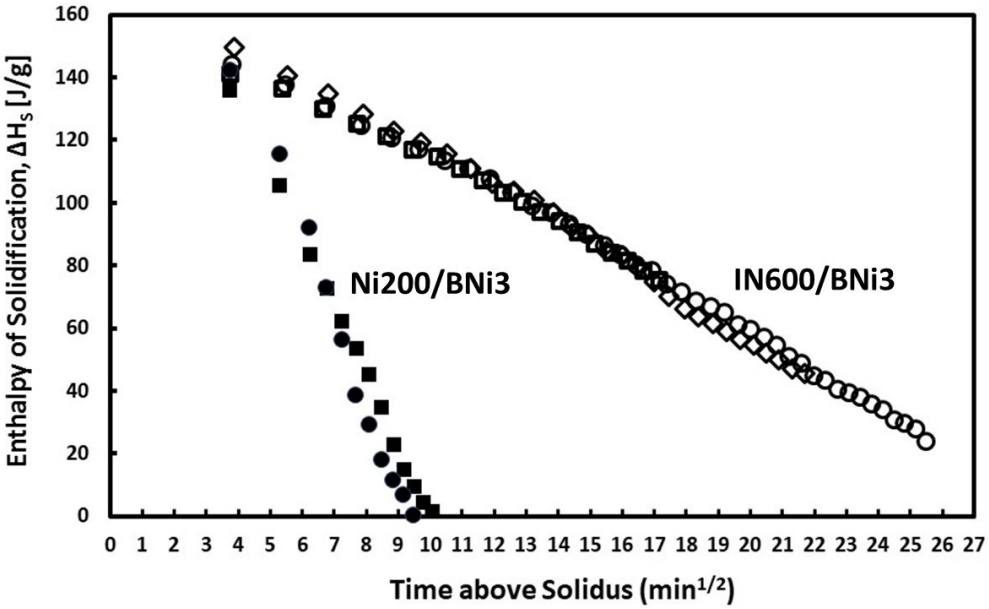

Figure 6-2 - Enthalpy of solidification vs. time above solidus obtained from cyclic cooling data (Figure 6-1). Data for 30 and 40 cycle DSC IN600/BNi-3 experiments also included in addition to an additional 20 cycle Ni200/BNi-3 specimen. T_{MAX} = 1075°C.

6.2.2 Microstructural Examination

The microstructure of the filler metal (FM) region of the joint resulting from furnace quenching (≈ 50°C/min cooling) immediately upon attaining 1075°C (approx. 9 min above the solidus) and after 20 cycles at a peak temperature of 1075°C is shown for the Ni200/BNi-3 and IN600/BNi-3 couples in Figure 6-3 and 6-4, respectively. The quenched samples of both specimens show evidence of isothermal solidification and associated formation of a diffusionally affected zone (DAZ) despite any extensive braze time. As the layer labels indicate, the ISZ and DAZ thickness is lower for the Ni200 joint compared to the IN600 joint. The lamellar eutectic region also known as the athermally solidified zone (ASZ) displayed by both quenched specimens

is associated with the cooling/solidification of liquid phase similar to that described in previous chapters. The ASZ of the Ni200/BNi-3 appears considerably less homogenous than that observed for IN600/BNi-3; the primary (γ-Ni) dendrites transitioning to coarse, globular binary eutectic which terminates with a much finer script-like ternary eutectic away from the original interface. The ISZ layer in both samples is somewhat difficult to discern because of the dynamic nature of the quenched condition. In particular, the Ni200 shows evidence of ongoing dissolution and melting of a previously formed DAZ layer. This phenomenon was also observed by Ruiz-Vargas et al. [71].

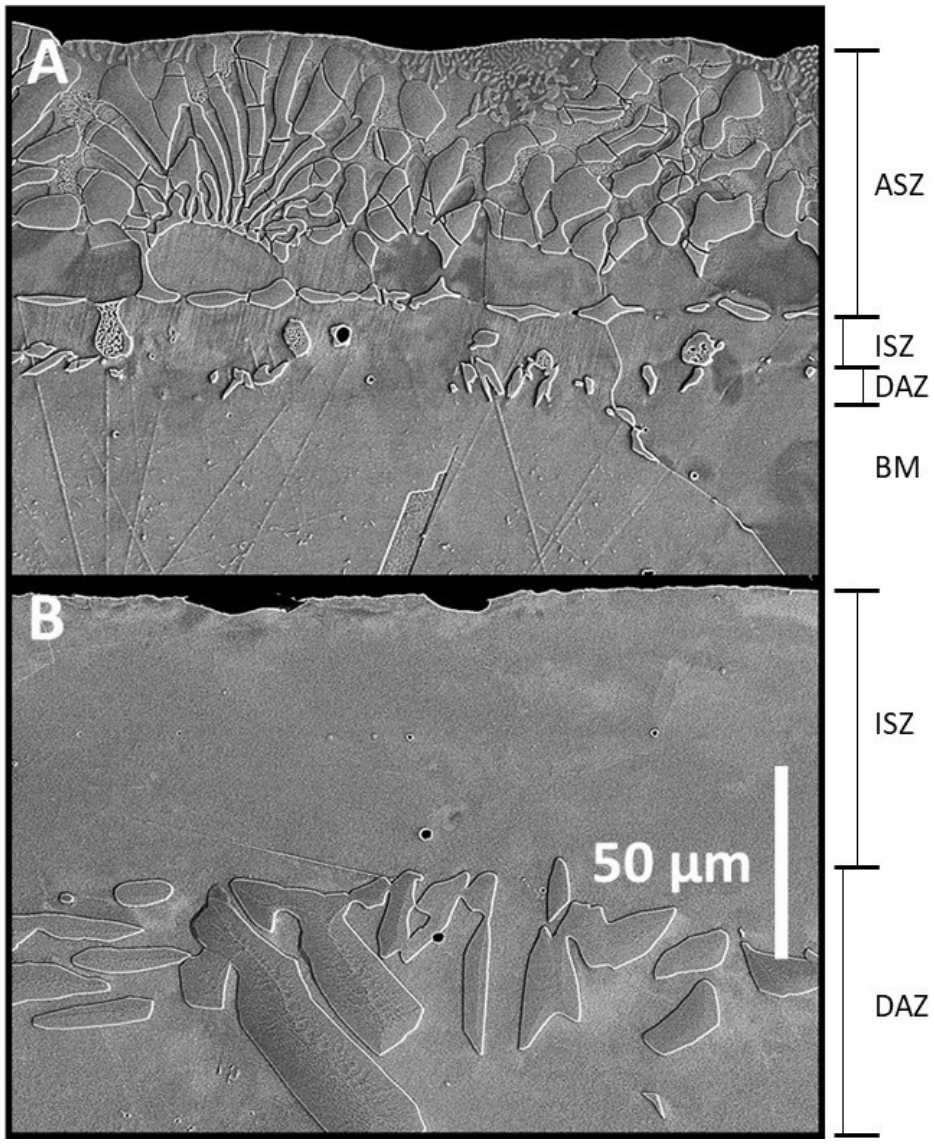

Figure 6-3 - Joint region of Ni200/BNi-3 heated to 1075°C followed by furnace quenching (A) and cycled a total of 20 times (B). Total liquid duration: approx. 6-8 min (quenched) and 105 min (cycled).

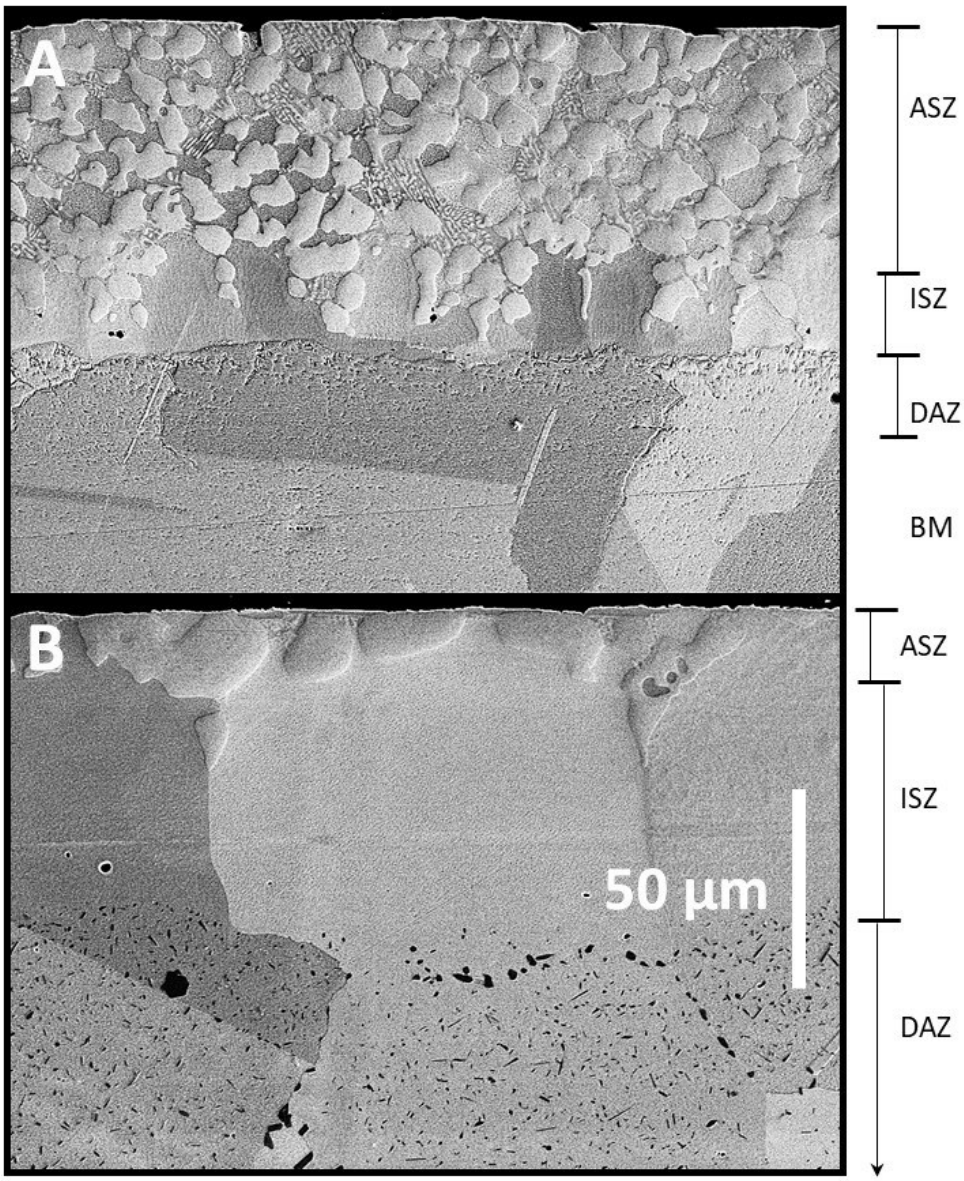

Figure 6-4 - Joint region of IN600/BNi-3 heated to 1075°C followed by furnace quenching (A) and cycled a total of 20 times (B). Total liquid duration: approx. 6-8 min (quenched) and 300 min (cycled).

As predicted by the DSC results, no discernible traces of ASZ were observed after extensive cyclic heating to 1075°C (20 cycles) for Ni200/BNi-3, while athermally solidified eutectic is clearly still present for IN600/BNi-3, albeit to a minor extent. Some degree of BM dissolution has also occurred as indicated by the width of the final isothermally solidified region (ISZ) (w_o) relative to the thickness of the initial liquid phase i.e. 40 µm. This w_o was measured to be 83±9 µm and 76±15 µm for the IN600/BNi-3 and Ni200/BNi-2 joints, respectively. Specimens

were ground and polished to the middle of the FM/BM disc such that a total 20 w_o measurements could be made. The +/- values represent the variability in the spread thickness of the liquid FM over the base metal rather than measurement error. Since the DSC data measures the entire sample liquid, the average w_o was deemed an accurate representation of the liquid gap.

A higher magnification view of the 20 cycle *diffusionally affected zone* (DAZ) is displayed in Figure 6-5 for both couples. The microstructures of the cycled specimens indicate that the elevated quantities of Cr (and Fe) in IN600 have clearly altered the morphology and distribution of the borides, favoring a greater distribution of finer borides as opposed to the coarse, globular network observed for Ni200.

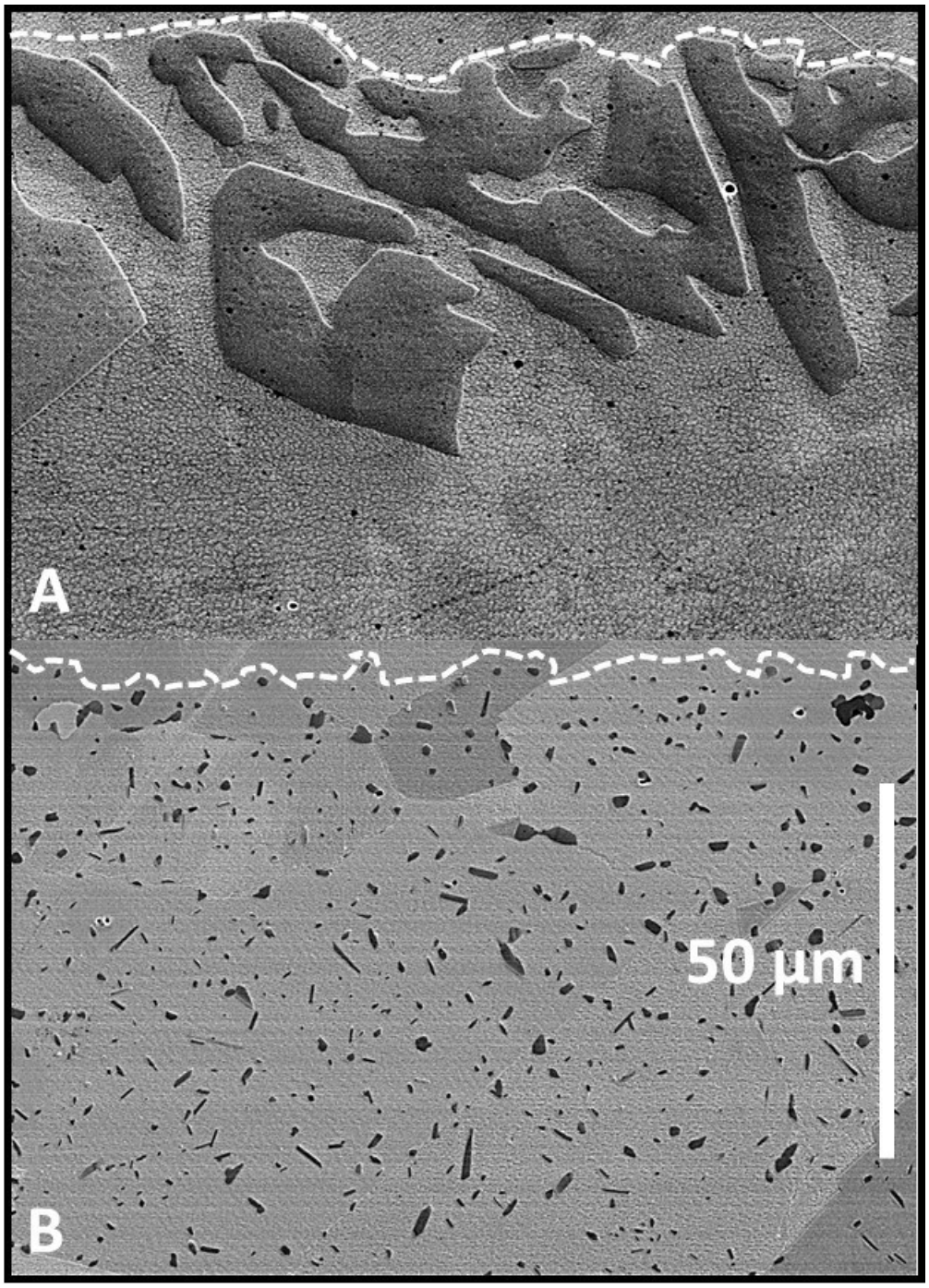

Figure 6-5 - Diffusionally affected zone (DAZ) of the 20 cycle Ni200/BNi-3 (A) and IN600/BNi-3 (B) couples. Dashed line denotes DAZ/ISZ interface. T_{MAX} = 1075°C.

6.2.3 SEM-EDS Compositional Analysis

Compositional profiles measured perpendicular the joint of each specimen for 0 and 20 cycles were obtained using a series of EDS point scans, beginning from the unaltered BM through the DAZ and extending to the edge of the ISZ (i.e. the ASZ layer was not included), the results are

presented in Figure 6-6 and Figure 6-7. These measurements focussed on the composition of the solid-solution γ-Ni phase, and therefore any measurements inadvertently made of the secondary boride phases in the DAZ were omitted.

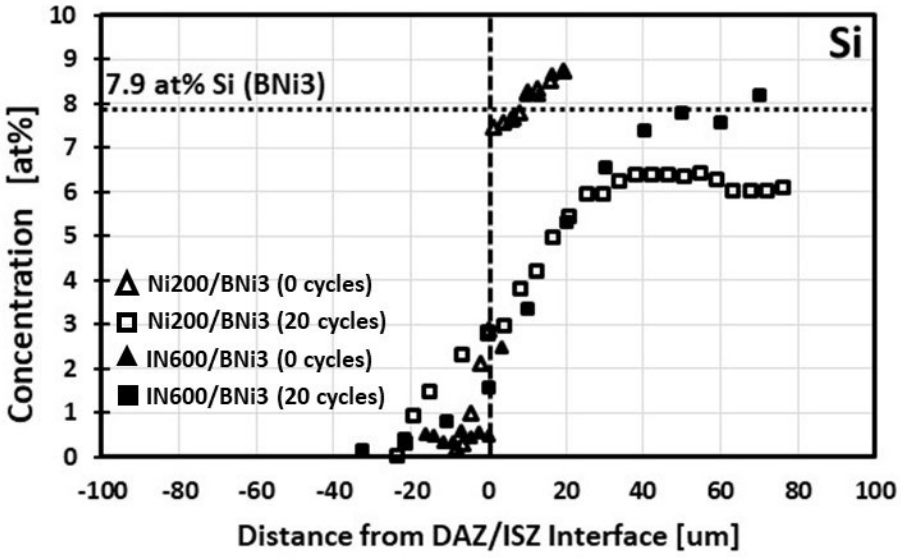

Figure 6-6 - Silicon EDS compositional profiles of cycled and quenched Ni200/BNi-3 and IN600/BNi-3 couples (Figure 6-3 and Figure 6-4). T_{MAX} = 1075°C.

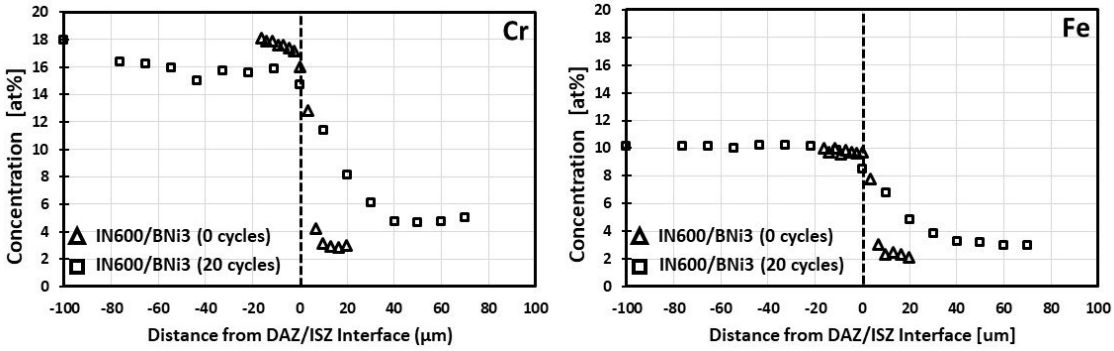

Figure 6-7 - Cr and Fe EDS compositional profiles of 20x cycled and quenched Ni200/BNi-3 and IN600/BNi-3 couples (Figure 6-3 and Figure 6-4). T_{MAX} = 1075°C.

The Si profiles for both quenched specimens are essentially identical with minor quantities of Si (< 2 at% Si) diffusing into the DAZ and Si concentrations similar to that of the original FM in the newly formed ISZ. In all cases the interfacial (ISZ/DAZ) Si concentration appears to be relatively constant ranging from 2-3 at% Si for both couples.

In the 20 cycle samples, Silicon has penetrated to significantly greater depth within BM (DAZ) of Ni200 as compared to IN600. In fact, the Si content within the DAZ of the cycled IN600

sample has not changed from the 0-cycle sample. Furthermore, the gradient within the Ni200 ISZ stabilizes below the nominal Si concentration of the FM (7.9 at% Si) which correspond to a decrease of approx. 2 at% Si. Comparatively, the IN600 displays a much more continuous profile which varies from approx. 1.5 at% Si at the DAZ/ISZ interface to the nominal concentration of the FM. This Ni200 Si depletion in the ISZ and related increase in the DAZ is believed to be a result of homogenization of the joint following achieving complete IS after 100 min. With no solid/liquid interface present in the Ni200, the necessary phase equilibria which forces a high Si content in the ISZ is removed. By comparison, the IN600/BNi-3 which never attained complete isothermal solidification, must always obey the phase equilibria between the ISZ/Liquid layer.

Overall, Figure 6-7 indicates that Fe and Cr diffuse into the ISZ to the extent that their concentrations stabilizes to 5 at% Cr and 3 at% Fe, respectively, from an initially Cr- and Fe-free FM. This further supports the melting peak shifting observed in Figure 6-1A, believed to be associated with BM dissolution and Cr and Fe diffusion into the liquid phase. Comparing the chemical distribution of the quenched and cycled specimens highlights the evolution of the chemical gradients associated with the concomitant growth of the ISZ and DAZ. Unlike Fe, significant depletion of Cr was observed within the DAZ matrix associated with the formation of the fine acicular Cr-rich borides. This feature was also observed for IN600 in the work of McDermid and Y. Miyazawa [111-112]. Such results are intriguing as they further support the crucial role Cr has on the rate of IS, whether it be a consequence of the nature of the resulting borides and/or its influence on the diffusivity of B.

Upon attaining complete Isothermal Solidification (IS), the final joint microstructure consists of two solid-solution phases separated by a diffusionally affected zone (DAZ), which is characterized by the presence of intermetallic boride precipitates and associated solute gradients (Figure 6-6 and Figure 6-7). Thus, the entire joint region of each specimen can be thought of as continuous solid solution γ-Ni(Si,Cr,Fe) with isolated borides (DAZ) and some degree of chemical heterogeneity. This is consistent with the diffusion path theory presented in the previous chapter. It was previously observed that Ni200 and IN600 display DAZ regions which differ drastically in terms of boride morphology and distribution. It was therefore of great interest to identify the chemical nature of the precipitates. The EDS results listed below in Table 6-1 represent the mean compositional values obtained for the DAZ Borides shown Figure 6-8 under various operating

conditions. As discuss in Chapter 3 (Experimental Methods), the 5kV voltage condition results in the most accurate and repeatable Boron measurements. The globular Ni-rich borides in the Ni200 DAZ correspond to the Ni_3B intermetallic while the fine Cr-rich borides observed in the IN600 DAZ correspond to CrB. Both these phases have been well documented in the literature [18, 30, 34, 40, 52, 71, 87, 92, 93, 100, 107-108]. It is therefore clear that the Cr content in IN600 is sufficient to promote the preferential formation of CrB rather than Ni_3B within the DAZ. The impact of this is the depletion of Cr within the DAZ region as confirmed in Figure 6-7. The CrB in the DAZ of IN600 specimens as compared to Ni_3B in Ni200 is considerably finer and evenly distributed as compared to very coarse globular Ni_3B, the degree of precipitate coarsening not observed in IN600. No distinction could be made between inter- and trans-granular precipitates. It is worth noting that the coarse borides present within the ASZ (Figure 6-3A and 6-4A) were measured to be Ni_3B for both Ni200 and IN600 joints.

Table 6-1 - Mean EDS results acquired for DAZ boride phase of BM/BNi-3 specimens for various operating conditions (at%).

Substrate	Voltage	Shell	Ni (L/K)	B (K)	Cr (L/K)	Fe (L/K)
Ni200	5kV	L	73.4	25.8	0.0	0.8
	15kV	L	68.3	27.8	1.9	2.0
	15kV	K	68.5	28.0	2.1	1.4
IN600	5kV	L	3.8	61.5	33.3	1.3
	15kV	L	4.7	62.6	31.5	1.2
	15kV	K	1.9	64.5	32.7	0.9

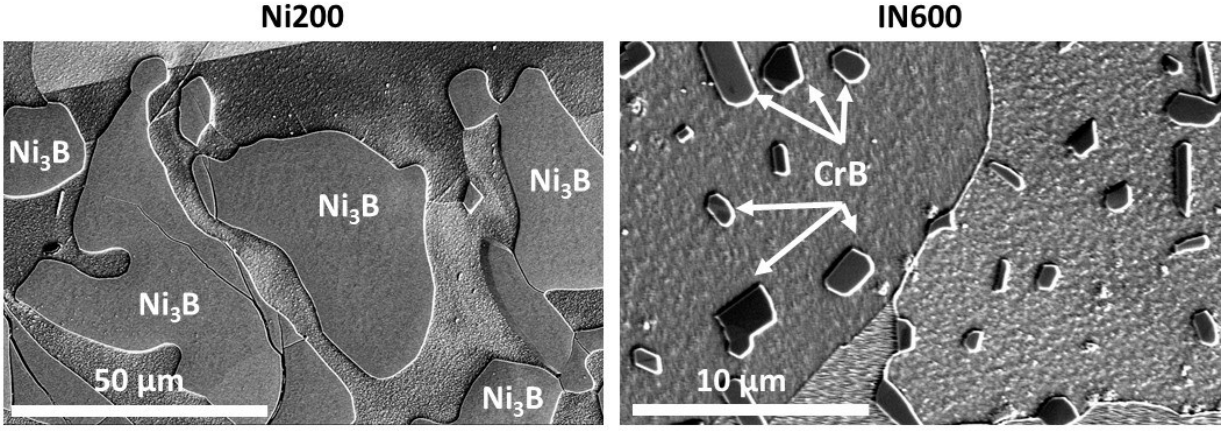

Figure 6-8 - Magnified Microstructure of DAZ for Ni200/BNi-3 and IN600/BNi-3 couples shown in Figure 6-5.

6.3 Analysis and Discussion

The microstructural observations above can be further validated through the application of thermodynamic modeling using Thermocalc software. Generated Ni200-Silicon-Boron and IN600-Silicon-Boron isothermal phase diagrams at the Ni-rich end are provided in Figure 6-9. The diagrams simulate the equilibrium conditions which occur within the DAZ i.e. progressive diffusion of B and to a lesser extent Si into the BM. The EDS profiles (Figure 6-6 and Figure 6-7) conclude that the Si concentration within the DAZ of the Ni200 and IN600 are < 3 at% and 1.6 at% Si, respectively. If it is also further assumed that the boron content within the DAZ must be less than the nominal concentration of BNi-3 i.e. 14.6 at% B, then the number of possible phases is greatly simplified. For example, in the absence of Fe and Cr (Ni200) a microstructure of γ-Ni and Ni_3B is thermodynamically predicted in the BM (DAZ). Comparatively, for IN600/BNi-3, the calculations predict γ-Ni + CrB. This is in excellent agreement with the experimental observations in Figure 6-5 and 6-8, showing that the differences in DAZ microstructure is a result of the requirements of thermodynamics and phase equilibria.

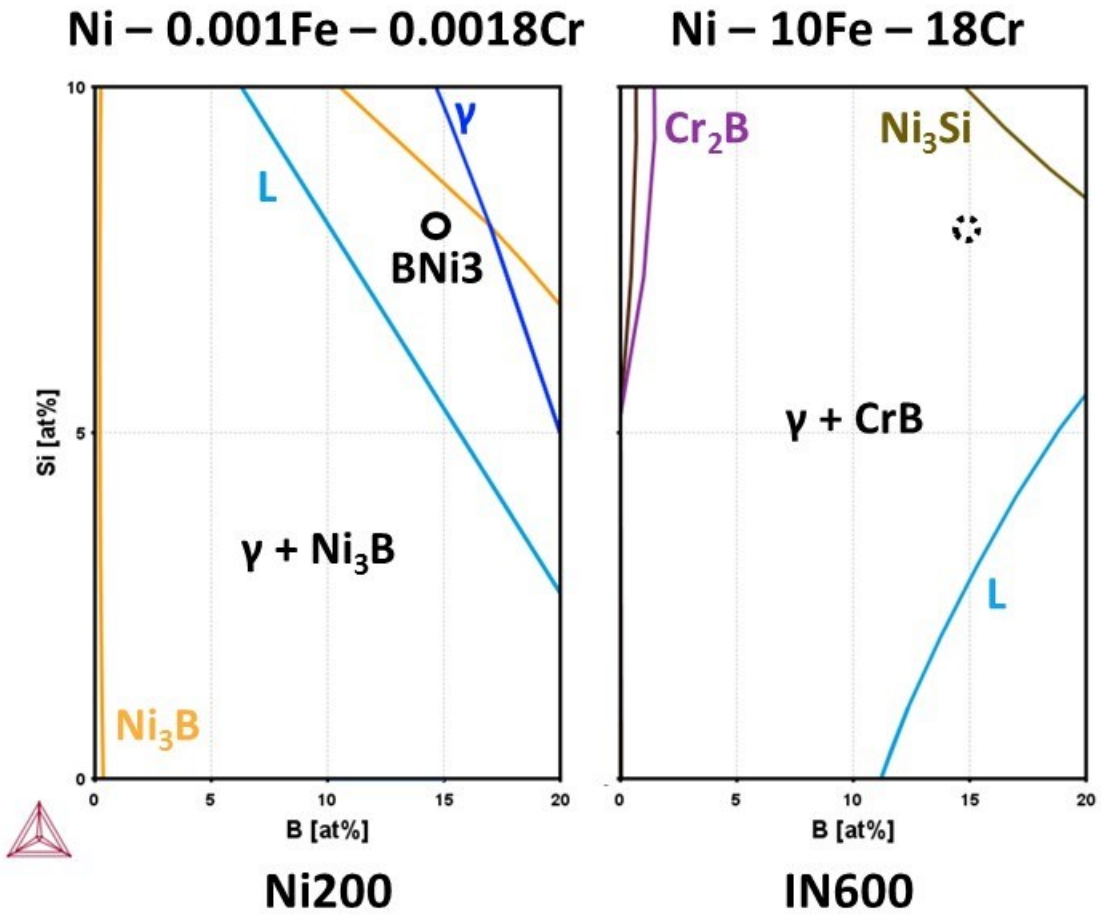

Figure 6-9 - Calculated Ni200-Si-B (A) and IN600-Si-B 1075°C isotherms.

Gale et al. examined the effect BM Cr content has on the wetting/spreading behavior of BNi-3 on Ni-Cr alloys in addition to the general morphology of the joint region [51, 99]. The rate of IS was not measured in these studies, but short cycle brazing of Ni-Si-B against substrates of pure Ni, Ni-5%Cr, Ni-10%Cr, Ni-15%Cr and Ni-20% Cr were used to examine the influence of Cr of the DAZ microstructure. Only γ-Ni + Ni_3B were found in the DAZ for Cr contents from 0 to 10 wt% Cr. The work indicated the stability of chromium borides at 15 and 20 wt% Cr. This result is consistent with the experimental observations and Thermocalc predictions of the current study. Additionally, Miyazawa et al. demonstrated that increasing the Cr content of the FM from 5 to 10 %, had a negligible influence on the DAZ microstructure of an IN600 substrate [112]. This supports the conclusion that the Cr content within the BM is the largest contributor to DAZ microstructure with a critical content needed for the borides to transition from Ni_3B to CrB.

To complete the current phase characterization, DSC was once again implemented to identify the various borides by their remelt temperature. This was accomplished by heating Ni200/BNi-3 and IN600/BNi-3 specimens to a peak temperature of 1300°C either directly, or after being cycled to a peak temperature of 1075°C for 20 cycles, as shown in Figure 6-10. The latter would enable determination of the melting point of the borides and/or their associated eutectic through the observance of an endothermic peak during heating. No appreciable melting of either BM was likely to occur since the melting points of Ni200 and IN600 are 1440°C and 1410°C, respectively. As expected, the specimens heated directly to 1300°C did not display any appreciable endothermic peaks corresponding to the melting of the DAZ as it had not developed to an appreciable extent from the lack of IS. Furthermore, the direct heat traces for Ni200 and IN600 couples are nearly identical with the exception of a small peak observed for the Ni200/BNi-3 between 1080 and 1105°C. Based on the findings of the previous chapters, it is now known that the DAZ of Ni/BNi-3 couples forms a Si-lean Ni-Ni_3B eutectic which melts at approx. 1092°C, indicating that the DAZ did form to a minor extent when heated directly to 1300°C (Chapter 5).

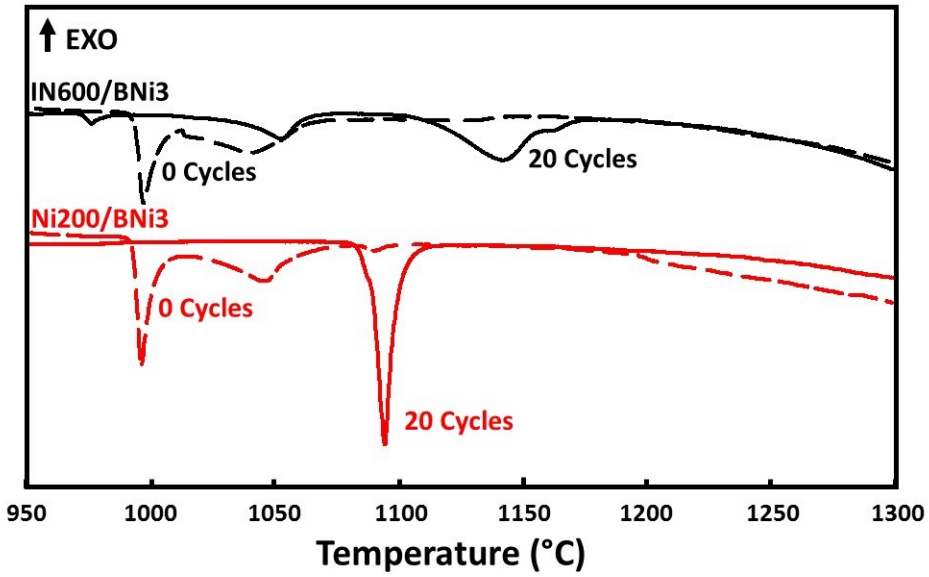

Figure 6-10 - DSC heating traces for Ni200/BNi-3 and IN600/BNi-3 couples heated immediately to 1300°C (Dashed) and after 20 cycles at a peak temperature of 1075°C (Solid).

A large, distinct peak is observed near 1092°C for the 20 cycle Ni200/BNi-3 couple that has undergone complete IS with the associated well developed DAZ. As the 20 cycle IN600/BNi-3 specimens did not attain complete IS (Figure 6-1) some remelting of residual ASZ was observed in the range of 1045°C and 1075°C. Further heating to 1350°C indicated a second larger melting

peak between 1100 and 1170°C corresponding to melting of the Cr-rich boride DAZ region in IN600 specimens (Figure 6-5). If brazing takes place above the melting temperature of the DAZ, the liquid phase becomes persistent and IS is no longer possible or prohibitively slow, as shown in the previous chapter on a Ni-Si-B braze couple [113]. The observed melting of the DAZ in the current IN600/BNi-3 couple is consistent with the work of Ojo et al. wherein the formation of a persistent liquid phase was observed at 1160°C but not at 1050°C along with the near-elimination of the DAZ borides during TLPB of IN600/Ni-Cr-B [100]. Thermocalc modeling implemented in the current work predicted the melting of the γ-Ni(Cr,Fe)/CrB eutectic at approx. 1150°C, which would constitute the DAZ generated at lower temperatures i.e. 1075°C. The formation of the Cr-borides which comprise the DAZ are therefore a result of brazing below the eutectic temperature of Ni-Cr-Fe-B of approx. 1150°C. This has been shown by numerous authors wherein complete elimination of DAZ borides is achieved above 1150°C, this however results in aggravated BM dissolution and the formation of a persistent liquid phase [100, 108, 111].

6.3.1 Base Metal Dissolution

The influence that BM dissolution has over the TLPB process and analysis of the DSC enthalpy measurements can best be understood with reference to Figure 6-11. BM dissolution is governed by the difference between the initial composition of the FM (liquid phase), C_o and the liquidus of the particular BM/FM couple, $C_{\alpha,L}$. Dissolution of the BM will occur until the composition of the liquid phase transitions from C_o to $C_{\alpha,L}$ (**1** → **2**, Figure 6-11). This results in widening of the gap from W_o to W_f, and a corresponding increase in the quantity or mass of the liquid phase at a given

temperature from m_o to m_f. The changing composition could also alter the enthalpy of solidification obtained from 100% liquid tests e.g. BM//FM, from $\Delta H(C_o)$ to $\Delta H(C_{\alpha,L})$.

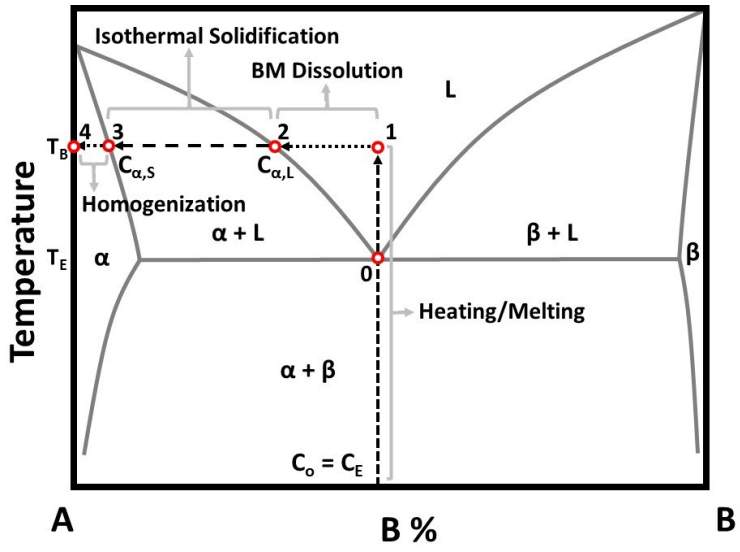

Figure 6-11 - Hypothetic binary phase diagram illustrating stages of TLPB.

BM dissolution and associated changes in the composition of the liquid phase clearly occur in the current work, as evidenced by the widening of the liquid phase from the initial ≈ 40 µm expected in the case of no dissolution, as confirmed by the IN625/BNi-2 couples 1050°C examined in Chapter 4 (Figure 6-3 and Figure 6-4). Dissolution is also evidenced by comparing the initial melting peak to that obtained from the 2nd melting cycle (Figure 6-3). This is most evident in the case of the IN600, wherein the first sharp melting event shifts to lower temperatures after the first cycle, as a result of uptake of Cr and Fe into the liquid phase. Comparatively, although BM dissolution clearly occurred in both Ni200 and IN600, the same peak does not appear to shift for Ni200, rather it decreases in magnitude practically indiscernible from the baseline. This however causes an increase in the magnitude and onset temperature of the following broader peak. As discussed in the previous chapter, this shifting of the melting peak to higher temperatures in the case of Ni200/BNi-3 is due to dissolution of the BM and an enriched Ni concentration.

In the absence of dissolution, such as that observed previously in Chapter 5, the unaltered enthalpy and mass of the starting filler metal were used to calculate the liquid fraction remaining [78]. Dissolution requires some degree of widening and/or an increase in the mass of liquid phase. The liquid composition will also vary based on the degree of dissolution as governed by thermodynamic equilibrium at a specified temperature. However, given sufficient knowledge of

the chemical/solute distribution before and after BM dissolution, it is possible to account and correct for such changes using the following formulae:

$$L_f = \frac{\Delta H^c{}_m}{\Delta H_o} = \frac{D_{mf} * B_C * \Delta H_m}{\Delta H_f} \quad \textbf{Eq. 6-1}$$

Where; ΔH_m is the raw DSC measured enthalpy of solidification {J/g} (Figure 6-2), B_C a correction factor which accounts for the thermal/signal dampening which occurs due to the presence of BM as opposed to the BNi-3 foil alone, ΔH_o {J/g}. This correction is obtained using the coated BM//BNi-3 couple enthalpy measurement ΔH_{BM} {J/g}. i.e. $B_C = \Delta H_o/\Delta H_{BM}$. ΔH_f is the enthalpy {J/g} of the braze ball created given the composition and degree of dilution (Si or Cr) observed for the quenched BM/BNi-3 couple. Lastly, D_{mf} is a mass correction factor which takes into account the increase in mass of the liquid phase resulting from BM dissolution, determined by the change in composition of the liquid phase.

Dilution was determined experimentally by first measuring the bulk or overall composition of the ISZ/ASZ region for the zero hold (quenched) samples shown in Figure 6-3A and Figure 6-4A. This composition was measured using SEM-EDS in addition to the unaltered BM away from the joint area and the BNi-3 FM only. FM only measurements were made after cyclically heating a braze foil to 1350°C for a total of 5 cycles, thereby providing the composition of the BNi-3 without the effects of any diffusional solidification. Comparing the initial composition of the liquid without any BM dissolution i.e. BNi-3 alone (e.g. 9.71 at% Si) to that of the quenched ISZ/ASZ joint region of specimens determines the change in joint composition resulting from BM dissolution. For instance, for IN600/BNi-3 at 1075°C the extent of BM dissolution is such that Cr and Fe contents in the initially Cr- and Fe- free BNi-3 increase to 2.36 and 1.50, respectively. Inputting the compositional measurements into the following simple mass balance equation enables determination of the mass fraction of BM dissolved into the liquid joint region due to dissolution, $\mathbf{f_{BM}}$;

$$X_i = X_{BM} \cdot f_{BM} + X_{FM} \cdot (1 - f_{BM}) \quad or \quad f_{BM} = \frac{(X_i - X_{FM})}{(X_{BM} - X_{FM})} \quad \textbf{Eq. 6-2}$$

where, X_i is the wt% of a chosen element (e.g. Cr) measured in the quenched ISZ/ASZ, while X_{BM} and X_{FM} are the wt% of the chosen element measured in the BM and FM only, respectively. Table 6-2 provides the relevant wt% values used in Eq. 6-2 as well as the calculated f_{BM} values, expressed

as a percentage. The predicted %BM is very similar for the IN600 for all 4 element calculations. Approx. 13% of the original BM dissolved into the FM region for the IN600/BNi-3 couple. In the case of Ni200/BNi-3 which, aside from Boron, only differs from the BM by Si, the liquid phase is essentially diluted with more Ni (from the Ni200) leading to a decrease of approx. 15-16 % in the overall Si concentration. Boron was omitted from such analysis due to its segregation as intermetallics and difficulties regarding quantitative EDS measurements of light elements.

Table 6-2 - EDS-SEM measurements obtained from quenched Ni200/BNi-3 and IN600/BNi-3 couples (at%).

Material	Area	**Si**	**Cr**	**Fe**	**Ni**
IN600	ASZ (X_i)	8.18	2.36	1.50	88.0
	BM (X_{BM})	0.30	17.7	9.93	72.1
$\%f_{BM}$		16%	13%	13%	11%
Ni200	ASZ (X_i)	8.26	0.03	0.30	91.4
	BM(X_{BM})	0.19	0.05	0.23	99.5
$\%f_{BM}$		15%	-	-	15%
BNi-3 (X_{FM})		**9.71**	**0.04**	**0.29**	**90.0**

These values permit the calculation of the mass correction factor, $D_{mf} = (1\text{-}f_{BM})$, which allows the creation of an additional braze ball with a composition predicted by D_{mf}. In the case of the Ni200/BNi-3, 15% pure Ni powder purchased from Alfa Aesar was added to a BNi-3 foil. For the IN600/BNi-3 case, filings from the IN600 base metal were taken and 13% by weight were added to a BNi-3 foil. In both cases these mixtures were melted and solidified several times within the DSC until homogeneous. The final heating trace was used to measure the actual enthalpy value, ΔH_f corresponding to the simulated composition of the liquid phase resulting from BM dissolution. Representative DSC heating traces of these braze balls (BB) are shown in Figure 6-12. Also included are the 2nd heating traces from the actual braze joints (Figure 6-1). Overall, the shape of the melting signals obtained from the BB and the diluted fillers of the joint are essentially identical, indicated that the proper amount of dilution was determined. The enthalpy of solidification for the BNi-3 + Ni200 (15 wt%) and BNi-3 + IN600 (13 wt%) braze balls (ΔH_f) were 249 and 248 J/g,

respectively. Therefore, the two couples are essentially the same, however, both displayed an enthalpy reduction i.e. 90% of the enthalpy measured for the unaltered BNi-3.

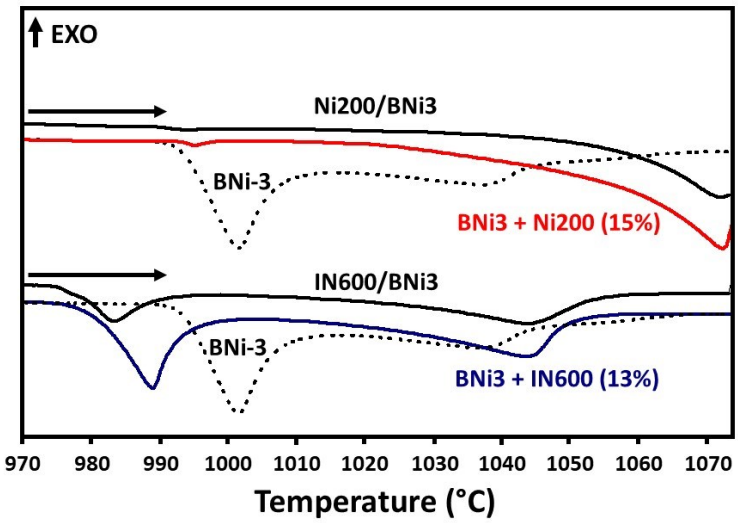

Figure 6-12 - Comparison between the DSC signals obtained for the 2nd heating trace of the Ni200/BNi-3 and IN600/BNi-3 couples and their corresponding braze balls as predicted by EDS measurements. T_{MAX} = 1075°C.

Applying the correction described in Eq. 6-1 to the raw ΔH_m values plotted in Figure 6-2, enables plotting of the BM dissolution corrected liquid fraction remaining, L_f data versus time ($min^{1/2}$) above solidus as shown in Figure 6-13. As the data is highly linear it is possible to quantify the solidification rate or depletion of the fraction of liquid phase in accordance with E. 6-1:

$$L_f = -k_L\sqrt{t} + L_o \qquad \textbf{Eq. 6-3}$$

Where, L_f is the corresponding liquid fraction remaining at time t, $-k_L$ the isothermal solidification rate constant $\{min^{-1/2}\}$, and L_o the initial liquid fraction present at t = 0. From Eq. 6-3, the time for complete isothermal solidification t_f, can therefore be expressed when $L_f = 0$ or:

$$t_f = \left(\frac{L_o}{k_L}\right)^2 \qquad \textbf{Eq. 6-4}$$

Figure 6-13 highlights the significant difference in the rate of IS displayed by the Ni200 and IN600.This may be related to modification of the diffusivity of B in Ni in the presence of Fe and Cr or more likely the driving force governing the formation of Ni_3B versus CrB. The corrected data reveals that for the current systems, accounting for BM dissolution yields only a small reduction in the liquid fraction values of the curves. This is due to the counter balancing influence

of the reducing D_{mf} factor in the numerator and lower diluted liquid phase enthalpy, ΔH_f in the denominator of equation 6-1.

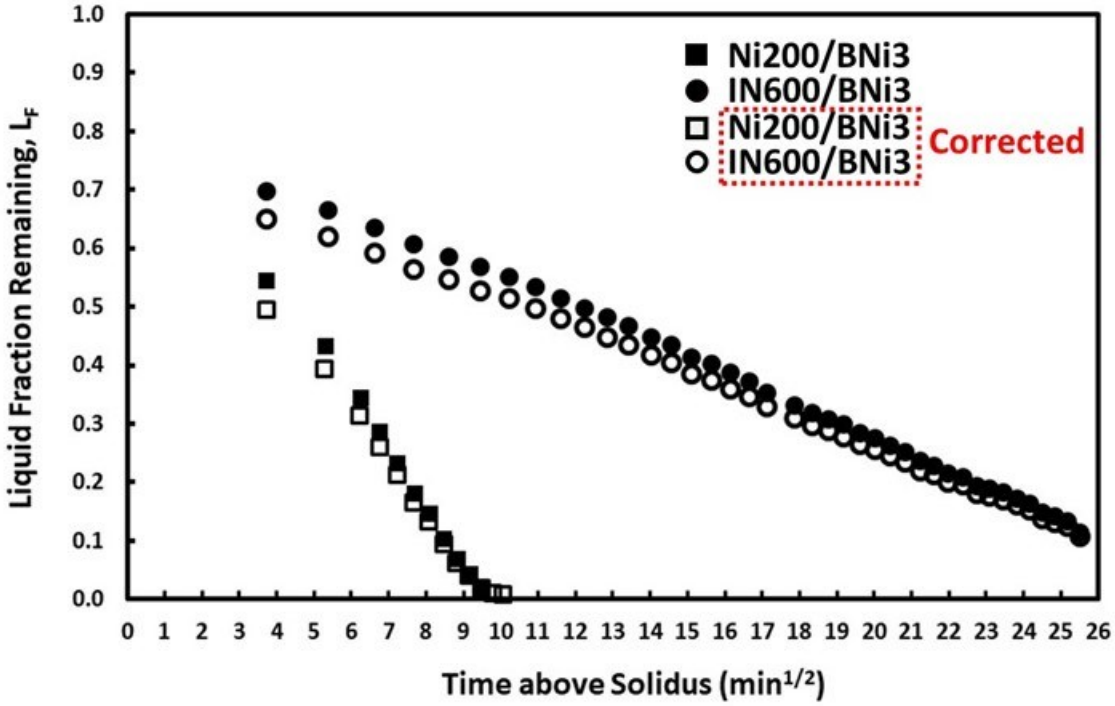

Figure 6-13 - Liquid fraction remaining versus time above solidus of Ni200/BNi-3 and IN600/BNi-3 couples obtained from 20x cyclic DSC cooling results, T_{MAX} = 1075°C. Blank markers indicate data corrected for BM dissolution.

In related work and Chapter 5 [78], it was shown that L_f measurements from the DSC can be converted to the width of liquid phase remaining in the gap, $2W_t$ {μm} providing that the thickness of the braze gap, $2W_o$ is known:

$$2W_t = \frac{\Delta H_t}{\Delta H_o} 2W_o = L_f 2W_o \qquad \textbf{Eq. 6-5}$$

Combining equations 6-3 and 6-5:

$$2W_t = 2W_o\left(-k_L\sqrt{t} + L_o\right) = -k_w\sqrt{t} + 2W_i \qquad 2W_t \to 0, \quad \sqrt{t} = \frac{2W_i}{k_w} \qquad \textbf{Eq. 6-6}$$

Where, $k_w = 2W_o k_L$ {μm/$min^{1/2}$} and $2W_i = 2W_o L_o$ {μm}. Alternatively, the width of the solidified ISZ, $2W_{ISZ}$, can be obtained by subtracting the width of the remaining liquid phase, $2W_t$ from the thickness of braze gap, $2W_o$ as follows:

$$2W_{ISZ} = k_w t^{1/2} + 2W_{ISZo} \qquad \textbf{Eq. 6-7}$$

For each sample, a value of $2W_o$ was obtained from multiple measurement of ISZ thickness made on post-braze polished cross-sections of the DSC samples as shown in the far right column of Table 6-3. Using these measurements, the liquid fraction data of Figure 6-13 was replotted as liquid width remaining, $2W_t$ (Figure 6-14A) and width of the ISZ, $2W_{ISZ}$ (Figure 6-14B). The plots show that repeated enthalpy measurements made using the DSC can provide a measure of the degree of IS in terms of either the $2W_t$ or $2W_{ISZ}$. This thickness change has been validated in related work by measuring the width of the ISZ and is in excellent agreement [78]. Both plots indicate a Y- intercept value $2W_{ISZo}$ and $2W_i$ at zero braze time, indicating that some amount of diffusional solidification occurs very early on in the brazing process. This will be discussed further below.

The plot of Figure 6-14B is useful in allowing the prediction of the isothermal solidification time, $t_x^{1/2}$ for any gap width. This is also known as the maximum brazing clearance or MBC_x. The MBC is the largest gap width that will undergo complete IS in a specified braze time. For example, when considering a full gap size $2W_o = 100$ μm, a braze joint made using Ni200 would undergo complete IS in 32 minutes, while the same joint made using IN600 would take 206 minutes to reach complete IS. This slower IS kinetics in the IN600 system is also indicated by the linear-regression analysis performed on the MBC plot (Figure 6-14B) which reveals rate constants of 12.7 and 4.3 $\mu m/min^{1/2}$ for the Ni200 and IN600 joints, respectively. The results clearly demonstrate the marked influence BM selection has on the TLPB behavior, necessitating considerably lengthier brazing cycles in the case of the Cr and Fe bearing IN600.

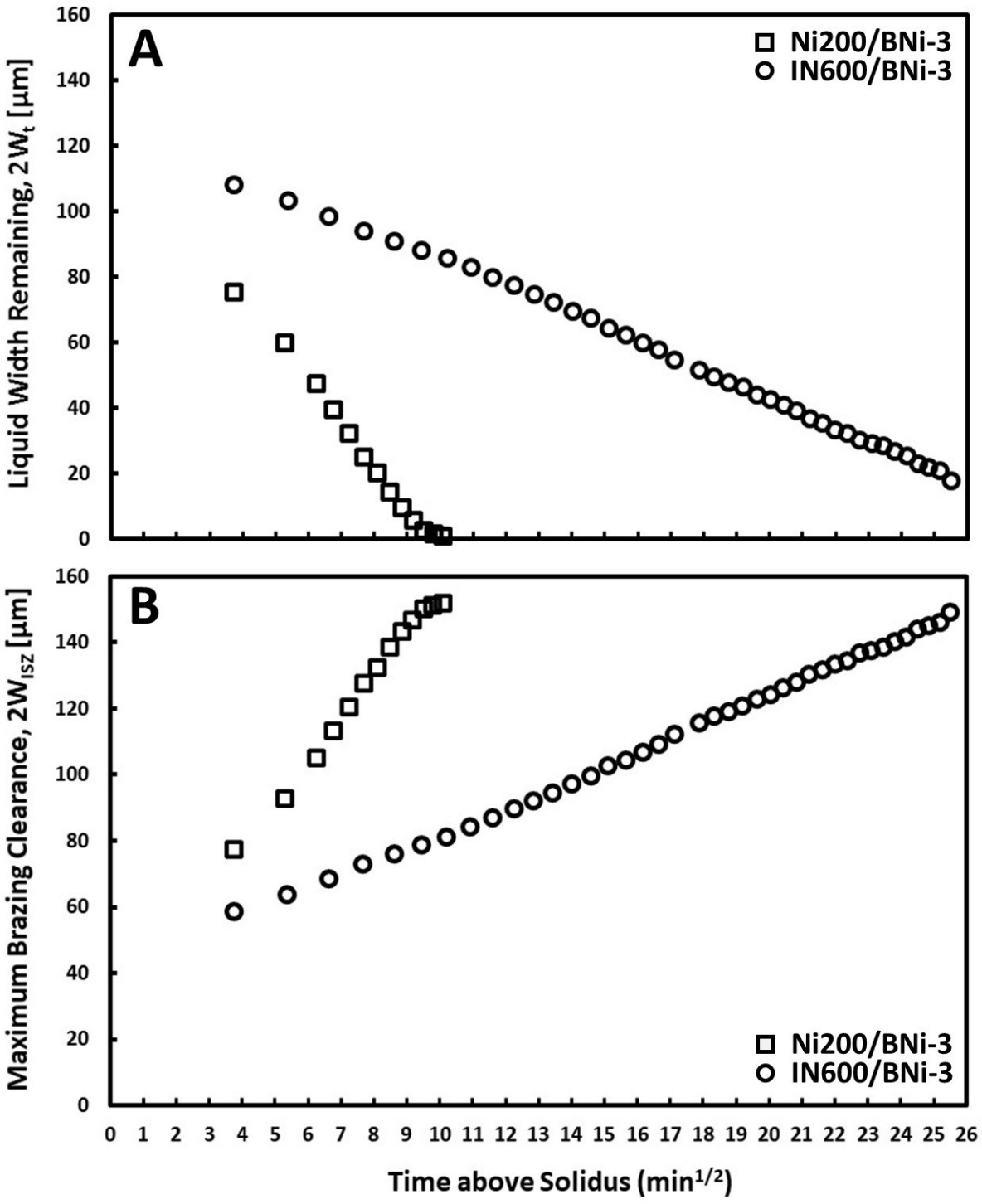

Figure 6-14 - Corrected liquid width remaining, $2W_t$ (A) and maximum brazing clearance, $2W_{ISZ}$ (B) versus time above solidus of Ni200/BNi-3 and IN600/BNi-3 couples obtained from DSC cooling results. T_{max} = 1075°C.

Table 6-3 - Linear regression data obtained from Figure 6-14(B).

BM	$t_f^{½}$ (min$^{1/2}$)	k_w (µm/min$^{1/2}$)	$2w_{ISZo}$ (µm)	$2w_{to}$ (µm)	D (m^2/s)	$2w_o$ (µm)

Ni200	**10.3**	**12.7**	**28**	**98.6**	**$2.9(10)^{-10}$**	**152±30**
IN600	**25.6**	**4.3**	**39**	**119.4**	**$2.1(10)^{-11}$**	**167±18**

As described in detailed in Chapter 4, Ni-based superalloy brazing with boron containing filler metals is characterized by an initial boron uptake (IBU). This is a rapid growth of a DAZ region during initial heating to the braze temperature which can be determined from an MBC plot for the time taken to heat from the solidus to the liquidus temperature, 4 min (2 $min^{1/2}$) of liquid duration. The quenched microstructures (Figure 6-3 and Figure 6-4) represent approx. 3 $min^{1/2}$ of time above solidus, show a measurable DAZ layer already developed. Ruiz-Vargas et al. believed some non-linear rapid initial solidification phenomenon transpired during the early melting stages as supported by the thin isothermally solidified zone (ISZ) observed in similar interrupted (quenched) Ni/Ni-Cr-Fe-Si-B couples [71-107]. The linear regression analysis results (Table 6-3) and the MBC plot of Figure 6-14 indicate that both couples also exhibit evidence of an IBU. At a liquid duration time of 2 $min^{1/2}$ the predicted isothermally solidified $2W_{ISZ}$ layer is 53.4 and 47.6 μm (or 26.7 and 23.8 μm on either side of a full joint) for the IN600 and Ni200 joints, respectively.

Comparison of the kinetics and TLPB behavior is most generally quantified based on the time required to achieve complete IS, as shown below in Eq. 6-8 [78,100, Chapter 4]:

$$t_f^{1/2} = \frac{2W_o}{4erf^{-1}\left(\frac{C_s}{C_o}\right)D^{1/2}} \qquad \textbf{Eq. 6-8}$$

Where, $2W_o$ is the initial full gap width {μm}, erf^{-1} the error function, C_s and C_o the concentration of the diffusing element in the BM and initial BNi-3, respectively, and D the apparent diffusivity {μm^2/min}. Alternatively, $\mathbf{t_f}$ can be readily identified empirically given the solidification behavior displayed by each couple in Figure 6-14A, as $2W_t \rightarrow 0$. Under such conditions, Eq. 6-6 and 6-8 are of the same form making it possible to obtain a value for the corresponding apparent diffusivity, D. Strictly speaking, Eq. 6-8 is only applicable to the isothermal solidification stage and the value of $2W_o$ used should be the liquid width at the beginning of IS, $2W_{to}$. This value was obtained taking the full joint width measured from metallography ($2W_o$ in Table 6-3) and subtracting the $2W_{ISZ}$ width calculated above for an LD of 2 $min^{1/2}$. This value of $2W_{to}$ is listed in Table 6-3 and was substituted into Eq. 6-8 to solve for the apparent diffusivity, D, assuming values of 14.6 at% B and 0.30 at% B for C_o and C_s. The results

(Table 6-3) yielded apparent diffusivity values an order of magnitude in difference for the two couples and is within the range of existing published data obtained for similar systems [88].

Given the similarity of the two base metals i.e. both Ni-rich single phase solid-solution alloys, it can be concluded that the significant differences in the TLPB behavior of the two couples observed is primarily a consequence of the driving force governing the formation and growth of their respective borides (Ni_3B and CrB) during IS. In part, growth is likely determined by the concentration of boride formers in the base metal. For the Ni200/BNi-3 system, since Ni is the boride former this concentration is essentially 100%. For the IN600/BNi-3 the Cr boride former concentration is only 18% which, as evident in Figure 6-7 results in some solute depletion within the solid-solution γ-Ni of the DAZ. Therefore, since IS involves the reactants B and Ni (or Cr) combining to form a product Ni_3B (or CrB) the limited quantity of reactants should influence the reaction rate and the isothermal solidification rate. TLPB involving reactive diffusion can be better understood in terms of the nature and/or type of boride(s) and that certain superalloys are inherently more amenable to TLPB due to the nature of borides formed. For instance, as observed in related work [78] examining the far more complex and established superalloy Inconel 625, a variety of Cr-rich borides are known to form based on the composition of the equilibrium thermodynamics of Boron in IN625. IN625 contains greater concentration of Cr as well as substantial quantities of Molybdenum and Niobium as compared to IN600, and, consequently TLPB of IN625/BNi-2 (Ni-Cr-Si-B-Fe) couples displayed rates intermediate between that of Ni200/BNi-3 and IN600/BNi-3 of this study. This indicates that proper selection and compatibility between FM and BM plays a significant role during TLPB wherein boride precipitation controls the rate of IS.

6.3.2 Boron Distribution in the Diffusionally Affected Zone

The physical properties the boride(s) formed clearly influences the kinetics of TLPB. Firstly, the stoichiometry of the boride indicates how much boron can be contained per mol during TLPB (formation and growth of boride). The density of the boride(s) would also contribute in this manner. However, precipitation of Ni_3B (Figure 6-5) occurs to much greater volume fractions albeit to considerably lesser depths into the DAZ in comparison to the CrB in IN600. Therefore, although the CrB formed in IN600 contain more B than Ni_3B, (i.e. 24.7 versus 6.0 wt% B, respectively) boride morphology and the limited quantity of boride formers (Cr) appears to alter

the maximum permissible distribution of borides throughout the DAZ. Additionally, low volume fractions of a particular boride would require the growth of the DAZ to greater and greater depths in order to consume the B from the liquid phase. This would likely inhibit further Boron diffusion due to the considerably greater diffusion distances required for the B to encounter the elevated Cr contents of the BM free of solute depletion.

Image analysis was therefore applied to the SEM images acquired for the DAZ region of all couples examined in the current work in order to quantify the boride volumetric distribution. This involved measuring the relative area occupied by the boride phases within the DAZ e.g. γ-Ni(Fe,Cr) and CrB, as a function of increasing depth, as shown below in Figure 6-15. The discontinuous shape of profiles, particularly for Ni200 are a consequence of singular, coarse borides penetrating to greater depths (see Figure 6-5), which is generally not observed for the more homogeneous and finely distributed CrB observed in IN600/BNi-3 couples. As discussed in Chapter 4, accurate area fraction analysis was difficult within the first 5 μm of depth due to a non-planer ISZ/DAZ interface. In this case the first two data points were assumed to be the same as the 3rd depth data point.

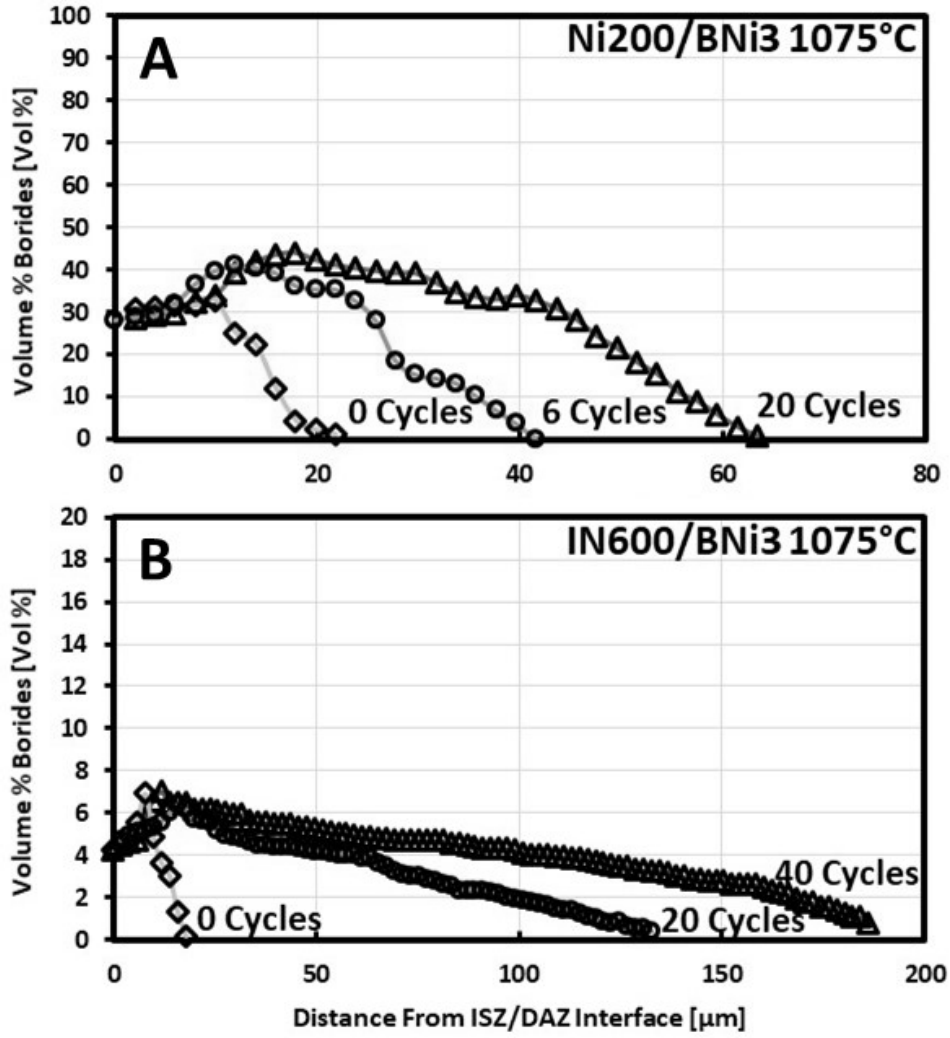

Figure 6-15 - Volumetric boride concentration as a function of depth into the BM (DAZ) for Ni200/BNi-3 (A) and IN600/BNi-3 (B) couples brazed for different lengths of time (cycles).

Comparing the volumetric boride profiles of Figure 6-15, it is evident that precipitation of the Ni_3B occurring within the Ni200 develops to a much higher area fraction compared to CrB in IN600. The lower area fraction of borides in IN600 also results in a significantly wider DAZ zone. For example, the 20 cycle Ni200 and 40 cycle IN600 samples represent close to complete isothermal solidification. Given that the boron content within the original FM was the same for both joints, its redistribution into the DAZ of a lower volume CrB case, required the growth of a thicker DAZ layer.

The boride distribution measured for Ni200/BNi-3 and IN600/BNi-3 couples subject to intermediate brazing times e.g. quenched (0 cycles), 6 cycles (Ni200) and 20 cycles (IN600) were

also analyzed as a means of correlating the kinetic results obtained from the DSC (Figure 6-13) to the evolution of the DAZ during IS, as shown in Figure 6-16. This was accomplished by approximating the accumulated volume for each profile as a function of DAZ depth, by performing a right Riemann summation of the data acquired from the image analysis. These accumulated values, V_{ac}, were then divided by total boride volume, V_T obtained for the time required to achieve complete IS, t_F (Table 6-3). Some extrapolation was required as complete IS was not achieved for IN600/BNi-3 even after 40 cycles. When the volume % boride reaches 100%, this represents the redistribution of all the B originally in the FM into the DAZ (i.e. complete IS).

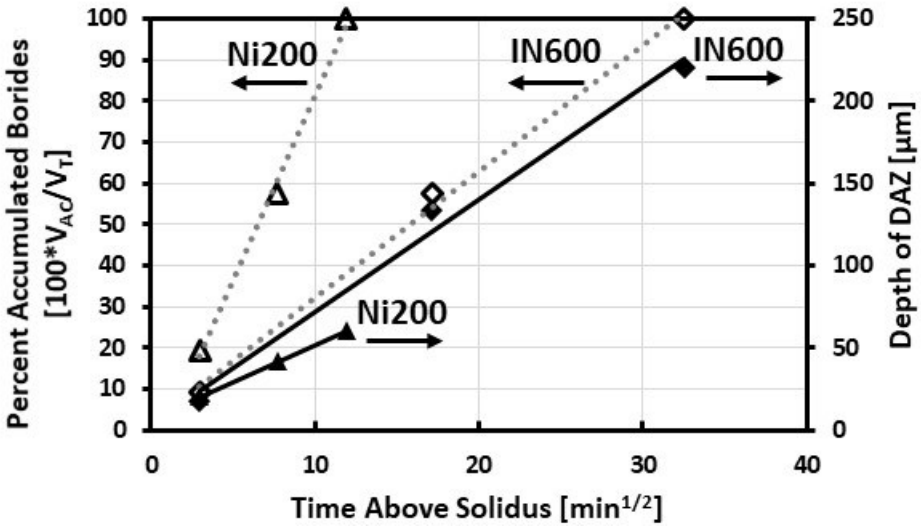

Figure 6-16 - Relationship between the volume % of borides and DAZ depth as a function of time above solidus ($min^{1/2}$) for Ni200/BNi-3 and IN600/BNi-3 couples.

The linearity of the curves further supports the fact that IS is controlled by a type of reactive diffusion and layer thickness growth of the borides, the thickness and/or volume being proportional to the square root of time. It is interesting to note that the rate of growth of the DAZ thickness is lower in the Ni200 case compared to the IN600. However, the higher volume fraction of borides in the Ni200 DAZ results in a significantly higher rate of B redistribution from the FM to the DAZ, resulting in thinner final DAZ layer and shorter IS time.

Given knowledge of the density, Boron content and experimentally measured volume fraction of the borides and γ-Ni, it is possible to predict the depth of DAZ based on the total quantity (volume) of Boron available using a volumetric balance. This predication is based on the mass balance equation previously derived in Chapter 4, as:

$$w_{DAZ} = \frac{w_{ISZ} C_o}{X_{DAZ} f_i \rho_i} \qquad \text{Eq. 6-9}$$

Where; w_{DAZ} is the predicted DAZ layer thickness, w_{ISZ} is the isothermally solidified layer thickness as a function of liquid duration time as determined from Eq. 6-7 and the DSC measurements, C_o is the volume concentration of B in the original filler metal (i.e. 0.252 g/cm^3 for BNi-3), X_{DAZ} is the average area fraction of borides within the DAZ, f_i is the weight fraction of boron in the particular boride (e.g. CrB, Ni_3B or more generally M_xB_y) and ρ_i is the density of the boride.

Eq. 6-9 demonstrates that the relationship between the DAZ thickness and the ISZ thickness is dependent on the type of boride formed. For the cases of Ni_3B (f_i = 6.03 wt% B, ρ_i = 8.07 g/cm^3) and CrB (f_i = 24.7 wt% B, and ρ_i = 6.25 g/cm^3) [53], Eq. 6-9 simplifies to $2w_{DAZ} = 0.52w_{ISZ}/X_{DAZ}$ and $0.16w_{ISZ}/X_{DAZ}$, respectively. Figure 6-17 plots the relationship between the DAZ depth and the volume fraction of borides for the case of complete IS were w_{ISZ} was taken to be the full w_o or 75 μm. At the extreme, assuming the DAZ was 100% boride (X_{DAZ} = 1) or a continuous boride layer, the DAZ layer necessary to 'consume' all the B from the FM would only be 17.2 μm for the IN600 (CrB) case and 39.8 μm for the Ni200 (Ni_3B) case. The curves show that a lower boride fraction in the DAZ requires a thicker DAZ layer to be developed.

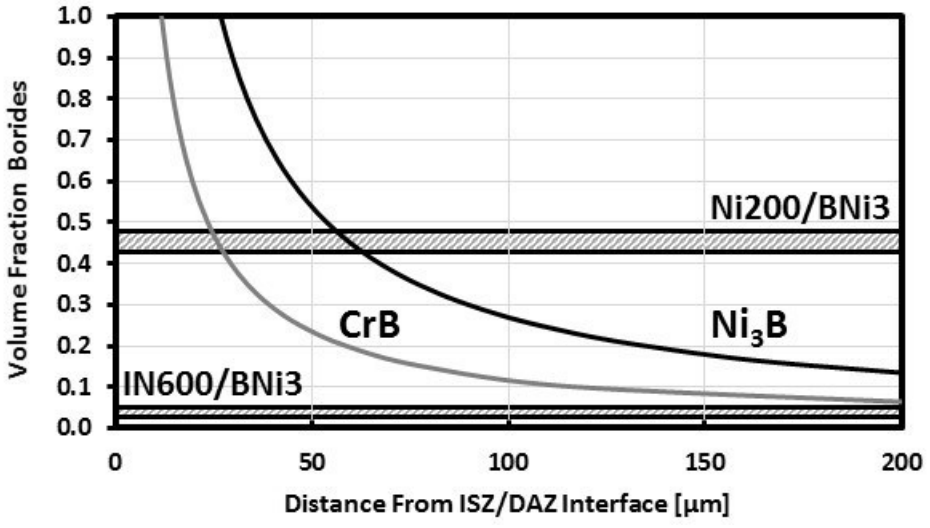

Figure 6-17 - Calculated relationship between the volume fraction and DAZ depth for Ni_3B and CrB borides. Overlays denote range of arithmetic means calculated for Ni200/BNi-3 and IN600/BNi-3 couples.

The arithmetic mean for the area fraction of borides, X_{DAZ}, obtained from the profiles displayed in Figure 6-15 are included in Figure 6-17 as a range for both Ni200 and IN600. The intersection of these values with the curve predicts a DAZ depth of approx. 60 μm for Ni_3B (Ni200/BNi-3) which is in excellent agreement with microstructural observations. Comparatively, given the low volume fraction displayed by IN600, the predicted depth is between 250 and 200 μm as the curve associated with CrB gradually approaches the arithmetic mean for IN600. This is also in good agreement with the measured DAZ thickness of the IN600/BNi-3 braze couple. These results show that as the volume fraction of a given boride phase decreases the DAZ depth eventually approaches an infinite thickness, thereby necessitating extensive DAZ depths which would significantly reduce the rate of IS due to the longer diffusion distances required. Since the volumetric distribution of the borides is governed by the system (BM/FM) and temperature, the results further support the notion that certain TLPB couples may be more amenable for TLPB. It should be noted however that it may be possible to increase the apparent volume fraction through proper selection of BM and FM such that the formation of the boride(s) is assisted. For instance, in the case of IN600, the use of a FM with greater quantities of Cr may minimize solute depletion in the DAZ thereby favoring more extensive precipitation of CrB.

To summarize, the kinetics of TLPB involving precipitation of borides is governed by both the type (M_xB) and distribution (vol. %) of the precipitated boride(s). The type of boride being determined by equilibrium thermodynamics while the maximum permissible volume fraction being highly material dependent. For instance, in Ni200 the lack of chromium favors the formation of Ni_3B precipitating as a coarse network of Ni_3B at very high-volume fraction, thereby displaying the most rapid rates of TLPB. Comparatively, the elevated levels of Cr present in IN600 and most superalloys favor the formation of Cr-rich borides i.e. CrB, which despite containing more Boron are distributed scarcely within the DAZ (< 5 vol. %). Since the surface area of the faying surface remains constant, Boron must penetrate to greater depths in order to continue diffusional solidification.

The boride distribution results provide an additional tool in explaining the considerable difference observed in terms of the kinetics and TLPB behavior for the current systems. Furthermore, the volumetric boride concentration can provide a wealth of information regarding the initial heating/melting stage and initial boron uptake phenomenon since the Ni_3B and CrB form

in-situ immediately upon exceeding the solidus temperature. The Cr-depletion observed in the γ-Ni within the DAZ for IN600/BNi-3 (Figure 6-7) directly correlates to the experimentally determined DAZ depths. Both couples also displayed similar initial boron depths slightly below 20 μm.

6.4 Conclusions

The primary purpose of the present study was to investigate the correlation between the kinetics of TLPB and microstructural evolution particularly with regards to mass transport and precipitation of Boron as borides. The following summarizes the principal findings acquired through the detailed examination:

1. A method of correcting for the degree of BM dissolution and the resulting increase in the quantity of liquid phase was developed based on changes in the solute concentrations of the BM and liquid (ASZ).
2. The considerable difference in the solidification rate of the two alloys is directly linked to the concentrations of boride formers e.g. Ni for Ni_3B (Ni200) and Cr for CrB (IN600), such that a lack thereof will cause an appreciable reduction in the rate of IS.
3. The growth rate of the DAZ layer (W_{DAZ}) was demonstrated to be proportional to that of the ISZ (W_{ISZ}) thereby further supporting the dependence of boride precipitation on the rate of IS. The rate of which is governed by the nature (density, boron content, volume fraction) of the borides formed in accordance with mass conservation.
4. Examination based on the volume fraction and mass conservation proved effective in quantifying TLPB particularly in the initial stages and provide insight into how the compatibility of BM and FM play a significant role in optimizing TLPB.

CHAPTER 7 Assessing Base Metal - Filler Metal Compatibility during TLPB of Ni-based Superalloys with Boron Brazing Alloys

E.D. Moreau, S. F. Corbin

Department of Mechanical Engineering, Dalhousie University,
1360 Barrington Street, P.O. Box 15,000, Halifax, Nova Scotia, B3H 4R2, Canada

Abstract

The influence two boron-containing filler metals (FM), BNi-2 and BNi-3 have on the TLPB behaviour Nickel-based superalloy IN718 was assessed in detail in terms of solute transport mechanisms, kinetics and microstructural evolution. This was accomplished using DSC analysis in addition to detailed SEM-EDS microstructural and image analysis. The results indicate that for similar degrees of brazing beyond the FM liquidus temperature, BNi-3, which displayed the greatest compositional difference from the IN718 displayed a significant aggravated BM dissolution and gap widening. This led to higher complete isothermal solidification times, despite a higher rate of isothermal solidification (IS) using BNi-3. EDS and quantitative image analysis performed within the DAZ concluded that differences observed in the rate of IS were related to the amount and type of borides forming in the DAZ. The lack of Cr in the BNi-3 favoured the formation of Cr-poor:B rich Cr(Mo,Nb)B borides, leading to the highest rate of B uptake by the base metal. Joints made from the Cr containing BNi-2 FM displayed a combination of Cr rich:B poor CrB and Cr(Mo,Nb)B borides leading to lower rates of B uptake.

7.1 Introduction

Transient Liquid Phase Bonding (TLPB) is a joining method which relies on the diffusion of atomic species between a liquid and solid enabling joining via diffusion induced isothermal solidification (IS) [9, 83]. It provides a means of joining advanced components used in a wide assortment of demanding applications ranging from dissimilar metals, ceramics, and more often nickel based superalloys. Usually Ni-superalloys are joined using low melting Ni based filler metals (FM) containing Boron in addition to other elements which act as potent melting point depressants, enabling joining at relatively low temperatures [14-15]. Although Boron-containing FMs display an excellent combination of wetting, spreading, cost and self-fluxing properties in comparison to the considerably more costly Au and Pd FMs, they tend to form intermetallic borides along the joint which can greatly deteriorate mechanical performance [17-18, 29, 84-100, 107,108]. This has generated the incentive to develop means of eliminating such phases either through post processing or manipulation of the FMs [92,59,60,61,62,93].

TLPB involves four stages: (1) heating/melting, (2) base metal dissolution (BMD), (3) isothermal solidification and (4) homogenization [9]. In the first stage, a joint is heated to the brazing temperature, and in the process eventually melts; enabling wetting and spreading along the base metal (BM). The following stage (2), BMD is essentially the chemical equilibration between the liquid phase (e.g. FM) and the BM which may occur concomitantly between the FM solidus temperature and once the peak hold temperature is achieved, depending on the heating rate. The subsequent IS stage (3) involves diffusion of the melting point depressants and solute atoms from the liquid phase to the BM leading to diffusion induced solidification. Lastly, an additional homogenization stage (4) is occasionally adopted to reduce any chemical gradients which may exist in the joint region, yielding a joint indistinguishable from the unaltered BM. Due to the relative simplicity of examining isothermal processes such as stages 3 and 4, both have been the focus of most of the studies related to assessing the TLPB response of a variety of couples [92]. Comparatively, the BMD process is a transient process which occurs during heating wherein equilibrium is continuously re-established as the temperature is increased making it inherently difficult to study empirically, analytically or numerically [36, 114].

Although it is well established that the nature of the BM has a marked influence on the TLPB behavior as demonstrated in the previous chapter, no systematic studies have been

performed which examine the influence FM composition has on the TLPB response and BMD in particular, even despite the growing number of FMs continuously developed. Examining such effects in any detail is inherently difficult as the melting range (solidus and liquidus) of FM's are governed by their composition, making TLPB comparisons at the same braze temperature difficult. Furthermore, differences in the FM liquidus and braze temperature could potentially aggravate BMD which can significantly alter both the composition and quantity of the resulting liquid phase.

The goal of this work was to directly compare the dissolution and isothermal solidification rate during TLPB of a IN718 brazed with two filler metals, BNi-2 and BNi-3. Both filler metals contain similar compositions of the MPD's of Si and B. The important filler metal alloy elements of Cr and Fe are present in BNi-2 but absent in BNi-3. Therefore, the study has the potential to isolate the influence that Cr and Fe, present in the filler metal, has on the TLPB behaviour of an important superalloy base metal.

7.2 Results and Discussions

7.2.1 Influence of FM Composition on BMD

The difficulty in distinguishing the difference FM composition has on the kinetics of TLPB relates to the interrelationship between FM chemistry and their melting characteristics. For instance, as revealed by DSC traces obtained for the BNi-2 and BNi-3 foils alone in Figure 7-1, the liquidus of BNi-2 is approx. 30°C lower than that of BNi-3 as a consequence of Cr and Fe additions. Thus, a greater degree of overheating, and therefore BMD would be expected for BNi-2 for any given temperature. A typical brazing temperature of 1050°C was adopted for BNi-2 while BNi-3 required brazing at 1075°C for a similar degree of overheating past the liquidus temperature (+10°C). In this manner the influence temperature has on BMD is comparable enabling one to observe the effects of differing FM composition. It should be noted however that the peak temperature may have an influence on the various component/phases present e.g. borides, grain size. Examination of the IN718/BNi-2 braze couple at 1075 °C was therefore also carried out.

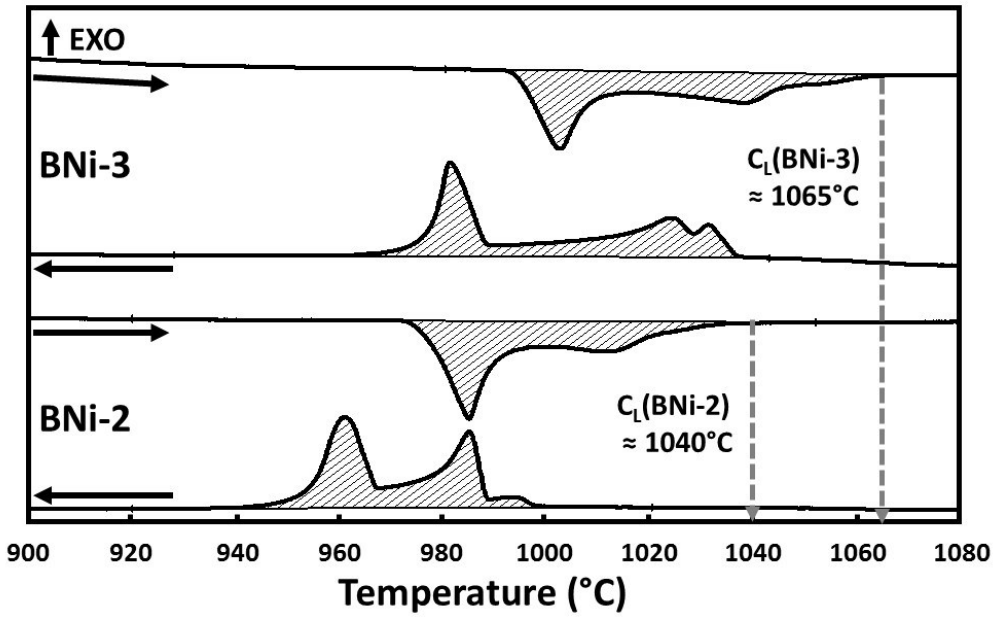

Figure 7-1 - DSC heating and cooling traces of BNi-2 and BNi-3 filler metals.

The general shape of the melting peaks displayed in Figure 7-1 is essentially identical for the two FMs, despite the presence of Fe and Cr in BNi-2, indicating a similar solidification sequence/mechanism for the two FMs. The presence of three (3) distinguishable thermal events indicates that both alloys possess a slightly off-eutectic composition. It is now well documented from both literature and the previous chapters that solidification for said FMs involves the sequential solidification of primary solid solution γ-Ni(Cr, Fe, Si), γ-Ni/Ni_3B binary eutectic, and either γ-Ni/Ni_3B/CrB or γ-Ni/Ni_3B/β-Ni_3Si ternary eutectics- the major difference being that the Cr concentrations in the BNi-2 is sufficient that an additional Cr-rich boride phase participates in the eutectic reactions (quaternary eutectic) [71].

The cyclic DSC traces of the IN718/BNi-2 and IN718/BNi-3 couples are shown below in Figure 7-2 and Figure 7-3, respectively. The heating traces are stacked such that the first cycle is at the bottom and further cycles stacked sequentially above. Cooling cycles are stacked such that the first cycle is at the top and subsequent cycles stack below. Both couples demonstrate a progressive decrease in the enthalpy of melting and/or solidification with each cycle such that a flat DSC trace with no thermal events visible is achieved well before the 19th cycle. This flat baseline indicates no melting or solidification and therefore complete IS. Comparatively, significant shifting of the initial sharp, low-melting point peak is apparent from the heating traces and is much more severe for IN718/BNi-3 e.g. 995 to 980°C as compared to 977 to 973°C for

IN718/BNi-2. The new melting peak behaviour becomes consistent with the 2nd and subsequent melting cycles. This behaviour is due to the dissolution of IN718 into the liquid phase. BMD results in the transfer of IN718 components (Cr, Fe, Nb, Mo, etc.) to migrate into the liquid phase modifying its composition and solidus temperature. Since in practice, some degree of overheating is required, BMD is inevitable. However, as the results show, the lack of Fe and Cr in the BNi-3 appears to result in greater melting point suppression given comparable overheat temperatures. The following broader peak also decreases in magnitude with each cycle but does not seem to display any significant shifting.

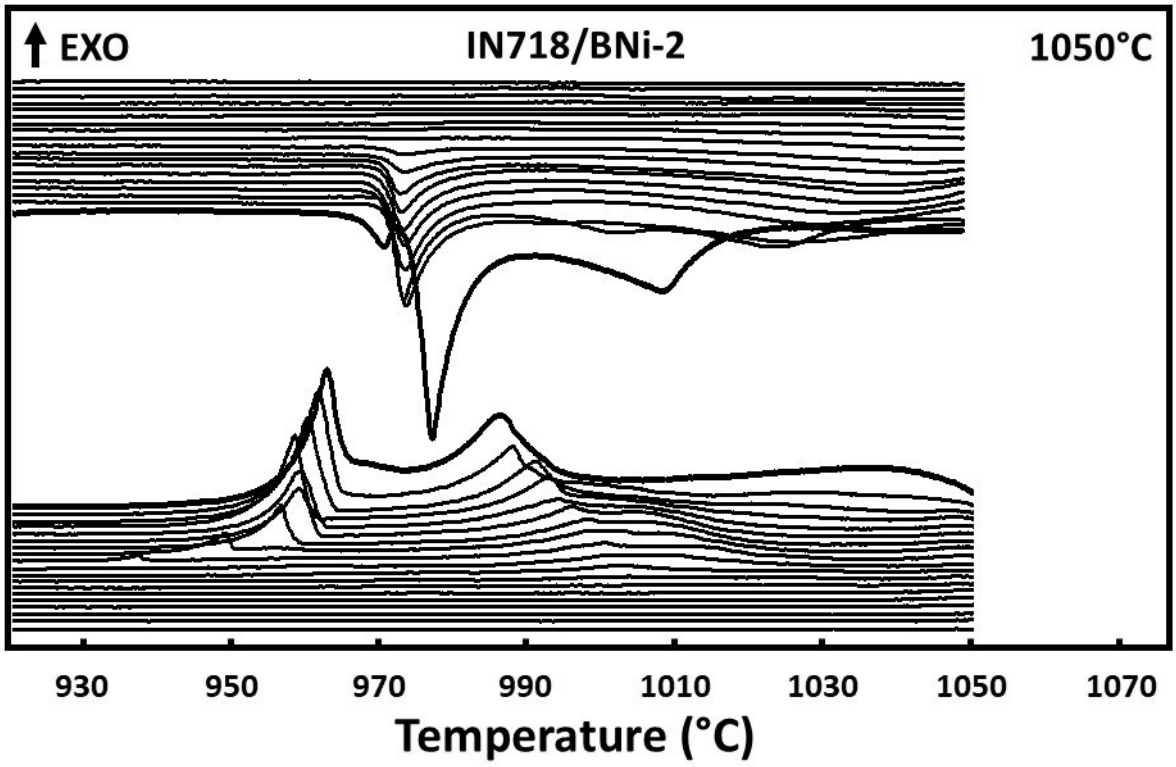

Figure 7-2 - Cyclic DSC heating (Top curves) and cooling (Bottom curves) traces obtained for IN718/BNi-2 couples at 1050°C.

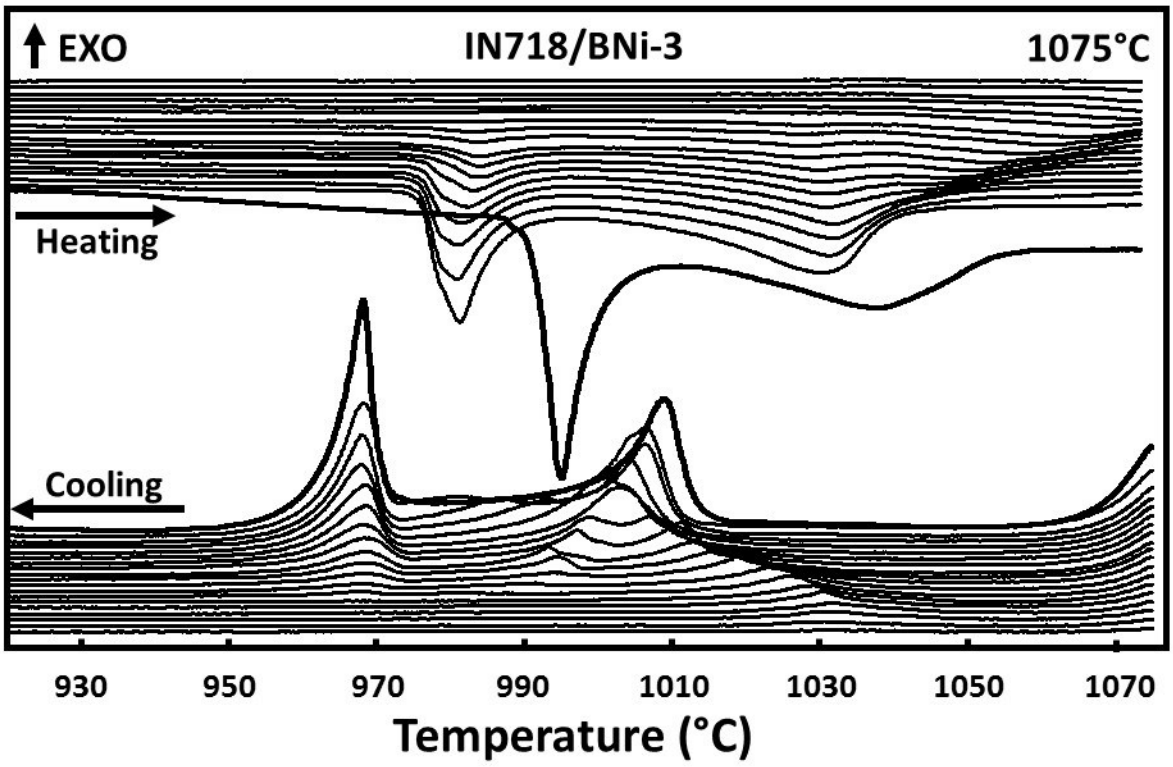

Figure 7-3 - Cyclic DSC heating and cooling traces obtained for IN718/BNi-3 couples at 1075°C.

Microstructural examination of the two couples was investigated to better understand the peak shifting observed for the two couples, both immediately upon attaining their respective peak temperatures and after being subject to 20 cycles, the results are shown below in Figure 7-4 and Figure 7-5. Quantifying the degree of BMD based on dimensional braze joint widening is most effectively achieved using the complete IS solidified microstructure (Figure 7-4B and Figure 7-5B) since it is easier to visually distinguish the isothermally solidified zone (ISZ)/diffusionally affected zone (DAZ) interface. Clearly, IN718/BNi-3 undergoes more dissolution, with an ISZ layer of approximately 70 μm, as compared to IN718/BNi-2 which, at approximately 50 μm displays less evidence of widening than the initial interlayer thickness of approx. 40 μm measured for the IN625/BNi-2 in Chapter 4 where BMD was negligible. This substantial dissolution in the case of BNi-3, further supporting the peak shifting observed for this couple. This dissolution process is more clearly documented in Figure 7-6 which presents the microstructure of a series of IN718/BNi-3 braze joints quenched from peak temperatures of 995, 1020, 1020, 1050 and 1075°C. Increased widening of the gap occurs as the filler metal undergoes progressively more melting. Interestingly, the formation of the DAZ layer as a result of B diffusion and precipitation into the

base metal (BM) occurs immediately upon melting at 995°C. Despite BM interface melt back due to dissolution, a DAZ layer is maintained in IN718. Therefore, diffusion of B into the BM occurs simultaneously during heating up to the braze temperature as documented by Ruiz-Vargas et al. examining Ni/BNi-2 couples [107]. Furthermore, comparing Figure 7-6 to the heating traces obtained for BNi-3 and IN718/BNi-3, as shown in Figure 7-1 and 2, respectively, reveals that the first notable increase in BMD which occurs between 1020 and 1050°C, likely corresponds to the second melting event (binary eutectic). Similarly, the subsequent increase in BMD from 1050 – 1075°C encompasses the third melting event corresponding to melting of primary γ-Ni.

Comparing Figure 7-4A and Figure 7-5A, reveals another interesting artifact of the IN718/BNi-3 couple, the epitaxial growth of primary γ (ISZ) for the quenched specimens which is not as clearly resolved for BNi-2 - rather a narrow band of ISZ appears to be occupied by needle like borides (Dark). Also, the DAZ formed in the quenched BNi-2 appears to be wider than that observed for BNi-3.

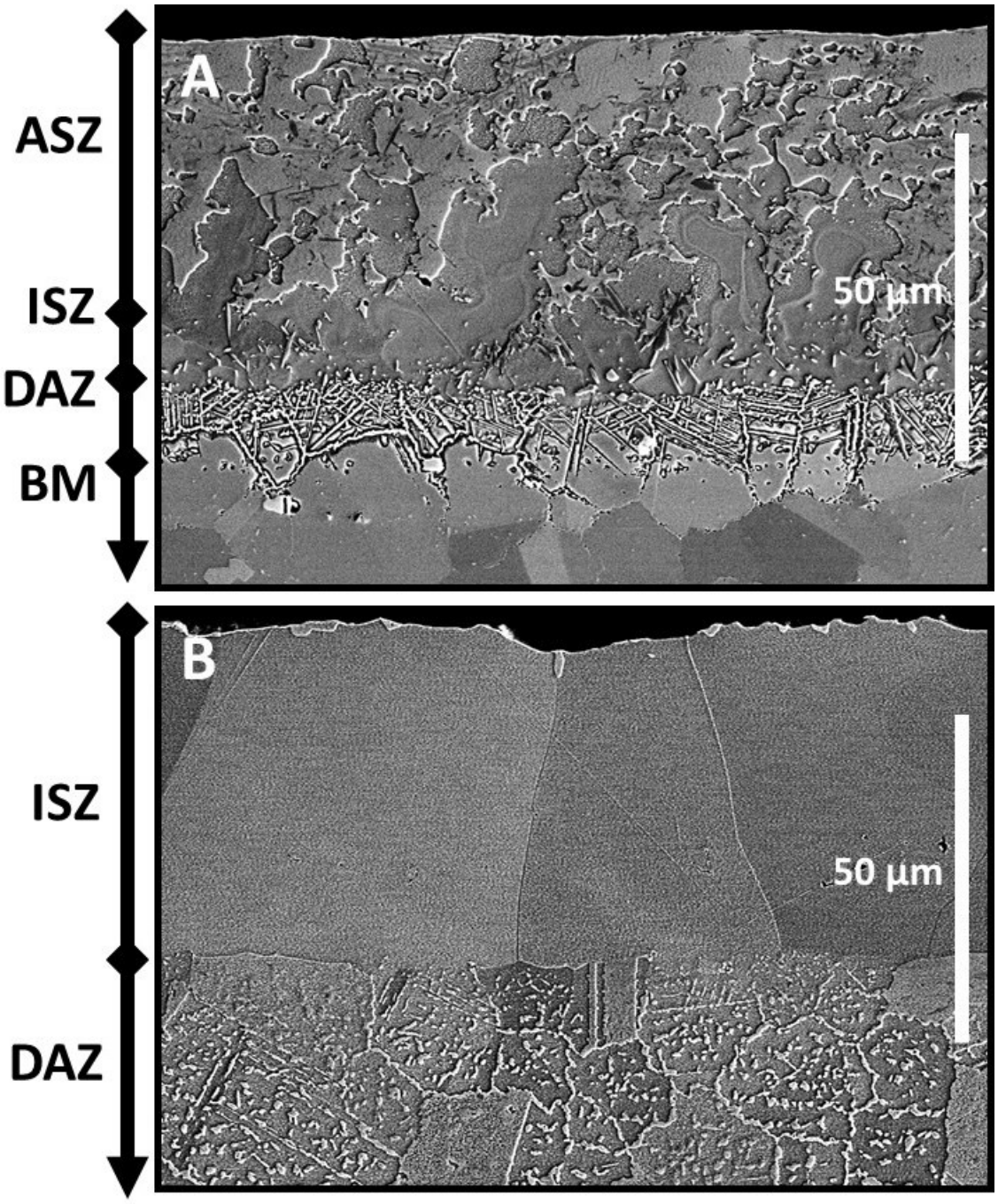

Figure 7-4 - SEM micrographs of IN718/BNi-2 couples; after immediate cooling from 1050°C (A) and after being subjected to 20 cycles at a peak temperature of 1050°C (B).

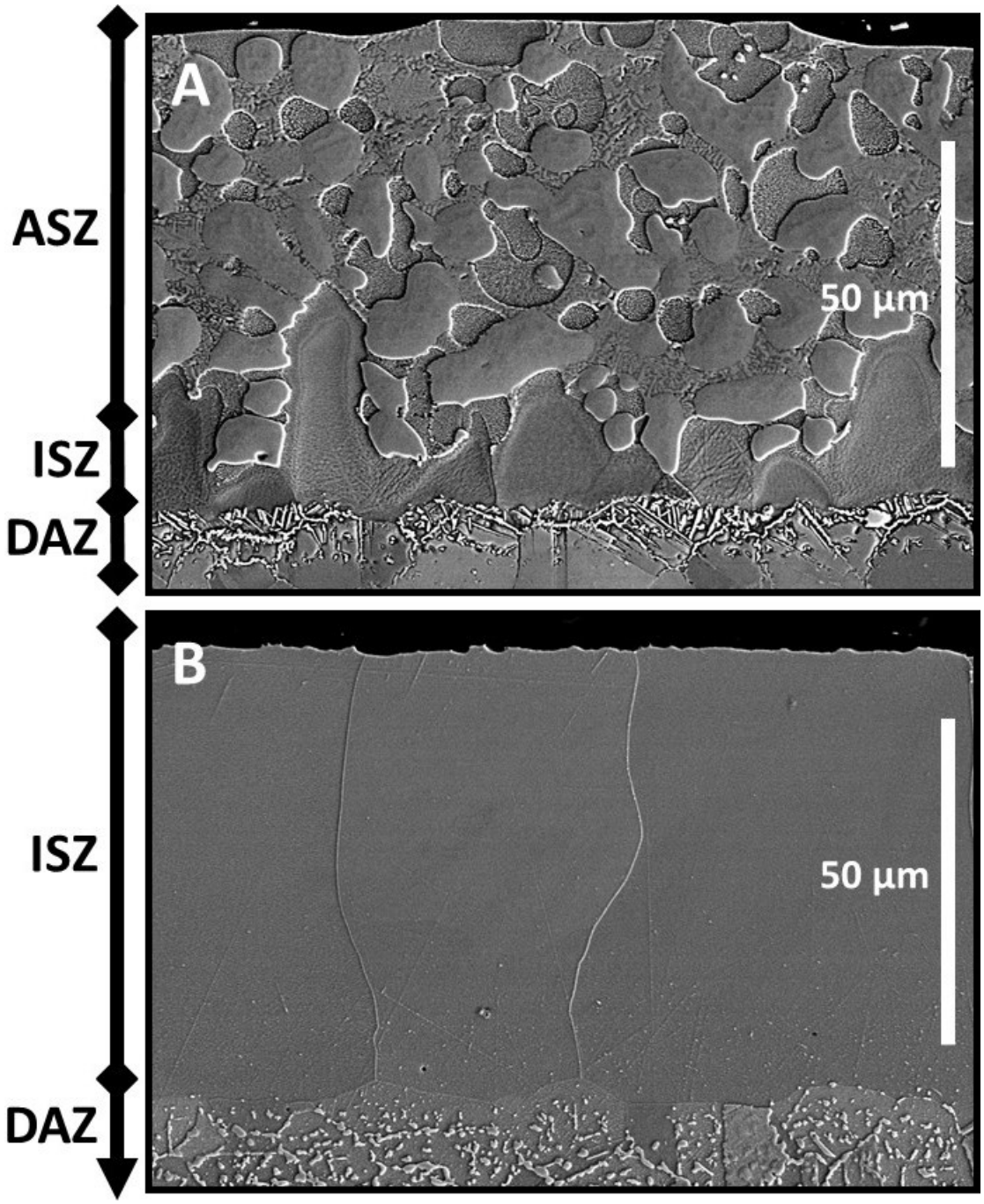

Figure 7-5 - SEM micrographs of IN718/BNi-3 couples; after immediate cooling from 1075°C (A) and after being subjected to 20 cycles at a peak temperature of 1075°C (B).

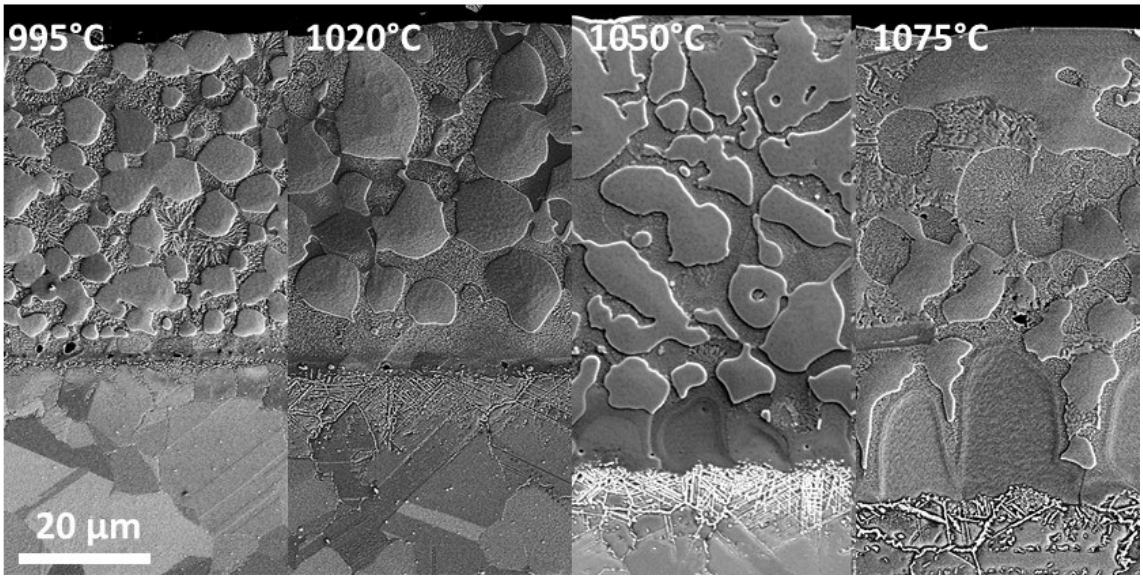

Figure 7-6 - SEM images illustrating evolution of BMD as a function of peak temperature. Microstructures obtained from quenched IN718/BNi-3 specimens (t = 0).

A measure of the "bulk" composition of the liquid phase was obtained using box scans of the ASZ region of the quenched specimens. The results are provided below in Table 7-1 along with the composition of the unaltered BNi-2, BNi-3 and IN718. For the IN718/BNi2 and /BNi-3 couples the liquid phase exhibits solute uptake of Cr, Fe, Mo and Nb. Although minor, the IN718/BNi-2 appears to be enriched with Nb and Mo, which is beneficial as it infers that the resulting ISZ contains the solute primarily responsible for the mechanical properties of IN718. The EDS measurements should be taken in a qualitative, relative manner due to the experimental error associated with such EDS measurement.

Table 7-1 - Bulk composition of the liquid phase as determined by EDS analysis.

Material(s)	Composition [at%]					
	Si	Cr	Fe	Ni	Nb	Mo
IN718/BNi-2	**7.56**	**8.23**	**4.06**	**79.23**	**0.61**	**0.3**
BNi-2	**8.7**	**6.74**	**3.31**	**81.13**	**0**	**0**
% f_{BM}	**14%**	**11%**	**5%**	**7%**	**19%**	**14%**
IN718/BNi-3	**8.39**	**1.89**	**1.85**	**87.47**	**0.36**	**0.04**
BNi-3	**9.71**	**0.04**	**0.29**	**89.96**	**0**	**0**
% f_{BM}	**14%**	**9%**	**14%**	**7%**	**11%**	**2%**

IN718 (BM)	**0.53**	**20.29**	**19.6**	**54.35**	**3.16**	**2.07**

The DAZ is easily distinguished by the widespread presence of both inter- and intra-granular borides beginning at the DAZ/ISZ interface, eventually diminishing at greater depths into the BM as illustrated in Figure 7-7. Upon closer inspection of the IN718/BNi-2 braze couple, the borides consist primarily of two types made distinguishable via BSE: a lighter globular-type and darker cuboidal-type. Extensive EDS analysis performed on the various borides confirmed that the darker phases were, as expected, lean in heavier elements e.g. Cr, Mo, Nb as compared to the far more prevalent irregular lighter phase (see Table 7-2). The IN718/BNi-3 braze couple only exhibited the lighter boride phase. Due to the inability to accurately measure boron using EDS, the measurements should only be interpreted in a semi-quantitative manner. Nonetheless, there is a definite distinction between the two principal borides found, based on their Cr, Mo and Nb contents. As mentioned in Chapter 4, Bai et al. [94] provides compelling evidence for the predominant formation of MB type borides in the DAZ, while MB_2, M_5B_3 and M_3B_2 were also detected, in the W free IN718 BM. Lastly, it also appears as though the lighter, globular phases which appear to preferentially partition to the grain boundaries are the dominant boride found, and the only type found at greater depths, as well documented in the work of Jamaloei et al. [108]. Thus, due to the lack of structural information in addition to the limitations of EDS analysis for accurate determination of Boron, the two principal borides detailed in Table 7-2 will be referred to as the Cr-rich boride (dark, cuboidal) and Cr(Mo, Nb)B (light, irregular).

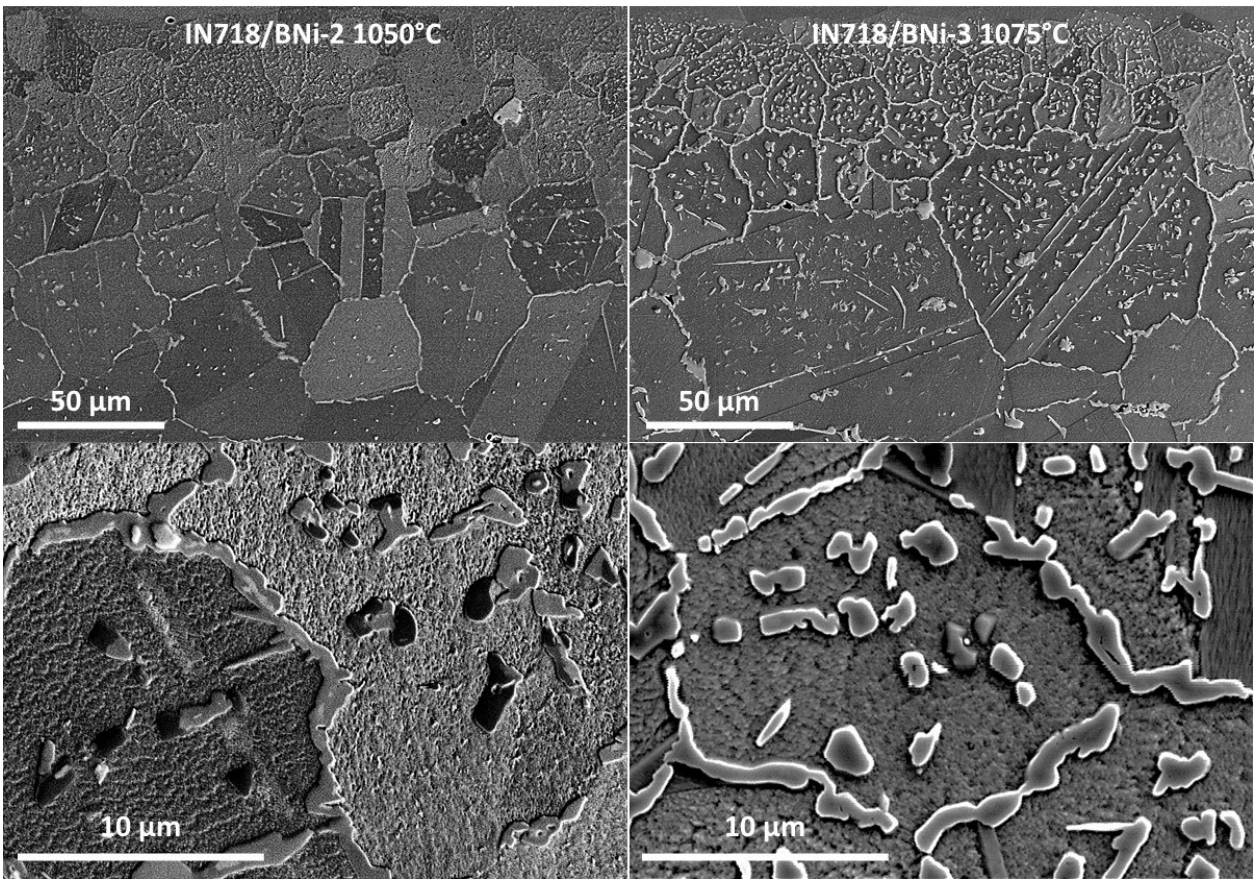

Figure 7-7 - Low (Top) and high (Bottom) magnification images of DAZ region of IN718/BNi-2 (1050°C, left) and IN718/BNi-3 (1075°C, right) couples.

Table 7-2 - Mean compositional results from EDS examination of boride phases (at%).

Base Metal		B	Cr	Fe	Ni	Nb	Mo
IN718	Dark	**56.9**	**37.3**	2.6	1.0	0.2	2.0
	Light	**68.1**	**18.5**	1.2	0.9	**7.3**	4.0

Additional DSC tests were performed to further characterize the boride phases in accordance with their onset temperatures and melting enthalpies. This involved heating of the IN718/FM couples to 1300°C (onset melting of IN718) either directly or after being subject to complete IS using 20 cycles at 1050°C (BNi-2) or 1075°C (BNi-3), the results are shown below in Figure 7-8. The DSC traces heated directly to 1300°C, (i.e. labelled 0C in the figure) indicates the melting of the BNi-2 or BNi-3 filler metal in the expected temperature range. No additional events are observed for either braze couple until approx. 1150°C, above which a subtle endothermic peak is observed for both couples. A large baseline drift, on setting around 1225°C is believed to be associated with incipient melting of the BM based on the reported melting range of

IN718 e.g. 1260-1336°C [SMC-045 Inconel Alloy 718, Special Metals Corporation (2007)]. This was confirmed by heating a sample of the IN718 without a FM foil up to 1300°C (see dashed trace) which exhibited this same baseline drift.

No melting is observed at the prior braze temperature after the couples are cycled for 20 cycles (traces labelled 20C) and then immediately reheated through to 1300°C, which further confirms complete IS was attained. This is consistent with diffusional solidification of the original FM liquid. It is apparent that the subtle peak present in the 0C condition between 1150°C and 1225°C increases in magnitude after complete IS. This further supports the understanding that IS of Boron-containing FMs involves the formation of a diffusionally affected zone. This DAZ layer, which consists of metal boride precipitates in a matrix of base metal elements exhibits a melting range which is lower that the BM melting range. The significantly thicker DAZ layer present in the 20C versus the quenched samples, evident by comparing Figures 6A and 7A with Figure 8, supports the increasing 1150 to 1225°C melting enthalpy. This data is significant as it demonstrates an upper limit for TLPB of IN718 using B-containing FMs e.g. < 1150°C. Once the DAZ melts there is no longer a 'sink' for B in the solid state. Therefore, the B remains indefinitely in the liquid, leading to a persistent liquid phase. This issue is clearly illustrated in the work of Shamsabadi et al [115] in their study of brazing IN738 and IN718. Complete IS of the joints was observed at brazing temperatures of 1050 and 1100°C. However, a "wavy" interface, no DAZ and the lack of IS was observed at a brazing temperature of 1150°C.

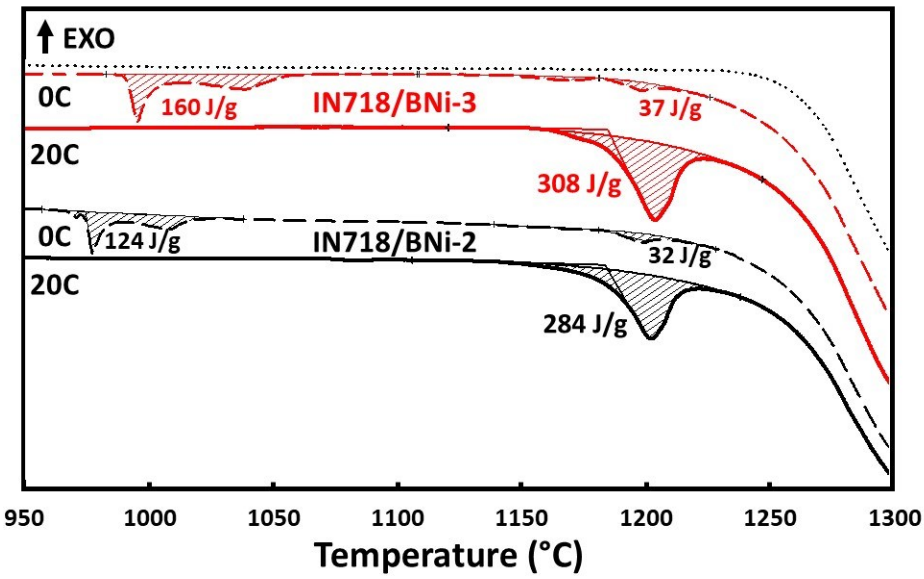

Figure 7-8 - DSC heating traces of IN718/BNi-2 and IN718/BNi-3 Couples heated to 1300°C directly (0C, dashed) and <u>after</u> cycling (20C, solid) at T_{MAX} = 1050 and 1075°C, respectively. Dotted line represents baseline results obtained for IN718 w/o FM.

An additional IN718/BNi-2 couple was subject to cyclic DSC heating at a peak temperature of 1075°C in order to further validate the influence that temperature/overheating has on the degree of BMD in comparison to the compositional effects, the results shown below in Figure 7-9. Comparing Figure 7-9 to Figure 7-2 it is evident that the +25°C increase in peak temperature yields only minor changes in the melting and solidification behaviour.

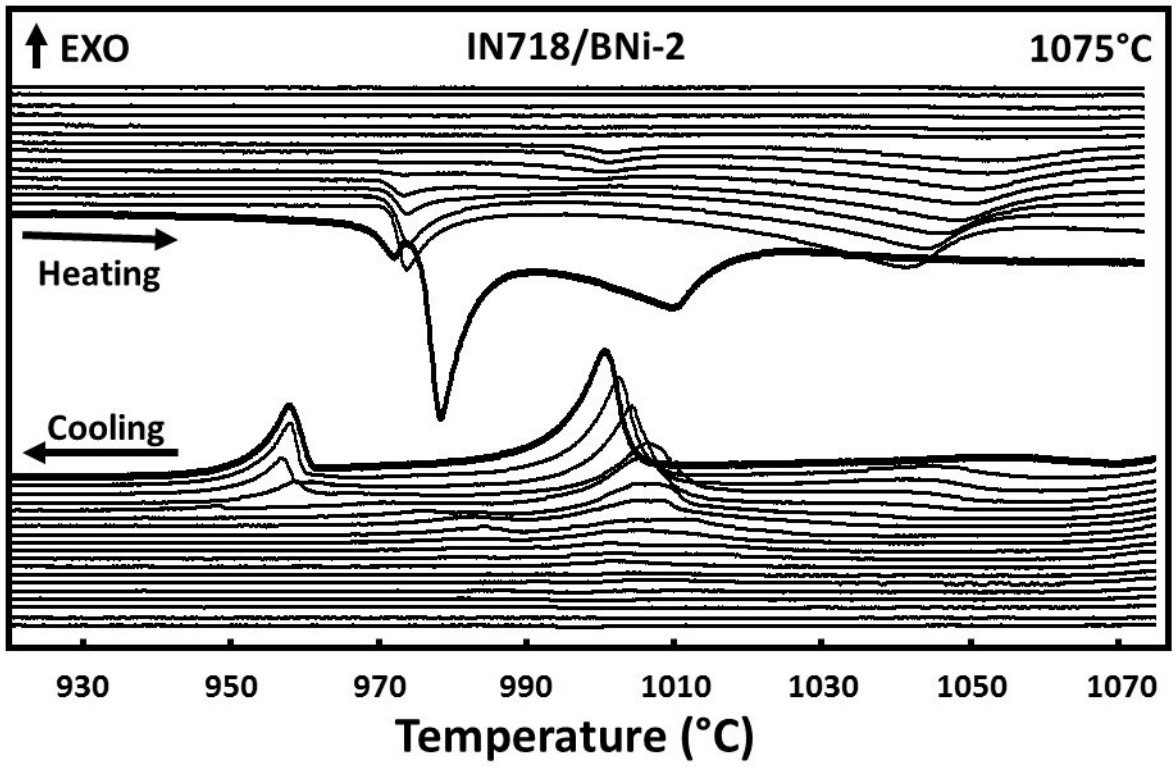

Figure 7-9 - DSC heating and cooling traces for IN718/BNi-2 after cyclic heating to a peak temperature of 1075°C.

The microstructures of the quenched and cycled IN718/BNi-2 1075°C couple are provided below in Figure 7-10. The microstructure of the 1050 and 1075°C cycled IN718/BNi-2 specimens are essentially identical with the exception of a slightly greater quantity of BMD observed at 1075°C as inferred by the thickness of the ISZ layer. Comparatively, the quenched microstructures (Figure 7-10A and Figure 7-4A) reveal that the additional +25°C resulted in a decrease in the overall volume fraction of interfacial borides, more distinguishable epitaxial growth of the ISZ layer and the presence of more coarse needle like Cr-rich borides (dark). These results confirm that increased overheating, and thus temperature is not solely responsible for the increased BMD observed for IN718/BNi-3 at 1075°C, which is further supported by the negligible shifting of the thermal events displayed in Figure 7-9.

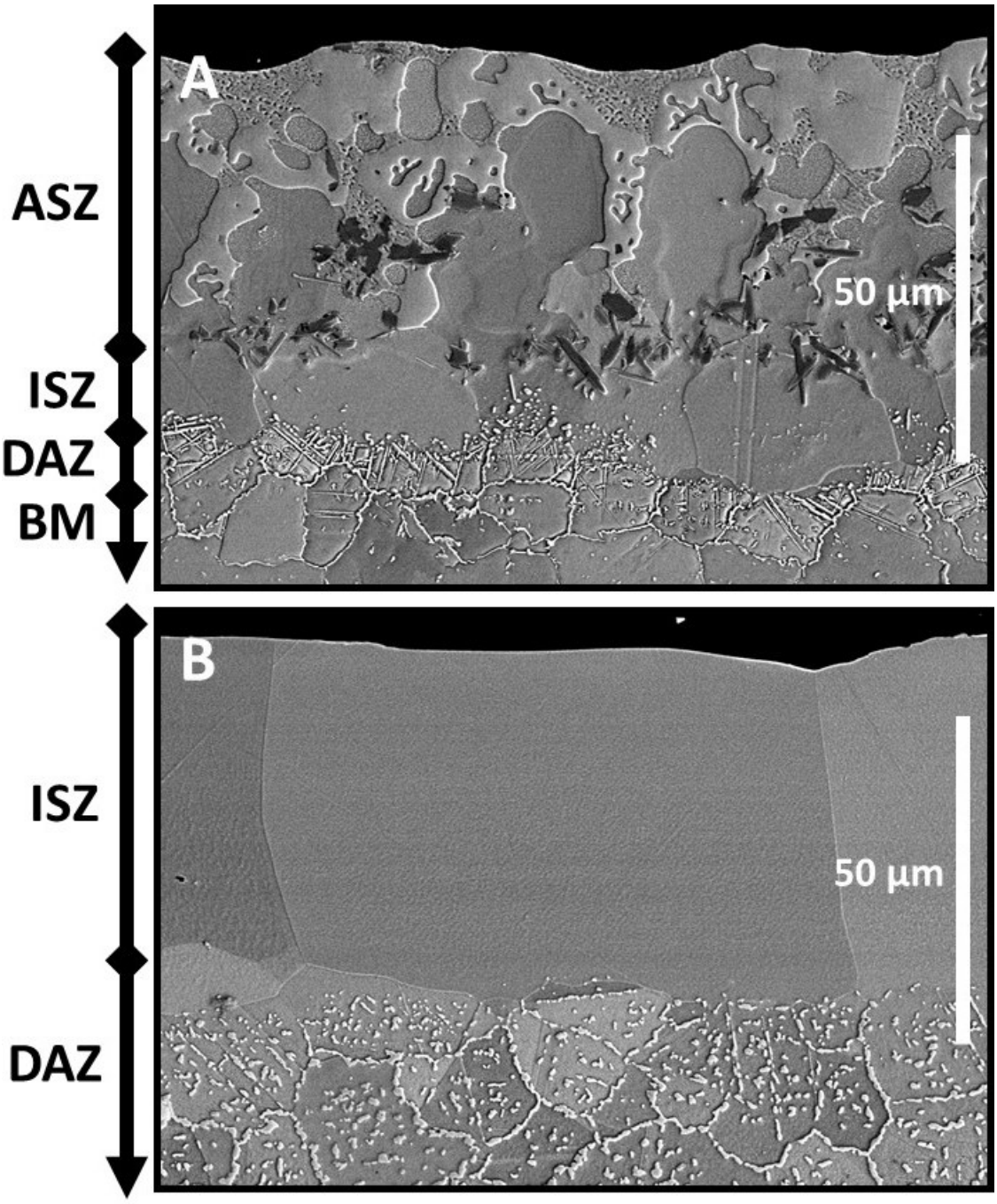

Figure 7-10 - SEM micrographs of IN718/BNi-2 couples; after immediate cooling from 1075°C (A) and after being subjected to 20 cycles at a peak temperature of 1075°C (B). Approx. liquid duration: 6-8 min (quenched) and 280 min (cycled).

EDS line scans were performed perpendicular to the faying surface of the cycled specimens within the γ-Ni matrix in order to monitor the compositional variance within the ISZ and DAZ as illustrated below in Figure 7-11. No marked difference was observed in term of the Si distribution

for the couples under investigation, despite evidence of BM dissolution for IN718/BNi-3. Thus, the Si profile was omitted from the current work for clarity and brevity. The Fe distribution reveals an appreciable counter diffusion of solute from the BM to the ISZ layer to the extent that the initially Fe-free BNi-3 is enriched to the concentration of the BNi-2 foil. Meanwhile, that of the ISZ layer of the IN718/BNi-2 specimens increased above the initial concentration of 2.6 at% to approx. 6 at% Fe. This is accounted for by a marked quantity of Fe depletion in the first 20 μm of the DAZ layer. Note that EDS analysis below the DAZ/ISZ interface used spot analysis of the 'matrix', avoiding the boride precipitates. Therefore, this lower Fe content on the matrix (or BM) is due to Fe diffusion into the ISZ since the Fe content of the boride particles was measured to be minute.

The compositional profiles of Cr, Mo and to a lesser extent Nb display different behavior. Specifically, their depletion within the matrix of the DAZ occurs over a longer distance, extending 60 μm below the DAZ/ISZ interface. This corresponds to the region of dense boride precipitates depicted in Figure 7-7. This is expected as it is well known that the borides formed within the DAZ are typically bound with boride formers such as Cr, Mo, W, etc. and as confirmed by the compositional analysis of Table 7-2 [92]. Depletion of Cr from the bulk composition of 18% down to below 12% near the DAZ/ISZ within the solid solution γ-Ni phase of the DAZ is most severe for IN718/BNi-2 at 1050°C followed by IN718/BNi-3 (1075°C) and IN718/BNi-2 at 1075°C. It is believed that a greater degree of Cr depletion within the DAZ results from a greater quantity of precipitation of the darker Cr-rich borides observed in the IN718/BNi-2 1050°C specimen. Interestingly, the significant Fe uptake into the ISZ layer displayed by IN718/BNi-3 does not occur to the same extent for the case of Cr. Lastly, significant depletion of Mo and Nb clearly transpired within the DAZ and consequently, limited diffusion in the ISZ. The lack of Nb in the ISZ was also reported by Pouranvari et al. [85]. The Nb and Mo depletion of the DAZ is most significant in the IN718/BNi-3, particularly at greater depths into the DAZ. This suggests that more of the lighter boride phase, which is richer in Mo and Nb, is forming in the BNi-3 couple.

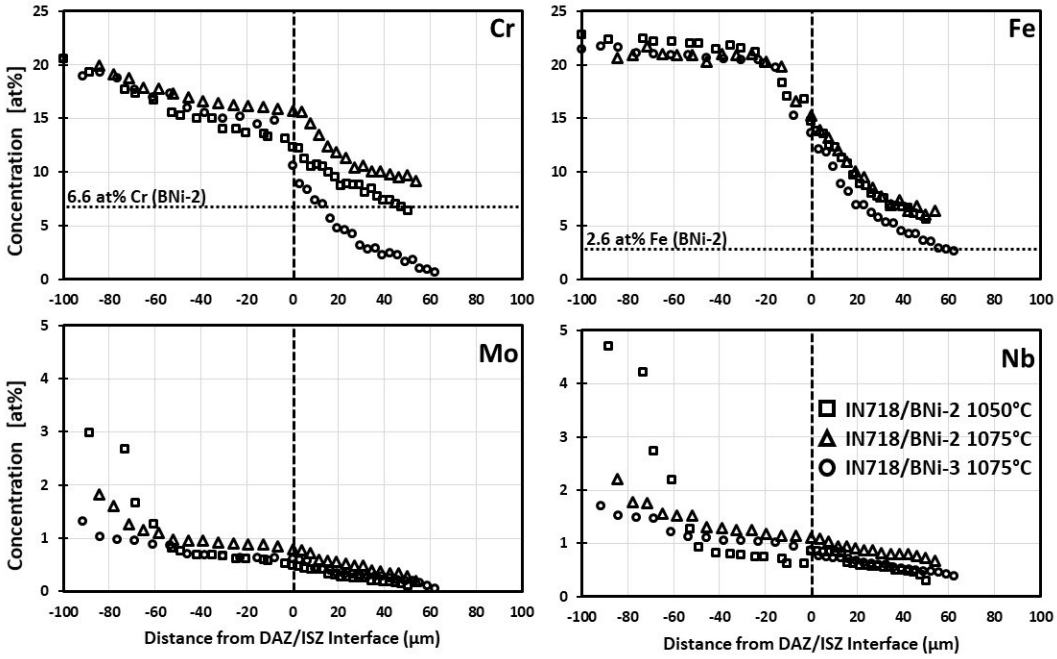

Figure 7-11 - SEM-EDS compositional profiles of all 20x cycled IN718/FM couples examined.

7.2.2 Determining the Influence of FM Composition on the Rate of IS

The cooling enthalpy values acquired from the cyclic DSC traces can be evaluated in a qualitative manner to observe the way they decrease as a function of the FM and temperature. This was accomplished by plotting the enthalpy values determined experimentally from the cooling peaks of Figure 7-9. The data is plotted versus the square root of time above solidus (see Figure 7-12). In earlier related work, J. Chapman [32] performed a detailed examination on the influence surface treatment had on the TLPB behaviour of IN718/BNi-2 couples at 1050°C. A subset of Chapman's work documented the TLPB kinetics of IN718/BNi-2 at 1050°C using identical specimen preparations methods as those used in the current thesis. The linear regression analysis obtained from numerous iterations of the work, which included enthalpy, liquid fraction and $2W_{ISZ}$ will be combined with the data acquired in the current work to enhance overall precision. Overall, the range of enthalpy measurements is similar for all three braze joints. Comparatively, both BNi-2 couples displayed similar TLPB responses despite the +25°C difference. There is some indication that the rate of enthalpy reduction is higher at the 1075°C.

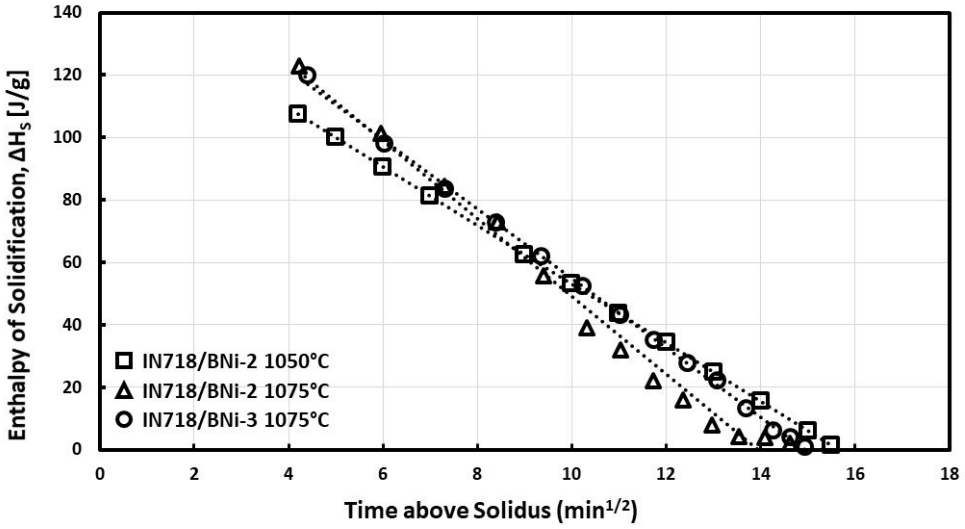

Figure 7-12 - Enthalpy of solidification value obtained from cyclic DSC results versus time above solidus for all IN718 couples under investigation. IN718/BNi-2 1050°C values include data from ref. [116].

In previous work a method was developed to correct for the increase in liquid phase associated with BMD [Chapter 6]. Using this method, it is possible to distinguish the differences in the TLPB behavior of different FM/BM couples. In the absence of dissolution, previous work used the enthalpy and mass of the starting filler metal to calculate liquid fraction remaining [78]. Dissolution requires some degree of widening and/or an increase in the mass of liquid phase. The liquid composition may also vary based on the degree of BMD as governed by thermodynamic equilibrium at a specified temperature. Given sufficient knowledge of the chemical/solute distribution before and after BM dissolution it is possible to account and correct for such changes using the following formulae as reported in Chapter 6]:

$$L_f = \frac{D_{mf} * B_C * \Delta H_m}{\Delta H_f} \qquad \text{Eq. 7-1}$$

Where; ΔH_m is the DSC measured enthalpy of solidification {J/g} (Figure 7-12), B_C a correction factor which accounts for the thermal/signal dampening which occurs due to the presence of BM, as opposed to the FM alone. This correction is arrived at by measuring the enthalpy of the FM alone, ΔH_o {J/g} (Figure 7-1) and when in the presence of the coated BM//FM couple, ΔH_{BM} {J/g} using the method described in Figure 3-1B. Thus, $B_C = \Delta H_o/\Delta H_{BM}$. For the IN718/BNi-2 and IN718/BNi-3 systems ΔH_o was measured as 240 and 266 J/g and ΔH_{BM} was measured as 206 and 255 J/g, leading to B_c values of 1.16 and 1.04 respectively. ΔH_f is the enthalpy {J/g} of the braze

ball created given the composition and degree of dilution observed for the quenched BM/FM couple, using the method described in Figure 3-1C. Lastly, D_{mf} is a mass correction factor which considers the increase in mass of the liquid phase resulting from BMD, determined by the change in composition of the liquid phase.

Experimentally, D_{mf} was determined by first measuring the bulk (overall) composition of the ASZ region for the zero hold (quenched) samples already discussed in Table 7-1. The percentage values shown in Table 7-1 are indicative of the % of BM (by weight) required to dissolve into the liquid and account for the resulting change in composition of the liquid phase from that of the original FM. For instance, for IN718/BNi-2 at 1050°C, the extent of BM dissolution is such that Cr and Fe contents in the initially Cr- and Fe- free BNi-3 increase to 2.36 and 1.50, respectively. Inputting the compositional measurements into the following simple mass balance equation enables determination of the mass fraction of BM dissolved into the liquid joint region due to dissolution, $\mathbf{f_{BM}}$;

$$\boldsymbol{X_i = X_{BM} \cdot f_{BM} + X_{FM} \cdot (1 - f_{BM})} \quad \textit{or} \quad \boldsymbol{f_{BM} = \frac{(X_i - X_{FM})}{(X_{BM} - X_{FM})}} \qquad \textbf{Eq. 7-2}$$

Where, X_i is the wt% of a chosen element (e.g. Cr) measured in the quenched ISZ/ASZ, while X_{BM} and X_{FM} are the wt% of the chosen element measured in the BM and FM only, respectively. Table 7-1 provides the relevant wt% values used in Eq. 7-2 as well as the calculated f_{BM} values, expressed as a percentage. Boron was omitted from such analysis due to its segregation as intermetallics and difficulties regarding quantitative EDS measurements of light elements. These values permit the calculation of the mass correction factor, $D_{mf} = (1\text{-}f_{BM})$, which allows the creation of an additional braze ball with a composition predicted by D_{mf}, thus providing the actual enthalpy value, ΔH_f corresponding to the simulated composition of the liquid phase resulting from BM dissolution. Braze balls with 19.5 and 19.7 wt% IN718 were created to represent the diluted liquid phase for the IN718/BNi-2 1050°C, IN718/BNi-2 1075°C, and IN718/BNi-3 1075°C braze couples, respectively. The braze balls were processed as described in method C of Figure 3-1 and the ΔH_f determined to be 243 and 239 J/g for the IN718/BNi-2 1075°C, and IN718/BNi-3 1075°C, respectively. These results show that the dilution of IN718 into the BNi-2 has little influence over the original FM enthalpy, while enthalpy is lowered by approximately 10% in the BNi-3 case. This agrees with the larger change in melting range observed in the BNi-3 braze couple and the more

significant change in composition, going from an Cr and Fe free composition to one containing these elements.

Applying the correction described in Eq. 7-1 to the raw ΔH_m values plotted in Figure 7-12 enables plotting of the BM dissolution corrected liquid fraction remaining, L_f data versus time ($min^{1/2}$) above solidus as shown in Figure 7-13. As the data is highly linear it is possible to quantify the solidification rate or depletion of the fraction of liquid phase in accordance with q. 7-1:

$$L_f = -k_L\sqrt{t} + L_o \qquad \textbf{Eq. 7-3}$$

Where, L_f is the corresponding liquid fraction remaining at time t, $-k_L$ the isothermal solidification rate constant $\{min^{-1/2}\}$, and L_o the initial liquid fraction present at t = 0. The data reveals that the rate of solidification, K_L is highest in the couples brazed at 1075 °C, resulting in slightly shorter IS completion times. This response is expected since mass transport of B into the BM should increase with increasing temperature.

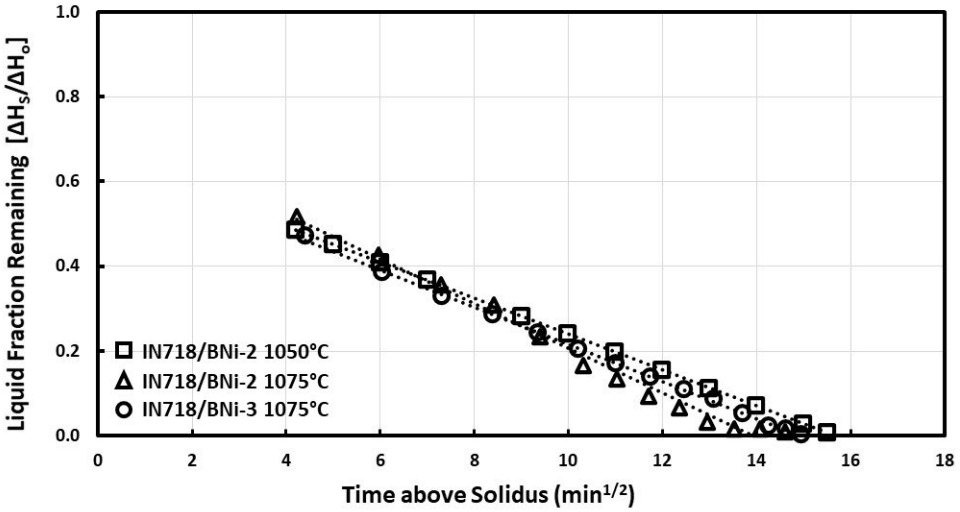

Figure 7-13 - Liquid fraction remaining versus time above solidus for all IN718 couples under investigation. IN718/BNi-2 1050°C values include data from ref. [116].

As outlined in Chapter 4, L_f measurements from the DSC can be converted to the width of liquid phase remaining in the gap, W_t (μm) and the corresponding extent of IS, W_{ISZ} (μm) provided

that the thickness of the braze gap, W_o is known. On a full joint basis this yields the following expressions for the liquid width remaining ($2W_t$) and ISZ width ($2W_{ISZ}$) of;

$$2w_t = \frac{\Delta H_t}{\Delta H_o} 2W_o = L_f 2W_o \quad \text{Eq. 7-4}$$

$$2W_{ISZ} = k_w t^{1/2} + 2W_{ISZo} \quad \text{Eq. 7-5}$$

For each sample, a value of $2W_o$ (the full gap width) was obtained from multiple measurement of ISZ thickness made on post-braze polished cross-sections of the cycled DSC samples as shown in Table 7-3. Using the $2W_o$ measurements, the liquid fraction data of Figure 7-13 was replotted as liquid width remaining, $2W_t$ and width of the ISZ, $2W_{ISZ}$ which is analogous to the *maximum brazing clearance*, $2W_{MBC}$. These are displayed in Figure 7-14 and Figure 7-15, respectively. Figure 7-14 demonstrates that all three joints have similar starting liquid widths at the peak braze temperature. Therefore, in the current case the different rates of IS observed for the three samples governs the IS completion time.

Table 7-3 - Linear regression parameters and mean measured width values obtained for the full joint region and ISZ obtained from quenched and cycled specimens. IN718/BNi-2 data includes data from ref. [116].

	Linear Regression Results						Measured
FM	T (°C)	t_f (min)	$-k_L$ ($min^{-1/2}$)	L_o (%)	K_W ($\mu m/min^{1/2}$)	$2W_{ISZo}$ (µm)	$2W_o$ (µm)
BNi-2	1050	245	0.04	66	4.8	38	100±6*
BNi-2	1075	195	0.05	73	5.7	29	108±14
BNi-3	1075	222	0.04	66	5.7	45	124±10

***With regards to the data obtained from ref. [32], as the FM spread less than in the current study such that $2W_o$ = 114 µm. This was accounted for in the generation of the MBC curve and data of Table 7-3 (above). The value of 100 µm is included for comparison which was measured for IN718/BNi-2 1050°C (current work) wherein spreading was in excess of 96% over the faying surface.**

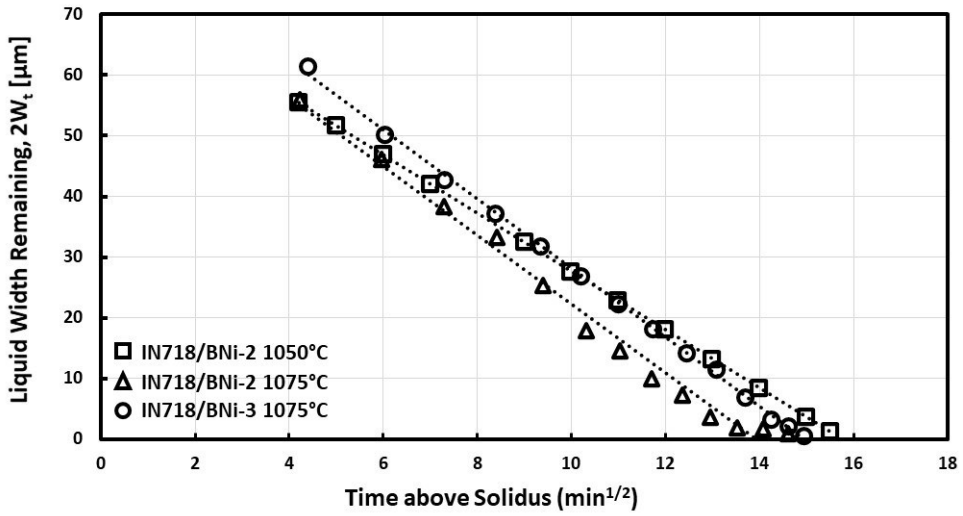

Figure 7-14 - Liquid width remaining, $2W_t$ versus time above solidus for all IN718 couples under investigation. IN718/BNi-2 1050°C values include data from ref. [116].

The W_t curves of Figure 7-14 emphasize the influence of different levels of BMD for the braze couples. The higher dissolution in the IN718/BNi-3, results in higher initial liquid widths and is the primary reason for the longer isothermal solidification time for this couple. The rate of liquid removal appears slightly higher in the IN718/BNi-3 couple. This is more clearly seen in the $2W_{ISZ}$ curves of Figure 7-15. The advantage of the $2W_{ISZ}$ curve is that the Y-intercept and slope of the curve (i.e. the rate of IS) is independent of the starting gap size $2W_o$. Therefore, the TLPB behaviour of the couples can be more directly compared even though differences in BMD produced different $2W_o$ values. The level of IBU is highest for the IN718/BNi-3 sample and lowest for the IN718/BNi-2 1075°C sample. The rate of IS in the joints brazed at 1075°C is similar although slightly higher for the BNi-2 joint. The MBC curves for the IN718/BNi-2 brazed at 1050°C and 1075°C overlap for much of the braze time plotted. This is due to the counterbalancing contributions of a low IBU but higher IS rate in the 1075 °C and the higher IBU but lower IS rate in the 1050°C case. Consistent with the current results, Pouranvari et al. also demonstrated that IN718/BNi-3 required longer times to attain complete IS, as compared to IN718/BNi-2 when brazing was carried out at 1100°C. However, only the solidification time was quoted, so that the relative contribution of IBU and rate of IS to this solidification time was not possible to determine [85].

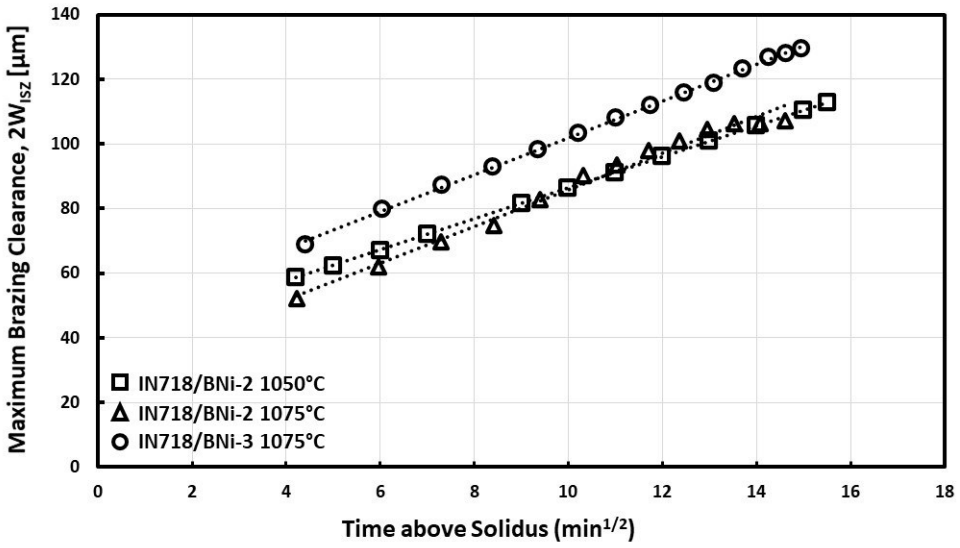

Figure 7-15 - Maximum brazing clearance, $2W_{ISZ}$ versus time above solidus for all IN718 couples under investigation. IN718/BNi-2 1050°C values include data from ref. [116].

To further examine the TLPB behaviour of the braze couples, detailed image analysis was applied to all specimens to determine the volume fraction of borides as a function of depth into the DAZ. This involved measuring the total area fraction occupied by borides for an area 127 µm wide by increments of 2 µm and/or 1 µm of depth into the DAZ for the cycled and quenched specimens, respectively. In other words, each measurement involved measuring the volume fraction occupied by the borides in a 254 µm^2 area (cycled specimens); subsequent measurement made in increments of 2 µm (cycled) or 1 µm (quenched) into the DAZ (away from the ISZ/DAZ interface). The results from the image analysis are displayed in Figure 7-16. Referring to the quenched (0 cycle) samples, the overall volume fraction of borides for the IN718/BNi-2 at 1050°C is the highest. This is consistent with the images of the quenched samples presented in Figure 7-4A, Figure 7-5A and Figure 7-7A, where the DAZ is more developed in the 1050°C sample. This lower braze temperature results in less melt back of the BM, which likely preserves the DAZ layer to a greater extent.

With regards to the 20-cycle samples, the higher boride volume fraction persists for the IN718/BNi-2 1050°C to a depth of 70 µm. At greater depths, the boride volume fraction is similar for all three joint types. Overall, the volume fraction of borides in the IN718/BNi-2 and BNi-3 couples brazed at 1075°C are close although slightly higher in the BNi-3 couple in the first 70 µm of the DAZ. As outlined in the previous chapters, it is expected that higher boride volume fractions

in the DAZ would lead to higher rates of IS. At first glance the results of Figure 7-16 don't appear to support this trend since the IN718/BNi-3 couple has the highest rate of IS (i.e. K_w = 6.12 μm/min$^{1/2}$) and the IN718/BNi-2 couples at 1050°C and 1075°C have lower but comparable rates (K_w = 4.12 and 3.94 μm/min$^{1/2}$, respectively).

This apparent discrepancy can be understood with reference to the factors that contribute to B re-distribution from the liquid phase into the base metal DAZ as detailed in previous chapters. It was shown that the total mass of boron in the DAZ was related to the volumetric distribution using the following relationship:

$$\boldsymbol{m_{BDAZ} = \sum_{i=1}^{n} V_{DAZ} X_{DAZ} f_i \rho_i} \qquad \textbf{Eq. 7-5}$$

Where, X_{DAZ} is the volume fraction of borides presents within the DAZ layer, V_{DAZ} the volume of the DAZ layer, f_i the boron content (% wt) of the boride, i and ρ_i the specific gravity {g/cm^3} of the precipitate (boride) phase, i. The relationship is based on the fundamental mass balance of Boron and emphasizes that although the final distribution of borides (V_{DAZ} and X_{DAZ}) plays a significant role in predicting the extent of TLPB, in systems involving numerous borides, the influence of f_i and ρ_i also play a role in dictating the rate of B uptake by the base metal and rate of solidification.

For instance, although the chemical similarity between BNi-2 and IN718 and the lower braze temperature reduced the degree of BMD, the 1050°C braze condition favored the precipitation of an additional boride which has a lower B content f_i. For example, Figure 7-7 indicates a greater precipitation of the Cr-rich:B-poor borides within the first 60 to 70 μm of the DAZ for the 1050°C sample. According to Eq. 7-5 this could translate into a lower boron mass within the DAZ, and thus a lower rate of IS, despite the fact that the total volume fraction of borides is higher.

The EDS line scan results (Figure 7-11) further support this hypothesis wherein the IN718/BNi-2 specimen at 1050°C displays the highest Cr, Nb and Mo depletion at depths down to 70 μm. This supports the measurements of a higher overall boride volume fraction, while the greater Cr depletion supports the fact that a higher fraction of these borides are of the Cr-rich:B-poor type.

The IN718/BNi-2 1075°C exhibits the lowest boride volume fraction according to Figure 7-16. Consistent with this, it also exhibits the lowest level of Cr, Nb and Mo depletion within the DAZ matrix. However, it has a rate of IS that is the highest, although close to that observed for the IN718/BNi-3 1075°C sample. Interestingly, Figure 7-11 suggests that this sample displayed the least amount of Cr depletion in the DAZ matrix, indicating that, while the boride volume fraction is lower, a higher fraction of these borides are Cr-poor:B-rich, leading to the highest rate of boron mass redistributed into the DAZ.

Finally, Figure 7-16 shows that the IN718/BNi-3 1075°C sample exhibits an intermediate volume fraction of borides extending through the DAZ volume. It also has an intermediate level of Cr, Mo and Nb solute depletion with the DAZ for the first 70 μm, but the highest Nb and Mo solute depletion at greater depths (Figure 7-11). This evidence, together with the lack of darker borides in the DAZ (Figure 7-7) indicates that the formation of Cr-poor:B-rich borides are consistently favoured within the whole depth of the DAZ of this sample. However, the Cr depletion is slightly higher than that measured for the IN718/BNi-2 1075°C. Therefore, it is suggested that more Cr-rich:B-poor borides are forming in this couple, leading to a slightly lower rate of IS.

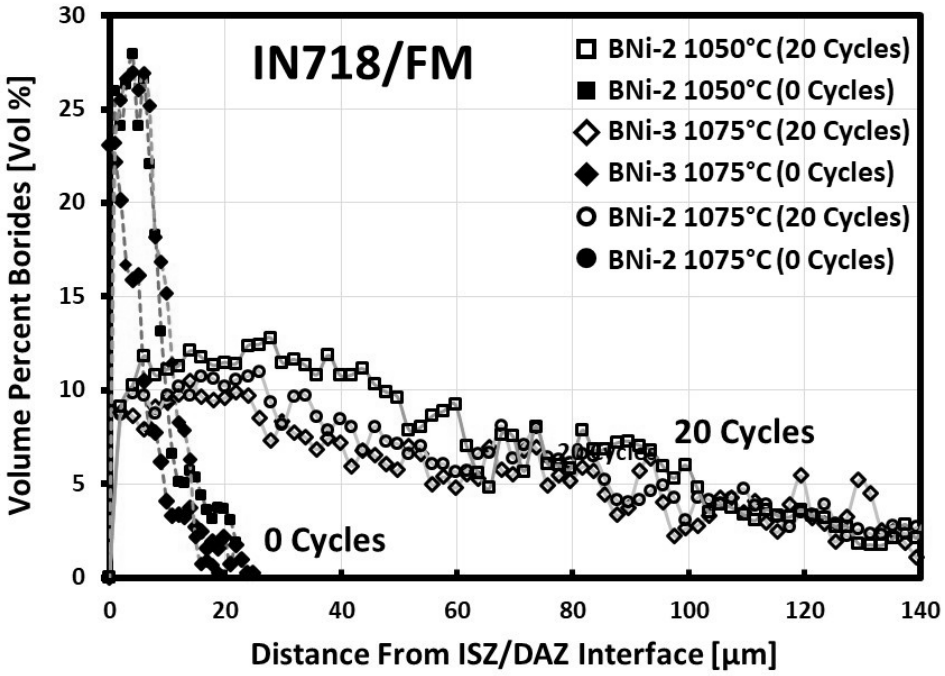

Figure 7-16 - Volume % values for boride content obtained from image analysis of DAZ for all IN718 couples examined.

7.3 Conclusions

The results acquired in the current body of work have been summarized below:

1. A marginal increase in the degree of BMD was observed for BNi-3 as compared to BNi-2 under comparable brazing conditions. This was supported by microscopy and DSC measurements an believed to be a result of the large compositional differences between BM and FM.

2. DSC measurements in conjunction with image analysis further support the understanding that IS is governed by diffusive transport of B from the liquid (FM) to the BM as borides.

3. Boride precipitation in IN718 consists of two primary phases, a Cr-rich Boron phase likely corresponding to CrB and a Cr(Mo, Nb)B phase. The latter was shown to contain a greater quantity of B and less Cr.

4. In all instances the majority of the borides appeared to be of the Cr(Mo, Nb)B type which aside for possessing a greater boron content were observed to penetrate to the greatest depths into the BM. The IN718/BNi-2 1050°C condition displayed the greatest quantity of

the CrB in addition to Cr(Mo,Nb)B, believed to be favored by the excess Cr. The higher boride volume fraction at 1050°C was counter balanced by the lower boron content in the CrB phase, just that the rate of boron uptake and isothermal solidification in this sample was the lowest.

5. The IN718/BNi-2 1075°C condition resulted in a lower volume fraction of borides in the DAZ but also less boron-poor CrB formation. This resulted in the highest rate of IS.

6. The IN718/BNi-3 1075°C displayed a rate of IS slightly lower than that observed for the IN718/BNi-2 at 1075°C, which is attributed to reduce precipitation of the Cr-poor:B-rich boride in the DAZ.

7. The work highlights the complex compromise between the total quantity of liquid (governed by BMD i.e. BM/FM compatibility) and the rate of solidification (governed by the type of borides). FM composition has an influence on both these TLPB factors, which ultimately controls the total isothermal solidification time for a braze joint.

CHAPTER 8 The Role of Braze Alloy Cr-content on the TLPB behaviour of Ni-Based Alloys using BNi-2

8.1 Introduction

The detailed analysis applied to the Ni200 and IN600 base metals (Chapter 6) was also performed in an identical manner but with the Cr containing BNi-2 FM rather than BNi-3. The cumulation of these two bodies of work provides a thorough and complete interpretation of the effect's Cr (and other solutes) on the TLPB behavior of Ni alloys. For instance, the Ni200 and IN600 couples formed using BNi-3 represent how the Cr content within the base metal (BM) influences TLPB. By substituting BNi-3 with BNi-2 the influence of Cr in the Filler on TLPB can be examined. Due to their compositions as pure metal and ternary alloy respectively, the Ni200 and IN600 greatly simplify evaluation. It was shown in Chapter 5 and 6 that diffusion of B into pure Ni results in the preferential precipitation of Ni_3B (Figure 8-1A) however when sufficient Cr is present such as in IN600 e.g. 18 at% Cr, Cr-rich borides are formed (Figure 8-1B) as governed by equilibrium thermodynamics. By repeating the same tests with BNi-2 it is possible to witness the role counter diffusion of Cr and/or Fe between FM and BM has on TLPB, as it is well established that B diffusion away from the liquid phase is favored and that of Si is limited.

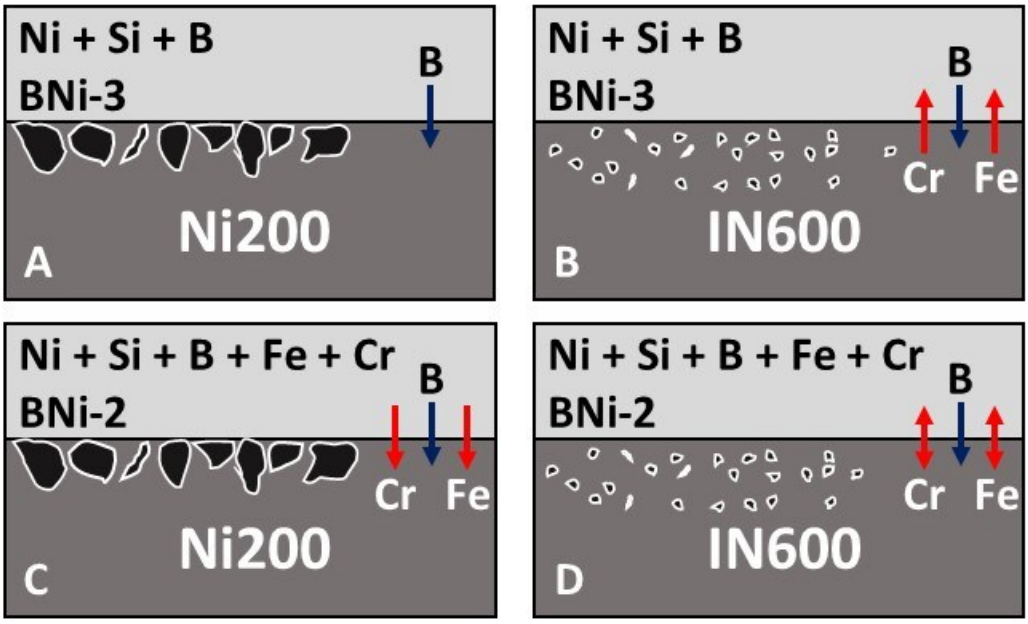

Figure 8-1 - Schematic representing the possible solute transport mechanisms during evaluation of Ni200 (Ni) and IN600 (Ni-Cr-Fe) base metals with BNi-2 (Ni-Cr-Fe-Si-B) and BNi-3 (Ni-Si-B) filler metals.

In Chapter 6 it was determined that appreciable Cr depletion transpired within the DAZ region of IN600 which could have hindered further precipitation due to a shortage of boride formers e.g. Cr in IN600 as Cr_xB. By comparison, precipitation of Ni_3B in Ni200 is rapid and transpires unimpeded due to the semi-infinite source of Ni provided by Ni200 and consequently displays very rapid rates of IS and thus short brazing cycles, t_{IS}. This phenomenon was also observed for IN625/BNi-2 and IN718/BNi-2 at 1050°C wherein two boride phases were present; a Cr-rich Boride primarily forming within grains and similar to the morphology and composition reported for IN600 and an additional Cr-rich boride which contained appreciable concentrations of Mo and Nb and precipitated preferentially in grain boundaries but also within the grains. Since the boride type (stoichiometry) is governed by the BM, but be limited by Cr depletion, it was of interest to ascertain whether the FM containing Cr could reduce that depletion such that the precipitation of borides was promoted.

8.2 Experimental Results

8.2.1 Thermal Analysis and TLPB Behavior

Figure 8-2 shows the representative heating and cooling traces obtained for the BNi-2 FM alone. Complete melting and/or solidification involves three distinct events involving eutectic melting of

the various phases as documented as explained in previous chapters, γ-Ni, Ni_3B, β-Ni_3Si and CrB. Most importantly, is that melting begins at approx. 973°C and is complete below 1050°C. When the BNi-2 is assembled into a half-joint by placing either Ni200 or IN600 in the crucible, diffusion between FM and BM is enabled once melting of the FM occurs. Consequently, changes in the nature of the thermal events occur due to TLPB phenomenon such as BM dissolution and IS, as illustrated in Figure 8-3. The first heating cycle is shown as a dashed line with subsequent cycles stacked vertically above this 1st cycle. The cooling cycles are stacked with the first cool on top and subsequent traces in sequence below. The overall reduction in the magnitude of the melting and solidification peaks is clearly shown to reduce as the cycles and braze time increase. This reduction is more significant for the Ni200 specimens indicating a much more rapid rate of isothermal solidification. The Ni200/BNi-2 specimens exhibited no melting/solidification in the DSC traces, indicating complete IS well before the full 20 cycles. This is in contrast to the IN600 samples which have not undergone complete IS within the 20 cycles, as evidenced by the presence of residual endothermic/exothermic peaks on the DSC traces.

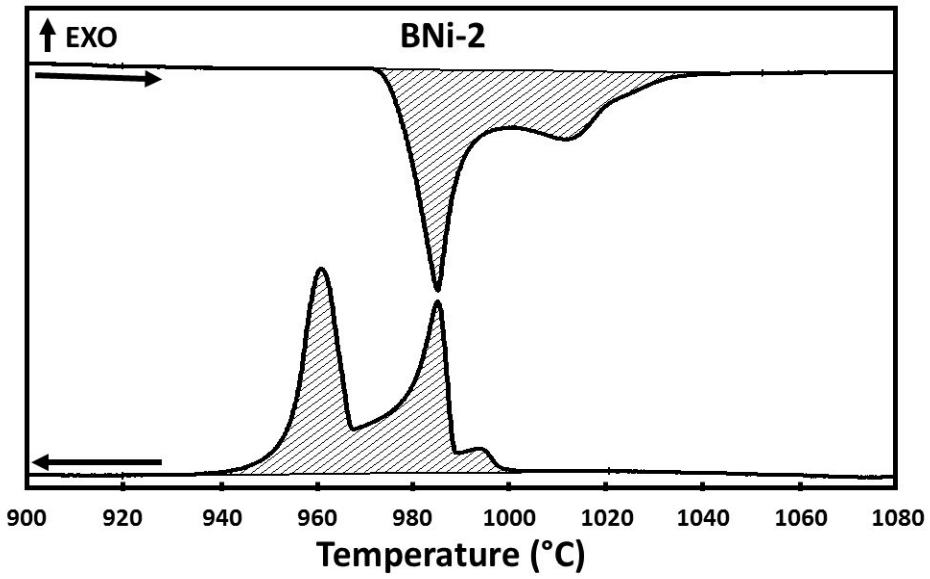

Figure 8-2 - DSC heating and cooling traces of the BNi-2 FM.

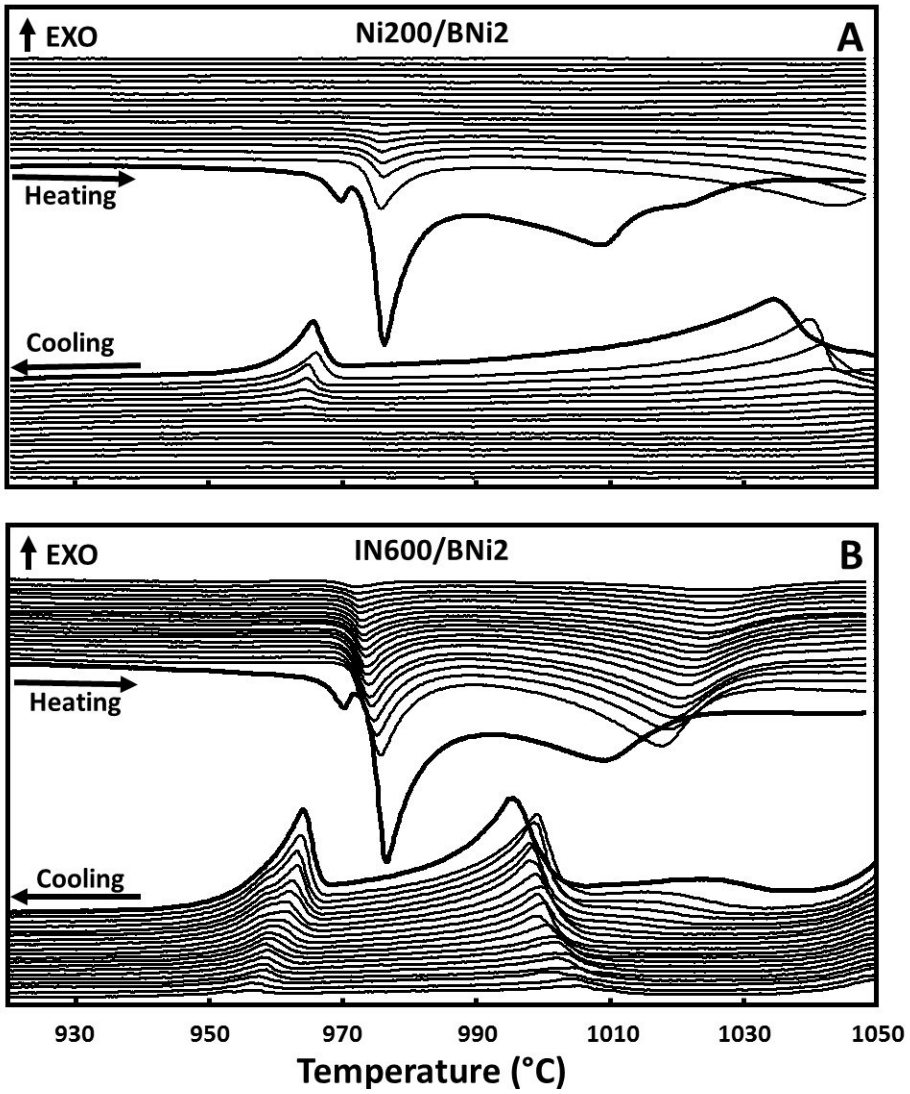

Figure 8-3 - Cyclic DSC heating (A) and cooling (B) results for Ni200/BNi-2 and IN600/BNi-2 half-braze joints. T_{MAX} = 1050°C.

Figure 8-4 and Figure 8-5 reveal the microstructure of Ni200/BNi-2 and IN600/BNi-2 couples obtained as a result of furnace quenching (≈ -50°C/min) immediately upon attaining the peak temperature of 1050°C (A) and following the full 20 cycles (B). The microstructure of the quenched specimens consisted of three regions characteristic of a TLPB joint solidified prior to attaining complete IS; a diffusionally affected zone adjacent to the BM (DAZ), a thin solid solution γ-Ni region (ISZ), and a highly eutectic region associated with the athermal solidification of the remaining liquid phase (ASZ). As the layer labels indicate, the ISZ and DAZ thickness is lower for the Ni200 joint compared to the IN600 joint for the quenched samples shown in Figure 8-4A

and Figure 8-5A. The ISZ layer in both samples is somewhat difficult to discern because of the dynamic nature of the quenched condition. In particular, the Ni200 shows evidence of ongoing dissolution and melting of a previously formed DAZ layer. This phenomenon was also observed by Ruiz-Vargas et al. [71]. The quenched specimen displays a distinct DAZ as evidenced by the network of borides separating the thin ISZ from the BM. As observed in Chapter 6, the Cr-content of the IN600 (18 at% Cr) favored the homogenous precipitation of fine Cr-rich borides for the IN600/BNi-2 as opposed to Ni_3B for Ni200/BNi-2. As compared to the results obtained for BNi-3 wherein significant BM dissolution was observed for both Ni200 and IN600, only Ni200/BNi-2 showed clear signs of BMD, the severity of which was similar to that observed for Ni200/BNi-3. Very little BMD was observed for IN600/BNi-2 which is likely attributed to the compositional similarity between the liquid phase (BNi-2), C_o, and the IN600, C_L, as observed for IN718/BNi-2 and IN718/BNi-3 at 1075°C (Table 7-1). The severity of the BMD is best understood using the cycled specimens as quenched specimens since the ISZ layer is well developed and distinguishable from the DAZ. The lower BMD is further validated by the lack of peak shifting observed from the heating traces of IN600/BNi-2 at 1050°C as compared to that observed for IN600/BNi-3 at 1075°C (Chapter 6).

No significant difference was identified with regards to the microstructure of BM/BNi-2 and BM/BNi-3 joints, other than the presence of coarse angular phases (dark) observed within the ISZ/ASZ regions in the quenched of IN600/BNi-3 sample. These are Cr-borides that are formed due to the Cr content present in BNi-2. This BNi-2 influence is further supported by the presence of coarse Cr-rich borides in quenched IN718/BNi-2 in the previous chapter. In both the IN600/BNi-3 and IN718/BNi-3, the lack of Cr in the FM resulted prevented the formation of the dark, Cr-rich borides in the ISZ of the quenched samples.

The lack of any ASZ in the cycled Ni200/BNi-2 of Figure 8-4B further supports the DSC results where no melting/solidification events were observed in the DSC signal. Traces of residual

ASZ observed in IN600/BNi-2 also support the DSC results wherein subtle melting/solidification peaks were present even after the 20 cycles.

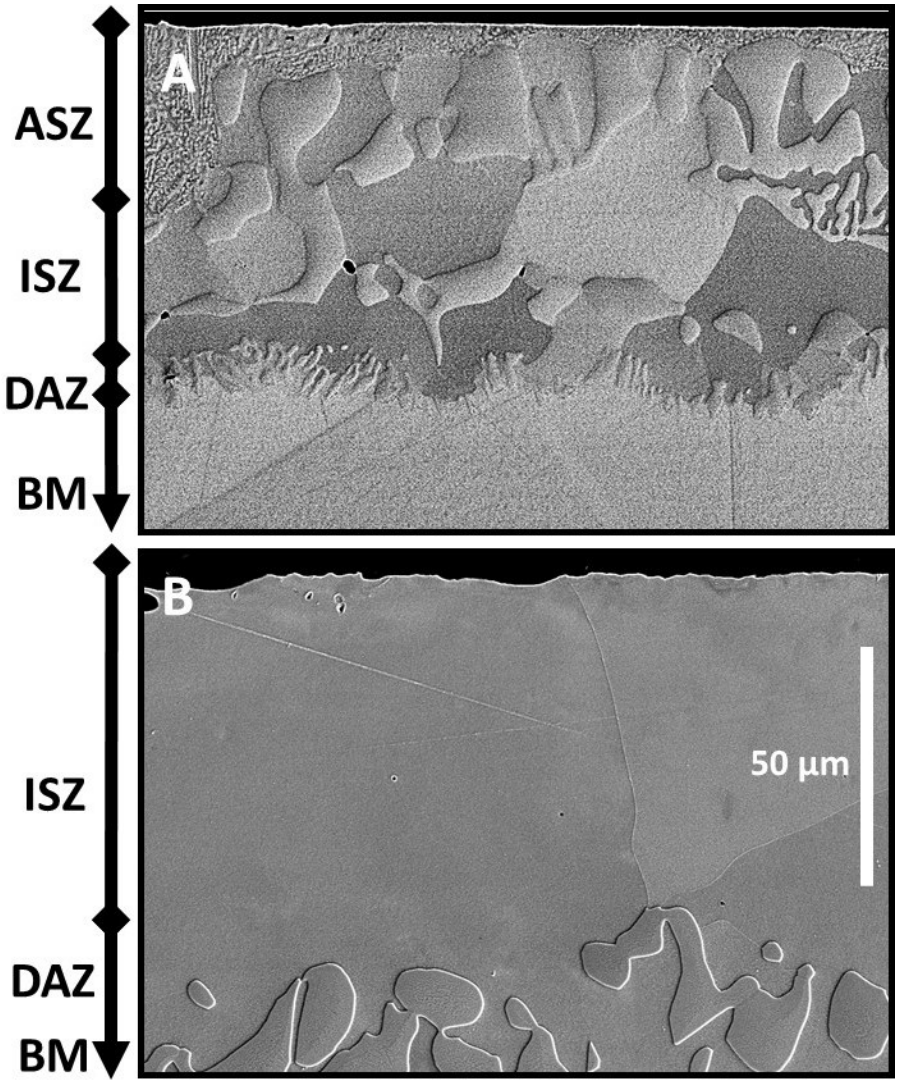

Figure 8-4 - Joint region of Ni200/BNi-2 heated to 1050°C followed by furnace quenching (A) and cycled between 870°C and 1075°C a total of 20 times (B). Approx. liquid duration: 6-8 min (quenched) and 172 min (cycled).

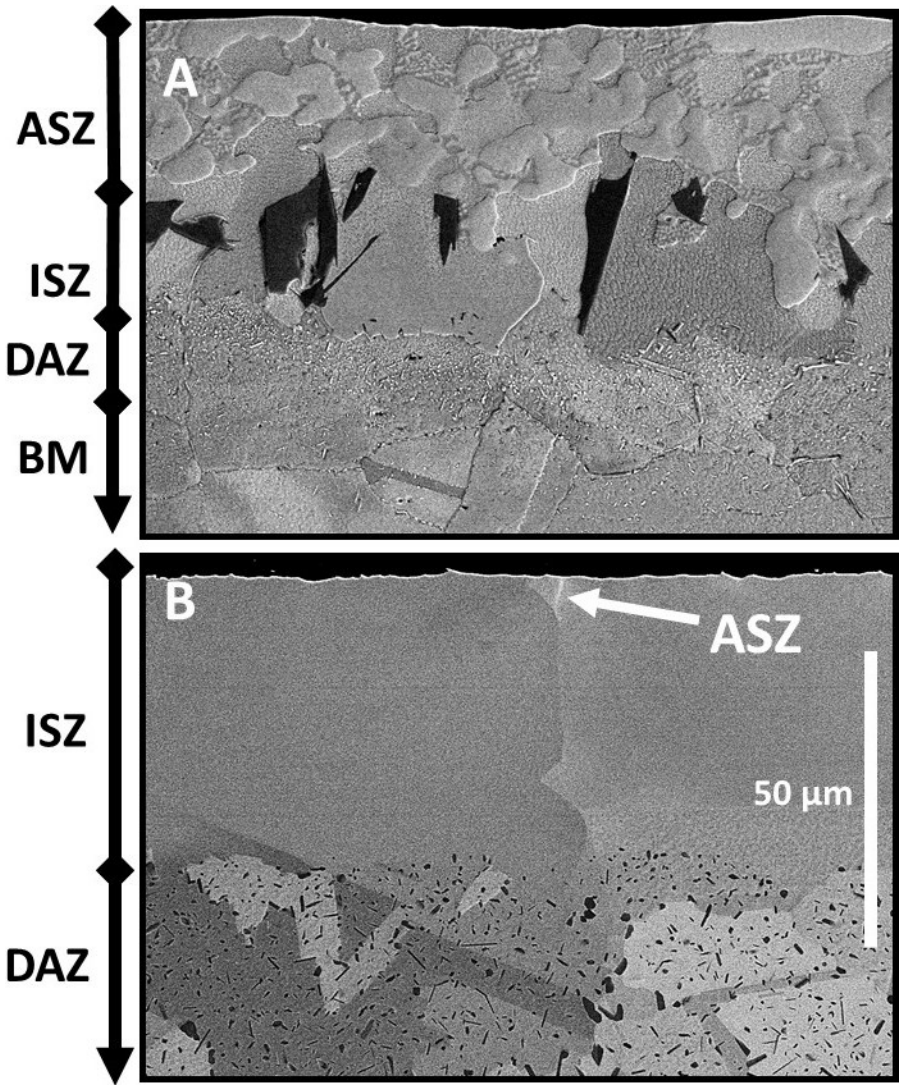

Figure 8-5 - Joint region of IN600/BNi-2 heated to 1050°C followed by furnace quenching (A) and cycled a total of 20 times (B). Approx. liquid duration: 6-8 min (quenched) and 280 min (cycled).

Compositional profiles measured perpendicular to the joint of each 20 cycles specimen were obtained using a series of EDS point scans, beginning from the edge of the ISZ (i.e. the ASZ layer omitted) and extending 100 µm past the ISZ/DAZ interface, the results presented in Figure 8-6. These measurements focussed on the composition of the solid-solution γ-Ni matrix phase with in the DAZ, and therefore any measurements inadvertently made of the secondary boride phases in the DAZ were omitted.

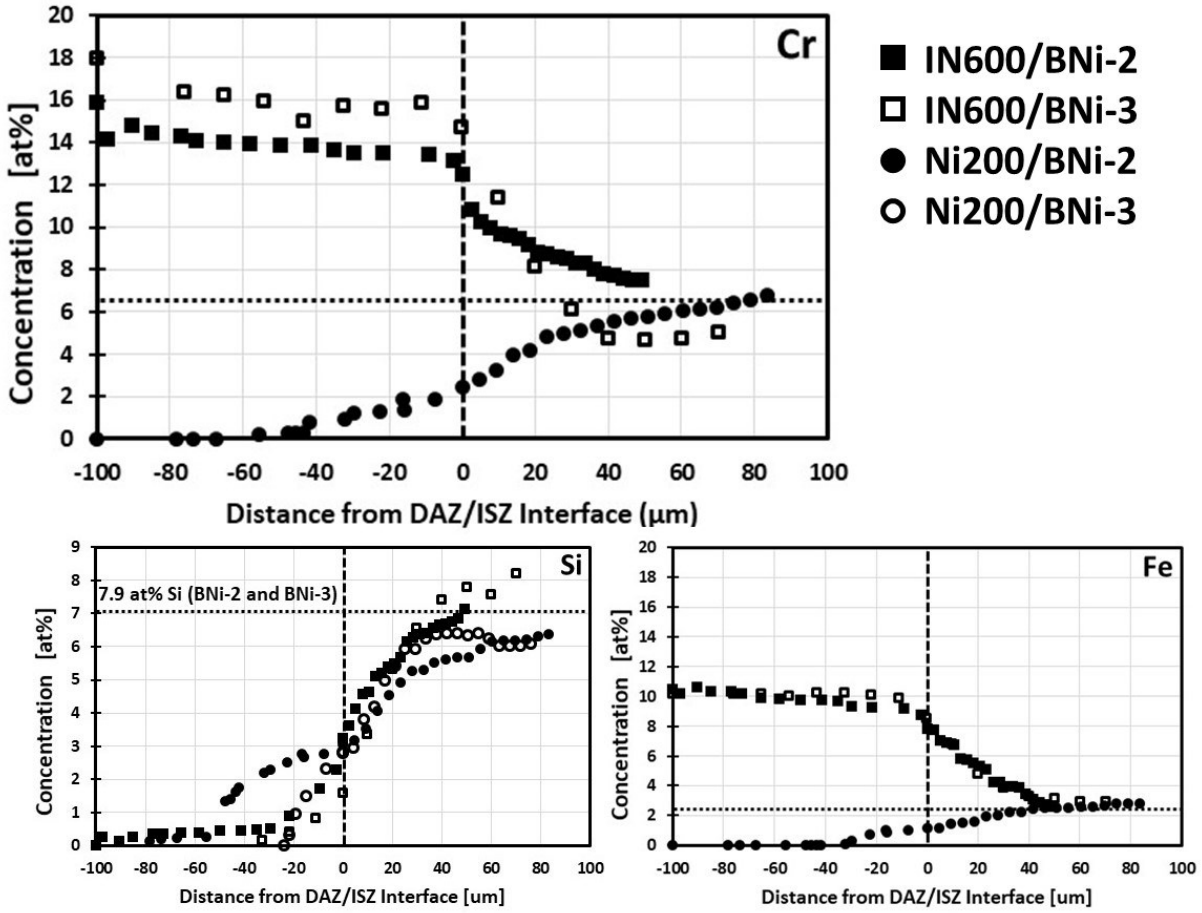

Figure 8-6 - EDS compositional profiles of 20x cycled Ni200/BNi-2 and IN600/BNi-2 couples. Ni200/BNi-3 and IN600/BNi-3 data obtained from Chapter 6 added for comparison. T_{MAX} = 1050°C. approx. liquid duration: 280 min (IN600) and 95 min (Ni200).

All the couples examined displayed significant chemical gradients throughout the joint region, especially within the ISZ. Figure 8-6 indicates that in all cases Cr interdiffusion results in an ISZ concentration which approaches the concentration of the original BNi-2 FM, indicated by the dashed line. The ISZ of the IN600/BNi-2 couple is somewhat more enriched in Cr versus Ni200/BNi-2 and IN600/BNi-3. This is expected since this is the only braze couple where Cr initially exist in both the base metal and filler metal. As the Cr content of the unaltered IN600 is approx. 19 at% Cr, an appreciable degree of solute depletion has clearly transpired within the measured 100 µm of DAZ. This is related to the formation of Cr-rich borides as opposed to Ni_3B in the DAZ, depleting the surrounding γ-Ni of Cr which would otherwise exist in solid-solution with the Ni. This depletion is somewhat higher in the IN600/BNi-2 couple versus the IN600/BNi-

3 couple. The significant Cr content within the ISZ of the IN600/BNi-3 couple is further evidence of base metal dissolution in this case and the shifting melting behaviour observed for this sample.

Chromium and iron have diffused into the Cr and Fe free Ni200, albeit to a limited extent. The negative concentration gradient of Cr and Fe in the Ni200/BNi-2 ISZ and its associated drop in concentration compared to the original BNi-2 composition represents dilution of the liquid phase caused by BM dissolution. The Fe profiles for IN600/BNi-2 and IN600/BNi-3 couples are similar in appearance despite differences in BMD observed between these samples. It can be concluded that the significant BM dissolution exhibited by the IN600/BNi-3 sample occurred in order to establish a solid/liquid phase equilibrium that is similar to that established with the Fe and Cr containing BNi-2, which exhibited a small level of BM dissolution. No solute depletion of Fe in the DAZ occurred, which is expected as Fe does not participate in the formation of the Cr-rich borides; the Fe content at the interface is essentially the same as the nominal Fe content of the IN600.

In all cases the interfacial (ISZ/DAZ) Si solute concentrations appear to be relatively constant, as demonstrated in the previous chapters. However, the aggravated BMD observed in both Ni200 specimens, has results in a "dilution" or reduction in the Si content, particularly in the last layers of the ISZ. Si diffusion into the BM and DAZ is generally within 20 μm, except for the Ni200/BNi-2 couple where Si diffuses to greater depths. This Si depletion in the ISZ of the Ni200 joints is believed to be a result of homogenization of the joint following complete IS far before the time required for the full 20 cycles. Comparatively, the IN600/BNi-2, which never attained complete isothermal solidification, must always obey the phase equilibria between the ISZ/Liquid layer.

Above, it was observed that Ni200 and IN600 display DAZ regions which differ drastically in terms of boride morphology and distribution. It was therefore of great interest to identify the chemical nature of the precipitates. The EDS results listed below in Table 6-1 represent the mean compositional values obtained for the DAZ Borides shown Figure 6-8 under various operating conditions. The globular Ni-rich borides in the Ni200 DAZ correspond to the Ni_3B intermetallic while the fine Cr-rich borides observed in the IN600 DAZ correspond to CrB. Both these phases have been well documented in the literature [33-35]. It is therefore clear that the Cr content in IN600 is sufficient to promote the preferential formation of CrB rather than Ni_3B within the DAZ.

The impact of this is the depletion of Cr within the DAZ region as confirmed in Figure 8-6. The CrB in the DAZ of IN600 specimens as compared to Ni_3B in Ni200 is considerably finer and evenly distributed as compared to very coarse globular Ni_3B, the degree of precipitate coarsening not observed in IN600. No distinction could be made between inter- and trans-granular precipitates. It is worth noting that the coarse borides present within the ASZ (see Figure 8-4A and 8-5A) were measured to be Ni_3B for both Ni200 and IN600 joints.

Figure 8-7 provides the representative microstructure full-joint region to better highlight the transition from ISZ to DAZ to unaltered BM. For instance, although the Ni_3B observed for Ni200/BNi-2 are massive in comparison to the Cr-borides (IN600) they only extend to approx. 60-70 μm into the DAZ. By comparison, the fine, homogenous distribution of Cr_xB initially displays a significant volume fraction which gradually decreases to a boride-free BM at over 150 μm. As demonstrated in previous chapters, the volume fraction of the borides as a function of depth within the DAZ can provide valuable information with regards to the TLPB response of a system and can be measured relatively easily. Figure 8-8 reveals the results of the image analysis performed on the cycled Ni200/BNi-2 and IN600/BNi-2 samples to assist in assessing the microstructures presented in Figure 8-7. For comparison purposes, the previous results from Chapter 6 for the Ni200/BNi-3 and IN600/BNi-3 are also included. The results clearly demonstrate that, although the precipitation of Ni_3B occurs at relatively high volume fractions directly adjacent to the ISZ/DAZ interface, they only penetrate 50 to 60 μm into the BM. Overall, the magnitude and distribution of the Ni_3B is slightly influence by the filler metal type for the Ni200 case primarily through a deeper penetration of boride volume into the DAZ for the BNi-3 case. Comparatively, the CrB precipitates form at considerably smaller volume fractions but to a greater depth into the IN600 BM. In this case, the volume fraction of borides is slightly increased over the entire DAZ depth when the BNi-2 filler is used for brazing.

Averaged EDS results from boride precipitates were obtained for the Ni200/BNi-2 and IN600/BNi-2 couples to assist in comparing the nature and distribution of the borides resulting from the use of BNi-2 versus BNi-3, as shown in Table 8-1. The EDS data acquired previously for the Ni200/BNi-3 and IN600/BNi-3 couples (Table 6-1) were also added to facilitate comparison. In the case of Ni200, the use of BNi-2 versus BNi-3 does not alter the composition of the Ni_3B particles formed. For the IN600 BM, the results clearly show an overall decrease in Boron and

corresponding increase in Cr in the finely dispersed Cr_xB precipitates resulting from the use of the BNi-2 FM as opposed to the Cr-free BNi-3. This is similar to that observed for IN718/BNi-2 and IN718/BNi-3 couples (Chapter 7) wherein the additional Cr (and Fe) present within the BNi-2 caused a preferential formation of Cr-rich borides near the ISZ/DAZ interface. Although the boride volume fraction profiles demonstrate a greater volume fraction of Cr_xB borides in the DAZ of the IN600/BNi-2, the borides contain less boron and more Cr when BNi-2 is used. This is supported by the higher Cr-depletion in DAZ matrix of the IN600/BNi-2 shown in Figure 8-6, leading to the conclusion that the additional Cr resulting from the adoption of BNi-2, aggravates solute depletion due to the preferential formation of borides containing more Cr. The implication these observations have on the rate of isothermal solidification will be discussed below.

Table 8-1 - Mean EDS results acquired for DAZ boride phase of 20x cycled BM/BNi-2 and BM/BNi-3 specimens (at%).

	FM	Shell	Ni (L)	B (K)	Cr (L)	Fe (L)
Ni200	*BNi-2*	L	73.7 ± 1.8	25.9 ± 2.0	0.1 ± 0.0	0.6 ± 0.2
	BNi-3	L	73.4 ± 22	25.8 ± 1.6	-	0.8 ± 0.1
IN600	*BNi-2*	L	0.2 ± 0.1	54.6 ± 1.0	45.0 ± 0.9	0.2 ± 0.2
	BNi-3	L	3.8 ± 2.1	61.5 ± 0.9	33.3 ± 2.2	1.3 ± 0.9

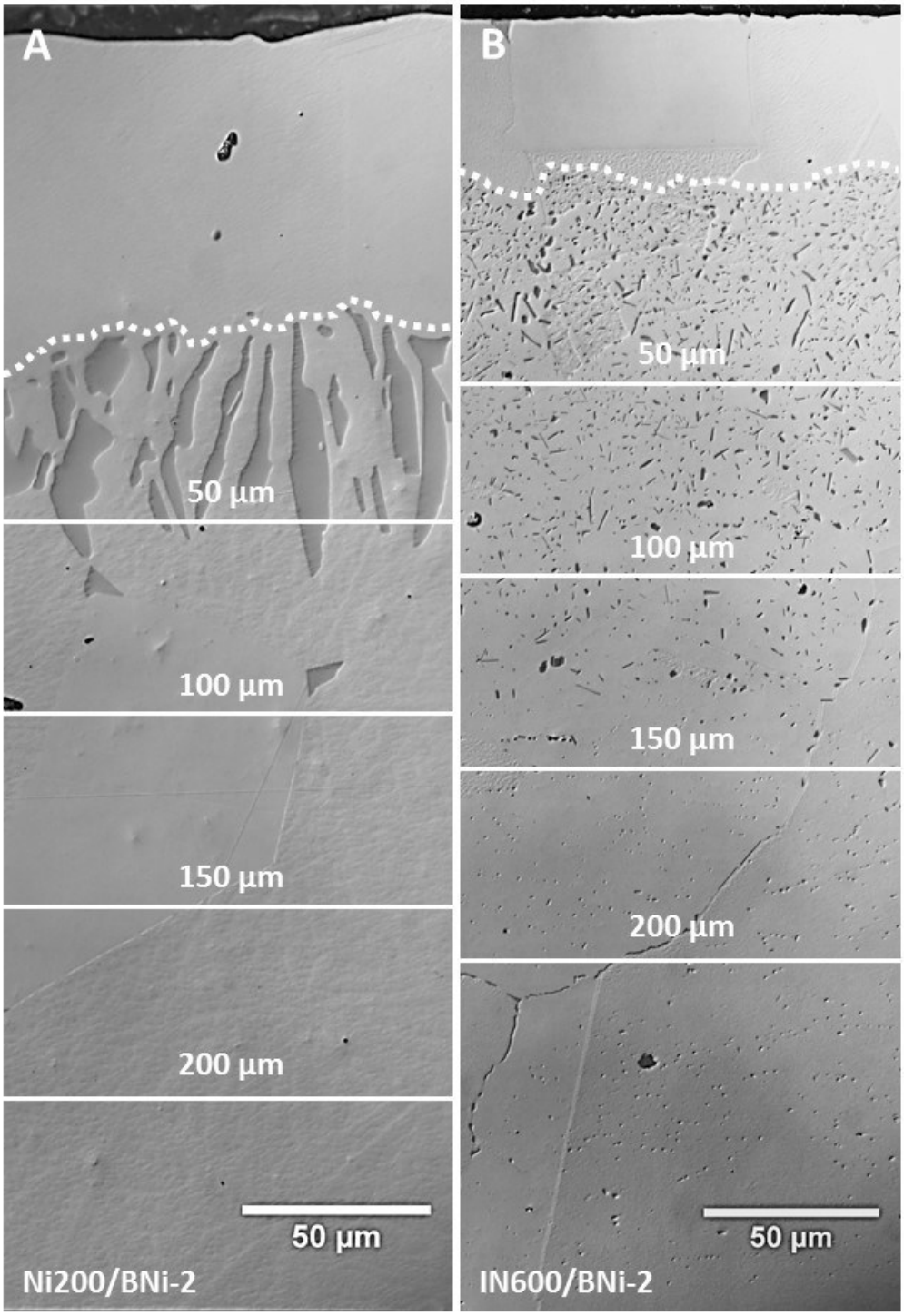

Figure 8-7 – Complete joint region of cycled Ni200/BNi-3 (A) and IN600/BNi-3 (B) 20x cycled DSC couples. Dashed line denotes DAZ/ISZ interface, marked distances are with reference to center of DAZ/ISZ interface. T_{MAX} = 1050°C. approx. liquid duration: 280 min (IN600) and 95 min (Ni200).

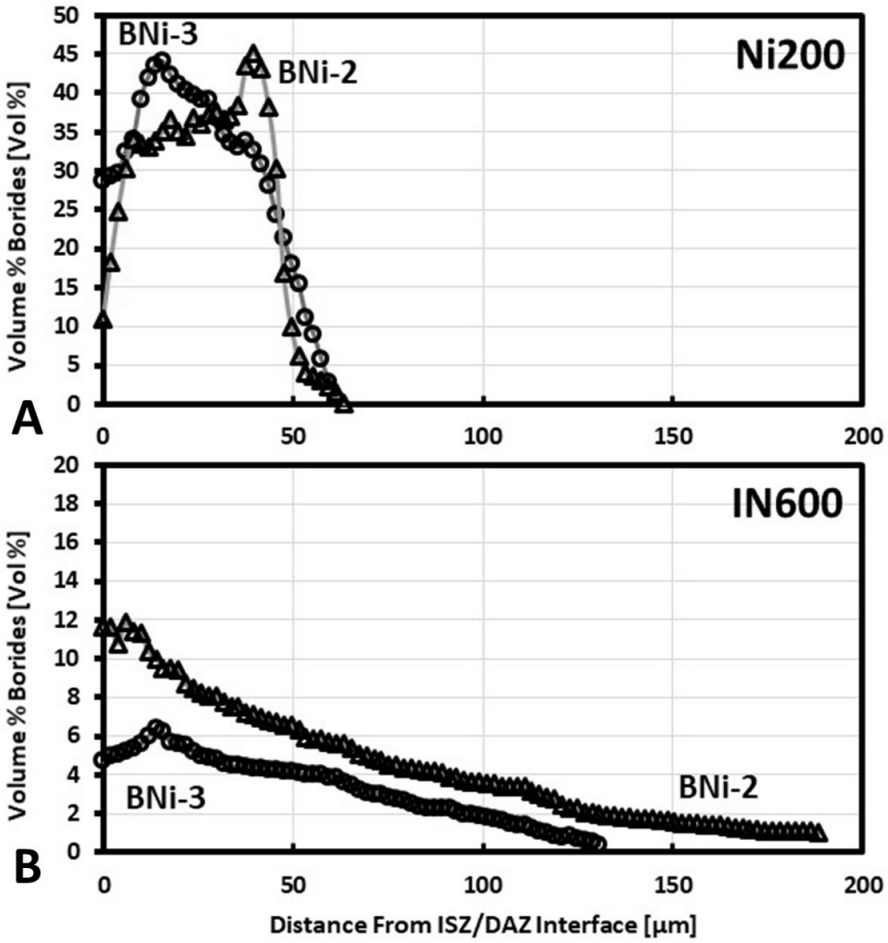

Figure 8-8 - Volume fraction of borides as a function of depth into BM from the ISZ/DAZ interface for 20x cycled Ni200/BNi-2 (A) and IN600/BNi-2 (B) DSC specimens. T_{MAX} = 1050°C. Approx. liquid duration: 280 min (IN600) and 95 min (Ni200).

8.2.2 Kinetics of TLPB for Ni200 and IN600 BMs with FM Composition

As demonstrated in previous chapters, the repeated enthalpy measurements acquired from the DSC data in Figure 8-3 can describe the rate of solidification based on the rate at which the enthalpy decreases as a function of time. The gradual decrease in the enthalpy of solidification plotted versus the square root of time above solidus, is shown below in Figure 8-9 for the current couples.

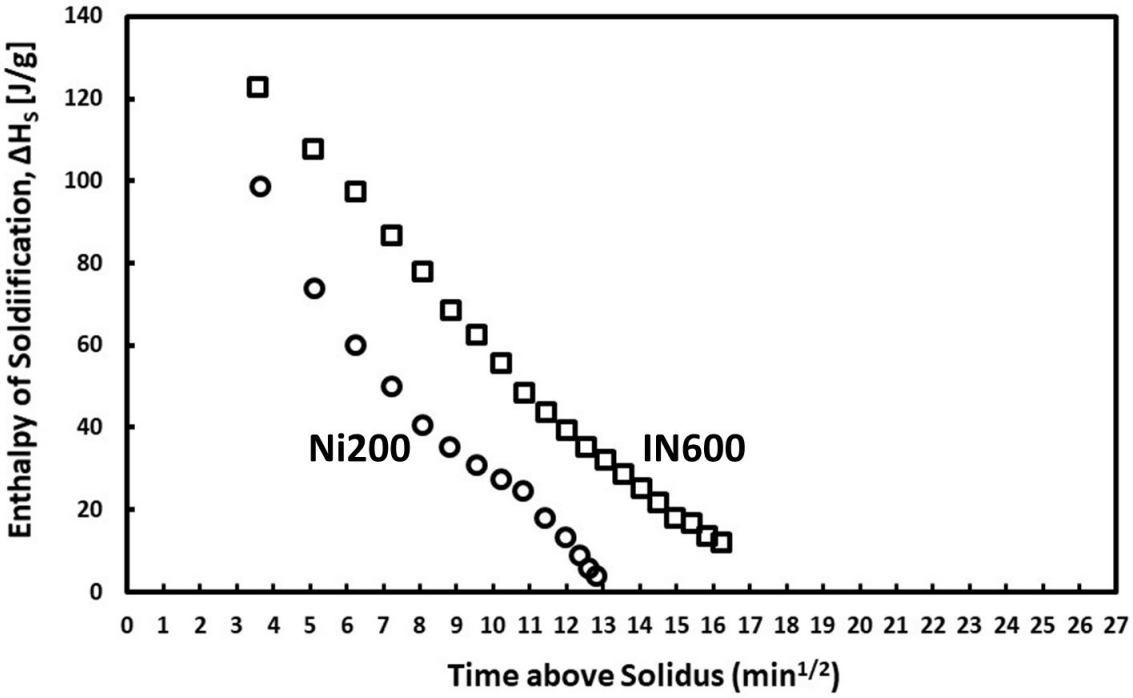

Figure 8-9 - Enthalpy of solidification value obtained from 20x cyclic DSC results versus time above solidus for Ni200/BNi-2 and IN600/BNi-2 couples. T_{MAX} = 1050°C. approx. liquid duration: 280 min (IN600) and 95 min (Ni200).

As described in Chapter 3.1 – Differential Scanning Calorimetry (DSC), enthalpy values can be converted into more meaningful measurement of the fraction of liquid present if knowledge of the theoretical or total enthalpy of the BNi-2 (Figure 8-2) is known. This requires an additional experiment involving cyclic melting/solidification of a typical BM/BNi-2 couple however with the faying surface covered in a thin layer of Y_2O_3 thereby preventing diffusional solidification, as described by the 100% liquid arrangement e.g. BM//FM in Figure 3-1. The value obtained from this technique must be corrected for a variety of phenomenon which would otherwise alter the enthalpy of solidification. This is accomplished using the following formula:

$$L_f = \frac{D_{mf} * B_C * \Delta H_m}{\Delta H_f} \qquad \textbf{Eq. 8-1}$$

Where; ΔH_m is the DSC measured enthalpy of solidification {J/g} (Figure 8-9), $B_C = \Delta H_o/\Delta H_{BM}$ which accounts for thermal/signal dampening. ΔH_f is the enthalpy {J/g} of a braze ball created given the composition and degree of dilution observed for the quenched BM/FM couple, using the method described in Figure 3-1. Lastly, D_{mf} is a mass correction factor which considers the increase in mass of the liquid phase resulting from BMD, determined by the change in

composition of the liquid phase. The DSC and EDS experimental values used to calculate the various correction factors are tabulated in Table 8-2 and Table 8-3. Table 8-2 displays the EDS results acquired from the solidified liquid phase of the quenched Ni200/BNi-2 and IN600/BNi-2 specimens, the unaltered BNi-2, and the Ni200 and IN600 substrates required for the calculation of D_{mf} (D_{mf} = 100 - % f_{BM}) in accordance with Eq. 3-2. The EDS results provide further evidence of the severe BMD observed for the Ni200/BNi-2 as evidenced by the overall reduction, or dilution of Si, Cr, Fe and Ni from the unaltered BNi-2 FM to that measured for the quenched Ni200/BNi-2. Comparatively, a negligible enrichment of the liquid phase in Cr and Fe was observed for IN600/BNi-2 due to the lack of BMD as inferred by the DSC data (Figure 8-3) and microstructural analysis (Figure 8-5).

Table 8-2 – Bulk composition of the liquid phase as determined by EDS analysis of quenched Ni200/BNi-2 and IN600/BNi-2 couples. T_{MAX} = 1050°C. approx. liquid duration: 6 - 8 min.

Material(s)	Composition (at%)			
	Si	Cr	Fe	Ni
BNi-2 (FM)	**8.7**	**7.7**	**3.3**	**80.1**
IN600	0.0	17.9	10.2	71.9
IN600/BNi-2	8.6	7.8	3.3	80.1
% f_{BM}	**0.8%**	**0.9%**	**0.3%**	**0.3%**
Ni200	0.19	0.05	0.23	99.5
Ni200/BNi-2	6.56	5.52	2.37	85.5
% f_{BM}	**25%**	**29%**	**31%**	**28%**

Table 8-3 – Various experimentally parameters used in L_f correction, Eq. 8.1.

BM	ΔH_o (J/g)	ΔH_{BM} (J/g)	B_c	D_{mf}	ΔH_f (J/g)	$2W_o$ (µm)
Ni200	240	206	**1.17**	**0.72**	**175**	166.8
IN600	240	216	**1.11**	**0.99**	**237**	98.44

The following plot illustrating the relationship between the liquid fraction remaining, L_f and time (Figure 8-10A) was therefore generated using Eq. 8-1, Figure 8-9, and Table 8-3 alongside the corresponding liquid width remaining, $2W_t$ vs. time (Figure 8-10B) obtained using the experimentally measured joint width, $2W_o$, as described in Chapter 4. The results demonstrate two key findings; (1) a significant depletion of the liquid phase occurs for both specimens during heating prior to attaining the peak temperature of 1050°C (approx. 2 $min^{1/2}$) and (2) the Ni200

displays considerably faster rates of IS as compared to IN600; attaining complete isothermal solidification, t_{IS}, by approx. 84 min (9 $min^{1/2}$) and 286 min (17 $min^{1/2}$), respectively. These results are similar to those observed for the Ni200/BNi-3 and IN600/BNi-3 couples examined in Chapter 6. The liquid width remaining, $2W_t$ can be converted to a measure of the width of solidified ISZ, or the "maximum brazing clearance" by acknowledging that the width of the isothermally solidified zone, $2W_{ISZ}$ is equal to the experimentally determined final gap width, $2W_o$ minus the width of the liquid phase remaining, $2W_t$ as detailed in Chapter 4. Thus, Figure 8-11 reveals the relationship between the growth of the ISZ, $2W_{ISZ}$ and time for Ni200/ and IN600/BNi-2 couples, alongside the data previously acquired for Ni200/ and IN600/BNi-3 (Chapter 6), to facilitate comparison. The results show that the rate of IS is similar for both IN600 couples, despite the considerably longer times required to attain complete IS as a consequence of the significant BMD displayed by IN600/BNi-3. The Ni200/BNi-2 and Ni200/BNi-3 couples also display similar rates of solidification however in both cases with similar degrees of BMD. Thus, for Ni200 the major deviation appears to be a consequence of the initial depletion of liquid phase, or initial boron

uptake (IBU). Linear regression was performed on the four sets of data shown in Figure 8-11, to further assist in comparing the two systems, the results tabulated in Table 8-4.

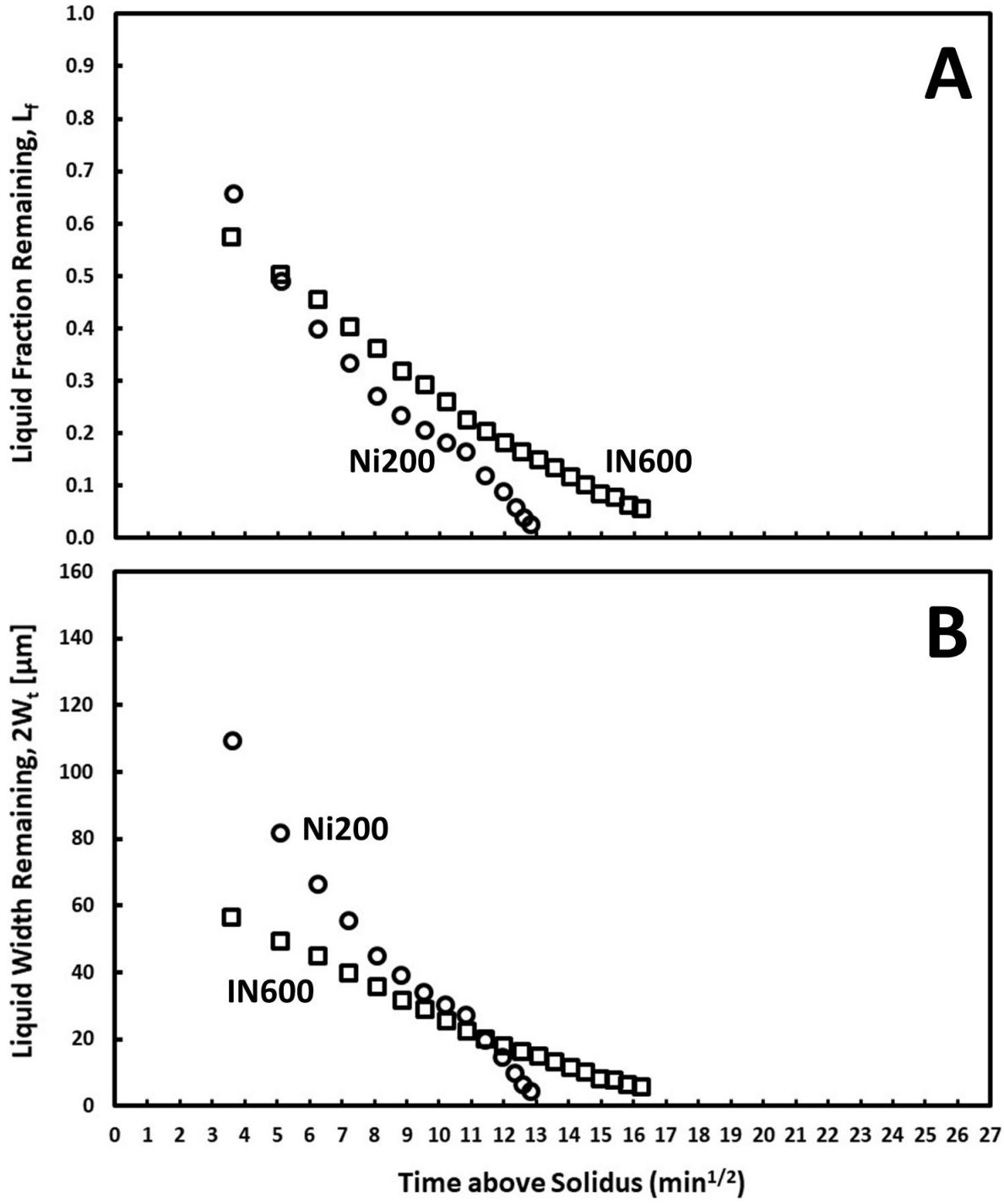

Figure 8-10 – Liquid fraction remaining, L_f (A) and corresponding liquid width remaining, $2W_t$ (B) versus the time above solidus for Ni200/BNi-2 and IN600/BNi-2 couples.

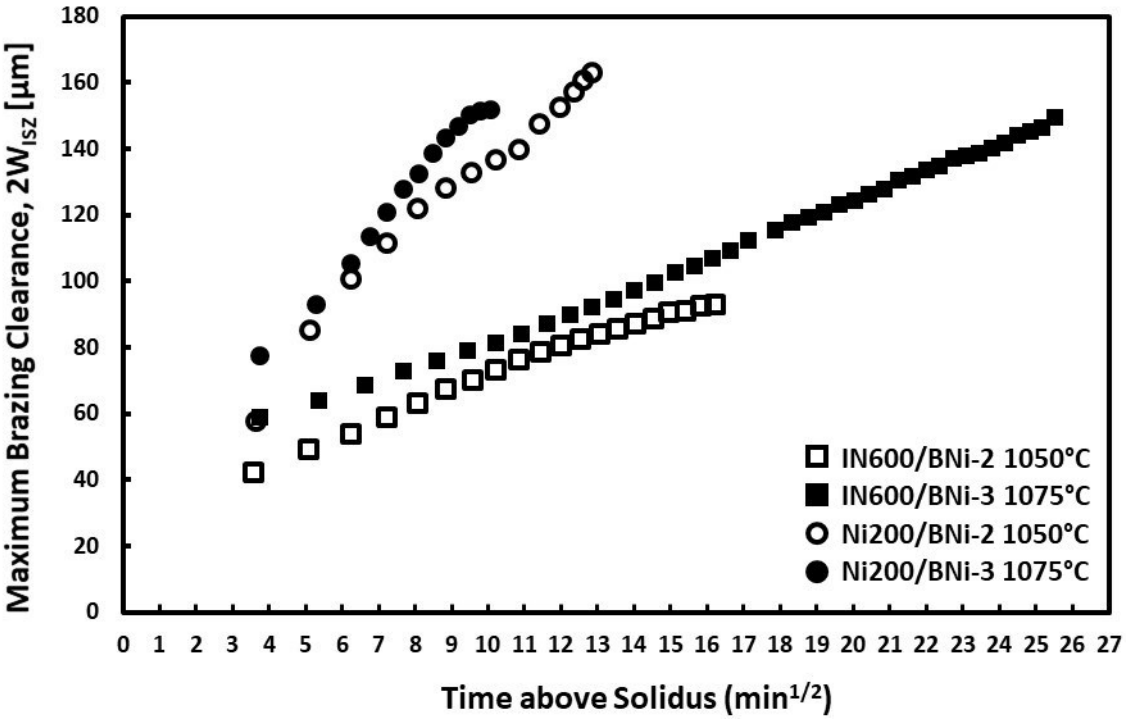

Figure 8-11 - Maximum brazing clearance, $2W_{ISZ}$ vs. time above solidus of Ni200/BNi-2 and IN600/BNi-2 obtained from cyclic DSC (20x) cooling results. Ni200/BNi-3 and IN600/BNi-3 data (Chapter 6) included for comparison.

In each case, the TLPB behavior can be understood according the initial boron uptake (IBU) and the rate of isothermal solidification. The former is believed to be highly dependent on the chemistry of the BM and FM and thus the phenomenon of BMD while the later is believed to be nature of the resulting borides (distribution, volume fraction and type).

As previously demonstrated, the redistribution of Boron from the liquid phase into precipitates within the DAZ can be expressed through a simple mass balance between the ISZ/DAZ interface if the boron content in the γ-Ni is assumed to be negligible as detailed in Chapter 4, Chapter 6, and Chapter 7. It therefore holds that the time required to attain complete IS

is governed by the total mass of Boron available in the FM and the manner in which it redistributed itself within the DAZ, as shown by the following formula:

$$\boldsymbol{m_{BDAZ} = \sum_{i=1}^{n} V_{DAZ} X_{DAZ} f_i \rho_i} \qquad \textbf{Eq. 8-2}$$

Where, X_{DAZ} is the volume fraction of borides presents within the DAZ layer, V_{DAZ} the volume of the DAZ layer, f_i the boron content (% wt) of the boride, i and ρ_i the specific gravity $\{g/cm^3\}$ of the precipitate (boride) phase, i. Since in the current case only a single boride phase was observed for either system e.g. Ni_3B for Ni200 and Cr_xB for IN600, the relationship can be easily tailored to each system using the results provided in Figure 8-8 (V_{DAZ} and X_{DAZ}) and Table 8-2(f_i). For instance, the nearly identical isothermal solidification rate, k_W of the IN600/BNi-2 as compared to IN600/BNi-3 may be directly linked to an overall compromise between the greater Boron content, f_{CrxB} of the borides reported for IN600/BNi-3, despite the generally lower distribution of borides compared to IN600/BNi-2. The variation in the boron content of the Cr_xB borides is believed to relate to the Cr-content and thus greater compatibility of the BNi-2 FM with the IN600 versus the Cr-free BNi-3, as it is clear that Cr is essential for the precipitation of borides. This is further supported by the greater Cr-content of the Cr_xB in the IN600/BNi-2 system. This superior compositional compatibility between the IN600 and BNi-2 is also likely responsible for the lack of any appreciable BMD only observed for IN600/BNi-2.

In the case of the Ni200 braze couples, the boron composition of the Ni_3B, f_i is identical for both the Ni200/BNi-2 and Ni200/BNi-3. Therefore, the slightly higher rate of IS observed in the Ni200/BNi-3 joint is due to the higher overall volume fraction, X_{DAZ} with the DAZ of this sample.

Table 8-4 - Linear regressions regression results obtained from L_f, $2W_t$ and $2W_{ISZ}$ plots for Ni200/BNi-2 and IN600/BNi-2 couples. Ni200/BNi-3 and IN600/BNi-3 data acquired in Chapter 6 added for comparison.

	$-K_L$ ($min^{-1/2}$)	L_o (%)	k_W ($\mu m/min^{1/2}$)	$2W_i$ (μm)	$2W_{iszo}$ (μm)	$2W_o$ (μm)	t_{IS} (min)
Ni200/BNi2	0.06	0.81	10.3	135	32	167	172
Ni200/BNi3	0.08	0.82	12.7	124	28	152	105
IN600/BNi2	0.04	0.70	4.1	69	30	98	306
IN600/BNi3	0.03	0.77	4.3	128	39	167	904

CHAPTER 9 Summary of Results

In the process of examining the TLPB behavior of various couples, a great deal of information was acquired which confirms a variety of key findings related to the mechanism governing TLPB with Boron-containing FMs. The results have been compiled in the various figures below for comparison. The main conclusions relating to the mechanisms governing TLPB e.g. IBU and Isothermal Solidification are summarized as follows:

9.1 Initial Boron Uptake and Base Metal Dissolution

Figure 9-1 plots the initial boron uptake (IBU or $2W_{iszi}$) and the maximum braze gap width ($2W_{MAX}$), formed through dissolution, for all braze joints examined within this study. In the absence of dissolution (i.e. the IN625/BNi-2 1050°C couple, 80±24 μm) the gap width ($2W_o$) produced by a single braze foil is 80 μm. The IN600/BNi-2 (98±6 μm) and IN718/BNi-2 (100±6 μm) braze joints show minor amounts of dissolution. For a given base metal, dissolution is, overall greater when the BNi-3 filler metal is used. This may be partly due to the higher braze temperature (i.e. 1075 versus 1050°C). However, each FM was brazed at 10°C above its liquidus which should minimize the influence of temperature (overheating) as opposed to chemical dissolution. The increase BMD at 1075 °C is more likely a consequence of the greater metallurgical incompatibility between the BM and FM, specifically, the fact that the Cr and Fe content is zero in BNi-3 and 7 and 3.15 wt%, respectively in BNi-2. With regards to this hypothesis the only exception is the Ni200/BNi-2 couple which shows the highest degree of dissolution. However, it is evident that this couple also has the highest degree of metallurgical incompatibility as the BM contains neither Cr nor Fe.

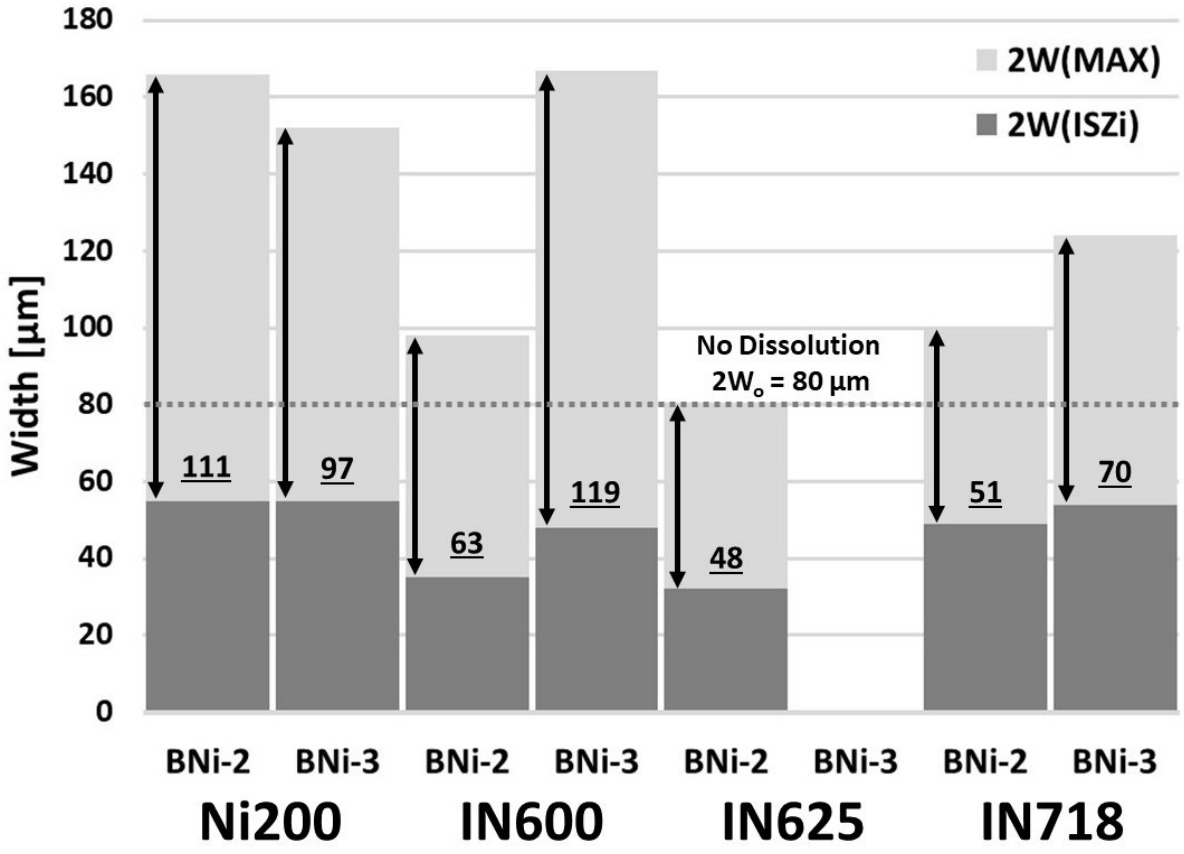

Figure 9-1 - Summary of the gap width values related to; BMD ($2W_{max}$) and the IBU ($2W_{ISZi}$) measured for all braze couples.

Figure 7-6 from Chapter 7 illustrates that during heating between the solidus and the braze temperature, dissolution, and the formation of a DAZ layer occur in parallel. This microstructural progression is further illustrated in the images of Appendix C (Figure C-5) for Ni200/BNi-3. The net result is an initial boron uptake by the BM which results in the in-situ formation of a DAZ layer and diffusionally solidified layer (or ISZ) once the braze temperature is reached. As outlined in Chapter 4, a measure of the ISZ layer (or W_{ISZi}) formed at the braze temperature can be determined from the MBC curve. This value is included in Figure 9-1. The IBU ranges from 32 to 55 µm and no clear trend can be observed with respect to the type of BM/FM used or the level of dissolution, resulting in the conclusion that its formation is relatively insensitive to these parameters. The liquid present when the braze temperature is first attained can be estimated as:

$$2W_{ti} = 2W_{max} - 2W_{ISZi} \qquad \text{Eq. 9-1}$$

These values are also included in Figure 9-1 (underlined values). The results further support the importance of considering both dissolution and IBU when determining the liquid width present as the isothermal solidification stage begins. For example, in the literature the simplification is often made that the starting liquid width used (Eq. 1-6) for determining the isothermal solidification time (or to estimate the apparent diffusivity from an experimentally determined IS time) is the starting foil thickness, in this case $2xW_{FM}$ = 80 μm. In the current study, this actual liquid width ranges from 48 to 119 μm depending on the relative contributions of dissolution and IBU formation.

In all cases, further examination of the IBU phenomenon was pursued through microstructural examination of samples quenched from the braze temperature (an equivalent liquid duration time of approx. 4 minutes). The microstructures of these samples for all braze couples is plotted in Appendix C, Figures C-1 to C-4. In certain cases, measuring the W_{ISZi} layer thickness is challenging in these quenched samples due to the non-planar nature of the ASZ/ISZ and ISZ/DAZ interfaces. Despite this, the thickness of the layers varied on the order of 10 to 30 μm. Given that these layers represent W_{ISZi}, they should be compared to half the $2W_{ISZi}$ values determined by the MBC plots (i.e. 16 to 27.5 μm). Therefore, the MBC plots correlate well with the microstructural data.

Figure 9-2 plots the boride area fractions for all the quenched samples determined by image analysis. In general, the DAZ layer penetrates the base metal to a depth of 15 to 20 μm with the IN625/BNi-2 couple exhibiting the higher depth.

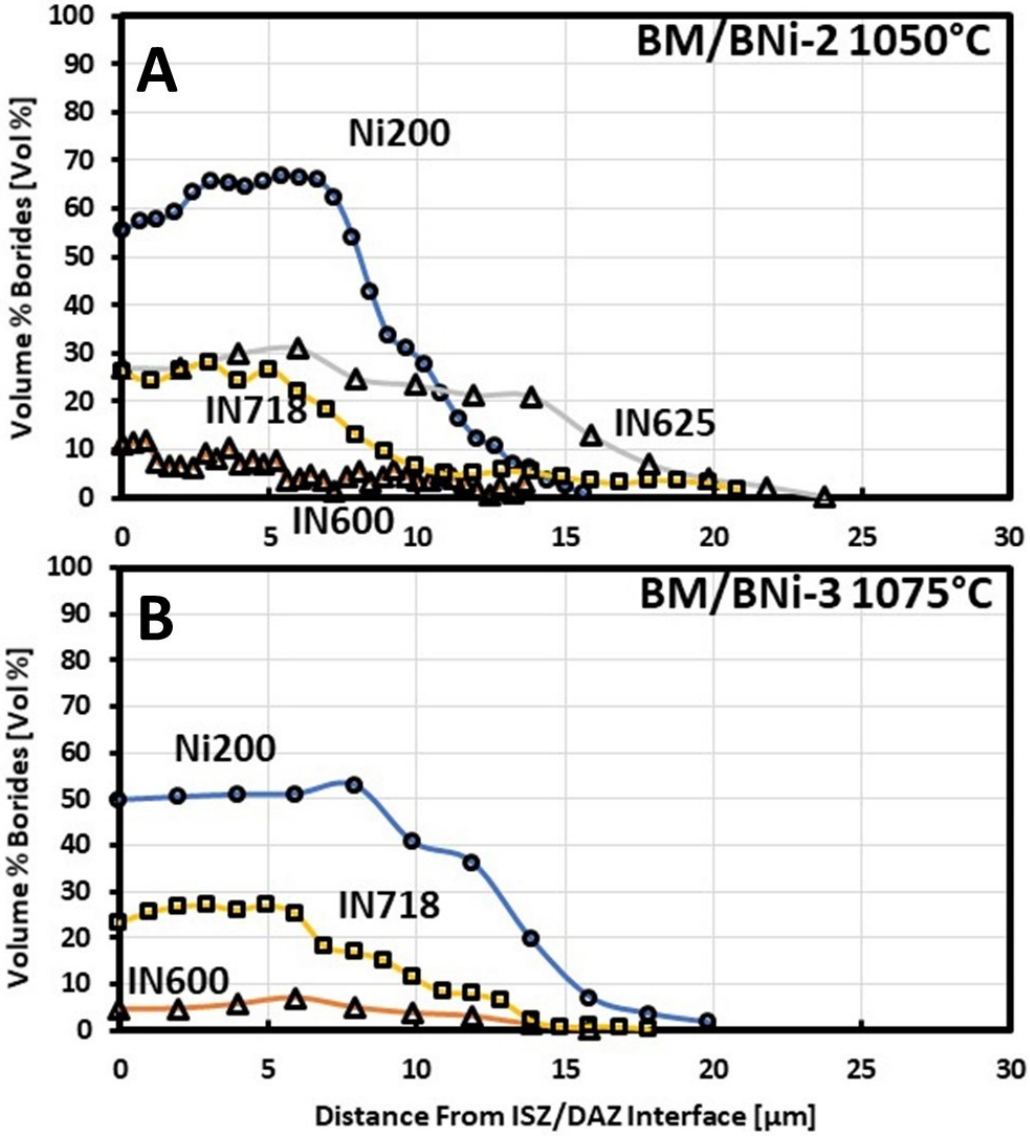

Figure 9-2 - Volume % boride profiles for all quenched BM/BNi-2 1050°C (A) and BM/BNi-3 1075°C (B) specimens (shown in Appendix C).

An estimate of the expected IBU thickness predicted by the boride formation in the DAZ can be determined from a modification of Eq. 4-12 (Chapter 4), as shown below:

$$\sum_{i=1}^{n} V_{DAZ} X_{DAZ} f_i \rho_i = V_{FM} C_o \qquad \textbf{Eq. 9-2}$$

Where the left-hand side is the summed mass of boron contained within the DAZ and the right-hand side is the corresponding boron that would be removed from the FM due to the boron redistribution. Dividing both sides by the common cross-sectional area yields the following:

$$\sum_{i=1}^{n} W_{DAZ} X_{DAZ} f_i \rho_i = W_{ISZi} C_o \qquad \textbf{Eq. 9-3}$$

$$W_{ISZi} = \frac{\sum_{i=1}^{n} W_{DAZ} X_{DAZ} f_i \rho_i}{C_o} \quad \text{Eq. 9-4}$$

Where, $\sum_{i=1}^{n} W_{DAZ} X_{DAZ}$ is a sum of all the area elements in Figure 9-2 and f_i and ρ_i have their previous meaning for the specific boride formed in the DAZ. Table 9-1 lists the values used in the right-hand side of the equation, as well as the calculated IBU thickness (W_{ISZi}). Note that in the absence of BMD, C_o e.g. the volume concentration of boron in the FM is equal to 0.247 g/cm^3, for BNi-2 and 0.252 g/cm3 for BNi-3. Since the braze couples undergo varying degrees of dissolution of a base metal containing no boron, BMD has the effect of reducing the boron concentration in the liquid phase. This was accounted for by dividing C_o by the dissolution factor $D_{mf} = 2W_{max}/2W_o$, where $2W_o$ was taken as 80 μm.

Table 9-1 - Summary of parameters used to calculate W_{ISZi} from Eq. 9-4.

BM	FM	D_{mf}	C_o (g/cm^3)	$\Sigma W_{Daz} X_{Daz}$ (μm)	f_i	ρ_i (g/cm^3)	W_{ISZi} (μm) Calculated	W_{ISZi} (μm) DSC/MBC
Ni200	BNi-2	2.08	0.119	6.51	0.060	8.07	26.7	27.5
	BNi-3	1.90	0.130	7.20	0.060	8.07	26.1	27.5
IN600	BNi-2	1.23	0.202	0.77	0.200	6.25	5.1	17.5
	BNi-3	2.09	0.118	0.69	0.247	6.25	9.0	24
IN625	BNi-2	1.00	0.247	4.58	0.214	6.202	24.2	16
IN718	BNi-2	1.25	0.198	2.66	0.214	6.202	17.8	24.5
	BNi-3	1.55	0.160	2.72	0.209	6.234	21.7	26.8

The calculated W_{ISZi}, using the boron redistribution mass balance, is in excellent agreement for the IN718/BNi-3 and Ni200/BNi-2 and BNi-3 couples. The biggest discrepancies exist for the IN600/BNi-2 and BNi-3 braze couples. This may be due to an underestimation in the area fraction of CrB in the DAZ. In these samples the precipitates were very fine such that image analysis may not have been able to measure all particles.

The modest discrepancies present for the IN718/BNi-2 and IN625/BNi-2 couples may relate to the fact that the DAZ consisted of light and dark borides with slightly different boron compositions. In the above analysis it was assumed that the relative ration of dark to light borides was 5%/95%. However, it was not possible to confirm this ratio accurately through the image analysis.

9.2 Isothermal Solidification

Table 9-2 summarizes all of the linear regression data acquired in current body of work, and subsequently used to generate the MBC plots illustrated in Figure 9-3. There are clear trends for the rate of isothermal solidification versus base metal type. The highest rates are exhibited by the Ni200, the lowest in the IN600 and intermediate in the IN625 and IN718 base metals. While the isothermal solidification time is dependent on both the degree of dissolution (i.e. gap widening) and rate of IS, Ni200 samples also show the shortest, IN600 the longest and IN625 and IN718 intermediate IS completion times. A recent review published by Pouranvari et al. examined the role of base metal composition on TLPB behavior [92]. The authors surveyed several Ni-based superalloy TLPB studies which examined the isothermal solidification time (t_{IS}) for a variety of base metals, filler metals and braze foil thicknesses at a reference temperature of 1100°C. They developed a normalized (t_{IS}) which attempted to account for the different foil thickness and filler metal compositions used. It was found that this normalized t_{IS} was reduced as the at% of boride formers in the base metal increased.

Table 9-2 - Summary of linear regression results obtained from all 20x cyclic DSC experiments.

	$-K_L$ ($min^{-1/2}$)	L_o (%)	k_W ($\mu m/min^{1/2}$)	$2W_i$ (µm)	$2W_{iszo}$ (µm)	$2W_o$ (µm)	t_{IS} (min)
Ni200/BNi2	0.06	0.81	10.3	135	32	167	172
Ni200/BNi3	0.08	0.82	12.7	124	28	152	105
IN600/BNi2	0.04	0.70	4.1	69	30	98	306
IN600/BNi3	0.03	0.77	4.3	128	39	167	653
IN625/BNi2	0.07	0.69	5.3	57	23	80	97
IN718/BNi2	0.04	0.66	4.8	62	38	100	245
IN718/BNi3	0.04	0.66	5.7	79	45	124	222

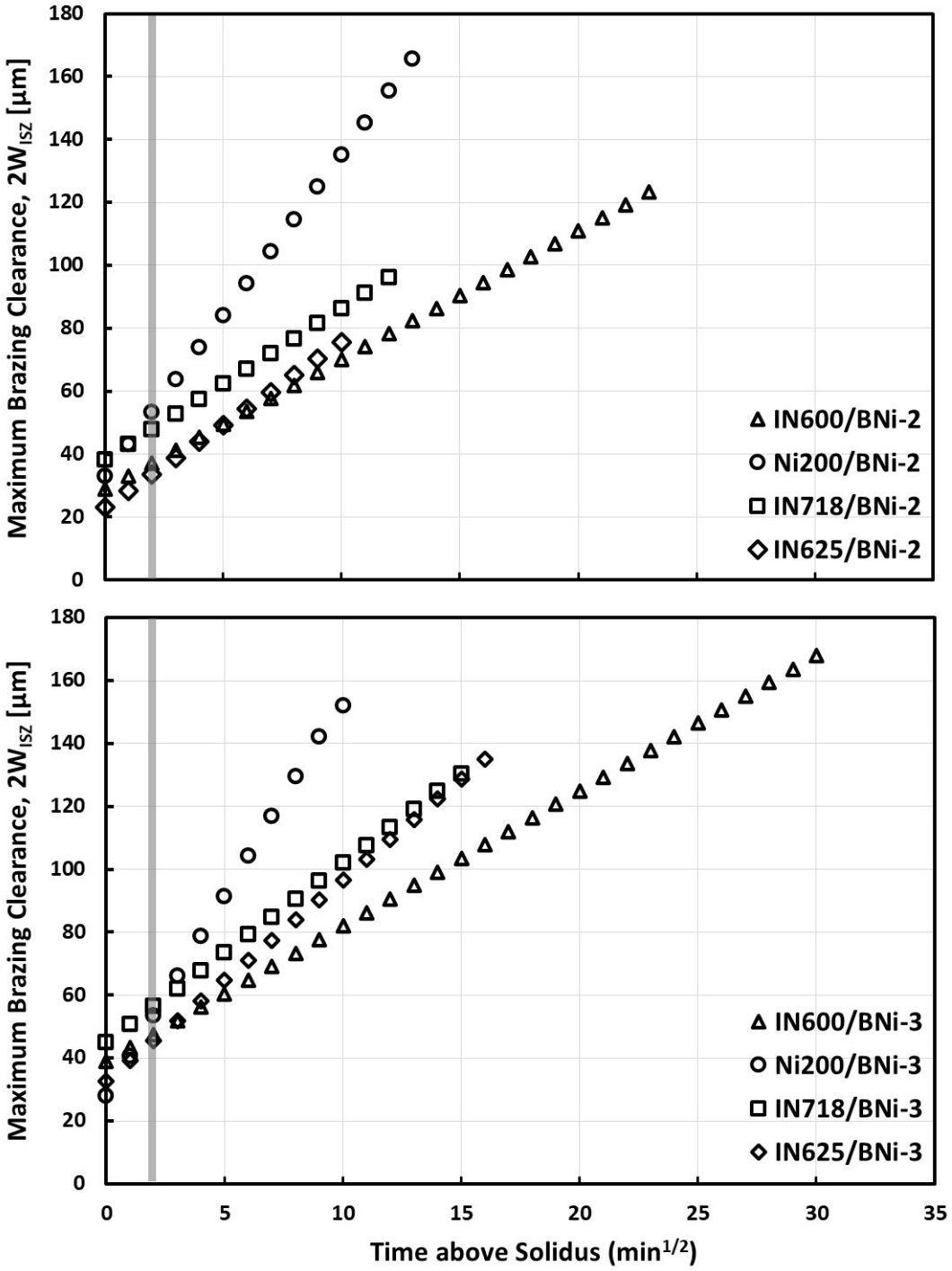

Figure 9-3 - Maximum brazing clearance, $2W_{ISZ}$ as a function of time above solidus for Ni200, IN600 and IN718 BMs for both BNi-3 and BNi-2 FMS. Shaded area denotes range of time ($min^{1/2}$) required to attain peak brazing temperature (1050 or 1075°C, at 20°C/min). IN718/BNi-2 data supplemented by ref. [116].

Table 9-3 lists the boride former content within the base metals of this investigation. It is important to observe that the thermodynamic favourability for the formation of Ni_3B in the Ni200 case, results in the highest boride former concentration, even though this is a commercially pure base metal. Once other boride formers are introduced and Ni_3B is no longer favoured, Ni was no longer considered a boride former.

Table 9-3 - Boride former content for various BMs, determined using ICP-OES results, Table 2-1.

BM	Primary Boride Constituents	Boride Former Concentration (wt%)				
		Ni	Cr	Mo	Nb	Total
Ni200	Ni	99.3	-	-	-	99.3
IN600	Cr	-	16.1	-	-	16.1
IN625	Cr, Mo, Nb	-	20.8	8.9	3.7	33.3
IN718	Cr, Mo, Nb	-	18.1	3.2	5.1	26.3

Both the rate of IS and the IS completion time are plotted in Figure 9-4A and Figure 9-4B as a function of the boride former concentration within the BM. The relationship between boride former content and the rate of IS is highly linear for a given filler metal used. The response of IS rate to boride former is more significant when BNi-3 and, as a consequence, brazing is done at a slightly higher temperature. This reinforces the conclusion that the rate of isothermal solidification is determined by the amount of boron redistributed from the liquid phase into the DAZ. Specifically, the total boride former content is a determining factor in the volume fraction and boron content of second particles precipitating in the DAZ layer. Figure 9-4B illustrates that a less straight forward relationship exists between isothermal solidification time and boride former content. This is due to the additional influence of base metal dissolution and gap widening, which is not a function of boride formation.

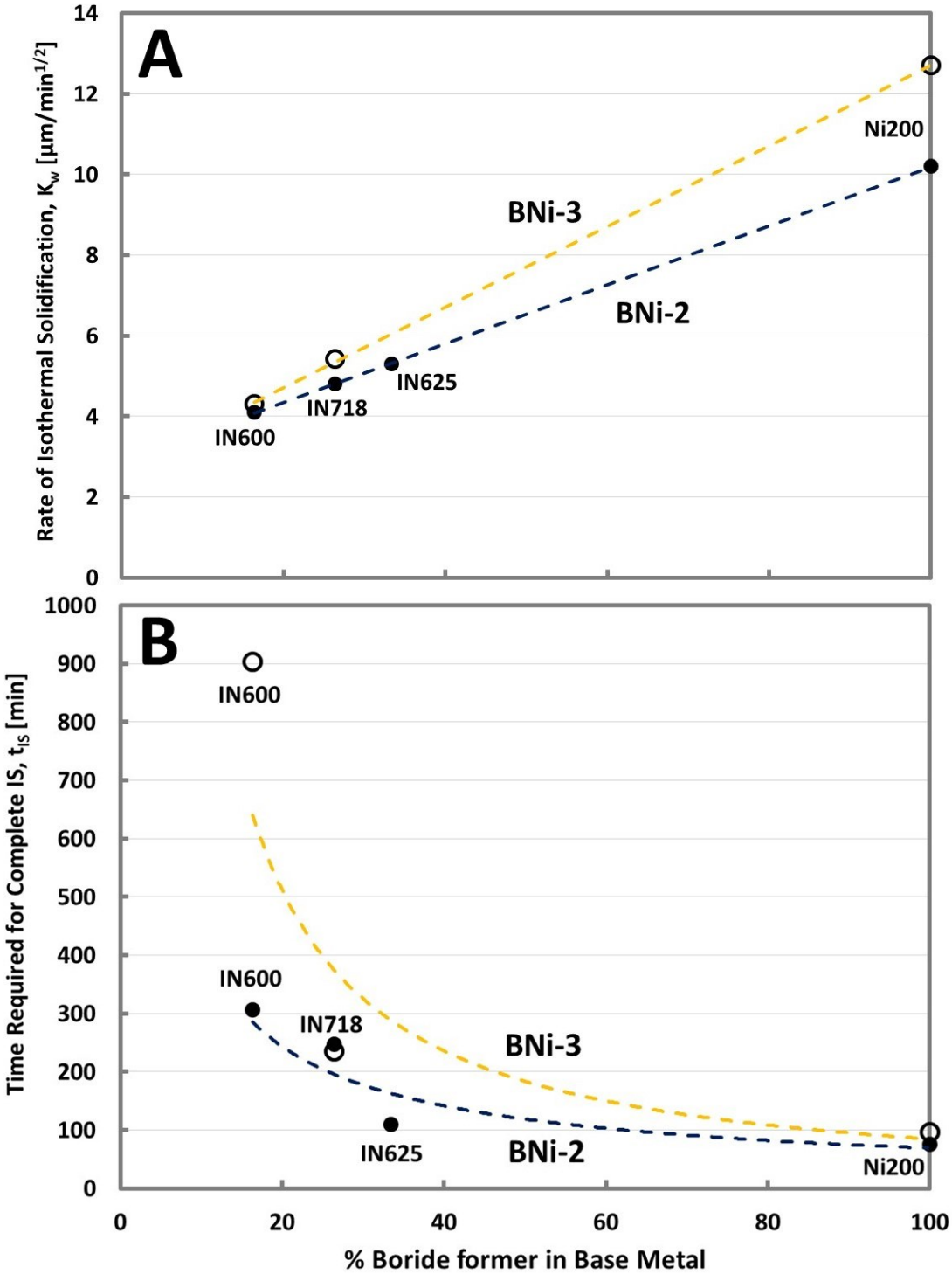

Figure 9-4 - Relationship between boride former content (wt%) and isothermal solidification rate, K_w, (A) and time required for complete isothermal solidification, t_{IS} (B).

A final confirmation of the boron redistribution argument can be made by examining the boride distribution for all the couples after IS has been completed (see Figure 9-5). The fraction of borides formed within the DAZ, their penetration depth and, as Table 9-1 shows, the boron content within the borides, f_i, vary greatly as a function of base metal type. It has also been observed that the level of dissolution varies greatly. Despite this, all braze couples were made using a single braze foil of repeatable size and weight. In the case of BNi-3 and BNi-2, the total boron mass in a single foil was 0.2208 and 0.2156 mg, respectively. From the boride distributions presented in Figure 9-5, the total mass of boron in the base metal upon IS completion can be determined by;

$$\boldsymbol{Mass\ of\ Boron\ in\ Base\ Metal} = A_o \sum_{i=1}^{n} W_{DAZ} X_{DAZ} f_i \rho_i \qquad \textbf{Eq. 9-5}$$

where A_o is the cross-sectional area of the foil (or base metal cylinder), all other parameters having their previous meaning.

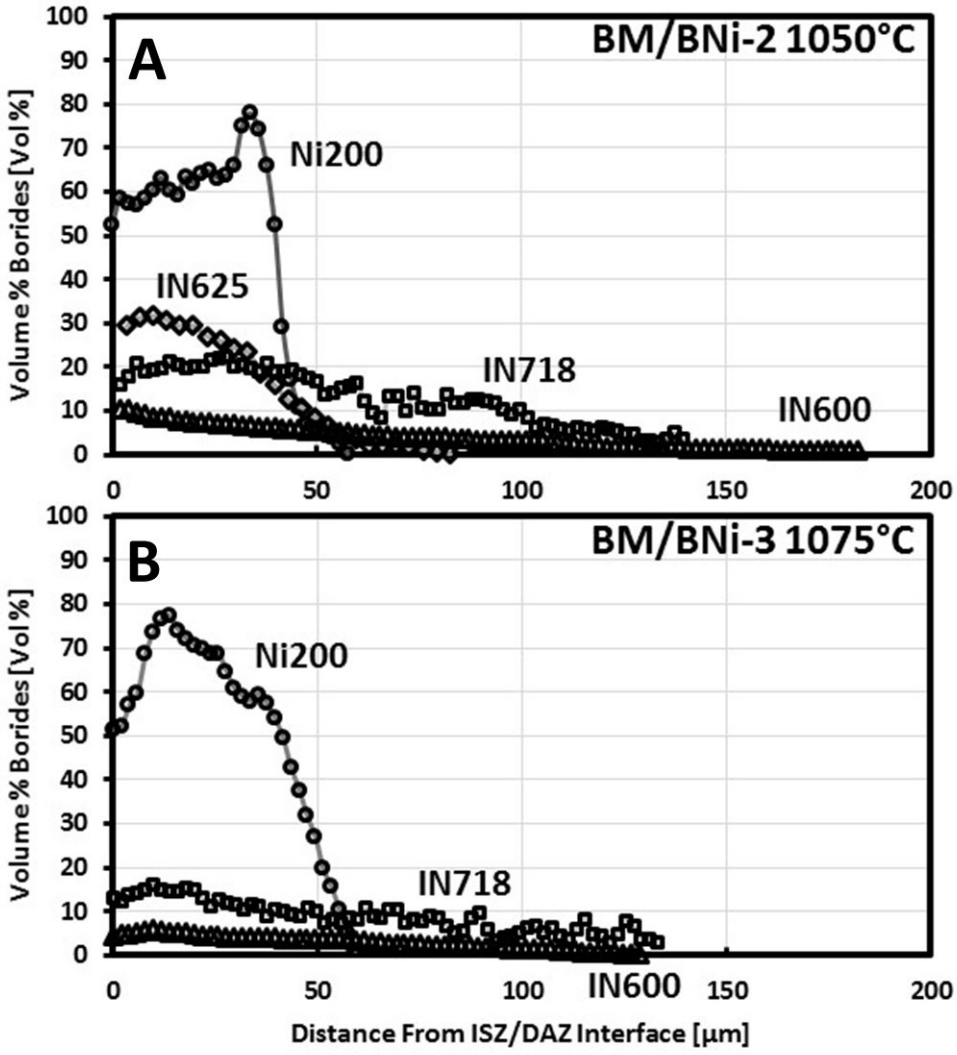

Figure 9-5 - Volume % boride profiles for 20x cycled BM/BNi-2 1050°C (A) and BM/BNi-3 1075°C (B) specimens.

Figure 9-6 plots the cumulative mass of boron contained within the base metal as a function of DAZ depth for each of the cycled specimens (complete IS), expressed as a % of the total boron mass contained within the filler metals. The Ni200/, IN625/ and IN718/BNi-2 braze couples all attain a boron content very close to that originally contained within the braze foil. Therefore, despite the many differences in the range of braze couples examined in this study, the same level of boron redistribution occurs when complete isothermal solidification is achieved. The IN600 braze couples and to a lesser extent the IN718/BNi-3 are an exception reaching about 80% and 90%, respectively, of the expected boron mass. In the case of IN600, this likely results from difficulties encountered during image analysis of the very fine CrB precipitates present within the

DAZ for these couples. In the case of IN718/BNi-3 and to some extent IN600, it may also be due to the fact that the area measurements encompassed by the images were insufficient to and therefore did not capture the full DAZ depth e.g. X_{DAZ} did not reach zero with the last area measurements made.

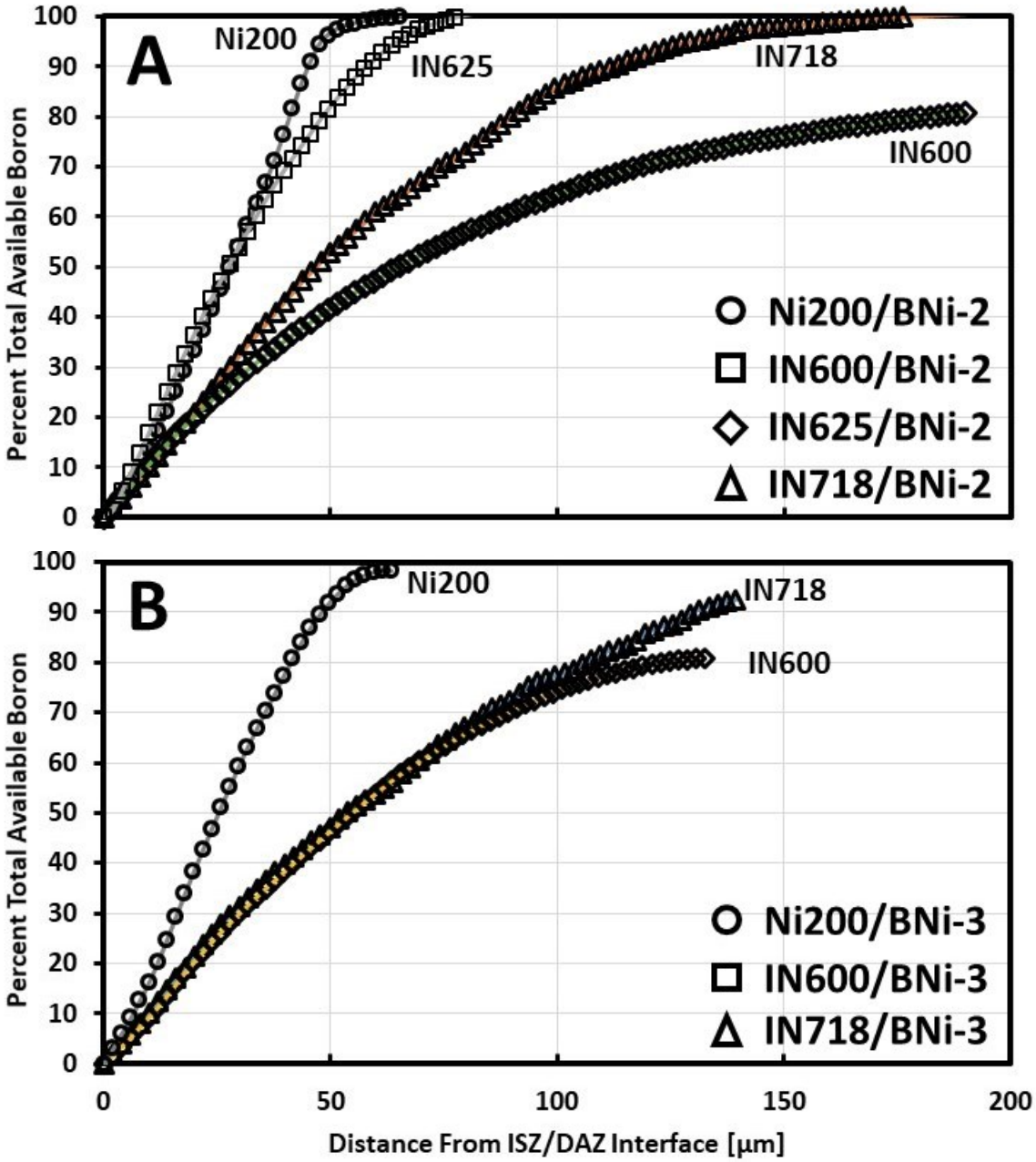

Figure 9-6 - Percent total available Boron as a function of depth into the DAZ for BM/BNi-2 (A) and BM/BNi-3 (B) couples. Measurements obtained from cycled (20x) DSC samples; 1050°C (BNi-2) and 1075°C (BNi-3).

CHAPTER 10 Conclusions and Future Work

The extensive DSC analysis demonstrated in the present body of work clearly reveals the impressive capability of DSC in examining the various aspects of TLPB. The technique can effectively provide a wealth of information regarding each of the stages; heating, melting, isothermal solidification and homogenization. For instance, DSC analysis can determine the solidification rate, maximum brazing clearance, remelt temperature, and qualitative information regarding BMD; all of which are of great importance to any vacuum brazing operation, but also crucial to understanding the thermal stability of the resulting microstructure. It is thus a very powerful tool which is highly amenable to TLPB, with a great deal of potential for effective and efficient screening/characterizing of TLPB systems as compared to conventional means.

The importance of the current research relates to process optimization of vacuum brazing operations, more specifically, establishing guidelines in the selection of BM/FM couples. For instance, knowledge of the IBU phenomenon highlighted in the present work ensures that the gap width is sufficient to enable proper wetting/spreading which may be compromised in thin gaps. The results suggests that when brazing with Boron-containing FMs, BMs can be selected such that they're compositions favor appreciable precipitation of borides, which according to the current work is best achieved with increasing concentration of the stronger boride forming elements. BM and FM compatibility are also of great importance and large compositional differences should be avoided due to the generation of excess quantities of liquid phase which may extend the time required to achieve complete IS.

The following sections will highlight the principal conclusions drawn for each of the studies and how they relate to the mechanisms governing TLPB (e.g. IBU, BMD and IS) with boron containing filler metals, followed by potential areas for future work which seek to extend the proven effectiveness of the DSC method to additional systems to further validate the observations made and further understand the role the various process parameters play in TLPB.

10.1 Conclusions

The objective of the research was to reassess the current understanding of TLPB related to the mechanisms governing TLPB with Boron-containing FMs in comparison to conventional TLPB theory, due to the unique properties of Boron as a MPD. The main conclusions relating to the mechanisms governing TLPB are summarized as follows:

Initial Boron Uptake (IBU) – The IBU phenomenon observed for all specimens examined is believed to be a direct consequence of both Boron's insolubility in Ni and its rapid interstitial diffusivity. This was shown to be a result of the requirement to maintain equilibrium, given the significant differences in the diffusivity of Si and B. Immediately upon melting, boron diffuses ahead of the slower diffusing species (Si, Fe, Cr, Ni), into the BM where it precipitates immediately owing to its poor solubility in Ni. This established equilibrium favors continued solid-state transport (or segregation) of Boron to the existing borides, leaving behind the γ-Ni. The similar IBU values observed for all of the MB/FM examined is believed to be linked to the segregation behavior of B and Si, as the relative proportions were identical for both FMs.

The relationship between IBU and BMD was difficult to assess given the transient nature of heating and BMD process. The results demonstrated that BMD appears to enhance the overall severity of the IBU, however only to a minor extent. This results from partial dissolution/melting of the initial interfacial borides and associated modification of the composition of the liquid enhancing the rate at which the new DAZ is formed.

Base Metal Dissolution (BMD) - The consequence of BMD is an increase in the initial width and/or quantity of the liquid phase and modification of the liquid phase with the BM constituents. The severity of BM dissolution is overall greater for BM/FM couples displaying a greater degree of the compositional difference. Furthermore, as BMD follows IBU e.g. in-situ boride precipitation, its severity is likely attributed to the stability/type of boride phase formed. In theory (and in practice) BMD should be minimized as the composition of the FM approaches that of the liquidus of the BM-FM system. Such behavior is clearly represented by the simpler BMs (Ni and IN600).

Isothermal Solidification (IS) - The rate IS is directly related to magnitude and extent to which boron in redistributed from the liquid phase into the BM as borides (DAZ). Specifically, the total boride former content of a BM is a determining factor in the volume fraction and boron content of intermetallic precipitation in the DAZ layer. Consequently, BM chemistry play a far more significant role as compared to that of the FM. Despite the many differences in the range of braze couples examined in this study, the same level of boron redistribution occurs when complete isothermal solidification is achieved. Nonetheless, FM selection was shown to aggravate BMD which in turn altered the liquid phase(s) resulting in enhanced rates of solidification. However, the marked increase in the quantity of liquid phase necessitated longer times to achieve complete isothermal solidification.

The exhaustive research demonstrated a complex interplay between IBU, BMD and the rate of IS which could be effectively measured and quantified in a simple linear relationship. However, a less straight forward relationship exists between the isothermal solidification time, t_{IS} and boride former content. As the severity of the IBU was shown to be essentially independent of the BM/FM couples evaluated in the current work, one would expect that t_{IS} be a simple compromise between BMD and the rate of IS. However, it was shown that the undesirable increase in the liquid quantity that would be expected to lengthen t_{IS}, led to enhanced solidification rates due to modification of the liquid phase and preferential precipitation of Borides of greater boron content. Hence, the influence of BMD and/or gap widening is not a function of boride formation. Thus, although the rate of solidification was successfully directly linked to boride precipitation, the mechanisms of BMD are far more complex than generally acknowledged and thus is its importance in determining the most sought-after parameter in TLPB processes, t_{IS}, revealed.

10.2 Future Work

The successful application of the DSC methods described in the current body of work demonstrates immense potential of DSC as a novel means of efficiently screening and characterizing an essentially infinite combination of BM/FM systems. The following summarizes various areas of research related to TLPB of particular interest to the present work in addition to other areas of great commercial importance.

1 Examine the IN625/BNi-3 system at 1075°C, to complete the comparison between the two FMs BNi-2 and BNi-3 with the various BMs examined in the current work to further validate the conclusions established above.

2 Explore additional commercially available FMs containing greater or lesser concentrations of Boron such as BNi-4 (Ni-1.8B-3.5Si) and BNi-9 (Ni-3.6B-15Cr-1.5Fe), the former would be expected to accelerated IS owing to the reduced total boron content, the latter would enable one to further to isolate the influence Si has on the TLPB response.

3 Apply the various methods to the innumerable number of BMs currently available. Fundamental studies examining simple Ni-based alloys, such as Monel, Ni-Cu and Nitinol, Ni-Ti could provide a wealth of data related to the underlying mechanisms governing Boron precipitation.

4 Examine the TLPB response related to BM grain structure using the various DSC techniques demonstrated in the present work. This would be particularly suited for specialized manufacturing techniques such as powder metallurgy, directionally solidified and single crystal BM, all of which are of great commercial importance. Such work would permit far more effective quantitative examination on the effects of grain structure on the aforementioned TLPB mechanisms governing as.

REFERENCES

1 Properties and Selection: Non-Ferrous Alloys and Special-Purpose Materials. ASM Handbook. Vol. 2 (1992).

2 R. C. Reed, The Superalloys – Fundamentals and Applications. Cambridge University Press (2006). pp 217-282.

3 R. W. Messler, Joining of Materials and Structures: From Pragmatic Process to Enabling Technology. Elsevier Inc. (2004). pp. 3-44.

4 D. L. Olson, T. A. Siewert, S. Liu, G. R. Edwards, ASM Handbook Volume 6: Welding, Brazing, and Soldering. ASM International (1993).

5 I. Bhamji, M. Preuss, P. L. Threadgill, A. C. Addison, Solid-State Joining of Metals by Linear Friction Welding: A Literature Review. J. Mat. Sci. Tech. Vol. 27 (2011) pp. 2 – 12.

6 W.A. Owczarski, W.H. King, D.S. Duvall, Diffusion Welding of the Ni-base Superalloy, U.S. Patent# 3,530,568 (1970).

7 D. S. Duvall, W. A. Owczarski, D. F. Paulononis, TLP Bonding: A New Method for Joining Heat Resistant Alloys. Welding Journal Vol. 53(4) (1974). pp. 203-214.

8 W. D. MacDonald, T. W. Eager, Transient Liquid Phase Bonding Processes. The Metal Science of Joining (1992). pp. 93-100.

9 Tuah-Poku, M. Dollar, T. B. Massalski, A Study of the Transient Liquid Phase Bonding Process Applied to an Ag/Cu/Ag Sandwich Joint. Metallurgical and Materials Transactions A, Vol. 19, No. 3, 1988, pp. 675-686.

10 G. Wallis, and D. I. Pomerantz, Field-assisted glass-metal sealing. Journal of Applied Physics 40 (1969) pp. 3946–3949

11 M. Way, J. Willingham, R. Goodall, Brazing handbook 5th edition, AWS, 550 N.W. LeJeune Road, Miami, FL 33126. (2007)

12 Brazing Filler Metals. Int. Mat. Rev. (2019) pp. 1743 – 2804.

13 Dayton Process BV – Fluoride Ion Cleaning Process. Vac Aero International (2016).

14 Brazing Handbook 5th Edition, American Welding Society (AWS) - C3 committee on Brazing and Soldering. 550 N.W. LeJeune Rd. Miami, FL 33126, (2007).

15 P. Roberts, Industrial Brazing Practice, CRC Press. 2nd Ed. (2013) pp. 266-314.

16 Design World Article, New Materials Take the Heat in Aerospace Engine Design and Manufacture, Morgan Advanced Materials (2009).

17 S. D. Nelson, S. Liu, S. Kottilingam, J. C. Madeni, Spreading and Solidification Behavior of Nickel Wide-gap Brazes. Weld World Vol. 58 (2014). pp. 593-600.

18 S. K. Tung, L. C. Lim, Void Formation in Wide-gap Brazing using Prepacks of Nickel Base Braze Mixes. J. Mat. Sci. Tech. Vol.10 (1994). pp. 364-369.

19 T. V. Gaevskaya, I. G. Novotortseva, L. S. Tsybulskaya. The Effect of Boron on the Microstructure and Properties of Electrodeposited Nickel Films. Met. Finishing (1996). pp. 100-103.

20 J. T. Niemann, R.A. Garett, Eutectic Bonding of Boron-Aluminum Structural Component, Part 1. Welding Journal Vol. 53(4) (1974) pp. 175-183.

21 M. Weinstein, R. L. Peaslee, F. M. Miller, How to Choose Nickel-Based Filler Metals for Vacuum Brazing. Brazing Journal Supplement (2008) pp. 59-61.

22 B. Zorc, L. Kosec, Comparison of brazed joints made with BNi-1 and BNi-7 nickel-base brazing alloys. Rev. Metal. Madrid Vol. 36 (2000).

23 ASM Special Handbook - Heat Resistant Materials. ASM International (1992). pp. 218-343.

24 S. R. Shatynski, The Thermochemistry of Transition Metal Carbides. Oxidation of Metals Vol. 13(2) (1979

25 N. Birks, G. Meier, and F. Petit, Overview: Forming Continuous Alumina Scales to Protect Superalloys. JOM Vol. 46 (12). (1994) pp. 42-46.

26 S. Grisaffe, Coatings and Protection, The superalloys. Wiley Interscience, New York. (1972) pp. 341-370.

27 N. Czech, F. Schmitz, and W. Stamm, Microstructural Analysis of the Role of Rhenium in Advanced MCrAlY Coatings, Surf. Coat. Technol. Vol. 76/77 (1995) pp. 28-33.

28 T.B. Massalski, P.R. Subramanian, H. Okamoto, and L. Kacprzak: Binary Alloy Phase Diagrams, 2nd ed., ASM International, Materials Park, OH, 1990.

29 J.E. Ramirez, S. Liu, Diffusion Brazing in the Nickel-Boron System. Welding Journal, Supplement. (1992) pg. 365-376.

30 T. Tokunaga, K. Nishio, M. Hasebe, Thermochemical Study of Phase Equilibria in the Ni-Si-B System. J. Phase Equilibria Vol. 22 (3). (2001) pp. 291-299.

31 K.C. Anthony, J.F. Radavich, Solute Effects of Boron and Zirconium on Microporosity. Proc. 3rd Symposium, Claitor Publishing. (1976)

32 R.V. Miner, Effects of Silicon on the Oxidation, Hot-Corrosion, and Mechanical Behavior of Two Cast Nickel-base Superalloys. Metallurgical Transactions, Vol.8 (A). (1977) pp. 1949-1954.

33 B. Jansson, J. Agren, A thermochemical Assessment of Liquid-Solid Equilibria in Nickel-rich Ni-Si-B Alloys. J. Materials Science and Engineering Vol. 63. (1984) pp. 51-60.

34 S. Lebaili, S. Hamar-Thibault, *Acta Metall.,* (1987), Vol. 35(3), pp. 701-710.

35 A. Bondar, Boron - Chromium – Nickel. Landolt-Börnstein - Group IV Physical Chemistry (MSIT) Vol. 11E1 (2009) pp. 153-167

36 H. Nakagawa, C. H. Lee, T. H. North, Modeling of Base Metal Dissolution Behavior during Transient Liquid-Phase Brazing. Metallurgical Transactions A Vol. 22A (1991) pp. 543-555.

37 Y. Nakao, K. Nishimoto, K. Shinozaki, C. Kang, Theoretical Research on Transient Liquid Insert Metal Diffusion Bonding of Nickel Base Alloys. Transactions of Metal Welding Society Vol. 20 (1989). pp. 60-65.

38 S. Liu, D.L. Olson, G.P. Martin, G. R. Edwards, Modeling of Brazing Processes that use Coatings and Interlayers. Journal of Welding Research Supplement Vol.70(8) (1991) pp. 207s-215s.

39 D. A. Porter, K. E. Easterling, Phase Transformations in Metals and Alloys (3^{rd}). Chapman & Hall. (1992).

40 K. Ohsasa, T. Shinmura, T. Narita, Numerical Modeling of the Transient Liquid Phase Bonding of Ni using Ni-B-Cr Ternary Filler Metal. J. Phase Equilibria. Vol. 20(3) (1999) pp. 199-206.

41 A. Ghoneim. O. A. Ojo, Numerical Modeling and Simulation of a Diffusion-Controlled Liquid-Solid Phase Change in Poly Crystaline Solids. Computational mat. Sci. Vol.50 (2011) pp. 1102-1113.

42 C.W. Sinclair, Modeling Transient Liquid Phase Bonding in Multicomponent Systems. J. of Phase Equilibira. Vol. 20(4) (1999) pp. 361-369

43 C.W. Sinclair, G.R. Purdy, J.E. Morral, Transient Liquid-Phase Bonding in Two-Phase Ternary Systems. Metall. Matl. Trans. A. Vol. 31A (2000) pp. 1187-1192.

44 R. B. McLellan, The Diffusion of Boron in Nickel. Scripta Met. Mat. Vol. 33(8) (1995) pp. 1265-1267.

45 M. Hasaka, T. Morimura, Y. Uchiyama, S.Kondo, T. Watanabe, K.Hisatsune and T. Furuse, Diffusion of Copper, Aluminum and Boron in Nickel. Scipta Met. Mat. Vol. 29 (1993) pp. 959-962.

46 G. R. Johnson, Diffusion of Chromium and Silicon in Nickel Solid-Solution alloys of the Ni-Cr-Si System. J. High Temperatures – High Pressures Vol. 14 (1982) pp.695-707.

47 R. A. Swalin, A. Martin, R. Olson, Diffusion of Magnesium, Silicon, and Molybdenum in Nickel. J. Metals – AIME Trans. (1957) pp. 936-939.

48 St. Frank, U. Sodervall, Chr. Herzig, Fast Diffusion of Boron in the Intermetallic Compound Ni3Al. J. Intermetallics Vol. 5 (1997) pp. 221-227.

49 N.P. Wikstrom, O.A. Idowu, O.A. Ojo, M.C. Chaturvedi, Deviation from Conventional Transient Liquid Phase Bonding Models during Diffusion Brazing of Nickel-base Superalloys, Proc. 3rd int. Brazing and Soldering Conf. TX, USA (2006).

50 W.F. Gale, S. Orel, Microstructural Development in NiAl/Ni-Si-B-Ni Transient Liquid Phase Bonds. Metall. Mater. Trans. A, Vol. 27(7) (1996) pp. 1925-31.

51 W.F. Gale, E. Wallach, Microstructural Development in Transient Liquid-Phase Bonding. Metall. Mater. Trans. A, Vol. 22(10) (1991a) pp. 2451-57.

52 W.F. Gale, E. Wallach, Influence of Isothermal Solidification on Microstructural Development in Ni-Si-B Filler Metals. Mater. Sc. Tech. Vol. 7(12) (1991b) pp.1143-48.

53 J. Kucera, A. Buchal, A. Rek, and K. Stransky: *Kovove Mater.*, 1984, vol. 22, pp. 250–62.

54 I. A. Akimova, B. M. Mironov and A. V.Pokoev : Izv. V. U. Z. Tsvetn. Metall. Vol. 5 (1985).

55 Allison H.W., Samelson H. Diffusion of aluminum, magnesium, silicon, and zirconium in nickel. J. Appl. Phys. 1959;30(9):1419–1424.

56 Swalin R.A., Martin A., Olson R. Diffusion of magnesium, silicon, and molybdenum in nickel. J. Met. Vol. 9 (1957).

57 C. Hargather, S. Shanga, Z. Liu, Y. Du, Data Set for Diffusion Coefficients and Relative Creep Rate Ratios of 26 dilute Ni-X alloy systems from first-principles calculations. Data in brief Vol. 20 (2018) pp. 1537-1551.

58 C. Hargather, S. Shanga, Z. Liu, Y. Du, A First-Principles Study of Self-Diffusion Coefficients of FCC Ni. Comp. Mat. Sci. Vol. 86 (2014). pp. 17-23.

59 M. Pouranvari, A. Ekrami, A. H. Kokabi, Microstructure Evolution Mechanism during Post-bond Heat Treatment of Transient Liquid Phase Bonded Wrought IN718 Superalloy: An Approach to Fabricate Boride-Free Joints. J. Alloys and Compounds Vol. 723 (2017) pp. 84-91.

60 S. Hadibeyk, B. Beidokhti, S. A. Sajjadi, Effect of bonding time and homogenization heat treatment on the microstructure and mechanical properties of the transient liquid phase

bonded dissimilar GTD-111/FSX-414 TLP superalloys. J. Alloys and Compounds Vol. 731 (2018) pp.929-935.

61 A. Amirkhania, B. Beidokhtib, K. Shirvanic, M.R. Rahimipoura, Two-step Heating Transient Liquid Phase Bonding of Inconel 738LC. J. Mat. Proc. Tech. Vol. 266 (2019) pp 1-9.

62 S. Steuer, R. F. Singer, Suppression of Boride Formation in Transient Liquid Phase Bonding of Pairings of Parent Superalloy Materials with Different Compositions and Grain Structures and Resulting Mechanical Properties. J. Met. Matl. Trans. Vol. 45A (2014) pp. 3545-3553.

63 R. M. German, Sintering Theory and Practice. Wiley-VCH (1996).

64 K. Saida, Y. Zhou, T.H. North, The Influence of Base Metal Grain Size on Isothermal Solidification during Transient Liquid-Phase Brazing of Nickel. J. Matl. Sci. Vol. 28(1993) pp. 6427-6432.

65 K. Ikeuchi, Y. Zhou, H. Kokawa, T.H. North, Liquid-Solid Interface Migration at Grain Boundary Regions during Transient Liquid Phase Brazing. Met. Trans. Vol. 23A (1992) pp. 2905-2915.

66 Y. Zhou, T. H. North, Z. Wang, TLP-Brazing of Nickel-Numerical Modelling and Experimental Verification. Proc. 3rd Int. SAMPE Metals Conf. (1992) pp. M611-M619

67 E. Hinchy, M.J. Pomeroy, D.A. Tanner, The Effect of Single Crystal And Welded Substrates on The Development of Braze Microstructures. J. Alloys and Compounds Vol. 690 (2017) pp. 856-863.

68 A. Ghasemi, M. Pouranvari, Fast Isothermal Solidification During Transient Liquid Phase Bonding of Nickel Alloy Using Pure Copper Filler Metal: Solubility vs. Diffusivity, J. Met. Mat. Trans. A Vol. 50A (2019) pp. 2235-2245.

69 W. J. Boettinger, U.R. Kattner, K.W. Moon, J.H. Perepezko, DTA and Heat-Flux DSC Measurements of Alloy Melting and Freezing: Practice Guide. National Institute of Standards and Technology, Special Publication, (2006)

70 F. Long, Y.S. Yoo, C.Y. Jo, Journal of Alloys and Compounds 478(1):181-187, 2009.

71 J. Ruiz-Vargas, N. Siredey-Schwaller, P. Bocher, A Hazotte, First Melting Stages during Isothermal Brazing of Ni/BNi2 Couples. J. Mater. Proc. Tech. Vol. 213 (2013a) pp. 2074-80.

72 D.M. Turriff, S.F. Corbin, M. Kozdras, Diffusional Solidification Phenomena in Clad Aluminum Automotive Braze Sheet. Acta. Mater., Vol. 210(8) (2010) pp. 1332-1341.

73 S. Corbin, P. Lucier, Thermal Analysis of Isothermal Solidification Kinetics During Transient Liquid-Phase Sintering. Metall. Mater. Trans. A, Vol. 32(4) pp. 971-978.

74 M.L. Kuntz, S.F. Corbin, Y. Zhou, Quantifying Metallurgical Interactions in Solid/Liquid Diffusion Couples using Differential Scanning Calorimetry. Acta Mater., Vol. 53(10) (2005) pp. 3071-82.

75 Kunts, N. Weyrich, C. Leinenbach, Characterization of the Isothermal Solidification Process in the Ni/Au-Ge Layer System. J. Matter Sci. 2015 (50) 3835-3844

76 M. L. Kuntz, Y. Zhou, S. F. Corbin, A Study of Transient Liquid-phase Bonding of Ag-Cu using Differential Scanning Calorimetry. Metall Mater Trans A Vol. 37 (2006) pp. 2493–2504.

77 M. L. Kuntz, P. Panton, S. Wasiur-Rahman, Y. Zhou, S. F. Corbin, An experimental study of transient liquid phase bonding of the ternary Ag-Au-Cu system using differential Scanning Calorimetry. Metall. Mater. Trans. A Vol.8 (2013) pp. 3708–3720.

78 D.C. Murray, S.F. Corbin, Determining the Kinetics of Transient Liquid Phase Bonding of Inconel 625/BNi-2 Couples using Differential Scanning Calorimetry. J. Mater. Proc. Tech., Vol. 248 (2017) 92-102.

79 N. Weyrich, C. Leinenbach, Characterization of the isothermal solidification process in the Ni/Au–Ge layer system. J. Mat. Sci. Vol. 50(10) (2015) pp. 3835 – 3844.]

80 Signal Detection Info Sheet, SEM108, Hitachi High Technologies America Inc. (2007)

81 J. Ruiz-Vargas, N. Siredey-Schwaller, P. Noyrez, S. Mathieu, P. Bocher, N. Gey, Potential and Limitations of Microanalysis SEM Techniques to Characterize Borides in Brazed Ni-based Superalloys. J. Mater. Charac. Vol. 94 (2014) pp. 46-47.

82 Analysis of Boron with J. Berlin (Bruker), Energy Dispersive X-ray Spectrometry – Advances in Light Element Analysis with SDD Technology. Imaging and Microscopy (EMS) Vol. 13 (2011) pp. 19-21.

83 G. O. Cook, C. D. Sorensen, J. Mater. Sci., Vol. 46 (2011) pp. 5305-5323.

84 M. Pouranvari, A. Ekrami, Diffusion Brazing Metallurgy of IN718-BNi2-IN718, Pouranvari Supplement, Vol. 93 (2014) 60-s, Journal of Welding Research

85 M. Pouranvari, A. Ekrami, Diffusion Induced Isothermal Solidification during Transient Liquid Phase Bonding of Cast IN718 Superalloy, Canadian Metallurgical Quarterly, Vol. 53(1) (2014).

86 K. Tokoro, N.P. Wikstrom, O.A. Ojo, M.C. Chaturvedi, Variation in Diffusion-Induced Solidification Rate of Liquated Ni-Cr-B Insert during TLP Bonding of Waspalloy Superalloy. *Mat. Sci. Eng. A.*, Vol. 477A (2008). pp. 311-318.

87 S. Omori, Y. Hashimoto, K. Shoji, K. Hidaka, Y. Kohira, Funtai Oyobi Funmatsuyakin Vol. 18. (1972) pp. 316.

88 M.A. Arafin, M. Medraj, D.P. Turner, P. Bocher, Transient Liquid Phase Bonding of Inconel 718 and Inconel 625 with BNi-2: Modeling and Experimental Investigations. *Mat. Sci. Eng. A*, Vol. 447 (1-2) (2007) pp. 125-133.

89 S.K. Tung, L.C. Lim, M.O. Lai, Solidification Phenomena in Nickel Base Brazes Containing Boron and Silicon. Scripta Materialia, Vol. 34(5). (1996) pp. 763-769.

90 K.D. Partz, E. Lugscheider, High Temperature Brazing of Stainless Steel with Nickel-based Filler Metals, BNi-2, BNi-3, BNi-5 and BNi-7, *Welding Journal,* Vol. 62 (1983) pp. S160-S164.

91 A. Sakamoto, C. Fujimara, T. Hattori, S. Sakai, Optimizing Processing Variables in High-Temperature Brazingwith Nickel-based Filler Metals. *Welding Journal,* Vol. 68 (1989) pp. 63-67.

92 M. Pouranvari, A. Ekrami, A.H. Kokabi, Role of base-metal Composition in Isothermal Solidification during Diffusion Brazing of Nickel-based Superalloys, J. Science and Technology of Welding and Joining, vol. 23 (1) (2018) pp. 13-18.

93 B. Zhang, G. Sheng, Y. Jiao, Z. Gao, X. Gong, H. Fan, J. Zhong, Precipitation and Evolution of Boride in Diffusion Affected Zone of TLP Joint of Mar-M247 Superalloy. J. Alloys Compounds Vol. 695 (2017) pp. 3202-3210.

94 K. Bai, F.L. Ng, T.L. Tan, T. Li, D. Pan, Understanding non-parabolic solidification kinetics in Ni-based alloys during TLP bonding via thermo-kinetic modelling. J. Alloys and Compounds, Vol. 699 (2017), pp. 1084-1094.

95 A. G. Kvashnin, A. R. Oganov, A. I. Samtsevich, Z. Allahyari, J. Phys. Chem. Lett., Vol. 8 (2017) pp. 755-764A.

96 Schnell, A. Stankowski, E. deMarcos, Proc. of GT2006 ASME Turbo 2006: Power for Land, Sea, and Air. (2006) pp. 949-961.

97 X.J. Yuan, M.B. Kim, C.Y. Kang, Effects of Boron and Silicon on Microstructure and Isothermal Solidification during TLP Bonding of a Duplex Stainless Steel using Two Ni-Si-B Insert Alloys. J. Mater. Sci. Tech. Vol.27(7) (2011) pp. 1191-1197.

98 J.D. Schobel, N.H. Stadelmaier, Z. Metallkd. Vol. 56 (1965) pp. 856.

99 W. F. Gale, E. R. Wallach, Wettability of Nickel Alloys by Boron-Containing Brazes. Welding Research Supplement. (1991) pp. 76-79.

100 A.T. Egbewande, C. Chukwukaeme, O.A. Ojo, Joining of Superalloys Inconel 600 by Diffusion Induced Isothermal Solidification of a Liquated Insert Metal, J. Materials Characterization. Vol. 59 (2008) pg. 1051-1058.

101 J.E. Ramirez, S. Liu, Diffusion Brazing in the Nickel-Boron System. Welding Journal Supplement, AWS. (1992) pp. 365-375.

102 M. Abdelfatah, O.A. Ojo, Formation of Eutectic-type Microconstituents during Transient Liquid Phase Bonding of Nickel: Influence of Process Parameters, Proc. 3rd int. Brazing and Soldering Conf. TX, USA (2006).

103 S.V. Orel, L. Parous, and W. F. Gale: Welding Journal Vol.74 (9). (1995) pp. 319-324.

104 J.B. Clark, AIME Trans. 227, 1250 (1963).

105 R. Metselaar, Diffusion in Solids. Part One: Introduction to the Theory of Diffusion, J. Mat. Ed. 6 (1 and 2):229 (1984).

106 R. Metselaar, Diffusion in Solids. Part Two: Diffusion in Binary Systems, J. Mat. Ed. 7 (4):653 (1985).

107 J. Ruiz-Vargas, N. Siredey-Schwaller, N. Gey, P. Bocher, A Hazotte, Microstructure Development During Isothermal Brazing of Ni/BNi2 Couples. J. Mater. Proc. Tech. Vol. 213(1) (2013b) pp. 20-29.

108 A. D. Jamaloei, A. Khorramb, A. Jafari, Characterization of microstructure and mechanical properties of dissimilar TLP bonding between IN718/IN600 with BNi-2 interlayer, J. Mat. Proc. Vol. 29 (2017). pp. 447-457.

109 W. F. Gale, E. R. Wallach, Wetting of Ni alloys by Ni based Brazes. J. of Materials Science and Technology (6). (1990) pp. 170-175.

110 R. Aluru, N. I. Sofyan, J. W. Fergus, W.F. Gale, Wide-Gap Transient Liquid Phase Bonding of Single Crystal to Polycrystalline Nickel-base Superalloys: Microstructural Development and Mechanical Properties. ASM Proc. 7th int. Conf. Weld. Research. (2005) pp. 879- 883.

111 J. R. McDermid, M. D. Pugh, R. A. L. Drew, The Interaction of Reaction-Bonded Silicon Carbide and Inconel 600 with a Nickel-based Brazing Alloy. Met. Trans. A Vol. 20A (1989). pp. 1803- 1809.

112 Y. Miyazawa, T. Ariga, Brazing of Inconel 600 and SUS304 Stainless Steel with used of Rapidly Solidified Nickel-base Brazing Foil, J. Mat. Trans. Vol. 33(5) (1992), pp. 509-518.

113 E. Moreau and S.F Corbin, Application of Diffusion Path Analysis to Understand the Mechanisms of TLPB in the Ni-Si-B System. *Metall. and Mat. Trans. A,* Vol. 50(12), pp. 5678-5688, (2019)

114 X.P. Zhang, Y. W. Shi, A dissolution model of base metal in liquid brazing filler metal during high temperature brazing, Scripta Materialia Vol. 50 (2004). pp. 1003-1006.

115 A. Y. Shamsabadi, R. Bakhtiari, G. Eisaabadi, TLP Bonding of IN738/MBF20/IN718 System. J. Alloys and Compounds, Vol. 685 (2016) pp. 896-904.

116 J. M. Chapman, Determining the Influence of Surface Preparation on Transient Liquid Phase Bonding of Inconel 718/BNi-2. M.A.SC. Thesis Dissertation, Dalhousie University (2019).

117 Schneider, C. A.; Rasband, W. S. & Eliceiri, K. W. (2012), "NIH Image to ImageJ: 25 years of image analysis", Nature methods 9 (2007): 671-675.

APPENDIX A

Diffusion Path Analysis

In multicomponent systems such as ternary phase diagrams, a variety of phase, intermetallics and morphologies may form yielding layered sequences. Such results can be qualitatively interpreted using the concept of a *Diffusion Path* – A plot of on an isothermal diagram corresponding to the original interface of a diffusion couple. Established conventions for the technique were originally proposed by Clark et al. [104], which cover all possible morphologies, interfaces and compositional gradients possible in ternary systems. The greatest implication of ternary systems with regards to the resulting microstructure is the additional degree of freedom awarded, allowing for the existence of two-phase layers. The accepted conventions are provided below as a reference as described in the work of Clark et al [104-105].

1. The end points of a diffusion path correspond to the initial compositions of the respective diffusion couple halves (assuming infinite boundary conditions, semi-infinite). Otherwise, the composition at the surface is assumed. Furthermore, the diffusion time should be provided if composition is time dependent, see Figure A-1 below.

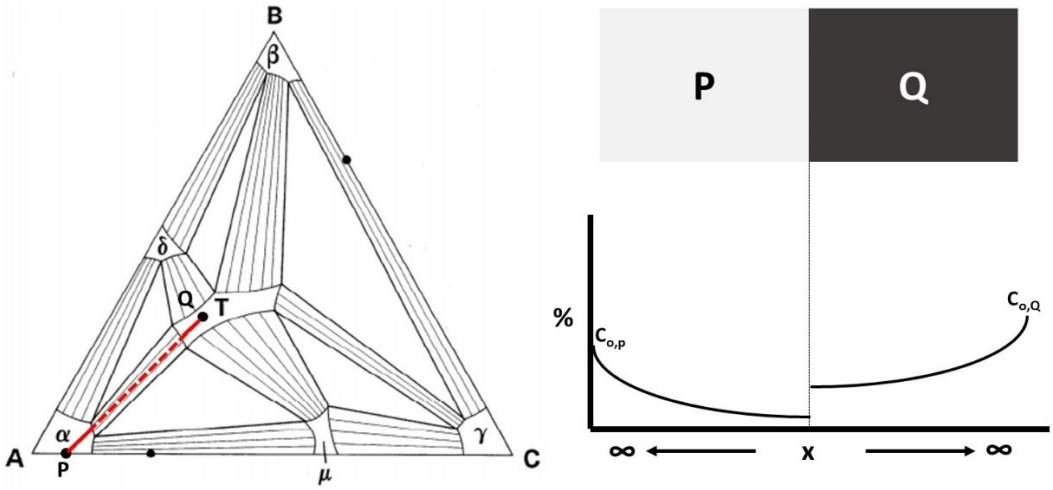

Figure A-1 – Schematic illustrating depicting diffusion path convention 1 [104-106].

2. A solid line (path) within a single-phase field indicates an existing layer of the phase in the couple (Figure A-2).

3. A dashed line (path) within a two-phase region denotes an interface b/w two phases (the composition of each indicated by tie lines), as shown in Figure A-2.

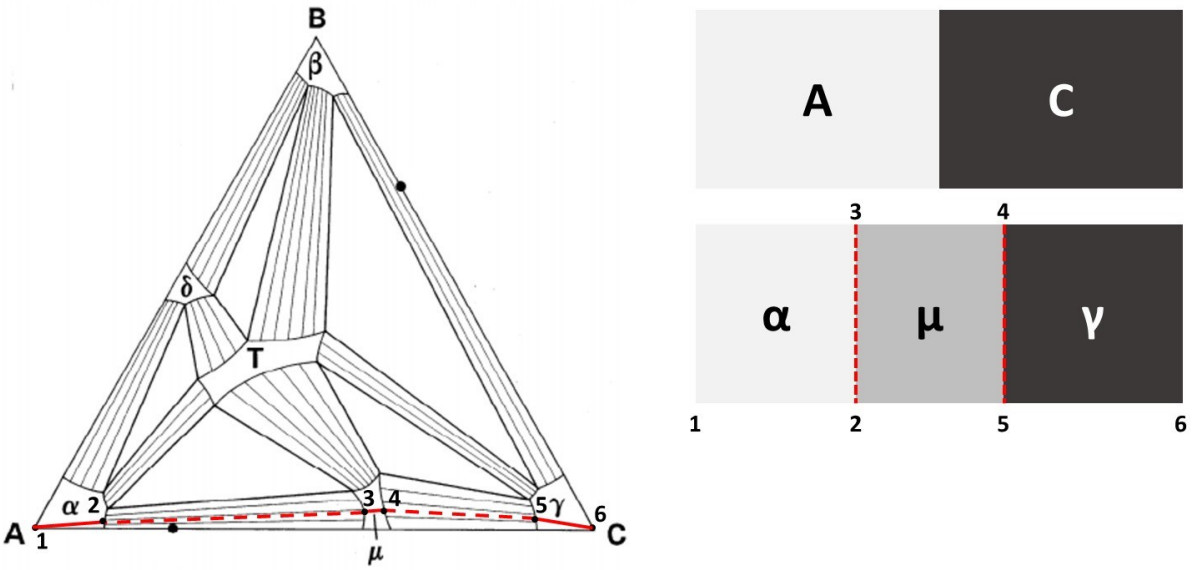

Figure A-2 – Schematic illustrating depicting diffusion path conventions 2 and 3 [104-106].

4. A solid line crossing a two-phase field such that tie-lines are "cut" represents a local equilibrium which exist in a columnar (dendritic) two phase region. (1) A path originating from a single-phase field enters and exits a two-phase region into a different single-phase region indicates a two-layer interface with interpenetrating columns of each phases rooted to their respective single-phase layers. (2) If the solid line leaves the two-phase region into a 3-phase field, the two-phase region is bounded by single-phase layers (different) or two-phase layers with a common phase or combination of both (Figure A-3 and A-4).

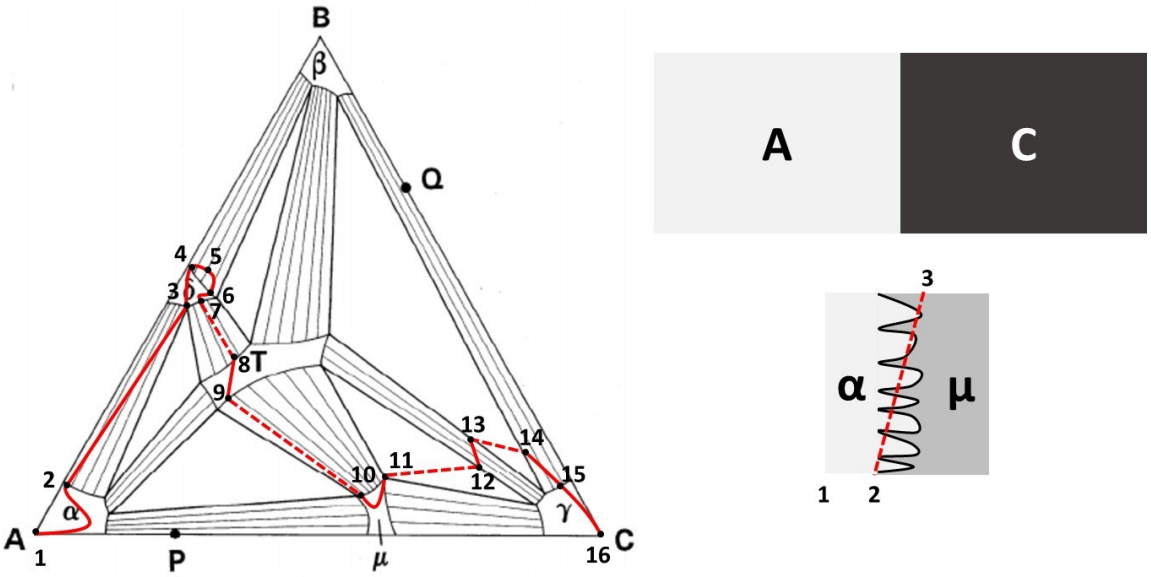

Figure A-3 – Schematic illustrating depicting diffusion path convention 4 [104-106].

5. A dashed line crossing a three-phase field indicates an interface possessing an equilibrium between three phases i.e. a two-phase layer adjacent to a single phase or adjacent two-phase layers with a common phase. (always dashed b/c 3-layer interface impossible, DOF)

6. A microstructure consisting of isolated precipitates (secondary phase within/surrounded by primary phase) transpires, in the event a solid path/curve crosses tie lines in a two-phase return to its original single-phase field.

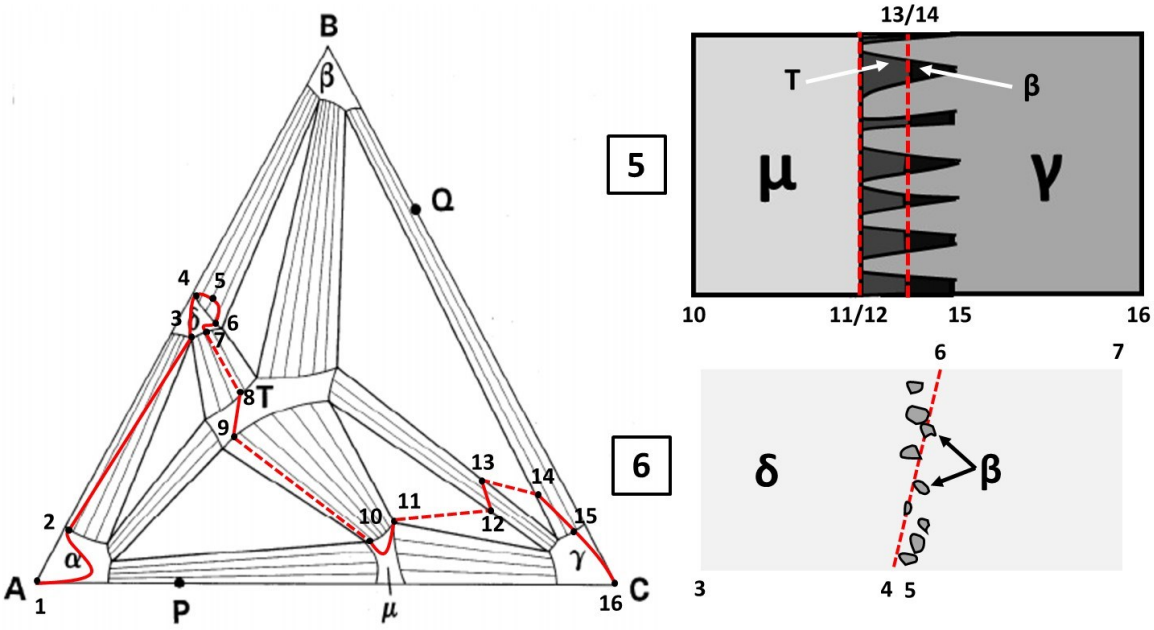

Figure A-4 – Schematic illustrating depicting diffusion path conventions 4(2), 5 and 6 [104-106].

7. Calculated lines are represented as dash-dot lines.

In reality, paths; 2-3, 12-13 and 14-15 are most likely curved rather than straight. Moreover, in certain cases a path may reorient itself parallel to the tie lines (thereby necessitating a dash line). The conventions cover all possible morphological features likely encountered in any ternary diffusion couple. It should be noted however, that such data assumes equilibrium conditions and therefore do not account for kinetics effects (layer thickness, boundary velocity), generally limiting analysis to qualitative predictions.

At first thought it may appear as though an essentially infinite number of diffusion paths may exist for a certain ternary system, as the only main constraint applies to the phase rule (DOF), however the requirement for mass conservation provides an additional constraint which greatly reduces the overall number of possible paths, as shown below in Figure A-5:

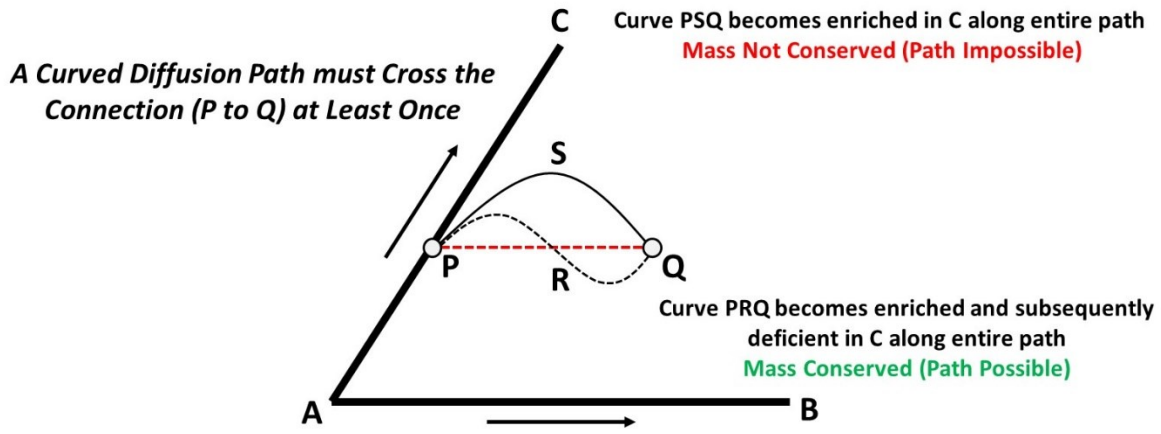

Figure A-5 – Schematic revealing the requirement for mass conservation for a given diffusion path.

Lastly, mass conservation (or mass balances) enables the prediction of layer thickness given proper assumptions related to the relative diffusivity of a phase i.e. the faster the diffusion rates the thicker the layer. The slower diffusion phases are therefore rate limiting, acting as diffusion barriers. Such analysis requires knowledge of the diffusivity of a phase at a given temperature, which, in many cases are unavailable for multicomponent systems.

APPENDIX B

Image Analysis

Image analysis was adopted in certain situations as a means of obtaining valuable information regarding the extent of TLPB based on the redistribution of boron from the liquid phase to the BM as borides (DAZ). Assessing TLPB manner provides an effective method of observing precipitation or initial boron uptake phenomena which transpire rapidly during heating which cannot be directly ascertained via DSC. The method relies on the fact that through the course of TLBP Boron is merely redistributed from the progressively diminishing quantity of liquid phase to the BM where it precipitates as borides – constituting the DAZ. Given that the solubility of B in γ-Ni is negligible, which in the present case is valid given the small dimensions of the DSC couples, TLPB. Thus, a known initial quantity/mass of FM one can predict the extent of TLPB based on the area/volume fraction of borides as a simple mass balance conservation of mass.

Image analysis was limited to SEM image as such images displayed considerably better contrast between the borides and γ-Ni. In most instances the image were acquired at 600x magnification, which was chosen principally based on the magnification required to resolve the majority of the DAZ, however in situations involving quenched specimens with very fine DAZs, magnification of 1000x were necessary. Image analysis was performed using Image J analysis software [117] and involved the following steps:

1. Rotating the image to obtain a DAZ/ISZ interface equidistant from the top of the image.
2. Cropping of the image such that the top of the image is immediately adjacent to the first borides encountered (top to bottom).
3. Varying the color threshold to best distinguish the boride phases (red) from the γ-Ni (Black), see Figure B-1.
4. Overlaying the modified image with a rectangular measurement "Box" the entire width, w of the image (≈ 212 μm at 600x or 127 at 1000x) and a height of Δh (3.3 μm at 600x, 1.98 μm at 1000x). See Figure B-2.
5. Performing the "Analyze Particles" operation using the included add-on given the following conditions:
    a. Size of Particles included in analysis: 0 to infinity
    b. Circularity: 0.0 to 1.0
    c. Include Holes: No

6. Repeating the previous step (4), however after moving the measurement volume down a distance of Δh, e.g. given Δh of 3.3 µm, the first measurement would be performed between 0 and 3.3 µm in depth, the 2nd measurement between 3.3 and 6.6 µm in depth, etc. until the bottom of the image is reached.
7. The summarized data are computed as the percentage of the area occupied by the borides (red) versus the total area e.g. Δh x w for each measurement. All data were then transferred to a spreadsheet for further analysis.

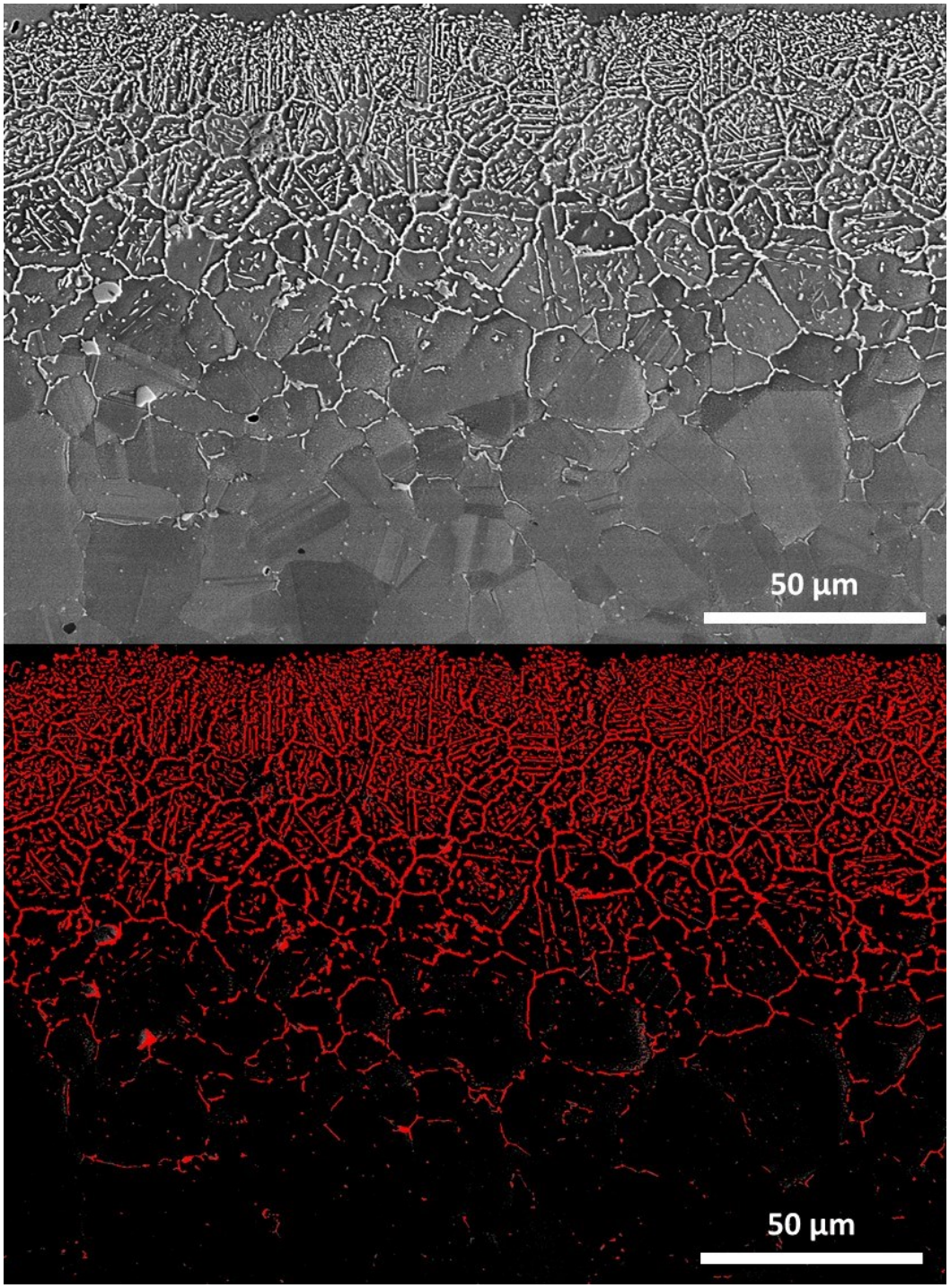

Figure B-1 – Example of application of color threshold to distinguish borides (red) from γ-Ni (black) in DAZ. All images taken at 600x, 15kV/15um and using mixed EBSD (70%).

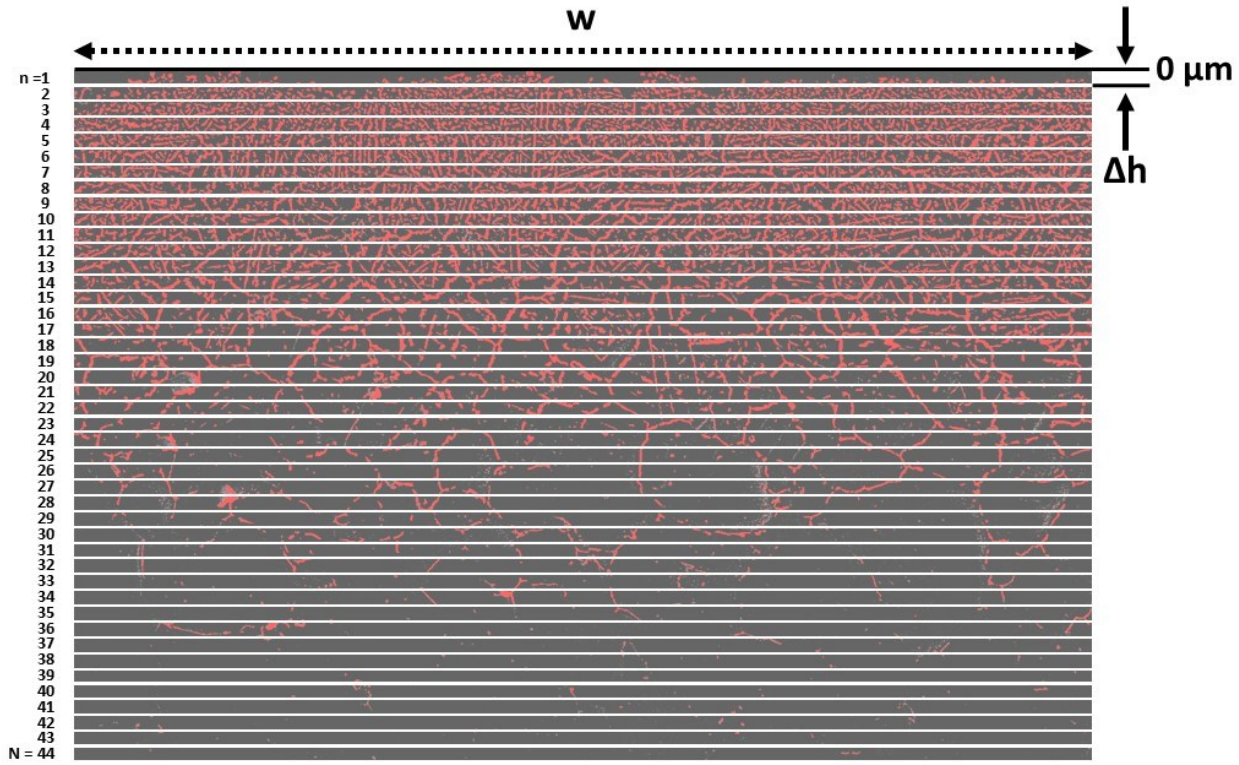

Figure B-2 – Example of sampling technique used to determine obtain volume fraction values. rectangular segments represent each (n) measurement volume.

Once an image was fully examined and transferred to spreadsheeted format, subsequent data analysis involved the following:

1. Plotting data: Volume percent borides (y-axis) cumulative depth e.g. $\Sigma\Delta h_i$ (x-axis). Although the results are actually area fraction measurements, the volume fraction and area fraction become interchangeable given the reasonable assumption of a homogenous radial distribution of the borides within the specimens.
2. In most instances, the DAZ/ISZ interface was slightly non-planar and therefore yields significantly lower volume % boride values as the measurements inadvertently include the volume occupied by the boride-free ISZ. Therefore, to remedy this issue the initial values were replaced by mean values obtained within the DAZ directly adjacent to the interface which clearly did not contain ISZ.
3. Arithmetic Mean: In certain cases, arithmetic mean values were obtained in order to simplify subsequent calculations as the volume % of borides generally decreases with increasing depth. This simply involved dividing the sum of all volume % values by the number of measurements e.g. $\Sigma V_i/N$.

4. Left-Riemann Summation: The integration of the volume % boride profiles provides a means of approximating the total quantity of Borides/Boron in the DAZ and can therefore be used alongside the DSC data to monitor the extent of TLPB. Given that the value of Δh are known, calculation simply involved multiplying the volume % boride by Δh_i for each individual measurement then summing the values.

APPENDIX C

Additional Quenched Microstructures

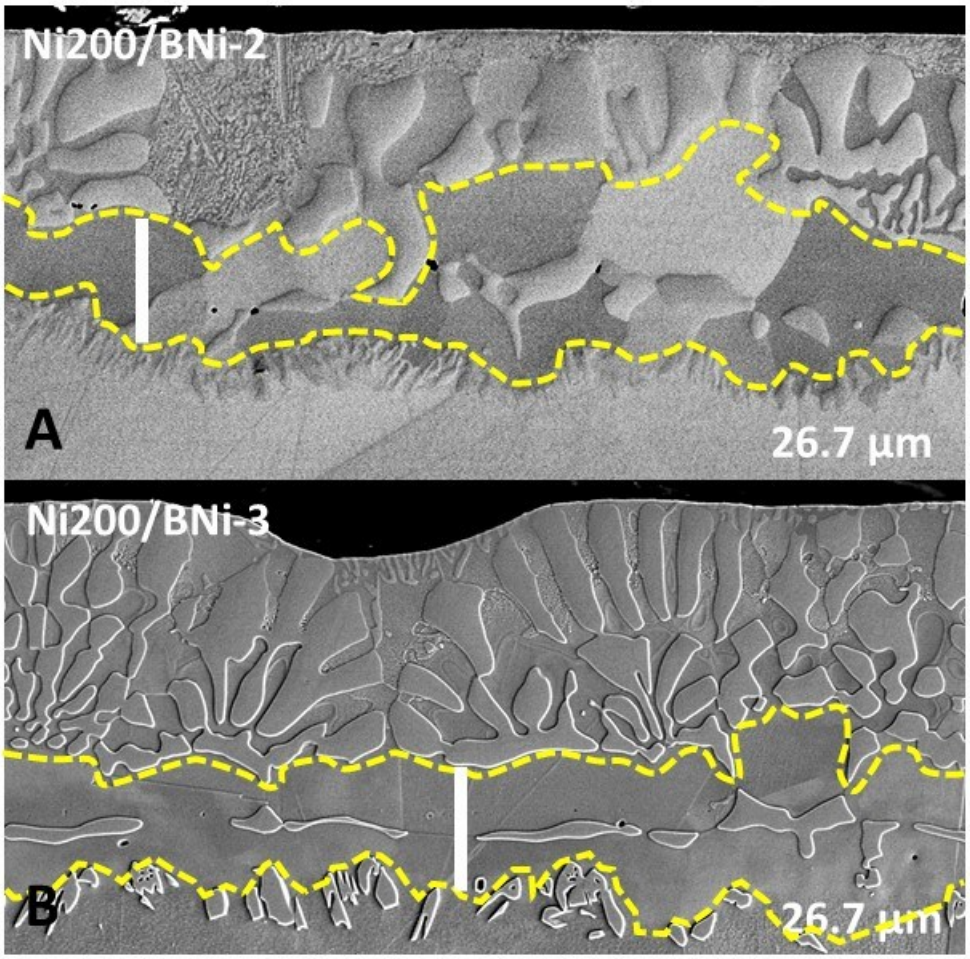

Figure C-1 - Joint region of quenched Ni200/BNi-2 (A) 1050°C and /BNi-3 (B) 1075°C specimens. Solid line representative of experimentally determined W_{ISZi} values, dashed lines denotes ASZ/ISZ and ISZ/DAZ interfaces. Approx. liquid duration: 6 - 8 min.

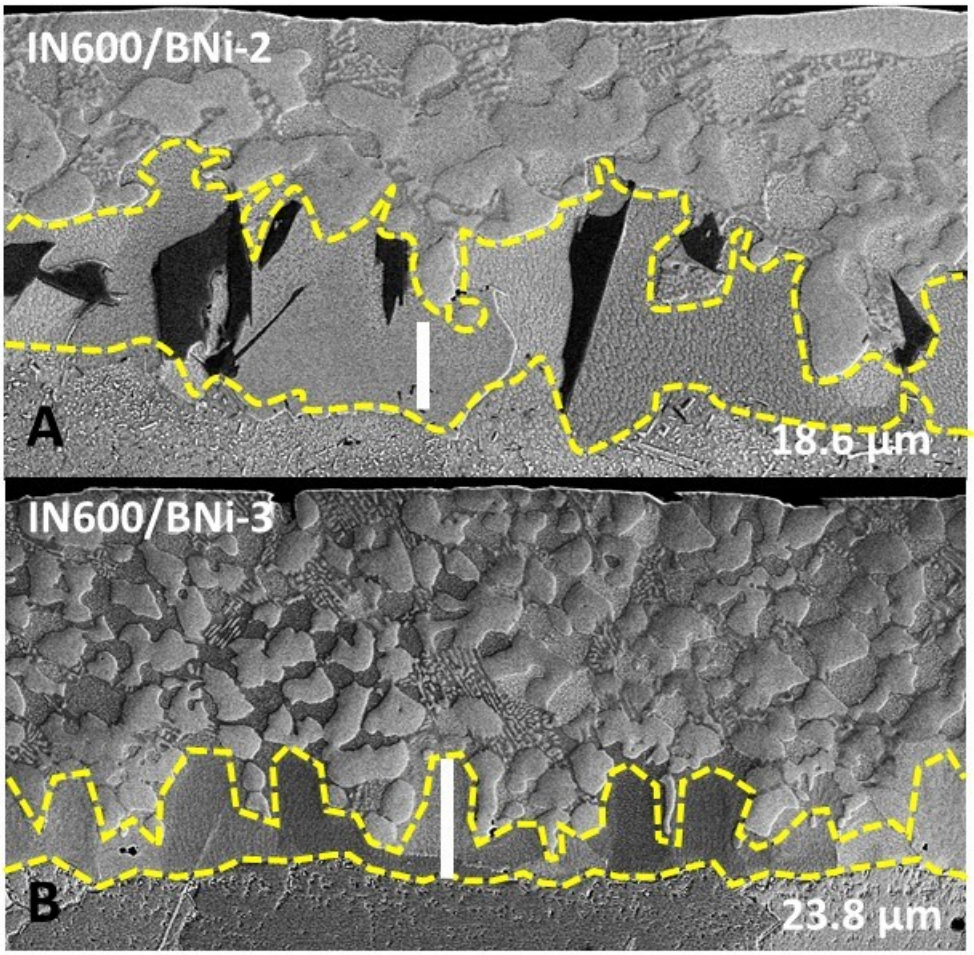

Figure C-2 - Joint region of quenched IN600/BNi-2 (A) 1050°C and /BNi-3 (B) 1075°C specimens. Solid line representative of experimentally determined W_{ISZi} values, dashed lines denotes ASZ/ISZ and ISZ/DAZ interfaces. Approx. liquid duration: 6 - 8 min.

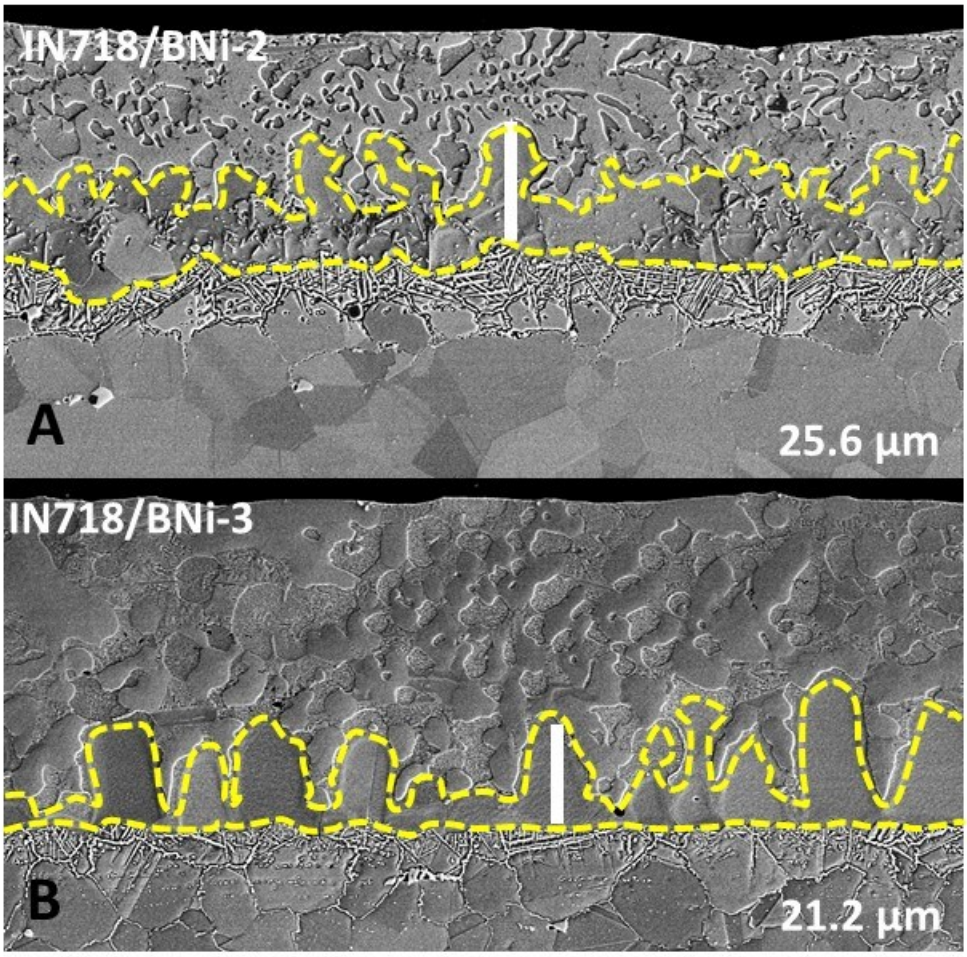

Figure C-3 - Joint region of quenched IN718/BNi-2 (A) at 1050°C and /BNi-3 (B) 1075°C specimens. Solid line representative of experimentally determined W_{ISZi} values, dashed lines denotes ASZ/ISZ and ISZ/DAZ interfaces. Approx. liquid duration: 6 - 8 min.

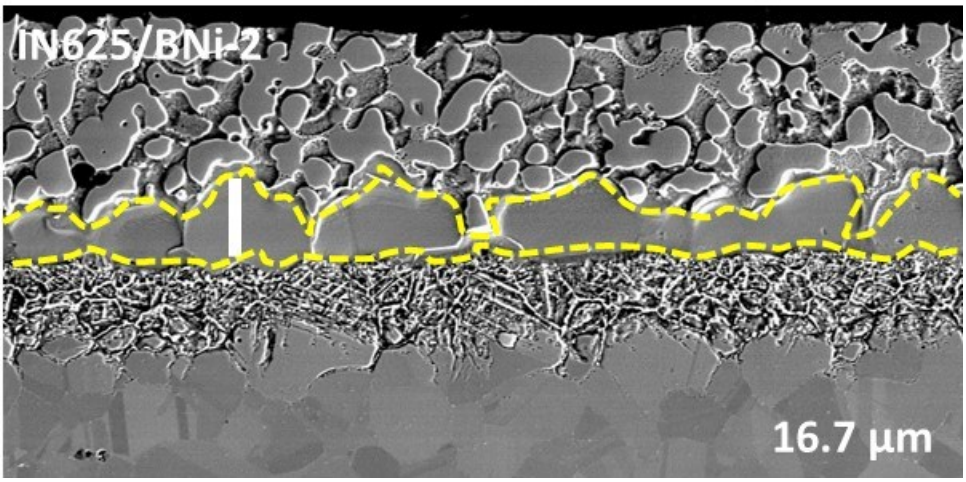

Figure C-4 - Joint region of quenched IN625/BNi-2 at 1050°C specimen. Solid line representative of experimentally determined W_{ISZI} value, dashed lines denotes ASZ/ISZ and ISZ/DAZ interfaces. Approx. liquid duration: 6 - 8 min.

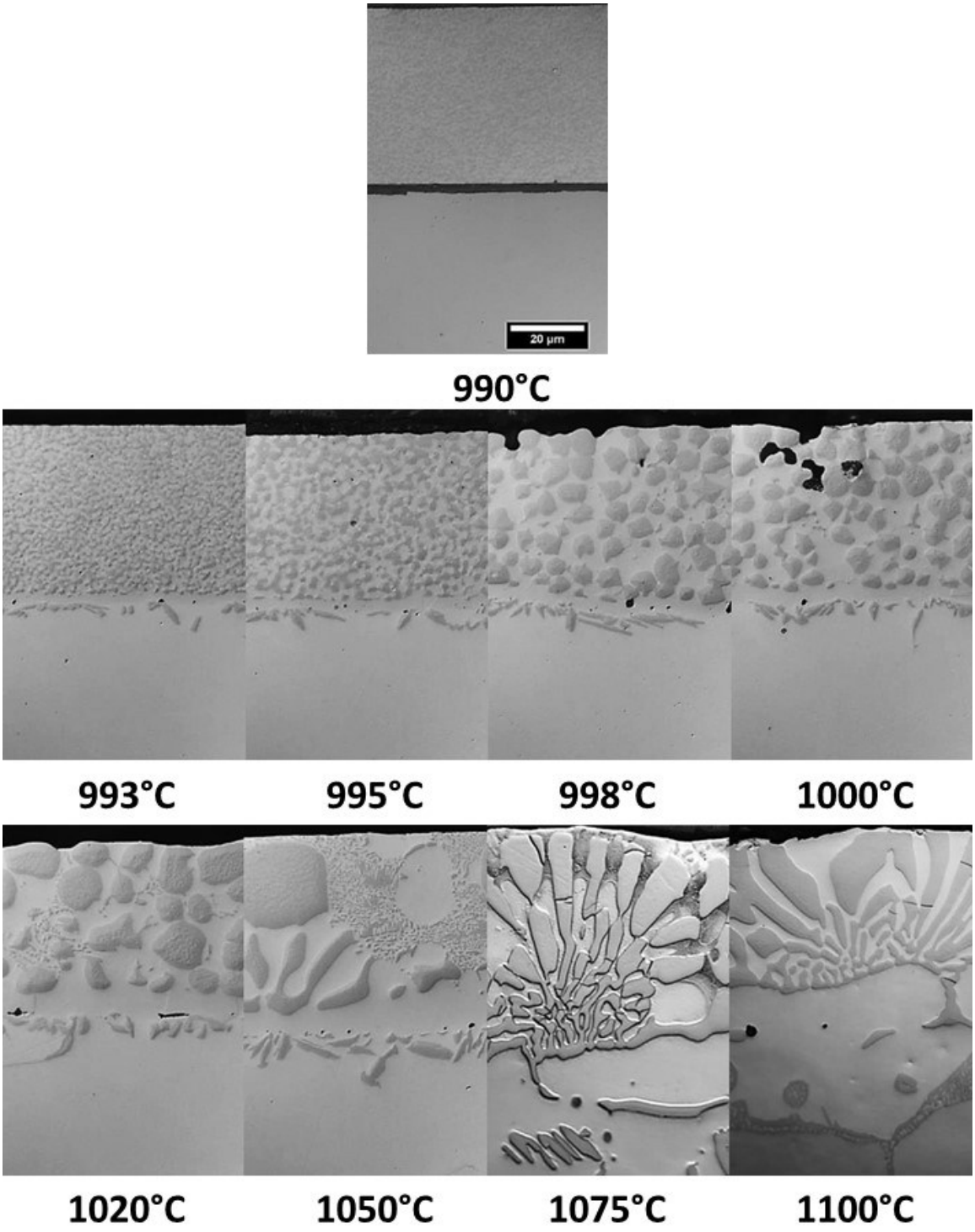

Figure C-5 - Evolution of joint region for Ni200/BNi-3 half-joint couples with increasing temperature. Microstructure obtained after quenching at corresponding temperatures.